A Systems Approach to Engineering Cancer Nanotechnologies

By

Geoffrey von Maltzahn

M.S. Bioengineering,
University of California, San Diego 2005

S.B. Chemical Engineering,
Massachusetts Institute of Technology 2003

Submitted to the Harvard-MIT Division Health Sciences and Technology in Partial Fulfillment of the Requirements for the Degree of

DOCTOR OF PHILOSOPHY IN BIOMEDICAL ENGINEERING

at the

MASSACHUSETTS INSTITUTE OF TECHNOLOGY

August 2009

Signature of Author:_____
Division of Health Sciences and Technology
August 20, 2009

Certified by:_____
Sangeeta N. Bhatia.
Howard Hughes Medical Investigator
Professor of Health Sciences & Technology/Electrical Engineering & Computer Science
Thesis Supervisor

Accepted by:_____
Ram Sasisekharan.
Edward Hood Taplin Professor of Health Sciences & Technology/Biological Engineering
Director, Harvard-MIT Division of Health Sciences and Technology

A Systems Approach to Engineering Cancer Nanotechnologies

By
Geoffrey von Maltzahn

Submitted to the Harvard-MIT Division Health Sciences and Technology on 8/20/2009 in Partial Fulfillment of the Requirements for the Degree of Doctor of Philosophy in Medical Engineering

Abstract

Nanotechnology has tremendous potential to improve the selectivity of cancer detection and therapy. Over the past three decades, advances in nanomaterial synthesis have produced impressive nanostructures with unique electromagnetic and therapeutic properties. These represent a powerful toolkit of building blocks through which multi-component nanosystems could be constructed. Yet, while biological systems produce higher-order functions through coordinated interactions between multiple nanoscale components, biomedical nanotechnologies to date have largely lacked systems-scale complexity. Considering that typical *in vivo* doses of diagnostic or therapeutic nanoparticles exceed 1 trillion nanoparticles, there is considerable opportunity to construct multi-component, interactive nanoparticle systems that perform sophisticated new functions *in vivo*.

This thesis takes a systems approach to engineering cancer nanotechnologies, where interactions between multiple nanoparticle populations are designed to generate emergent system properties for enhancing the sensing and targeting of cancer cells.

In the first section of this thesis, *direct* nanoparticle interactions are engineered to produce emergent properties for cancer sensing. Three classes of magnetic particles are developed that respectively enable: MRI detection of single cancer-associated proteases, performance of logical AND/OR operations using two cancer-associated proteases, and reversible sensing of antagonistic kinase/phosphatase enzyme pairs.

In the second section of this thesis, *indirect* mechanisms of nanoparticle interaction—where nanoparticles communicate at a distance via intermediates—are engineered to amplify nanoparticle targeting to regions of tumor invasion *in vivo*. Two nanosystems are synthesized wherein intravenously administered nanoparticles that have successfully targeted tumors broadcast the tumor's location to other nanoparticles in circulation to recruit their amplified local accumulation. In mice, one of these systems intravenously delivers >40-fold higher drug doses to tumors than non-communicating controls, leading to durable repression of tumor growth and significantly improved host survival.

Together, these systems highlight the potential for interactive nanoparticle systems to perform highly complex functions *in vivo*. In contrast to the current strategy of injecting large populations of nanoparticles that carry out identical, often competitive functions *in vivo*, this work promotes a paradigm of 'systems nanotechnology,' directed toward the construction of nanoparticle systems that produce emergent behaviors for enhancing *in vivo* diagnostics, regenerative medicines, and therapeutics.

Thesis Supervisor: Sangeeta N. Bhatia
Title: Professor

Acknowledgements

I am extraordinarily lucky to have been guided by wonderful mentors, friends, and family throughout my life. I owe you all of my gratitude and love.

To MIT: A truly special place, packed with brilliant, curious, and fun people and blessed with the fortune of being nestled in an area with horrid enough weather to keep everyone focused. Thank you for exposing me to enough confidence-shattering problems to teach me how to remain dedicated to them through periods of immense frustration. Stay tough, MIT.

To the Harvard-MIT Division of Health Sciences and Technology (HST): Thank you for introducing me to the fascinating world of biomedical problems and for challenging me to solve them.

To Sangeeta Bhatia: Foremost among the many inspiring mentors and colleagues in my life is Sangeeta. Thank you for your outstanding guidance, for sharing your passions for science and medicine with me, and for pushing me to follow my curiosity, even when sailing into unfamiliar territories. Through forays in drug release, lipid trafficking, x-ray actuated chemistry, remote-controlled enzymes, self-replicating therapeutics, autocatalysis, oligonucleotide delivery, bipolar nanoparticles, mass spectrometry, and Raman-coded materials, Sangeeta helped me to find my lovely way to the work described in this thesis. Thank you for the hours and hours of advice, for asking tough questions, and for being a dreamer.

To Shuguang Zhang: Your curiosity and energy are unparalleled. Thank you for taking me into your group as an inexperienced undergraduate 8 years ago and for generously sharing your fascination with nature with me. From you, I learned the importance of asking big questions and seeing things for what they could be.

To so many other mentors at MIT and beyond: Angela Belcher, thank you for your guidance, generous support, and inspiring perspective on biology. Michael Sailor at UCSD and Erkki Ruoslahti at the Burnham Institute for being fantastic collaborators, excellent mentors, and for saving me a lot of time by helping me shape my ideas before trying them out. Preetinder Virk, thank you for your high expectations and playful sense of humor as my undergraduate advisor. Jefferson Tester, for giving me perspective on how chemical engineers can impact this world. Michael Mohr for his wonderful lectures and dedication to helping students start their careers.

To everyone in the Laboratory for Multi-scale Regenerative Technologies (LMRT) both past and present: I couldn't have asked for a better bunch to share the ups, downs, confusions, false certainties, and authentic moments of success in research. In particular, to Todd Harris—my greatest thanks for being an incredible friend, a generous colleague, and for letting me watch you consistently do in a day what takes most people a week. Thanks most of all for staying even-keeled and keeping things fun, even when we felt like we were engineering nanoparticles to flush money down the toilet. To Joe Park, an honorary lab member and the single most productive individual I have ever met. Joe, you are an amazing collaborator, a great friend, and you just plain make things happen. I'm honored to have had the chance to work with you. To Alice Chen, you are the best—thanks for all the long chats and for telling me when I looked like death and needed to get some sleep. Stay brilliant and wonderful and everything else. To all of my UROPs, thank you for your incredible dedication, your excitement and patience, and for making me get organized now and then. I can't wait to see the awesome things you'll do next. To Austin Derfus, thanks for patiently getting me started and teaching me everything. I couldn't ask for a better guide to the world of 'nano.' To Amit Agrawal, thanks for your enthusiasm and lots of fun ideas. Salman Khetani, thanks for your humor, perspective, and good advice. To Dave Wood, for being no-nonsense and pretty dang smart. To Yin Ren for blossoming under my tutelage and being a lot of fun to work with. To a string of terrific lab managers: Jenn Felix, Kathryn Hudson, and Steve Katz, who kept things running smoothly, even when every single order was marked ASAP. To everyone else in LMRT—thanks so much!

Outside of lab, I have many friends to thank. The most important is Maxine, my very best friend. Thank you for being surprising, encouraging, hilarious, and both an honest critic and loving guide to me through this work. For these reasons and many more, I adore you. To my other friends, thank you for the great times, near and far. Please allow me to thank you formally over a drink.

Finally, this thesis is dedicated to my wonderful parents, sister Julia, and brother Phil: Without your guidance, patience, unwavering belief in me, and so much more this thesis would not exist. Thank you so much.

Biographical Information

EDUCATION

MASSACHUSETTS INSTITUTE OF TECHNOLOGY, Cambridge, MA *2005-Present*
Harvard-MIT Division of Health Sciences & Technology
Doctor of Philosophy (Ph.D.) Candidate, Medical Engineering, Medical Physics
Whitaker and NSF Graduate Fellow

UNIVERSITY OF CALIFORNIA, SAN DIEGO, LA JOLLA, CA *2005*
Masters of Science, Bioengineering

MASSACHUSETTS INSTITUTE OF TECHNOLOGY, Cambridge, MA *2003*
Bachelors of Science, Chemical Engineering; Biomedical Engineering, Minor

AWARDS AND HONORS

- Lemelson-MIT $30,000 Student Prize for inventiveness and innovation (2009)
- Harvard-MIT Martha Gray Prize for Excellence in Research (2009)
- Biomedical Engineering Society (BMES) Graduate Research Award (2008)
- MIT's Outstanding Undergraduate Research Mentor (2007)
- National Science Foundation Graduate Research Fellowship (2006)
- Hertz Fellowship Finalist (2005)
- Whitaker Doctoral Fellowship (2004)
- Randolph G. Wei Award for "MIT's most outstanding contribution in undergraduate research at the interface of life sciences and engineering" (2003)
- MIT Robert T. Haslam Cup for "outstanding professional promise in Chemical Engineering" (2003)
- Presented research to members of the U.S. Congress at 2003 Coalition for National Science Funding as MIT representative (2003)
- Mass High Tech: The Journal of New England Technology's "Whiz Kid" in Best and Brightest Engineering Students (2003)
- Johnson & Johnson/MIT Excellence in Biomedical Engineering Research Prize (2003)
- MIT Haslam Scholar for academic excellence in Chemical Engineering (2002)
- MIT Bioengineering Undergraduate Research Award (2002)
- MIT Haslam Scholar for academic excellence in Chemical Engineering (2001)
- Federal Water Quality Association Harvey Olem Scholarship (2000)
- Cardinal College Scholarship (2000)
- Presented summer research to US Surgeon General at NIH Poster Day (1998)

PUBLICATION RECORD

Submitted or Published Journal Articles:

1. G. von Maltzahn, J.H. Park, Schwöppe, E. Ruoslahti, R. Mesters, W. Berdel, E. Ruoslahti, M.J. Sailor, and S.N. Bhatia. "Nanoparticles that Communicate to Amplify Tumor Targeting *In vivo*." (*Submitted*) 2009.

2. T.J. Harris, G. von Maltzahn, M. Xu, P. Fung, S. Mo, J. Green, D. Anderson, and S.N. Bhatia, "Tumor-Responsive Electrostatic Coatings for Polymer Gene Delivery

Nanovectors." (*Submitted*) 2009.

3. A. Agrawal, D.H. Min, H. Zhu, A. Birjiniuk, G. von Maltzahn, T.J. Harris, D. Xing, P. Sharp, A. Charest, and S.N. Bhatia, "Functional Delivery of siRNA in Mice Using Dendriworms." (*Submitted*) 2009.

4. J.H. Park, G. von Maltzahn, L. Ong, A. Centrone, A. Hatton, S.N. Bhatia, and M.J. Sailor. "Cooperative Nanoparticles for the Photothermally-Triggered Delivery of Drugs to Tumors." (*Submitted*) 2009.

5. Z. Poon, S. Chen, A. C. Engler, H. Lee, E. Atas, G. von Maltzahn, and P.T. Hammond. "Ligand-Clustered 'Patchy' Nanoparticles for Modulated Cellular Uptake and *In vivo* Tumor Targeting." (*Submitted)* 2009.

6. G. von Maltzahn*, A. Centrone*, J. H. Park, R. Ramanathan, M. J. Sailor, A. Hatton, and S.N. Bhatia. "SERS-Coded Gold Nanorods as a Multifunctional Platform for Densely-Multiplexed Near-Infrared Imaging and Photothermal Therapy." (*In Press)* ***Advanced Materials*** 2009.

7. J.H. Park, L. Gu, G. von Maltzahn, E. Ruoslahti, S. N. Bhatia, and M. J. Sailor. "Biodegradable Luminescent Porous Silicon Nanoparticles for *In vivo* Applications." (*In Press)* ***Nature Materials*** 2009.

8. J.H. Park, G. von Maltzahn, L. Zhang, A.M. Derfus, D. Simberg, T.J. Harris, S.N. Bhatia, E. Ruoslahti, and M.J. Sailor. "Systematic Surface Engineering of Magnetic Nanoworms for *In vivo* Tumor Targeting." (*In Press*) ***Small***. 2009.

9. G. von Maltzahn, J.H. Park, A. Agrawal, N.K. Bandaru, S.K. Das, M.J. Sailor, and S.N. Bhatia. "Computationally-Guided Photothermal Tumor Therapy using Long-Circulating Gold Nanorod Antennas." (*In Press)* ***Cancer Research***. 2009.
   - This article was the Cover Feature of *Cancer Research*

10. J.H. Park, G. von Maltzahn, E. Ruoslahti, S.N. Bhatia, and M.S. Sailor. "Micellar Hybrid Nanoparticles for Simultaneous Magnetofluorescent Imaging and Drug Delivery." ***Angewandte Chemie***. 47 (38), 7284, 2008.

11. G. von Maltzahn*, Y. Ren*, D.H. Min, J.H. Park, J. Jayakumar, M.J. Sailor, and S.N. Bhatia. "*In vivo* Tumor Cell Targeting with 'Click' Nanoparticles." ***Bioconjugate Chemistry***. 19 (8), 1570, 2008.

12. T.J. Harris, G. von Maltzahn, M.E. Lord, J.H. Park, A. Agrawal, D.H. Min, M.J. Sailor, and S.N. Bhatia, "Protease-Triggered Unveiling of Bioactive Nanoparticles." ***Small***. 4 (9), 1307, 2008.

13. J.H. Park, G. von Maltzahn, M. P. Schwartz, E. Ruoslahti, S. N. Bhatia, and M. J. Sailor. "Magnetic Nanoworms for Tumor Targeting and Imaging." ***Advanced Materials***. 20 (9), *1630*, 2008.
   - This article was the Cover Feature of *Advanced Materials* and highlighted in the *Analytical Chemistry* Currents

14. G. von Maltzahn*, DH. Min*, Y. Zhang, J.H. Park, T.J. Harris, M.J. Sailor, and S.N. Bhatia, "Nanoparticle Self-Assembly Directed by Antagonistic Kinase and Phosphatase Activities." ***Advanced Materials***. 19 (21): *3579,* 2007.

15. A.M. Derfus, G. von Maltzahn, T.J. Harris, T. Duza, K.S. Vecchio, E. Ruoslahti, and S.N. Bhatia, "Remotely Triggered Release from Magnetic Nanoparticles." ***Advanced Materials***. 19 (22): 3932, 2007.

16. G. von Maltzahn, T.J. Harris, J.H. Park, D.H. Min, A. Schmidt, M.J. Sailor, and S.N. Bhatia, "Nanoparticle Self-Assembly Gated By Logical Proteolytic Triggers." ***Journal of the American Chemical Society***. 129 (19): 6064, 2007.
- This article was featured in the *Nature Nanotechnology* Research Highlights.

17. G. von Maltzahn*, T.J. Harris*; A.D. Derfus, E. Ruoslahti, and S.N. Bhatia, "Proteolytic Actuation of Nanoparticle Self-Assembly." ***Angewandte Chemie*** 41 (19): 3161, 2006.
- This article was highlighted as the Cover Feature of *Angewandte Chemie*.

18. G. von Maltzahn, S. Vauthey, S. Santoso, and S. Zhang, "Positively Charged Surfactant-like Peptides Self-Assemble into Nanostructures." ***Langmuir***. 19: 4332, 2003.

19. P.S. Ruggera, D.M. Witters, G. von Maltzahn, and H.I Bassen, "*In vitro* Assessment of Tissue Heating Near Metallic Medical Implants by Exposure to Pulsed Radio Frequency Diathermy." ***Phy Med Biol***. 48 (17): 2919, 2003.

Book Chapters and Reviews

T.J. Harris, G. von Maltzahn, and S.N. Bhatia, (2007). "Multifunctional Nanoparticles for Cancer Therapy, in Nanotechnology for Cancer Therapy." M.M. Amiji (ed.), Taylor and Francis/CRC Press. (*These authors contributed equally to this publication.)

PATENTS

G. von Maltzahn and S.N. Bhatia. "Interactive Nanosystems for Improved Disease Therapy and Diagnosis." (submitted 2008, pending)

G. von Maltzahn and S.N. Bhatia. "Highly-Parallel Enzyme Profiling *In vivo* Using Mass-Encoded Nanoparticle-Chaperoned Substrate Libraries." (submitted 2007, pending)

J.H. Park, G. von Maltzahn, S.N. Bhatia, M.J. Sailor. Preparation of Magnetic Nanoworms for *In vivo* Tumor Targeting. (Submitted 2007, pending)

J.H. Park, G. von Maltzahn, E. Ruoslahti, S.N. Bhatia, M.J. Sailor. "Method for Preparation of Micellar Hybrid Nanoparticles for Therapeutic and Diagnostic Applications and Compositions Thereof" United States of America Serial No. 61/075,144, Filed June 24, 2008.

C. M. Marcus, J. Marmurek, J. W. Aptekar, and G. von Maltzahn, "Telemetry through Remote Detection of Nanoparticles" United States of America Serial No. 61/020,248, Filed January 10, 2008.

A. Agrawal, T.J. Harris, G. von Maltzahn, and S.N. Bhatia "Delivery of Nanoparticles and/or Agents to Cells" United States of America Serial No. 11/952614, Filed December

7, 2007

G. von Maltzahn, A. Derfus, and S.N. Bhatia. "Remotely Triggered Release from Heatable Surfaces." United States of America Serial No. 60/969389, Filed August 31, 2007.

G. von Maltzahn, T. J. Harris, and S.N. Bhatia. "Triggered Self-Assembly of Nanoparticles *In vivo*", United States of America Serial No. 60/780959, Filed March 10, 2006.

PRESENTATIONS

G. von Maltzahn and S.N. Bhatia, "Nanoparticle-to-Nanoparticle Communication for Amplified Tumor Targeting." Platform Presentation. *ACS Invited Submission,* 2009

G. von Maltzahn, "Nanotechnologies for Targeting Energy and Drugs to Cancer." Platform Presentation. *Lemelson-MIT Student Prize Ceremony,* 2009

G. von Maltzahn and S.N. Bhatia, "Nanoparticle Signaling Networks for Amplified Tumor Targeting." *Koch Institute Focus Seminar Series,* 2008.

G. von Maltzahn and S.N. Bhatia, "Photothermal Tumor Destruction using Long-Circulating Gold Nanorod Antennas." Platform Presentation. *BMES,* 2008.

G. von Maltzahn and S.N. Bhatia, "Nanoparticle Self-Assembly Gated by Logical Proteolytic Triggers." Platform Presentation. *BMES,* 2007.

G. von Maltzahn and S.N. Bhatia, "Enzymatic Control of Nanoparticle Self-Assembly." Poster. *HST Forum,* 2007.

G. von Maltzahn and S.N. Bhatia, "Proteolytic Actuation of Nanoparticle Self-Assembly." Platform Presentation. *BMES,* 2006.

G. von Maltzahn and S.N. Bhatia, "Protease Triggered Nanoparticle Self-Assembly." Poster. *HST Forum,* 2006.

TEACHING

University of California, San Diego, *La Jolla, CA* *2004*
TA: Introduction to Bioengineering

- TA of class teaching engineering principles in the context of current UCSD bioengineering research. Instructed and advised team research proposals throughout the term.

Invited Speaker: *2006, 2007, 2009*
Facilitating Effective Undergraduate Research: A development series for graduate student mentors

- Advised on techniques for fostering effective communication between undergraduate students and graduate student mentors.

Research Mentor: MIT Undergraduate Research Opportunity Program *2005- 2009*

Served as direct mentor for 15 undergraduates.

Advised multiple undergraduate research projects and instructed students in experimental design, procedures, and data analysis.

Undergraduate Students Mentored to Date:

Alex Schmidt (2005-2006)
Rose A. Lee (2006-2007)
Lucy Zhang (2005- 2007)
- *2-time recipient of J&J/MIT Excellence in Biomedical Engineering Research Prize*

Ke Zhang (2006-2007)
Peter Fung (2006-2009)
- *Named MIT Amgen UROP Scholar for research excellence*
- *Awarded 2009 MIT J&J/BMES Excellence in Bioengineering Research Prize*

Jacqueline Douglass (2006-2007)
- *Awarded 2009 MIT J&J/BMES Excellence in Bioengineering Research Prize*

Steven Mo (2006-2008)
- *Named MIT Amgen UROP Scholar for research excellence*
- *University of Cambridge-MIT Exchange honoree*
- *MIT Burchard Scholar*
- *Awarded 2009 MIT J&J/BMES Excellence in Bioengineering Research Prize*

Prarthna Desai (2007-2008)
Renuka Ramanathan (2007-2008)
- *MIT Amgen UROP Scholar for research excellence*

Justin Lo (2008)
- *Accepted to Harvard/MIT MD/PhD Program*

Alona Birjiniuk (2008-2009)
Frank Giammo (Summer 2008)
Daniel Kim (2008-2009)
Luvena Ong (2008-2009)
- *MIT Amgen UROP Scholar*
- *Columbia University Amgen Scholar for research excellence*

MaryJue Xu (2008-2009)

Table of Contents

Table of Figures

Chapter 1. Introduction

1.0 Scope

Materials with nanoscale features have tremendous potential to impact both biological discovery and medicine. Nanoparticles (NPs), in particular, exhibit a number of unique electromagnetic, structural, and biological properties compared with their synthetic and natural mesoscopic, microscopic, and molecular complements. These properties include superparamagnetism(*1-3*), surface plasmon resonance(*4-7*), quantum confinement(*8, 9*), inherent catalytic activity(*10*), high surface areas for drug loading(*11-13*), favorable pharmacokinetic profiles(*14-17*), among others. Nanoparticles operate on the length scale of biological system components, yet leverage electromagnetic and biological properties that are often unique from biological components. As such, they have immense potential to improve disease diagnosis and therapy and have already produced a spectrum of technologies for cancer applications. Still, despite matching the size of biological components, biomedical nanoparticle systems have lacked the system-scale complexity of biological systems. **The overall goal of this thesis is to engineer higher-order nanoparticle systems wherein distinct nanoparticle populations interact to generate emergent system properties for enhanced cancer sensing and therapy.**

1.1 Cancer Detection and Therapy

Cancer killed more than 7 million people worldwide in 2002, surpassing the combined toll from AIDS, malaria, and tuberculosis(*18*). By 2020, the World Health

Organization projects over 16 million new cancer cases per year, increased from 10 million in 2000. Combating the growing incidence of cancer will require behavioral changes, improved detection technologies, and more selective and potent treatments.

Currently, cancer diagnosis proceeds from the macro- to the microscale, with progressively increasing diagnostic accuracy and invasiveness. Typically, patients exhibiting the sequelae of cancer, including weight loss, fatigue, nausea, pain, among many others; are identified during a physical exam and sent to undergo serological analysis alongside an imaging session to interrogate structural changes in the suspected regions. Serological quantification of tumor-associated biomarkers provides some initial molecular information regarding the presence of a tumor, but cannot provide a diagnosis in isolation. Clinical imaging modalities in use for cancer, including magnetic resonance imaging (MRI), x-ray computed tomography (x-ray CT), ultrasound, and others; provide structural information and can reveal aberrant regions of tissue growth to help inform subsequent procedures for performing tumor biopsies. Due to the deficit of molecular information provided by these techniques, remote imaging also falls short of providing a definitive diagnosis for the majority of cancers. Further, these techniques have limited capacity to discern early stages of neoplastic disease and to accurately predict tumor margins, where the macroscopic tissue abnormalities that generate MRI, x-ray, and ultrasonic contrast have yet to emerge.

Tumor biopsy provides the most direct molecular diagnosis of cancer, yet is also the most invasive technique. Once tissue has been removed from the tumor and neighboring lymph nodes through surgical, endoscopic, or percutaneous needle extraction procedures, histopatholoical methods are utilized to detect hallmark molecular and phenotypic cancer signs, identify the tissue of origin, grade the degree of differentiation

compared to normal tissue, and assess whether lymphatic metastases have been established. At this point, therapeutic considerations can be determined.

Because the cancers typically emerge as focal diseases, the surgical removal of early masses can be highly successful in containing further spread. Further, when substantial removal of tissue can be tolerated (eg. for tumors arising in skin, lung, breast, or colon), large resections of tumors and invasive margins can be successful in controlling late stage tumors. However, surgery alone is typically insufficient when disease has begun to metastasize and patients are prescribed regimens of radiation (extracorporeal or via implanted brachytherapies) and chemotherapy. Various forms of chemotherapy and radiation have served as the backbone of cancer therapies for the last 30-50 years(*19*). In a few cases, pharmaceutical agents have been able to exploit unique characteristics of cancers to evoke considerable tumor responses with minimal peripheral side effects. For example, the drug imatinib mesilate (or Gleevec^{TM}) precisely inhibits tyrosine kinase activity to extinguish the oncogenic function of bcr-abl fusions in chronic myelogenous leukemia (*20, 21*). However, the major fraction of our modern anti-neoplastic drug arsenal affects cancers via their propensity towards rapid cell division and growth (eg. alkylating, microtubule-inhibiting, DNA-intercalating, and topoisomerase-inhibiting agents, among others)(*19*). This feature of rapid cell division is not exclusive to tumors, however, and systemic exposure of these compounds affects digestive function, bone marrow proliferation, and hair growth.

Despite immense progress towards understanding the biological mechanisms of cancer, there have been relatively few translational advances in our therapeutic armamentarium against cancer(*22*). Particularly, while molecular approaches to

combating bacterial infections have proven an immense success in the past century, this paradigm has struggled to find distinguishing characteristics of cancers that are not also essential for normal tissue functions. A fundamental challenge facing the use of small molecule drugs in isolation for cancer therapy is that the vast majority of administered drugs (up to >99% of the administered dose) distribute in normal tissues and do not accumulate in tumors(*22*). This paradox of utilizing drugs that distribute without preference for focal regions of disease frequently restricts agent dosing to sub-efficacious levels due to systemic toxicity and lowers the barriers to evolving drug resistance.

1.2 Nanoparticle Toolkit for Biomedicine

There are now nearly twenty nanoparticle formulations in clinical trials or clinical practice(*23, 24*). These materials cover a diversity of applications, from cancer imaging and therapy to immunosuppression, antimicrobials, and cosmetics. Nanoparticles may be logically defined as synthetic or biological structures that are larger than molecular species (>1 nm), smaller than microscale complements (<1000 nm), typically smaller than what can be conveniently synthesized via top-down manufacturing methods (<200 nm), and have unique or improved characteristics from their bulk surroundings. To provide a biological perspective for this length scale, small molecules are typically on the order of a few nanometers, proteins are typically between ~5-20 nm, and human cells are generally >10,000 nm in diameter. In addition to properties derived from their ability to operate on the length scale of biological machinery, unique chemical and physical properties emerge in nanomaterials that distinguish them from their molecular and mesoscopic counterparts. Over the past several decades, these unique biological,

pharmacokinetic, chemical, and electromagnetic properties have attracted increasing interest in biomedicine for their potential to empower a diverse repertoire of functions, from ultra-sensitive molecular imaging to disease-targeted multi-drug delivery systems. For cancer in particular, systems of inorganic and/or organic nanoparticles may ultimately provide paradigm-shifting improvements in our ability to remotely detect early neoplastic changes *in vivo* and precisely usher drugs into established tumors with minimal side effects.

1.21 Materials for Cancer Imaging

Nanomaterials have been described that exhibit useful properties for many non-invasive imaging modalities, including agents for magnetic resonance (MR)(*1*), optical(*8, 25*), ultrasonic(*26, 27*), and x-ray computed tomography (CT) imaging(*28, 29*). As one of the earliest nanoparticle imaging agents, superparamagnetic iron oxide nanocrystals were ushered into medical imaging in the early 1980's (*2, 3*). Superparamagnetic nanoparticles are useful in medicine because, while they do not possess aligned permanent magnetic dipoles at room temperature that could drive agglomeration, in the external magnetic field of an MRI, their dipoles are able to efficiently dephase neighboring protons to provide locally-enhanced transverse (T2) relaxation rates compared with surrounding tissues(*30*). This technology has already generated two clinical contrast agents, Feridex IV™ and Combinex™, comprised of iron oxide cores that are surrounded by hydrophilic coatings of the branched polysaccharide dextran. More recent magnetic nanomaterials with enhanced magnetic dipoles and T2 relaxivities have been synthesized to improve MRI detection sensitivities (*31-33*). These new generations leverage increased control of

nanocrystal structure, more magnetic materials, and the use of doping strategies to increase traditional magnetic dipole strength (*31-33*).

Conductive metal nanoparticles such as gold, silver, and copper exhibit the property of plasmon resonance (*5-7*). The mobility of conduction band electrons in these materials enables alternating electro-magnetic fields of appropriate frequencies to drive resonant electron cloud oscillation. This process generates ultra-stable optical absorption coefficients at plasmon resonant frequencies of 10^4-10^6-fold higher than conventional organic fluorochromes(*6*). The frequency of nanoparticle plasmon resonance is a function of the material composition, crystal structure, surface chemistry, and nanoparticle size/shape (*5-7*). This multiparametric origin of plasmon resonance frequency has driven intense research into precise size- and shape-selective methods of synthesizing metallic nanocrystals, resulting in a rich spectrum of highly tunable structures such as core-shell nanoparticles, hollow metallic nanoparticles, and rod-, cube-, pyramidal-, polyhedral- and star-shaped nanoparticles (*7, 34-36*). Collectively, the electromagnetic properties of plasmonic nanomaterials have been harnessed to develop ultra-sensitive diagnostic(*37, 38*), spectroscopic(*39, 40*), and, recently, therapeutic technologies(*41-44*).

The geometric tunabilty of plasmon resonance frequency has provided a facile route towards tailoring the properties of particles for specific applications. In spherical gold nanoparticles, for example, this resonance peak is typically centered around ~520 nm, with relatively little change with increasing size. However, by synthesizing elongated rod-shaped, hollow, or core:shell gold nanoparticles the resonant frequency can be controllably moved throughout the visible and into the infrared (*36, 45, 46*). By tuning nanoparticle plasmon resonance into the near-infrared (~700-900 nm), where *in vivo*

tissue absorption coefficients drop by almost two orders of magnitude from the visible regime, the role of gold nanomaterials for *in vivo* applications has been considerably expanded. While this domain of electromagnetic energy does not provide the whole-body penetration of modalities such as MRI and X-ray CT, it can provide highly detailed molecular imaging within approximately a centimeter of the excitation source. Gold nanoshells (structures with a thin gold shell surrounding a dielectric silicon dioxide inner core) and gold nanorods have been utilized as contrast agents for the emerging medical imaging modalities of optical coherence tomography and photoacoustic imaging (*47-50*). Carbon nanotubes have also been shown to have useful near-infrared absorbance for photoacoustic imaging applications, but concerns of their *in vivo* toxicity have slowed potential clinical applications (*51, 52*). Given that gold nanomaterials (both molecular and colloidal) have been utilized safely in rheumatoid arthritis therapies for over 50 years(*53*), these materials are likely to have attractive safety profiles for clinical applications.

Fluorescent nanomaterials offer another useful imaging modality for interrogating biological behaviors. Organic fluorophores have been utilized in a variety of biological settings, both *in vitro* and *in vivo* for decades. In semiconductor nanoparticles with dimensions below the Bohr exciton radius, the distance in bulk materials between an excited electron and hole pair, quantum confinement occurs, which can produce highly efficient photoluminescence(*9, 54-57*). Quantum confinement in semiconductor nanoparticles has produced imaging agents with superior fluorescence intensity, enhanced photostability, and narrower emission spectra compared with organic fluorescent agents, as well as size-tunable fluorescence emission (*58*). By leveraging

these properties, semiconductor nanoparticles have already facilitated novel *in vivo* telemetric and diagnostic studies in mice, but clinical translation of these materials will require compositions without the toxic heavy-metals that are commonly utilized in their synthesis (*54, 58*). The most commonly used semiconductor nanoparticles are zinc sulfide-capped cadmium selenide quantum dots, but other quantum dots have been synthesized indium arsenide, indium phosphide, and silicon (*59*). The most useful of these materials are those that enable near-infrared imaging, due to the reduced optical attenuation of excitation and emission light *in vivo(60)*. As efforts to identify new safe materials continue to progress, these materials may usher a new frontier of optical molecular imaging technologies.

Nanoscale contrast agents have also been developed for the established clinical modalities of ultrasound and x-ray computed tomography (CT). Ultrasound contrast agents are typically gas-filled microbubbles that harness the acoustic impedance mismatch at gas: liquid interfaces to generate amplified ultrasonic reflectance(*61*). These agents are administered intravenously to provide vascular contrast and have been investigated for localized delivery as well through remote-controlled acoustic cavitation (*62*). Nanoscale agents have also been developed for target-mediated ultrasonic contrast enhancement (*63, 64*). X-ray CT reveals tissue density differences via changes in absorption of applied x-rays. Molecular contrast agents based on iodine have been utilized clinically due to iodine's high biocompatibility and relatively high atomic number (z=53). Recently, the increased atomic number and high material density of gold (z=79, ρ=19.3 g/cm^3) and bismuth sulfide (Bi z=83) nanomaterials have attracted interest

for x-ray CT angiography and a few nanoparticle reagents have been developed for *in vivo* angiography and lymph node detection (*28, 29, 65*).

1.22 Materials for Cancer Therapy

Nanotechnologies can have intrinsic therapeutic properties imparted by their carrier's structural, electromagnetic, and biochemical properties, or they can have therapeutic properties that are extrinsically imparted by biomolecules encapsulated within them or conjugated to their surface. In the latter category, nanoparticles provide the opportunity to improve upon the efficacy of molecular cancer therapies by controllably encapsulating, protecting, and programmably releasing drugs in target sites. In this manner, the potential also exists to apply pharmaceuticals with favorable disease activities, but which exhibit insufficient water solubility or excessive off-target toxicity as free drugs, in an appropriately designed nanoscale carrier.

One of the first classes of synthetic nanoparticles to reach the clinic for cancer therapy was drug-loaded liposomes. Liposomes are nanoscale carriers of various sizes with an internal aqueous compartment that is separated from the surrounding media by at least one enclosed lipid bilayer. Inspired by the structure of cellular membranes and internal organelles, liposomes have been desirable carriers due to their biocompatibility, ability to encapsulate hydrophobic and hydrophilic drugs, potential to house multiple internal compartments, and amenability to surface modification (*66-68*). To improve blood circulation times *in vivo*, lipids bearing polymers such as polyethylene glycol (PEG) became widely utilized in carrier synthesis (*69, 70*). These polymers deter protein opsonization to nanoparticle surfaces to delay macrophagic carrier recognition. The clinical formulation of liposomes, Doxil^{TM}, carries the chemotherapeutic doxorubicin

within a highly PEGylated lipid bilayer. Doxorubicin is a potent anti-tumor agent, whose cardiac toxicity has limited its clinical use. By sequestering this drug within liposomal carriers, cardiotoxicity was significantly diminished—enabling patient tolerance of higher drug doses and facilitating tumor-specific delivery. These first generation carriers have been engineered to encapsulate a diversity of drugs and slowly release them after administration (*71, 72*). Next-generation formulations aim to specifically accelerate drug release kinetics in tumors via enzyme destabilization, remote actuation, pH changes, or combined administration of enzyme-expressing bacteria to intensify the peak active drug concentrations in tumors and improve the potency of carriers (*72-76*).

Polymer-based vesicles resembling the structure of liposomes have been synthesized as well. These 'polymerosomes' are constructed out of diblock copolymers that are considerably larger than natural lipids in size, yet self-assemble into bilayer structures in a similar fashion to natural lipid bilayers(*77*). Due to the tunabilty of diblock polymer compositions, polymerosomes have the potential to be constructed of a diversity of materials. Initial PLA-based copolymer formulations have shown ~10-fold lower water permeability coefficients compared with lipid bilayers, providing highly robust external membranes for protecting encapsulated materials (*77-79*). These particles have been utilized for controlled drug delivery and encapsulation of a variety of protein and small molecule therapeutics (*79-81*). PEG-PLA and PEG-PLGA (poly(lactic co-glycolic acid)) block copolymers can also form spherical assemblies with a hydrophobic core (*82-84*). In these self-assembling nanoparticles, hydrophobic drugs are sequestered in the vehicle's PLGA core and slowly released over time. By tuning the relative lengths of the hydrophilic and hydrophobic blocks, drug encapsulation efficiency, drug release kinetics,

carrier size, and *in vivo* circulation times can be readily tuned, providing a more versatile architecture than lipid-based nanoparticle formulations(*85*). Moreover, because the nanoparticle structure is driven by a thermodynamically and kinetically-controlled self-assembly processes, the monodispersity of these nanoparticles can be optimized using microfluidic mixing technologies to provide another dimension of control over vehicle size and monodispersity(*85, 86*).

Micelles are another category of nanoparticles that have been widely composed of lipid- and polymer-based constituents(*87, 88*). As opposed to vesicles that form a bilayer structure with an aqueous interior compartment, micellar drug formulations contain a hydrophobic core surrounded by a hydrophilic shell(*88*). Micelles have been constructed from amphiphilic lipid, peptide, and polymer constituents to adopt spherical and elongated worm-like formations (*89-91*). Typically, hydrophobic drugs are encapsulated in the core of micellar formulations, but amphiphilic drugs have also been stably delivered as well through intercalation into the carrier shells (*88, 92, 93*). Further, stimuli-responsive amphiphilic block-copolymers have been developed to create responsive drug delivery vehicles that accept external cues (temperatures, pH, etc.) and modulate drug release kinetics accordingly (*94-96*).

Hybrid nanoparticles that combine the opportunities of lipid-based self-assemblies with polymer drug delivery vehicles have also recently been developed. One example is engineered to have a PLGA core that sequesters the anti-cancer drug doxorubicin with an outer layer of phospholipids to protect the surface and incorporate a second vascular-disrupting drug, combretastatin(*97*). This vehicle is able to temporally control the release of these two drugs to separately direct the disruption of tumor neovascular networks and

the death of cancer cells(*97*). Other formulations of PLGA with lipid-PEG coatings have been developed to improve the serum stability and provide tunable drug release profiles(*98*).

Another mechanism of tumor therapy involves the local deposition of thermal energy into tumor tissues. Thermal cancer therapies offer a means of specifically enhancing the current paradigms for cancer therapy, either through the application of mild (hyperthermia) or substantial (ablation) levels of heat. At high doses of energy, in the ablative regime, heating of tumors offers the potential to directly kill cancer cells, with broad applicability across multiple tumor types(*99*). In the hyperthermia regime, clinical trials have shown that heat treatments cause a spectrum of cellular and tissue effects that improve the efficacy of other therapies (*99-101*). In particular, hyperthermia synergizes with conventional chemotherapy and radiation regiments by inhibiting DNA replication and damage repair, preferentially killing nutrient-deficient cells, and increasing tumor blood flow and oxygen delivery(*100-104*). Furthermore, tumor hyperthermia enhances the delivery of antibody and emerging nanoparticle therapeutics by increasing the porosity of tumor vessels (*101, 105, 106*).

Recently, preparations of gold nanoshells have shown considerable efficacy for improving the precision of tumor ablation by intravenously targeting tumors and locally transducing otherwise benign NIR-light into heat (*41, 42, 48, 107-109*). The long precedence of gold nanoparticles in clinical rheumatoid arthritis therapies, make gold nanoshells or other gold plasmonic materials (eg. nanorods, nanocages, etc.) appealing new candidates for cancer therapy(*53*). Beyond locally damaging tissues with heat, these

materials could also be utilized to actuate local drug release in vessels or specific cells *in vivo(110)*.

The synthesis of nanoparticles with polar domains provides the potential to spatially separate multiple therapeutic functionalities on a single nanoparticle. Janus nanoparticles—named for Janus, the Roman God of doorways typically depicted with faces on the front and back of his head—have been engineered with two chemically distinct hemispheres or surfaces(*111*). These nanoparticles may be spherical (with opposing faces of unique composition), dumbbell-shaped (with two equal-sized spheres linked together), snowman-shaped, and may have other morphologies as well (*111-114*). The creation of nanoparticles with spatially separated chemical domains is a step towards replicating the controlled polarity exhibited in nature across many length scales(*115*). Separate hemispheres may be used to isolate and organize functional domains, sensing moieties, hydrophilic and hydrophobic therapeutics, or contrast agents that might be mutually inhibitory if randomly incorporated.

1.3 In vivo Nanoparticle Targeting for Imaging and Therapy

While the electromagnetic and therapeutic properties of nanoparticles make them promising candidates for medical applications, their actual utility for *in vivo* imaging and therapy depends on our ability to precisely direct them to regions of disease.

After *in vivo* administration, unprotected nanoparticles are rapidly opsonized by serum proteins and taken up by macrophages of the mononuclear phagocytic system

(MPS). Over the last 30 years a variety of nanoparticle coatings have been developed to deter this process to improve biocompatibility and delay macrophagic clearance. The first applications in nanomaterial imaging harnessed the normal uptake of nanoparticles by the MPS system as an indirect means of tumor detection. Particularly, dextran-coated superparamagnetic iron oxide contrast agents found a niche in the clinical detection of hepatic carcinomas(*1, 116*) and lymph node metastases(*117*) using MRI. For these materials, the primary regions of NP accumulation are in normal macrophage-rich liver, spleen, and lymph tissues (*1-3, 116*). In regions of cancer infiltration into these tissues, tumor cells displace normal tissue macrophages and diminish nanoparticle uptake and the resulting signal enhancement in MRI. This diminished signal enhancement relative to normal regions of these tissues has enabled enhanced identification of hepatocellular and splenic carcinomas and improved surgical planning for lymph node resections surrounding primary tumors (*2, 3*).

However, in order to utilize nanoparticles for cancer therapy and for remote detection of cancers outside of the liver and spleen, mechanisms for targeting nanoparticles *into* (instead of away from) tumors are required. As such, nanoparticle targeting has been explored for over 30 years in the hopes that diagnostic and therapeutic agents may illuminate and treat regions of neoplastic growth. The canonical approaches for targeting nanoparticles to cancers may be divided into two categories: passive (ligand-independent) and active (ligand-directed) targeting.

Passive targeting exploits structural, rather than biomolecular, aspects of the tumor microenvironment to allow preferential accumulation of nanoparticles over surrounding tissues. This mechanism for targeting tumors is also referred to as the

enhanced permeability and retention effect (EPR) and occurs because nanoparticles are able to selectively escape malformed angiogenic tumor blood vessels through transvascular pores that are not present in normal vessels (*118-121*). The pore sizes in vessels have been empirically shown to be a function of tumor type and implantation site and to typically enable transvascular transit of liposomal carriers between 200-400 nm in diameter (*119, 121*). Extravasated nanoparticles are then selectively retained in tumor tissues because tumors lack the functional lymphatics through which to clear them(*14, 122-126*). This mechanism of passive delivery has also been demonstrated to drive enhanced nanoparticle accumulation in other sites of inflammatory disease, including atherosclerosis(*127, 128*).

A few nanoparticle therapeutics, including DaunoXome™, Myocet™, Doxil™ and Abraxane™, have already entered clinical use for cancer treatment based on this mechanism of passive delivery. These formulations utilize long-circulating nanoparticle vehicles to enhance the delivery of drugs into tumors. The increased efficacy of these NPs compared to their small molecule and shorter-circulating counterparts illustrates the importance of tumor delivery in driving efficient tumor response.

In the realm of active targeting, biological or chemical ligands are conjugated to the surface of nanoparticles in an effort to program their attachment to receptors in the tumor microenvironment (*129-131*). For parenchymal tumor cell targeting, this strategy still relies on selective carrier extravasation from tumor blood vessels, but harnesses ligand-receptor interactions to specify the cellular uptake of materials. Initial targeted nanotechnologies leveraged the specificity of antibody-receptor interactions to provide a high carrier affinity for tumor cells(*25, 132-134*). More recently, nanotechnologies have

begun to harness genetic engineering strategies for reducing the size and immunogenicity of full antibodies, as well as alternative screening methodologies for identifying targeting ligands. Ligand screening technologies such as phage display and nucleic acid selection methods, for example, harness the respective amplification capabilities of bacteriophage replication in culture or PCR-based amplification of oligonucleotides *in vitro* to enable rapid screening of diverse libraries of $>10^{14}$ constituents(*135-138*). These techniques enable the selection of tumor targeting ligands, even in cases where the receptor is not known. Using such methods and others, a variety of ligand molecules have been developed for nanoparticle targeting, including aptamers(*139-141*), small molecules(*142*), and peptides(*143-146*). Importantly, polyvalent display of targeting ligands on nanoparticle scaffolds can dramatically enhance the carrier affinity over that of the free ligand. This effect is driven by multi-point attachment of carriers to multiple receptors and dominantly driven by a reduction in the rate of disassociation (k_{off}) of the complex(*147, 148*). This enables targeted nanomaterials to be constructed using low-affinity ligands in cases where polyvalent binding is expected to occur. For example, the affinity of polyvalently folate-modified dendrimers was found to exceed that of free folic acid molecules by over >100,000 fold(*149*).

Interestingly, while targeted formulations clearly direct receptor-specific cell targeting *in vitro*, a few recent studies have argued that modification of nanoparticles with tumor targeting ligands does not increase the macroscopic nanoparticle accumulation in tumors (*150, 151*). This inability for tumor cell targeting to amplify accumulation is postulated to arise because the rate-limiting step in tumor targeting is extravasation through trans-endothelial pores in tumor vessels(*152*). Therefore, while

targeting ligands on extravasated nanoparticles can direct receptor binding and internalization into specific tumor cell types, the total concentration of particles that escapes through pores in tumor vessels is not increased by ligand decoration. This has partially driven efforts to target receptors in tumor vessels instead of tumor cells(*153-155*), where nanoparticles in circulation may directly access target receptors.

In order to compare the published efficacy of passive and active targeting approaches, we collected quantitative data of nanoparticle targeting in mouse tumor models that was readily available in the literature and plotted both active and passive accumulation levels on a common axis for comparison(*31, 84, 92, 142, 156-168*) (**Figure 1.1**). This assembly of data includes a broad spectrum of nanoparticle sizes, shapes, and surface chemistries (spanning liposomes, iron oxide nanoparticles, dendrimers, carbon nanotubes and others) and utilizes antibodies, peptides, small molecules, and nucleic acid targeting moieties(*31, 84, 92, 142, 156-168*). While the considerable biological and experimental variability between data points (eg. different tumor types, implantation sites; nanoparticle carrier sizes, circulation times, etc.) prohibits quantitative comparison of individual data points, it is clear that overall both approaches to tumor targeting have produced very similar ranges of tumor targeting. Most strikingly, all the data points obtained in these preclinical tests reside between 0-20% ID/g, which, considering that experimental mouse tumor models are typically grown to ~100 mgs for targeting experiments, likely amounts to overall delivery of less than 2% of injected nanoparticles to tumor tissues, even in optimized formulations.

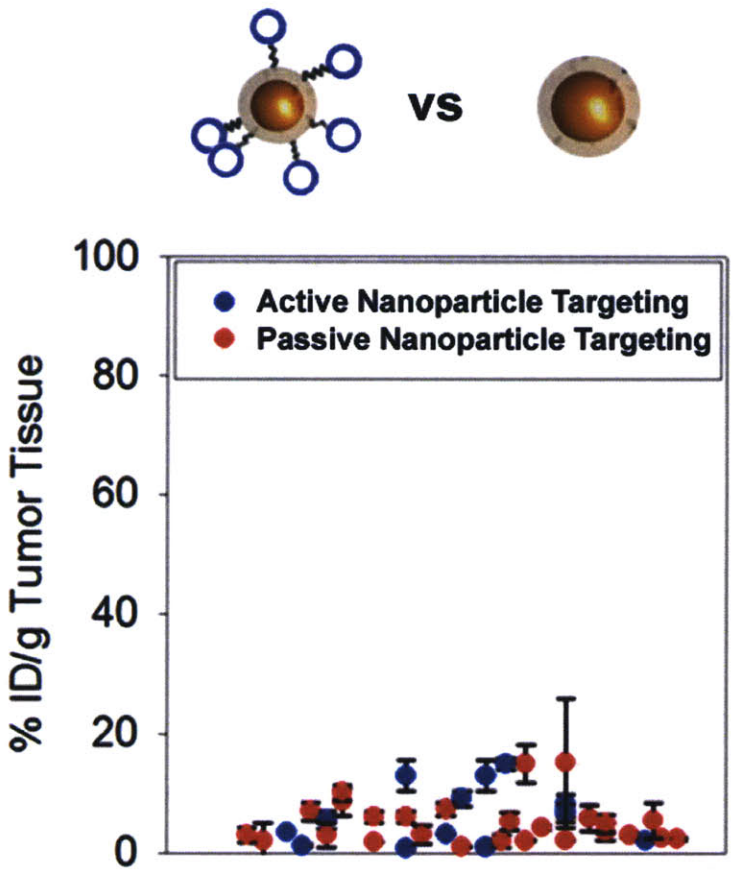

Figure 1.1. *Assembly of 'active' and 'passive' nanoparticle tumor targeting data from published sources.* Quantitative nanoparticle biodistribution data was collected covering a broad spectrum of nanoparticle sizes, shapes, and surface chemistries (spanning liposomes, iron oxide nanoparticles, dendrimers, carbon nanotubes and others) and diverse targeting ligands, including antibodies, peptides, small molecules, and nucleic acids (31, 84, 92, 142, 156-168). Abscissa plotted arbitrarily to separate data points.

A common element in both passive and active approaches to *in vivo* nanoparticle targeting is that nanoparticle characteristics are engineered at the scale of individual particles, via tuning of particle shape, size, surface chemistry, ligand type and abundance, among other considerations (*14, 16, 90, 141, 142, 145, 169-172*). For *in vivo* applications, these materials are typically administered in intravenous doses of over 1 trillion nanoparticles to perform identical, often competitive tasks (i.e. searching for the same

receptor). Considering the magnitude of these *in vivo* nanoparticle populations, we considered whether a systems engineering approach to designing interaction and communication between nanoparticles could improve their collective function.

1.4: 'Systems Nanotechnology' for Enhanced Cancer Imaging and Therapy

Nature provides abundant inspiration for engineering higher-order nanosystems with multiple nanostructured components to more effectively solve biomedical problems. In contrast to current *in vivo* nanoparticle systems composed of near-identical constituents, biological systems generate complex behaviors through collective interactions between multiple system components—enabling emergent processes such as computation, amplification, and dynamic communication. Indeed, complex behaviors emerge through component interactions across molecular, cellular, organismal, and populational length scales in nature. Three representative examples include the rapid tissue repair in blood coagulation; inflammatory cell signaling and recruitment to sites of infection; and ant foraging behaviors, where communication between individuals dramatically improves the efficiency of finding and retrieving food.

In contradistinction to current strategies for nanoparticle targeting that perform the singular function of vessel extravasation or receptor binding, the coagulation cascade couples molecular recognition events to signal processing and amplification mechanisms in order to orchestrate the rapid repair of injuries. The coagulation cascade consists of a group of zymogens (or pro-enzymes) that latently circulate throughout the bloodstream to survey for regions of vascular damage. In such regions, the enzyme tissue factor on

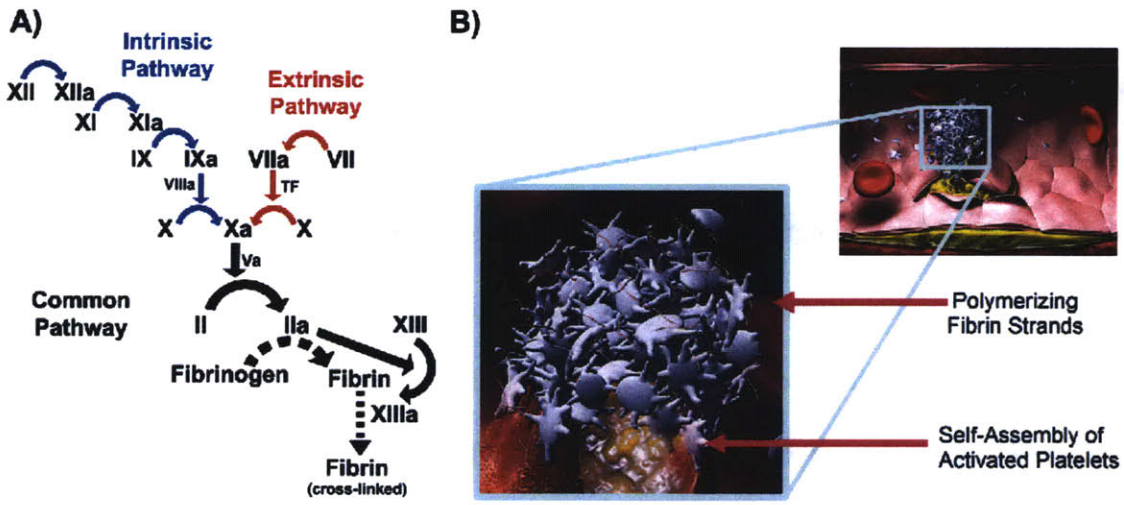

Figure 1.2. *Coagulation cascade molecular pathway and graphical depiction.*

extravascular cells becomes exposed and initiate the activation of circulating Factor X in the company of Factor VII and neighboring phosphatidylserine lipids. Factor X, alongside Factor V, then activates the enzyme thrombin, which performs the task of depositing a fibrin meshwork by cleaving short inhibitory peptides off of circulating fibrinogen precursors. In parallel, collagen exposure in wounds activates the intrinsic coagulation cascade, which propagates through Factors XII, XI, IX, and X to drive additional thrombin generation. In addition to directing the polymerization of fibrin, thrombin also performs a spectrum of other functions, including activation of additional Factor V and other latent factors to form positive feedback loops that intensify local signal amplification and activation of the circulating transglutaminase Factor XIII, which 'staples' fibrin polymers together by covalently linking specific glutamines to neighboring lysines. Disruption of the signal amplification mechanisms in blood coagulation can catastrophically diminish vessel repair kinetics—as illustrated by the genetic disorders haemophilia A and B, where the respective deficiencies of Factor VIII

and IX impair efficient thrombin formation through the intrinsic coagulation cascade and result in perfuse bleeding following even minor injuries (*173, 174*).

While individual nanoparticles have considerable biomedical promise, systems of multiple nanomaterials with engineered mechanisms of interaction could produce emergent, higher-level properties not exhibited by the components in isolation. **Inspired by the power of inter-component communication in natural processes, we considered the design of nanoparticle systems that interact to produce emergent behaviors with the capacity to enhance *in vivo* diagnostics, regenerative medicines, and other therapeutics.** Re-examining our emerging toolkit of nanomaterials, with the properties of individual nanoparticles serving as distinct nodes within multi-component systems, we can envision a vastly diversified functional space for nanoparticle systems to occupy. Further, given the control that pharmacological nanoparticle agents can exert on their local biological surroundings, cohesive systems of nanotechnological and biological constituents (engineered phage, viruses, proteins, cells) could be constructed where synthetic and endogenous bio/nanotechnological ensembles co-operate to more intelligently locate, diagnose, and provide therapy to regions of disease.

1.5 Biomedical Nanosystems to Date

Over the past decade, a spectrum of *in vitro* nanoparticle systems have been developed that utilize specific interactions between nanoparticles to emit amplified or altered signals as a result of biomolecular interactions(*37, 175-184*). The majority of these systems have been based on self-assembly mechanisms, whereby target interaction drives the assembly or disassembly of nanoparticles. Mirkin et al. pioneered the use of

multiple nanoparticle populations to sense disease targets *in vitro* by modifying gold nanoparticles to display short oligonucleotide sequences that allowed target DNA sequences to mediate nanoparticle-assembly(*37, 177*). Assembly of gold nanoparticles results in a red-shift of the ~520 nm surface plasmon resonance band, enabling optical detection either in solution or on surfaces. Improvements in this concept for sensing biomarkers via target-mediated nanoparticle assembly have generated systems with attomolar sensitivity for either DNA(*185*) or protein detection(*186*), as well as a broad spectrum of other technologies(*187, 188*). Elsewhere, Weissleder and colleagues developed analogous assays using magnetic nanoparticles (*179, 181, 182, 189*). These particles are similarly modified with biomolecular recognition elements to allow target-mediated assembly to occur. Here, as nanoparticles coalesce into nanoassemblies, magnetic domains coordinate to form an amplified cumulative dipole that more efficiently dephases protons in MRI(*190, 191*). These methods have facilitated the *in vitro* sensing of oligonucleotides, small molecules, and proteins via nanoparticle assembly (*179, 181, 182, 189*).

Extending upon this landscape of interactive nanosystems for *in vitro* sensing, this thesis aims to develop nanoparticle systems with mechanisms of interaction that could facilitate the improved sensing and targeting of disease *in vivo*.

Section I of thesis describes *directly*-interactive nanomaterials where dispersed nanoparticle systems *assemble* through the action of tumor-associated enzymes. These systems are designed to remain latent and dispersed in solution, but to rapidly assemble with one another upon exposure to programmed enzyme inputs. We present designs that enable nanoparticle systems to robustly respond to single proteases or to perform simple

logical operations using binary combinations of two protease targets. Finally, a nanosystem is developed to *dynamically* assemble and disassemble in response to antagonistic enzyme triggers.

Section II of this thesis describes mechanisms by which nanoparticles can *indirectly* interact with one another through secondary biological messengers *in vivo* to amplify tumor targeting and improve tumor therapy and imaging. Specifically, we design signaling networks wherein synthetic devices act as artificial inputs and outputs to endogenous biological cascades in order to robustly transmit and amplify communication between distinct populations of tumor-targeted nanoparticles. To construct these systems, this section initially describes the development of versatile surface chemistries for *in vivo* targeting and the coating and application of a new class of nanomaterials to cancer therapy. Finally, the construction and *in vivo* testing of two interactive nanosystems for amplifying nanoparticle tumor targeting is described.

Section I: Engineering *Direct* Nanoparticle Interactions for Cancer Sensing

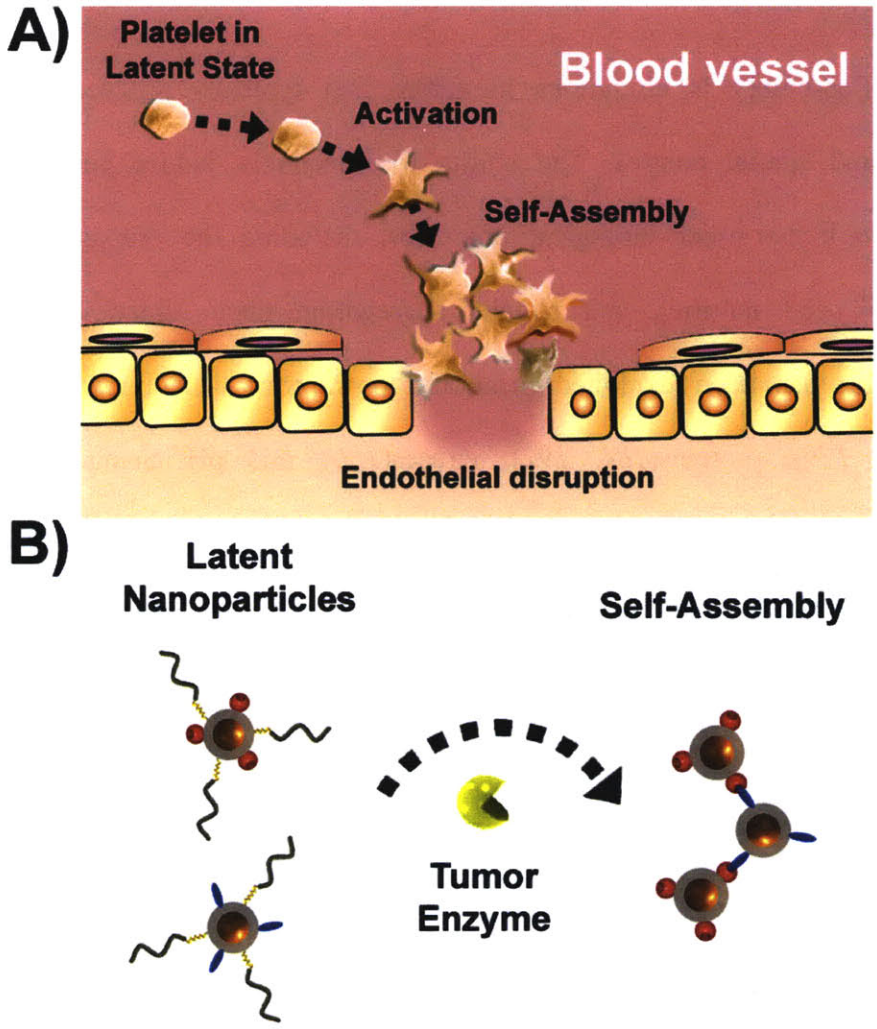

Scheme I. *Inspired by temporally- and spatially-regulated mechanisms of direct interactions in biology, the first section of this thesis describes nanoparticles that exist in a latent state and rapidly assemble with one another following activation by tumor enzymes.* A) In areas of injury, platelets that are circulating in a latent form become activated by local biochemical cues and aggregate to form an immobilized platelet plug. B) Inspired by this process, we set out to engineer mechanisms by which nanoparticles could latently circulated and be activated by tumor enzymes to rapidly self-assemble with one another.

Chapter 2: Protease Actuation of Nanoparticle Self-Assembly

2.0 Introduction

Self-assembly is ubiquitous in nature, but typically proceeds under precise temporal and spatial control. The ability to selectively induce complementarity is essential to higher-order biological processes, including the propagation of genetic information, cell motility, and platelet aggregation upon injury. Self-assembly of nanoparticles has been exploited primarily to improve sensitivity for detection of DNA(*177, 179*), proteins(*186, 192*), viruses(*180*), and pH changes(*193*) *in vitro*; however, mechanisms of initiating nanoparticle assembly which mimic biological control have yet to be described(*194, 195*). Development of inorganic nanoparticles that respond to biological actuation could enable triggered, hierarchical assembly of materials with emergent properties.

Here, inspired by thrombin-driven aggregation of platelets, we describe a general means by which enzyme activity may actuate the self-assembly of monodisperse nanoparticles. Superparamagnetic, self-complementary Fe_3O_4 nanoparticles are passivated by the attachment of inhibitory polymers that may be proteolytically removed by matrix metalloproteinase-2 (MMP-2), a protease correlated with cancer invasion, angiogenesis, and metastasis (*196-198*), to initiate self-assembly. We demonstrate that nanoparticle assembly amplifies the transverse (T2) relaxation of nanoparticle solutions in MRI, enables magnetic manipulation of assemblies with external fields, and allows

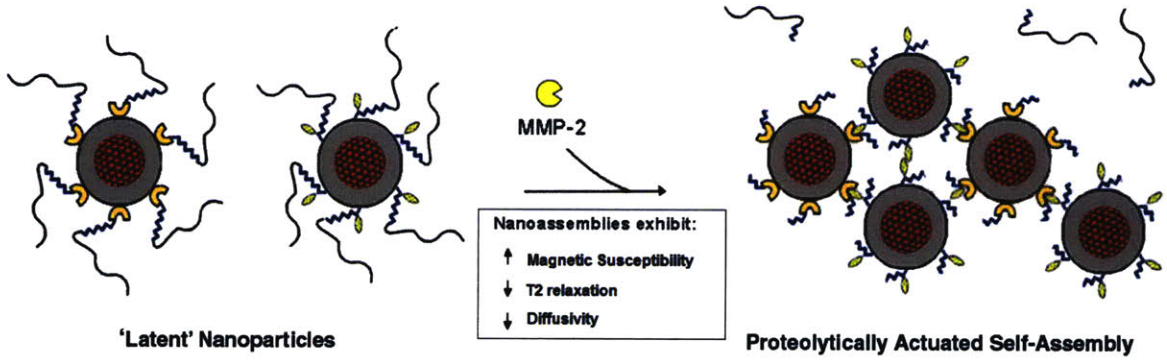

Figure 2.1. *Proteolytic Actuation of Self-Assembly Schematic*. Neutravidin- and biotin-functionalized superparamagnetic iron-oxide nanoparticles are passivated by the attachment of PEG chains that are anchored by MMP-2-cleavable peptide substrates (GPLGVRGC). Upon proteolytic removal of PEG via cleavage of the peptides, biotin and neutravidin particles self-assemble into nanoassemblies with enhanced magnetic susceptibility, T2 magnetic resonance relaxation, and lowered diffusivity.

magnetic resonance imaging of tumor-derived cells that produce MMP-2. In the future, this approach may enable site-selective immobilization and enhanced image contrast in regions of tumor invasion *in vivo*.

2.1 Results and Discussion

The synthesis of proteolytically-actuated, self-assembling nanoparticles involves modifying them to be self-complementary, but passivated by protease cleavable elements (Figure 2.1). Briefly, 50nm dextran-coated Fe_3O_4 nanoparticles, sized by analytical ultracentrifugation (Micromod, Germany), are modified with either biotin or neutravidin (Pierce, Rockford, IL) to generate two populations of particles. When combined in solution, these particles self-assemble through highly stable biotin-neutravidin interactions. To allow enzymatic control of particle assembly, the nanoparticle surfaces of both populations are modified with the MMP-2 peptide substrate, GPLGVRGC(*199*), which serves as an anchor for linear polyethylene-glycol (PEG) chains. PEG is a highly-

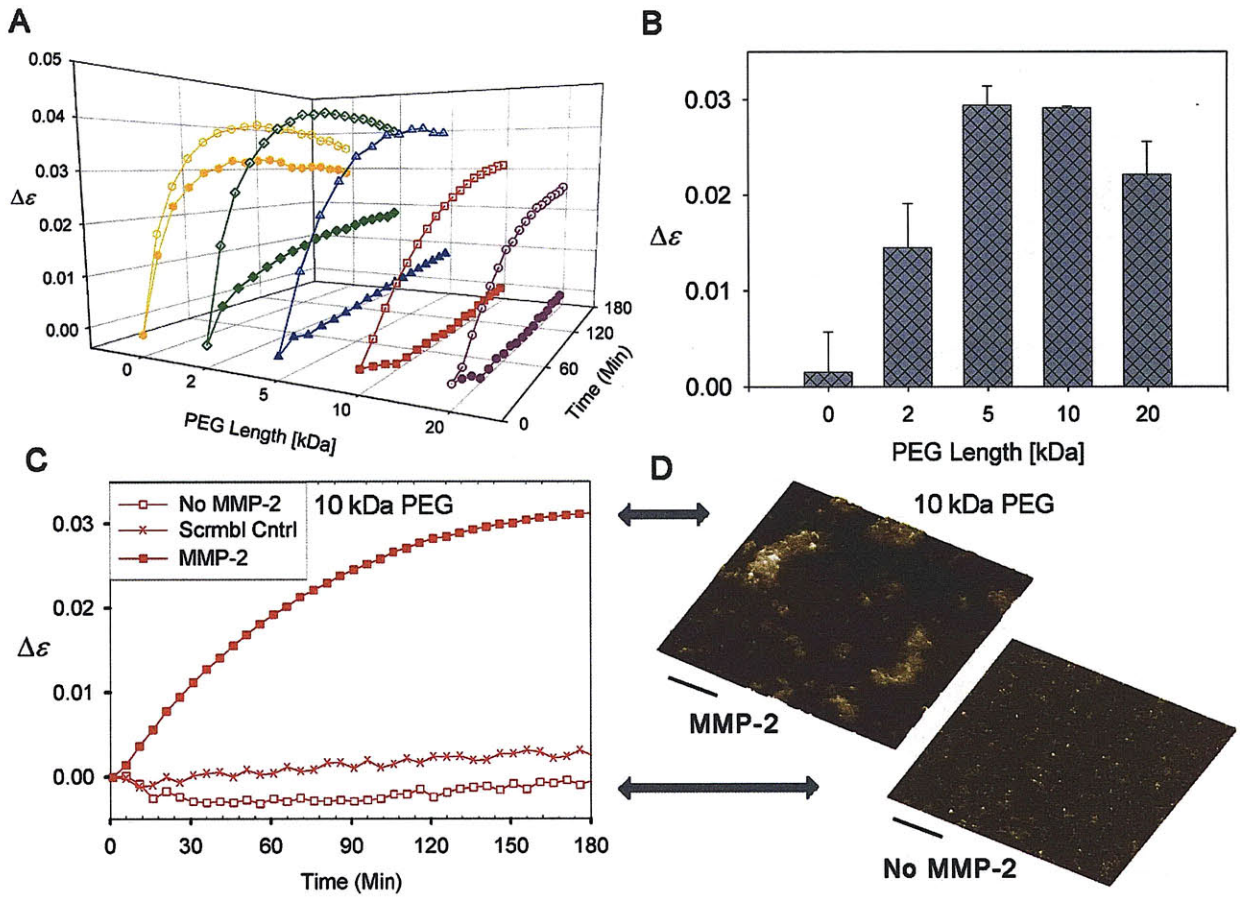

Figure 2.2. *Role of PEG length and Characterization of Assembly.* A) Changes in light scattering of nanoparticles over time with MMP-2 [11ug/ml] (hollow) or without MMP-2 (solid). Shorter (2 kDa, 5 kDa) PEG chains only partially inhibit self-assembly without MMP-2 whereas longer PEG chains (10 kDa, 20kDa) exhibit delayed aggregation kinetics in the presence of MMP-2. B) Difference in extinction coefficients with and without MMP-2 after 3 hours reveals optimal PEG chain length of 10 kDa C) Specificity of triggered self-assembly demonstrated by comparing peptide sequence of 10 kDa PEG tether. Nanoparticles with specific MMP-2 substrate aggregate in the presence of MMP-2 [11ug/ml] whereas particles with scrambled peptide do not. D) Atomic Force Micrographs of particle solutions in C confirm aggregation of particles in the presence of MMP-2. Scale bars are 500nm.

mobile, hydrophilic polymer with a large sphere of hydration that has been widely used to deter adsorption of proteins or cells on surfaces and to extend therapeutic circulation times *in vivo*(*200, 201*). We hypothesized that linear PEGs of appropriate lengths would inhibit association of 50 nm nanoparticles but still allow MMP-2 proteases (< 9 nm(*202*))

to cleave peptide linkers. To explore this idea we conjugated varying molecular weight PEGs (2, 5, 10, and 20 kDa) to biotin and neutravidin particles via MMP-2-cleavable linkers and tested their ability to assemble with and without MMP-2. The rate and extent of assembly was measured by monitoring changes in the solution extinction coefficient at 600nm due to nanoparticle assembly over time (Figure 2.2A). Assembly of PEG-coated biotin and neutravidin particles without MMP-2 was found to be inversely related to PEG molecular weight with almost complete inhibition of particle assembly at PEG chain lengths of 10 kDa or higher. Nanoparticles incubated with MMP-2 also aggregated at a rate inversely related to PEG chain length, likely due to a similar steric repulsion of MMP-2. Comparing the change in extinction coefficient of particles incubated with MMP-2 versus those without at 3 hours, the 5 kDa and 10 kDa PEGs allow the highest MMP-2-catalyzed assembly enhancement (Figure 2.2B). However, because the 5 kDa PEG cannot completely inhibit particle interaction in their native state, 10 kDa was chosen as the optimum surface modification.

To further verify that the particle assembly was due to the sequence-specific release of PEG by MMP-2, a scrambled linker with low cleavage-specificity by MMP-2, GPVGLRGC(*203*), was generated and conjugated to particles. The nanoparticles with the scrambled peptide exhibit markedly decreased assembly compared to the specific peptide sequence (Figure 2.2C). At 3 hours following MMP-2 addition, assembly of nanoparticles with specific MMP-2 substrates is detectable by a visible change in the light scattering of the solution, appearing more turbid. The sizes of nanoparticle assemblies, examined by atomic force microscopy (AFM), are as large as 0.5-1um after evaporation onto freshly-cleaved mica, suggesting assembly of 10's to 100's of particles.

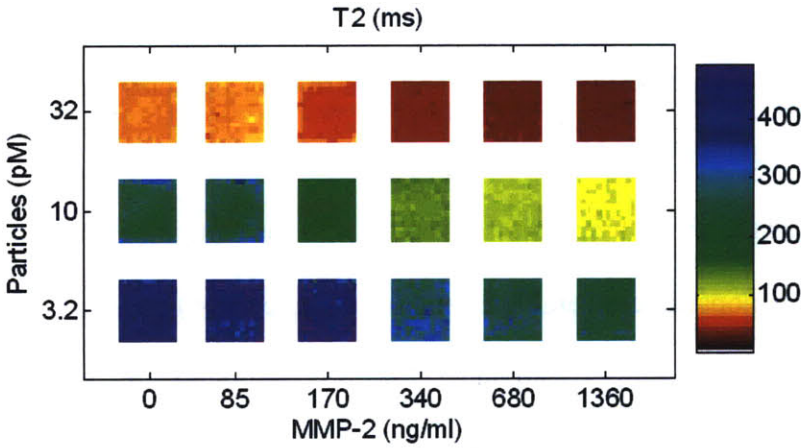

Figure 2.3. *MMP-2 Triggered Self-Assembly Results in Detectable Changes in T2 Relaxation Times*. With a 4.7T Bruker MRI, T2 changes were detectable due to particle aggregation over an order of magnitude variation in particle concentration, spanning typical values used clinically [2.6mg Fe/KG body weight]. Detectable aggregation is seen after 3 hours with the addition of 85, 170, 340, 680, and 1360 ng/ml MMP-2 for nanoparticle concentrations of 32 pM, 10 pM, and 3.2 pM respectively.

The nanoparticles that are not incubated with MMP-2 remain disperse with diameter of approximately 75 nm (Figure 2.2D).

Nanoassemblies of iron oxide particles that form upon proteolytic-activation acquire emergent magnetic properties that may be remotely detected with MRI. The coordination of superparamagnetic Fe_3O_4 magnetic dipoles in assembled nanoparticles amplifies the diffusional dephasing of surrounding water molecules, causing shortening of T2 relaxation times in MRI(*190, 191*). We demonstrate that measurement of T2 changes allows sensitive, remote detection of protease-triggered assembly across a ten-fold variation in particle concentration (Figure 2.3). The concentrations used correspond to 0.7-7 mg Fe/kg of solution, spanning the working concentrations typically utilized for tumor and lymphatic targeting *in vivo* (2.6mg Fe/kg body weight)(*204*). Nanoparticle solutions were incubated with varying concentrations of MMP-2 in a 384 well-plate and their T2 relaxation times were mapped using a Carr-Purcell-Meiboom-Gill (CPMG)

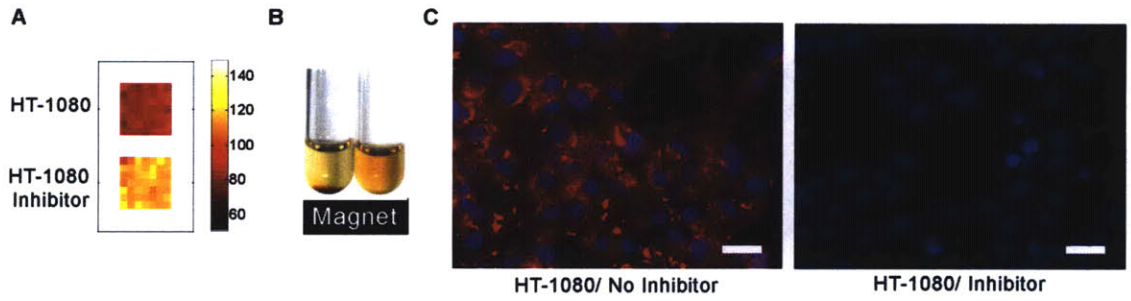

Figure 2.4. *Triggered Self-Assembly of Nanoparticles by HT-1080 Tumor-Derived Cells.* A) T2 mapping of Fe_3O_4 nanoparticles incubated for 5 hrs over HT-1080 cells that secrete active MMP-2 in a complex medium. Nanoparticle assembly amplifies T2 relaxation over cancer cells relative to cells incubated with the MMP inhibitor Galardin at 25uM. B) Activated nanoparticles are drawn out of solution by a strong magnet (left) while inactive nanoparticles (right) are not. C) Nanoparticles activated by tumor cells for 3 hrs are targeted to the cell surface with a magnetic field and visualized by epifluorescent microscopy using biotin-quantum dots [Em: 605 nm]. Assemblies are not targeted to cells if an MMP inhibitor is used. Scale bar reperesents 25 μm.

sequence on a 4.7T Bruker MRI. T2 shifts of greater than 150ms are observed by MMP-2 -triggered assembly in a 3.2 pM nanoparticle solution. For 10 pM and 32 pM concentrations, a T2 shortening approximately 50% of the starting value is observed after incubation with MMP-2. Nanoparticles at a 10pM concentration were sensitive to at least 170ng/ml [9.4U/ml] of MMP-2, which compares favorably with levels found in tumor tissue of MMP-2 expressing cancer cells [435 U MMP-2 per g](*203*).

Next, the utility of the protease-triggered nanoparticles was explored in complex biological specimens where non-specific protein adsorption is often problematic. Specifically, passivated nanoparticles were tested in cell culture medium above living, tumor-derived cells. We exposed nanoparticles to the human fibrosarcoma cell line, HT-1080, which constitutively expresses and activates MMP-2(*205, 206*). MMP-2 is part of the matrix metalloproteinase family, which includes soluble and membrane bound zinc binding proteases that play a role in regulatory protein processing and extracellular matrix remodeling(*207*). MMP-2 has cleavage specificity for Type IV collagen which is

the principal constituent of basement membranes; thus upregulation of MMP-2 activity leads to invasive proliferation and metastases of cancer cells by breaking down tissue barriers(*196, 197*). It's activity has been correlated with poor prognosis in breast, prostate, bladder and cervical cancers[208-210]. Nanoparticles were incubated over HT-1080 cells at a concentration of 10pM. After 5 hours, samples from the media were transferred to a 384 well plate and T2 maps were generated with MRI. A substantial shortening in T2 is detected in the media over HT-1080 cells versus media over HT-1080 cells incubated with the broad-spectrum MMP inhibitor Galardin (Figure 2.4A).

Triggered assembly of the nanoparticles can also be used to magnetically target nanoassemblies to cells. Similar to the T2 relaxivity enhancement in MRI, as the magnetic domains of coalesced nanoparticles coordinate to form an amplified cumulative dipole, they become more susceptibile to long-range dipolar forces(*211*). This phenomenon allows manipulation of the nanoassemblies with imposed magnetic fields, while isolated particles remain unaffected. Using a high-gradient permanent magnet, MMP-2 triggered assemblies of 1.5nM iron oxide particles can be visually drawn out of solution, while non-activated particles remain disperse (Figure 2.4B). To demonstrate that this can be extended towards targeting particles onto cancer cells, HT-1080 cultures were placed over a strong permanent magnet and incubated with nanoparticles at a 150pM concentration. After 3 hours, the media was removed and the cells were washed, fixed, and stained for aggregates using a biotinylated fluorescent probe. Bright fluorescent staining of particle assemblies is seen over HT-1080 cells, while weak diffuse staining, indicating little to no targeting, is seen over cells incubated with the inhibitor Galardin (Figure 2.4C).

2.2 Conclusions

To the best of our knowledge, this represents the first demonstration of protease-triggered nanoparticle self-assembly. Previously, our laboratories have demonstrated that peptide-modified semiconductor quantum dots could precisely target tumors in whole animals*(145)* and subcellular organelles in living cells(*212*). This work extends the ability of nanoparticles not only to target sites of interest, but to interact with the *processes* of disease by harnessing biological machinery to assemble nanomaterials with amplified properties. We show that polymeric protection can temporarily shield dissimilar complementary ligands, including both small molecules (biotin) and tetrameric proteins (neutravidin). Accordingly, as opposed to recent reports of proteolytic activation of cell-penetrating peptides[21] and peroxidase-initiated nanoparticle assembly[29-30], our approach can be considered entirely modular whereby key features may be altered without significant re-engineering. Formulations with new functionalities could be easily developed by substituting the complementary binding pairs, cleavable substrates (e.g. glycans, lipids, oligonucleotides), or multivalent nanoparticle cores (e.g. gold, quantum dot, dendrimer) to extend the capabilities of existing modalities.

2.3 Materials and Methods

Synthesis of Nanoparticle Probes

Protease-triggered, self-assembling nanoparticles were synthesized using 50nm amine-functionalized, dextran-coated iron-oxide nanoparticles (6.25pmol/mg Fe), sized by analytical ultracentrifugation (Micromod (Germany)). All peptides were obtained at >90% purity (Synpep) and all reagents were obtained from Sigma unless otherwise specified. A high gradient magnetic field filtration column was used between each conjugation (Miltenyi Biotec). For biotin probes, the *N*-Succinimidyl 3-[2-pyridyldithio]-propionamido (SPDP) was used to link cysteine-containing peptides [acetyl-KGPLGVRGC-X-Biotin] to particle amines and mPEG-SMB polymers (Nektar) were attached to peptide lysine.

Neutravidin nanoparticles were formed by modifying particles with biotinamidohexanoyl-6-amino-hexanoic acid N-hydroxy-succinimide ester and coating with a saturating concentration of neutravidin. The extinction coefficient of the solution at 600nm was measured during incubation to ensure no aggregate formation. Additionally, neutravidin coated particles were passed through a 0.1um filter to confirm mono-dispersity. Peptide linkers and PEG were functionalized to lysines on the neutravidin coated nanoparticles using the same methods described for biotin particle conjugations, but with the peptide sequence (KGPLGVRGC). The scrambled sequences used for control experiments were GVRLGPG instead of GPLGVRG.

Extinction coefficient, AFM, and Magnetic Field Migration Measurements

For all assembly experiments, equimolar ratios of particles were used. All extinction coefficient measurements were performed in duplicate in 384 well plates using

a SpectraMax Plus spectrophotometer (Molecular Devices, Sunnyvale CA). Biotin and neutravidin probes (0.5mg/ml) were mixed at equal ratios and 0.5ug of the recombinant catalytic domain of MMP-2 (Biomol,) in 6ul of 50 mM Tris, 5 mM CaCl2, 0.005% Brij-35, pH 7.5 buffer was added to 40ul probe solution at time zero. The same probe and MMP-2 concentrations were used for AFM and solution phase magnetic precipitation experiments. For AFM controls, 6ul of buffer without MMP-2 was added. AFM measurements were performed using a multimode, Digital Instruments AFM (Santa Barbara CA) operating in tapping mode using FESP Tips (Veeco Nanoprobe TM, Santa Barbara CA). AFM reactions were incubated for 3 hours, diluted, and evaporated on freshly-cleaved mica for analysis. In magnetic precipitation experiments, probe solutions were incubated with or without MMP-2 overnight and placed over a strong magnet for 2.5 minutes.

MRI detection of self-assembly

MRI images were taken on a Bruker 4.7T magnet, 7cm bore. Biotin-peptide-PEG and neutravidin-peptide-PEG nanoparticles were mixed together and serially diluted in 384 well-plate. Serial dilutions of recombinant MMP-2 in 6ul of TRIS buffer were added to each well. After 3 hours, a CPMG sequence of sixteen images with multiples of 10.45ms echo times and a TR of 5000ms were acquired. T2 maps were obtained for each well by fitting images on a pixel by pixel basis to the equation $y=M*\exp(-TE/T2)$ using MATLAB.

Cell culture

HT-1080 human fibrosarcoma cells (ATCC) were cultured in 24-well plates using Mininum Essential Medium Eagle (Invitrogen) with 10% fetal bovine serum (Invitrogen)

and 1% penicillin/streptomycin. For MRI experiments, the media was replaced with serum-free Dubelcco's Modified Eagle Medium (DMEM - Invitrogen) containing 10pM nanoparticle concentration. The broad-spectrum MMP-2 inhibitor Galardin (Biomol) was added at a concentration of 25uM in control cultures. Samples of 40ul were taken at 5 hours for MRI imaging using the same procedures for T2 mapping described above. For fluorescent labeling experiments, media was replaced with serum-free DMEM containing 200pM nanoparticle concentration and cells were placed over a strong magnet. After 3 hours, the media was removed and the cells fixed with 2% paraformaldehyde. The cells were permeabilized with 0.1% Triton-X in PBS and incubated with biotin quantum dots (EM: 605nm - Quantum Dot Corp). Nuclear staining was performed by incubating with 0.001% Hoescht for 1 min.

Chapter 3: Nanoparticle Self-Assembly Gated by Logical Proteolytic Triggers

3.1 Introduction

Complex diseases such as cancer emerge through the dysregulation of numerous molecular pathways. While these pathways may be inappropriately activated in cancer cells, they typically serve important purposes in normal physiology as well. Therefore, the single biomarker paradigm for diagnosis of diseases has largely failed to provide definitive diagnoses for neoplastic disease. To date, nanoparticle (NP) assembly has been exploited to probe for a host of *single* pathological inputs *in vitro*, including DNA(*37, 177, 179*), RNA(*179*), proteins(*186, 192*), viruses(*180*), and enzymatic activity(*181, 184, 192, 213*). While this methodology can be effective for *in vitro* applications, where multiple assays can be performed in parallel to interrogate multiple targets, the future development of highly diagnostic *in vivo* sensors may benefit from the ability to simultaneously monitor multiple aspects of disease. In this chapter we describe a method whereby inorganic nanocrystals may perform Boolean logic operations using two inputs associated with cancer invasion (MMP2 and MMP7). Disperse, superparamagnetic Fe_3O_4 NPs are designed to coalesce in response to logical AND or OR functions. In either system, NP self-assembly amplifies the T2 relaxation rate of hydrogen protons, enabling remote, MRI-based detection of logical operations. In the future, we believe that these sensors may be optimized to monitor a diversity of inputs *in vitro* and *in vivo*.

Logical operations were designed to analyze inputs of two matrix-metalloproteinases, a family of at least 26 members of secreted and membrane bound

proteases that have been studied extensively for their role in cancer(*197, 214*). In particular, matrix-metalloproteinase-2 (MMP2), is over-expressed in many cancers, including breast cancers, and is an indicator of cancer invasiveness, metastasis, angiogenesis, and treatment efficacy(*196, 198, 208-210, 215, 216*). MMP7, a protease with broader substrate specificity, is thought to facilitate early stages of mammary carcinoma progression(*217, 218*). In tissues excised from breast cancer patients, both MMP-2 and MMP-7 were expressed at statistically higher levels in carcinogenic than in normal breast tissues(*219*), highlighting their potential utility as dual markers of neoplastic inception. We demonstrate using dynamic light scattering (DLS), fluorescence, and MRI that logical sensors can probe samples for the presence of both MMP2 *and* MMP7 (AND function) or for the presence of either MMP2 *or* MMP7 (OR function).

3.2 Results and Discussion

To synthesize both sensor types, two kinds of NPs were initially engineered: one with a tethered ligand (biotin) and the other with its receptor (neutravidin). These particles were stable separately, but aggregated readily when combined. We sought to completely mask these groups by attachment of peptide-polyethyleneglycol (PEG) conjugates to conditionally prevent assembly. Previously, we demonstrated that two 10kDa PEG-modified NPs could mutually deter each other's binding(*184*). Here, by increasing the polymer weight to 20kDa, we demonstrate that modification of only one NP can completely inhibit the binding of an unmodified NP (Figure S2; Figure 2). Accordingly, we reasoned that by linking polymers to each particle via unique protease substrates, assembly could be restricted to occur only in the presence of both enzymes (Logical AND) (**Scheme 3.1**). Furthermore, by anchoring polymers to only the ligand NP

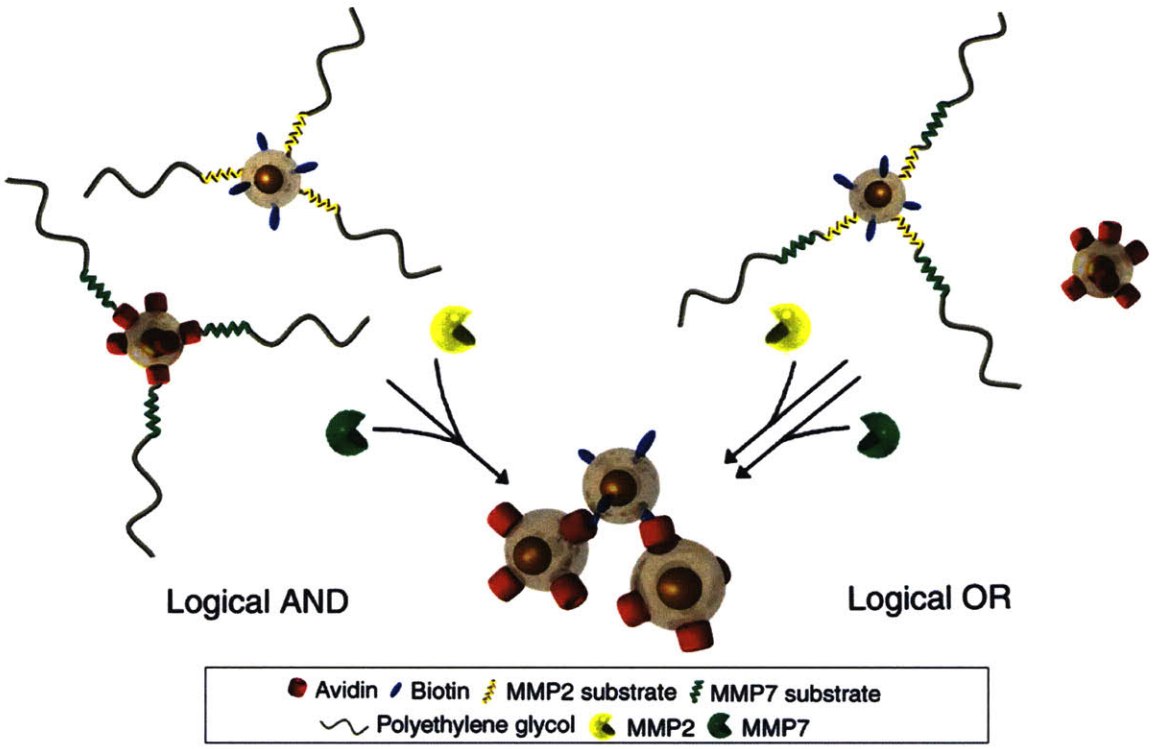

Scheme 3.1. *Schematic Representation of Logical Nanoparticle Sensors*. Self-Assembly is gated to occur in the presence of MMP2 and MMP7 (Logical AND) (Left) or in the presence of either or both proteases (Logical OR) (Right) by attachment of protease-removable polyethylene glycol polymers.

with a tandem peptide substrate (containing both enzyme cleavage motifs in series), we sought to actuate assembly in the presence of either *or* both of the enzyme inputs (Logical OR) (**Scheme 3.1**).

Peptide PEG polymers were synthesized by reacting the peptide N-terminus (or lysine residue for OR tandem peptide) with amine-reactive 20kDa methoxy-PEG-succimidyl α-methylbutanoate (see supplemental methods for details). Cysteine residues were incorporated at the C-terminus of peptides to allow oriented attachment of substrate polymers to NPs and TAMRA fluorochromes were incorporated distally to fluorescently monitor polymer removal. To begin AND NP synthesis, ligand particles were shielded with an MMP2 (Gly-Pro-Leu-Gly-Val-Arg-Gly)(*203, 220*) substrate-polymer and

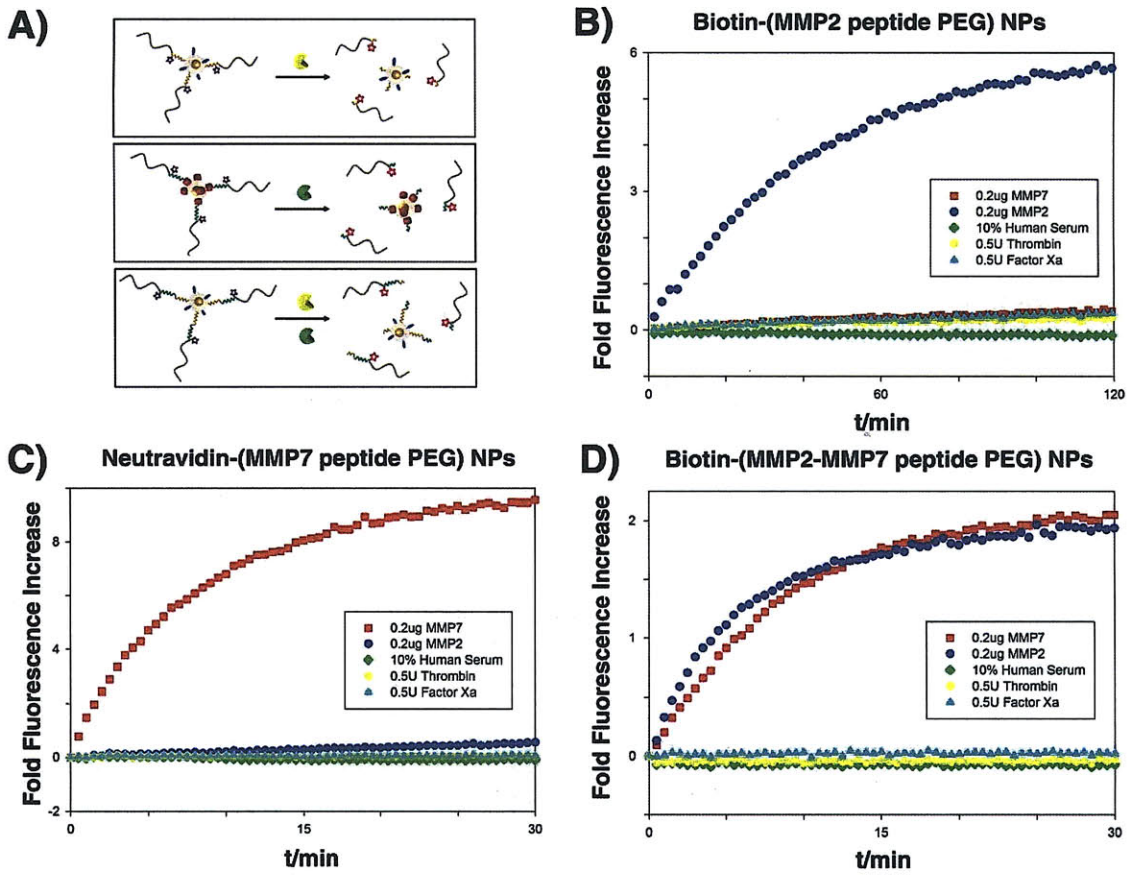

Figure 3.1. *Protease activation of substrate-linked TAMRA fluorescence.* A) Biotin-MMP2-PEG NPs, Neutravidin-MMP7-PEG NPs, and Biotin-MMP2-MMP7-PEG NPs (OR NPs) are incubated with proteases which, upon cleavage of substrates, relieve TAMRA fluorochrome quenching by NP core and increase solution fluorescence. B-D) NPs (40ug/ml; 50ul) were incubated with 0.2ug MMP2, 0.2 ug MMP7, purified human enzyme controls, or 10% human serum. Thrombin and factor Xa concentrations (10U/ml) were chosen to approximate 10x the activity present in human serum.

receptor particles were shielded with an MMP7 (Val-Pro-Leu-Ser-Leu-Thr-Met)(*221*) substrate-polymer. Enzyme specificity for these sequences was assessed by monitoring TAMRA fluorescence increase in the presence of various enzymes. Specific enzyme-substrate pairs rapidly increased TAMRA fluorescence as cleaved substrate fluorochromes diffused away from the quenching iron oxide cores (**Figure 3.1**). Non-specific pairs, including human thrombin, factor Xa, and serum, showed little

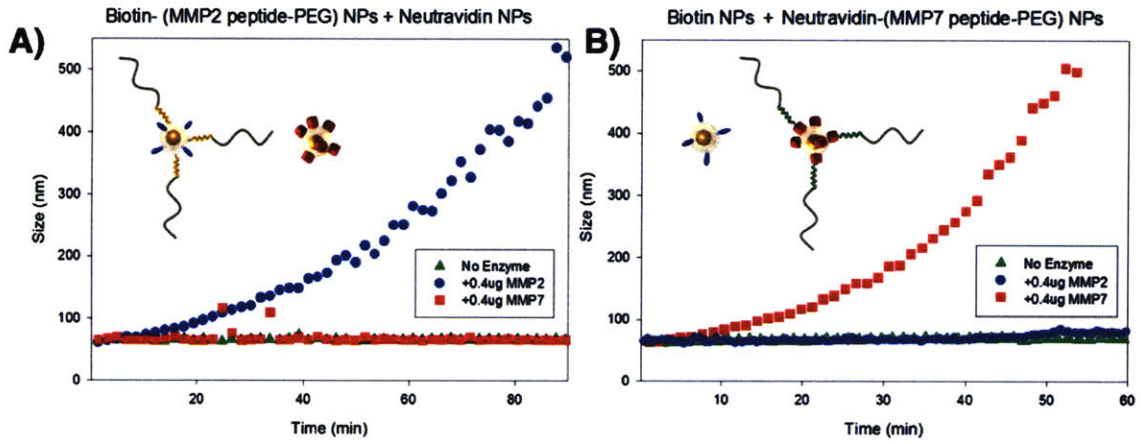

Figure 3.2. *Probing nanoparticle latency and specificity using dynamic light scattering.* a) Ligand-nanoparticles were masked with MMP2-PEG to inhibit assembly with unmodified receptor nanoparticles (40ug Fe/ml). Addition of 0.4ug MMP2 actuates nanoparticle assembly, while 0.4ug MMP7 or no enzyme is insufficient. b) Receptor-nanoparticles were masked with MMP7-PEG to inhibit assembly with unmodified ligand nanoparticles (40ug Fe/ml). Here, addition of 0.4 ug MMP7 induces assembly, while 0.4ug MMP2 cannot.

fluorescence increase. We next examined each enzyme's ability to actuate assembly of peptide-shielded particles in the presence of their unmodified cognate particles. Specific enzyme-substrate pairs rapidly catalyzed the formation of nano- and micro-assemblies when incubated with unmodified cognate NPs, while non-specific pairs negligibly affected population size (**Figure 3.2**). To investigate the relationship between peptide polymer removal and NP assembly, biotin-MMP2-PEG enzyme reactions were quenched at various timepoints (**Figure 3.3**) and incubated with receptor NPs. Following removal of ~50% of NP polymers, assembly begins, eventually revealing sufficient biotin to direct NP precipitation.

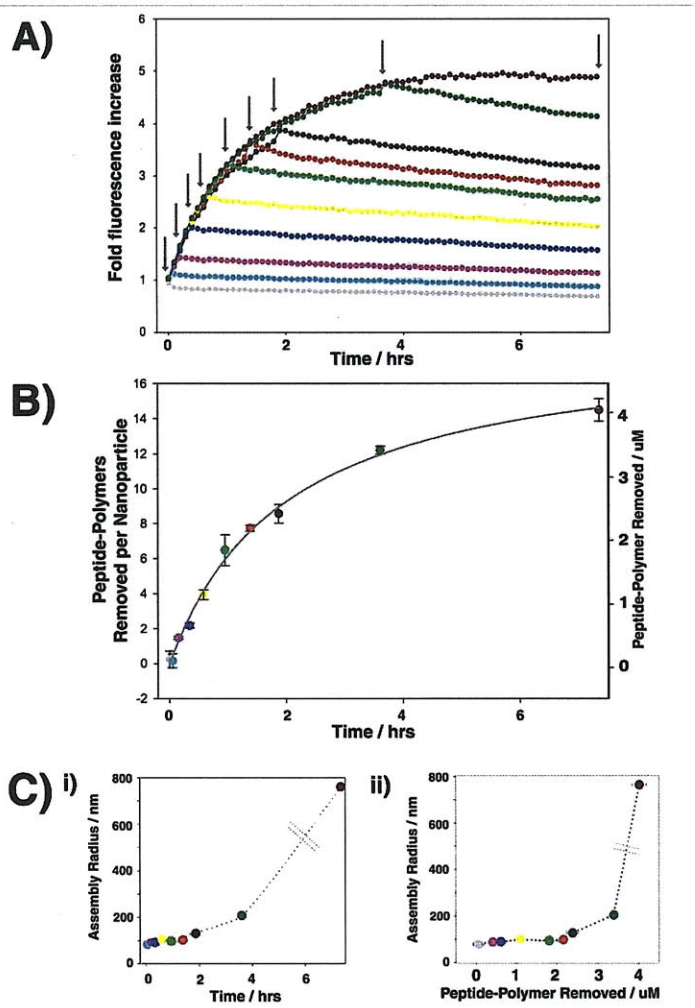

Figure 3.3. *Investigating assembly dependence on polymer removal.* A) Biotin-MMP2-PEG NPs (200ug Fe/ml) were incubated with MMP2 and TAMRA fluorescence was recorded over time. At various time points, reactions were quenched with addition of 20mM EDTA (quenching times indicated by arrows). B) The amount of free MMP2-PEG released in samples from (A) was quantified by TAMRA absorbance in solution after ultracentrifugation of NPs. Peptide-Peg removal is plotted vs MMP2 incubation time with data colors corresponding to those in (A). Polymer removal kinetics are consistent with the fluorescence de-quenching data in (A), suggesting that TAMRA quenching was largely mediated by fluorochrome-NP interactions over fluorochrome-fluorochrome interactions. C) i) Quenched ligand-MMP2-PEG samples from (A) were incubated with unmodified receptor NPs (each at 40ug/ml) for 24 hours at which time size was measured with DLS. The 7.5 hour MMP2 reaction precipitated during the incubation, indicating assembly is closely controlled by the degree of polymer removal between 4-6 hrs. ii) Assembly data is plotted vs. the polymer removal data of (B), demonstrating minimal assembly induction prior to removal of ~50% of NP polymers.

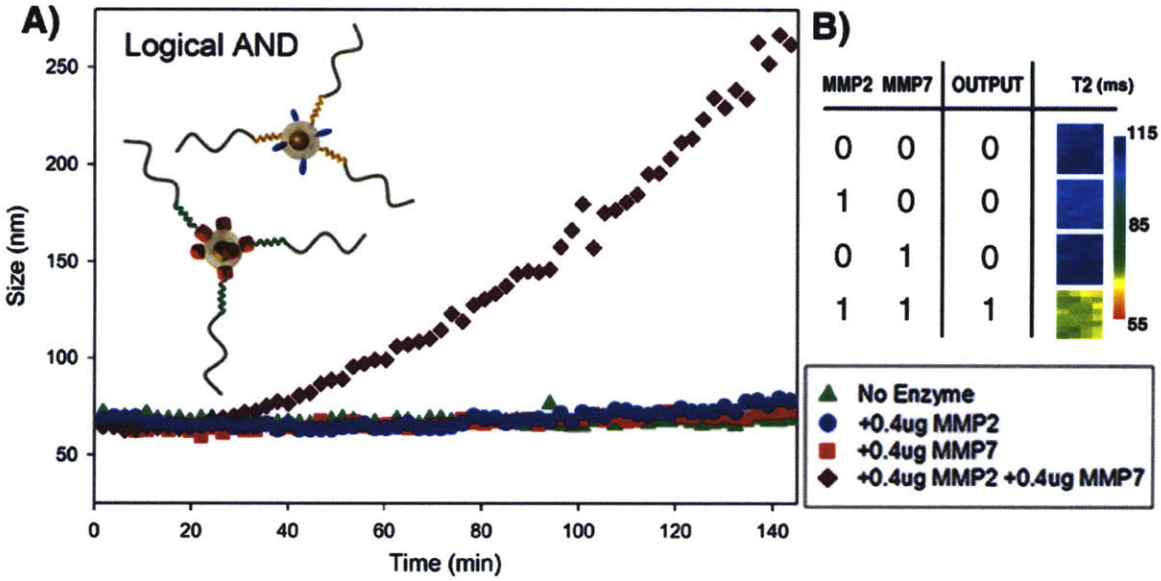

Figure 3.4. *Logical AND* a) Hydrodynamic radius in dynamic light scattering is only increased in the presence of both MMP2 and MMP7; either or none is insufficient to actuate assembly (40ug Fe/ml). b) Assemblies express AND logic in MRI. T2 relaxation decreases ~30% in 3 hours following addition of MMP2 and MMP7, with nominal changes following addition of either enzyme alone (7.5ug Fe/ml). at various timepoints (Figure S3) and incubated with receptor NPs. Following removal of ~50% of NP polymers, assembly begins, eventually revealing sufficient biotin to direct NP precipitation.

To create a logical AND NP system, MMP2-PEG ligand particles with MMP7-PEG receptor particles were combined. Here, in presence of either protease alone, assembly of NPs was prohibited by the PEG polymers remaining on the cognate particle (**Figure 3.4A**). In the presence of both proteases, however, NP self-assembly began and the population hydrodynamic radius increased 5-fold over 3 hours in DLS (**Figure 3.4A**). Further, nanoparticles were able to express AND logic in T2 relaxation changes, mapped using a 4.7T Bruker MRI. In the presence of both enzymes, T2 relaxation is enhanced by ~30% as compared to samples with either enzyme alone or none (**Figure 3.4B**). This enhancement is comparable to published magnetic relaxation sensors(*179, 180, 184*), and occurs at MMP2 concentrations that mimic tumor activity levels *in vivo* (4ug MMP2/ml = 221 U/ml vs. 435 U/g *in vivo*(*203*)).

A second system was constructed to actuate assembly in the presence of either of two proteolytic inputs (Logical OR). Here, only the particles containing the ligand were masked with peptide-linked polymers. To allow either enzyme to actuate assembly, a tandem MMP2-MMP7 peptide substrate was synthesized, containing both cleavage motifs in series (separated by an aminohexanioc acid spacer). Hydrodynamic radii increased more than 5-fold in the presence of either or both enzymes, indicating proper OR function (**Figure 3.5A**). Accordingly, OR NP T2 relaxation decreases ~40% in the presence of either or both enzymes, as compared to samples with no enzyme (**Figure 3.5B**).

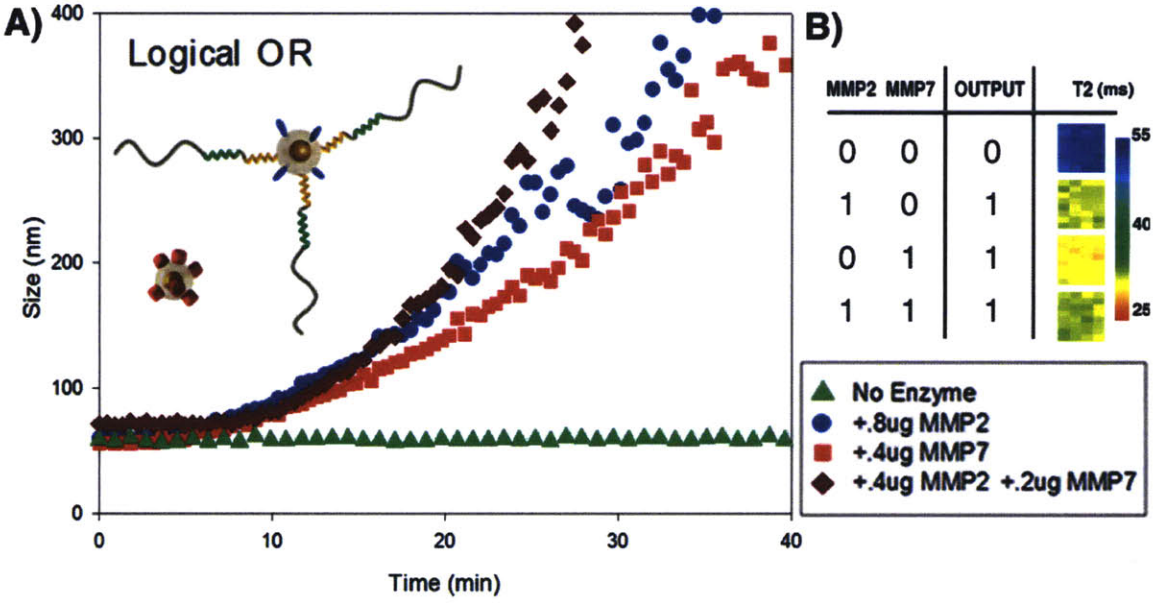

Figure 3.5 *Logical OR* a) Population hydrodynamic radius is increased in the presence of either or both MMP2 and MMP7 (40ug/ml Fe). b) MRI visualization of logical function demonstrates ~40% enhancement in T2 relaxation in the presence of either MMP2 or MMP7 or both enzymes (15ug/ml Fe).

3.3 Conclusion

In conclusion, we have demonstrated the synthesis of NPs that use Boolean logic to simultaneously monitor multiple biological processes associated with tumorigenesis. In the future, we anticipate that logical NP switches may enable more informative imaging of neoplastic transformation in optically opaque samples both *in vitro* and *in vivo*. The modular design of these logical NP sensors can be applied to other enzymatic triggers, complimentary ligand/receptor pairs, or NP cores (semiconductor, plasmonic). Looking further, logical NP switches may enable specific localization of the processes underlying malignant transformation *in vivo*, as proteolytically-assembled beacons in sites of neoplastic inception. Such interstitial assembly may amplify the retention of particles (by mechanical entrapment in the tumor interstitium) and allow MRI visualization of diagnostic logic functions.

3.4 Materials and Methods:

Unless otherwise stated all reagents were purchased from Sigma-Aldrich and all reactions were performed at room temperature.

Superparamagnetic iron oxide nanoparticles were synthesized according to the published protocol(*32*). Briefly, dextran-coated iron oxide nanoparticles were synthesized, purified, and subsequently cross-linked using epichlorohydrin. After exhaustive dialysis, particles were aminated by adding 1:10 v/v ammonium hydroxide (30%) and incubated on a shaker overnight. Aminated-nanoparticles were subsequently purified from excess ammonia using a Sephadex G-50 column and concentrated using a high-gradient magnetic-field filtration column (Miltenyi Biotec).

Peptide-Polymer synthesis: Peptides were synthesized in the MIT Biopolymers core to sequentially contain a lysine (for the attachment of polyethylene glycol polymers), a MMP-cleavage sequence, and a terminal cysteine (for linkage onto amines in the dextran coat or lysines on neutravidin (Pierce) proteins. Peptide purity was verified with HPLC and mass spectrometry. Amine-reactive 20kDa mPEG-SMB reagents (methoxy-polyethylene glycol- succimidyl α methylbutanoate) were purchased from Nektar Therapeutics. The following sequences were used in this investigation: (N->C) MMP2 substrate: G-K(TAMRA)-G-P-L-G-V-R-G-C-CONH2; MMP7 substrate: G-K(TAMRA)-G-V-P-L-S-L-T-M-G-C-CONH2; MMP7-MMP2 tandem substrate: TAMRA-G-K-G-V-P-L-S-L-T-M-Ahx-G-P-L-G-V-R-G-C-CONH2 where K(TAMRA) = Lys(DDE) substituted with 5(6)-TAMRA, TAMRA=5(6)-TAMRA, and Ahx= aminohexanoic acid. Peptides were reacted with polymers in PBS + 0.005M EDTA pH 7.2 at 500uM and 400uM, respectively, for >24 hours with shaking. Free peptide was removed by reducing with 0.1M TCEP and filtering using a G-50 Sepahdex column. The reduced polymer was then quantified using fluorochrome extinction and added to nanoparticle preparations as described below.

Ligand nanoparticle synthesis: Following each conjugation, nanoparticles were purified using a high-gradient magnetic-field filtration column (Miltenyi Biotec). Aminated nanoparticles (1mg Fe/ml) were simultaneously reacted with biotinamidohexanoyl-6-aminohexanoic acid N-hydroxysuccinimide ester and 4-Maleimidobutyric acid N-hydroxysuccinimide ester (.8mM and 1.2mM, respectively) in

0.1M HEPES 0.15M NaCl pH 7.2 buffer for 30 minutes. Purified nanoparticles (1 mg Fe/ml) were then combined with reduced peptide-polymers (1mM) in phospho-buffered saline + 0.005M EDTA pH 7.2 and incubated for >2hrs. Particles were again purified and used in subsequent assembly experiments.

Receptor nanoparticle synthesis: Aminated nanoparticles (1mg Fe/ml) were reacted with biotinamidohexanoyl-6-aminohexanoic acid N-hydroxysuccinimide ester (0.03mM) in 0.1M HEPES 0.15M NaCl pH 7.2 buffer for 30 minutes. Following filtration, nanoparticles (1 mg Fe/ml) were combined with a saturating concentration of neutravidin protein (Pierce, 5mg/ml) and incubated for >3hrs. The extinction of nanoparticle solutions at 600nm was monitored during neutravidin-coating to ensure cross-linking was not occurring. After purification, neutravidin particles were passed through a 0.2 micron filter to ensure removal of any aggregates. Neutravidin nanoparticles (1mg Fe/ml) were then reacted with 4-Maleimidobutyric acid N-hydroxysuccinimide ester (2mM) for 30 minutes, purified, and incubated with peptide-polymers (1mM) for >2hrs as before. Particles were finally purified from excess peptide-polymer and used in subsequent assembly experiments.

Dynamic light scattering studies: All dynamic light scattering experiments were performed in 100ul solutions of 0.1M HEPES 0.15M NaCl 0.005M $CaCl_2$ at 25°C with nanoparticles at 40ug Fe/ml (added at equimolar concentrations). To begin experiment, catalytic domains of MMP2 and MMP7 (Biomol) were added in 5ul to 95ul of nanoparticles or 5ul control buffer was added. Kinetic dynamic light scattering intensity

size measurements were taken using a Malvern ZS90 and hydrodynamic radius was plotted vs time.

Fluoresence activation experiments: NPs were incubated with various enzymes and TAMRA fluorescence was monitored (ex: 515nm/em: 580nm; cutoff 530nm) at 30sec intervals over time. Buffer was matched to DLS studies. Purified plasma proteins (Haematologic Technologies) were incubated with 40ug/ml NP samples in 40ul. For partial assembly studies, reactions were quenched with addition of 10% 0.2M EDTA.

Polymer quantitation: Triplicate partial activation samples were ultracentrifuged (50k, 30min) to precipitate nanoparticles. The supernatant was collected and TAMRA absorbance was quantified to determine peptide-polymer concentration.

MRI detection of nanoparticle self-assembly: MRI T2 mapping was performed using a 7 cm bore, Bruker 4.7T magnet. Nanoparticles were mixed together and serially diluted in 384-well plate, containing 95ul total sample/well. Recombinant MMP2 or MMP7 (Biomol) was pre-incubated at 37C for 30 minutes to activate and added in a total of 5 uL Tris-Cl (50 mM), CaCl2 (5 mM), Brij-35 (0.005%), pH 7.5 were added to each well. After 3 hr incubation, T2 relaxation maps were obtained. Data in each well was displayed by fitting images on a pixel by pixel basis to the equation $y=M*L10^{(-TE/T2)}$ using MATLAB.

Chapter 4: Reversible Nanoparticle Self-Assembly Under the Control of Antagonistic Enzyme Triggers

4.1 Introduction

The ability to dynamically control both the assembly *and* disassembly of biomolecular complexes is essential to higher-order biological processes, including the control of intracellular communication(*222*), gene expression(*223, 224*), and platelet aggregation upon injury(*225*). To date, assembly or disassembly of nanoparticles (NPs) has been exploited to improve sensitivity for detection of single biomolecular targets, including DNA(*177, 179*), small molecules, proteins(*186, 192*), and pH changes(*193*) *in vitro*; however, mechanisms of sensing that allow multiple, opposing stimuli to dynamically assemble *and* dis-assemble NPs have not been described. Development of inorganic nanoparticles that respond to multiple, antagonistic biological signals could facilitate sensing of the physiologic balance between opposing effectors of cellular and tissue function. Herein, we introduce a nanoparticle (NP) system where self-assembly is dynamically coupled to the balance between the classic antagonistic enzymes: tyrosine kinase and phosphatase. *In vivo*, these enzymes regulate cellular communication, gene expression, and ultimately cell life and death through the phosphorylation and dephosphorylation of tyrosine residues on other proteins [226, 227]. Their dysregulation contributes significantly to the development of cancer and other inflammatory diseases(*228, 229*). Here, kinase-induced superparamagnetic nanoassemblies enhance the T2 relaxation of hydrogen atoms at picomolar enzyme concentrations and are shown to be fully reversible by introducing excess phosphatase activity. In the future, these nanomaterials may be optimized to report the balance between these cytosolic

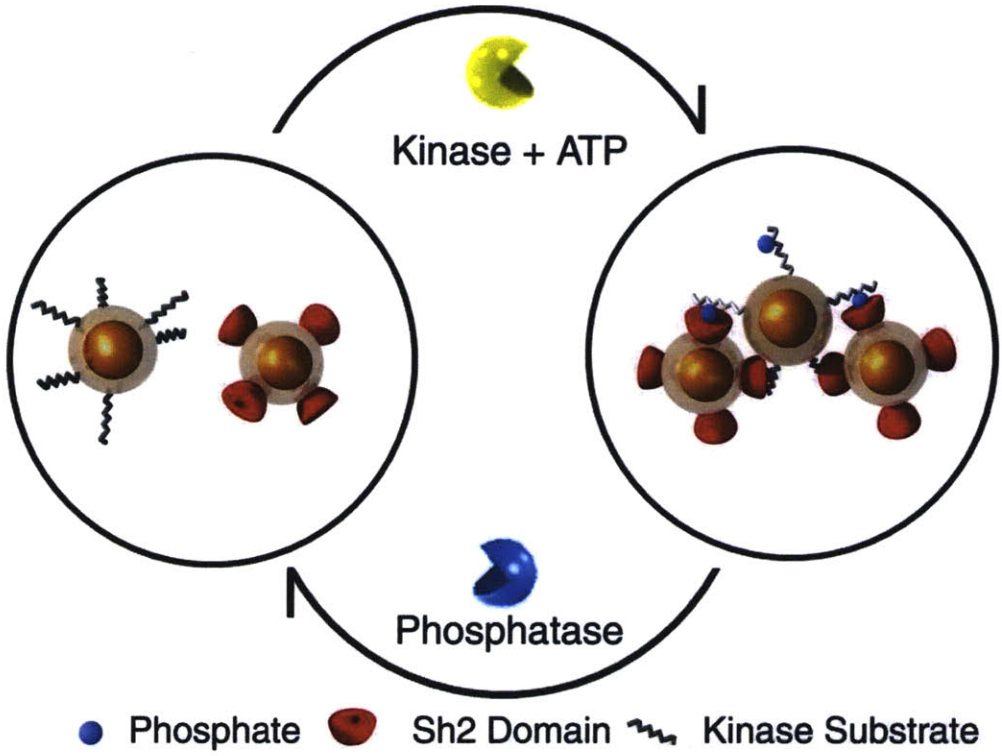

Scheme 4.1.: *Schematic of reversible nanoparticle self-assembly.* Polymer-coated, superparamagnetic NPs were modified to polyvalently display either a tyrosine-containing kinase substrate or an SH2 domain. NPs remain dispersed until kinases phosphorylate substrate NPs, triggering NP assembly via phosphopepetide-SH2 binding. Kinase-directed assembly amplifies the T2 relaxation in MRI and is fully reversible by phosphatase

enzyme activities and may facilitate new screens for inhibitors *in vitro* and *in vivo*. Additionally, extensions of this design logic may be synthesized to probe the dynamics of a diversity of antagonistic biologic processes.

4.2 Results and Discussion

To construct a system of NPs that could coalesce in the presence of kinase activity and re-disperse in the presence of phosphatase activity, two NP populations were synthesized (**Scheme 4.1**). The first population was modified with peptide substrates that

may be phosphorylated by Abl tyrosine kinase and dephosphorylated by a phosphatase. The second population was modified with Src Homology 2 (SH2) domains that recognize and bind the phosphorylated Abl kinase substrate in a sequence-specific manner.(*230*) Together, these NPs process kinase and phosphatase activities by assembling as peptides become phosphorylated and disassembling as phosphates are removed. Magnetic dipoles in NP assemblies coordinate and more efficiently dephase hydrogen protons in MRI, allowing T2 relaxation mapping of kinase function(*184, 231*). Conceptually, this design is akin to the kinase/phosphatase FRET sensors developed by Tsien et al (*232-234*) among many other fluorescence-based kinase sensors,(*235-238*) but instead of transducing enzyme activites into optical fluorescence changes, activity is encoded via NMR relaxation changes.(*182, 231, 239*) Recently, two gold NP-based approaches have sensed either kinase or phosphatase activity in irreversible, two-step assays.(*213, 240*) These designs provide new avenues for colorimetric screening of enzyme inhibitors, yet lack the capacity to continuously analyze both kinase and phosphatase balance. Similarly, while NP-based sensing of single analytes and proteases has been demonstrated,(*184, 231*) the extension of this technology to reversibly sensing multiple enzyme activities has not been accomplished.

We first set out to verify that phosphopeptide-SH2 domain binding could efficiently induce NP assembly at particle concentrations relevant to MR imaging. Dextran-coated iron oxide NPs were synthesized, cross-linked, and aminated according to published procedures.(*241-243*) The Crk SH2 domain was genetically modified to contain an (N- terminal) cysteine to allow convenient conjugation to NPs. GST-tagged cysteine-SH2 was expressed in bacteria, purified, and the GST affinity label was removed

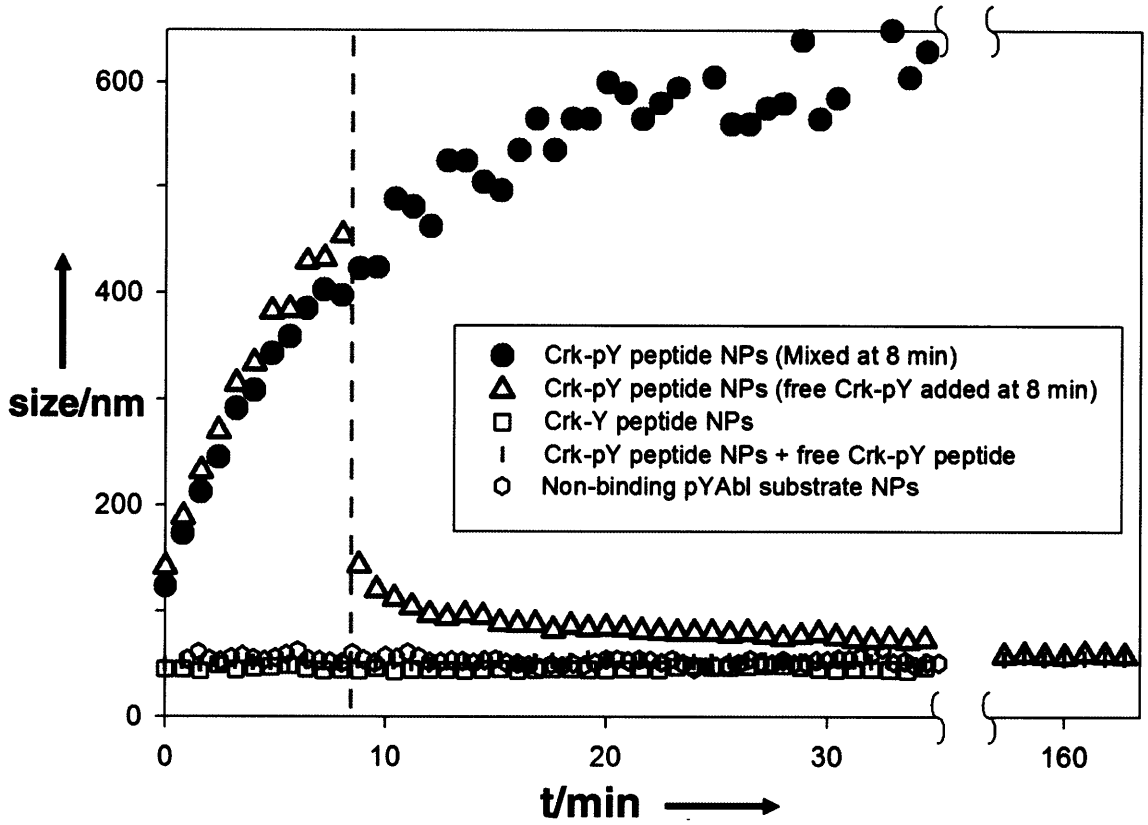

Figure 4.1. *Dynamic light scattering detection of nanoparticle assembly.* Phosphopeptide (pY) NP assembly with SH2 NPs. Upon addition of SH2 NPs to pY-peptide NPs, rapid increase in hydrodynamic radius was observed by DLS (filled circles). In the presence of free pY-peptide, NP assembly was not observed (vertical lines). Non-phosphorylated peptide and non-binding pY-peptide remain dispersed with SH2 NPs, demonstrating both sequence- and phosphate- specific peptide recognition by SH2 NPs (hollow square and hollow dot, respectively). Assembly was reversed by addition of excess free pY-peptide to the mixture after 8 min incubation (hollow triangles).

(see methods). Reduced cysteine-SH2 were conjugated to amine-NPs (~14 SH2 domains/NP) via highly flexible heterobifunctional linkers, containing 12 polyethylene oxide units (54.4 Å), to increase conformational freedom. In parallel, a phosphotyrosine (pY) sequence with low μM binding affinity to Crk SH2 (-QpYDHPNI-)(*230, 244*) was synthesized with an N-terminal cysteine and attached to a second population of NPs using the same linker (~15 peptides/NP). When combined, these NPs rapidly assembled

even at NP concentrations three orders of magnitude lower than the free peptide-SH2 affinity, as shown by the 10-fold hydrodynamic radius increase of 12 nM NPs within 15 minutes using dynamic light scattering (DLS) (**Figure 4.1**). In the presence of 200 μM free pY peptide, assembly was inhibited. Further, SH2-NPs were able to discriminate pY-NPs from Y-NPs (unphosphorylated tyrosine: ~13 peptides/NP) and from a phosphopeptide not expected to bind to CRK SH2 (EAIpYAAPFAKKKC: ~14 peptides/NP).[230] To test the reversibility of this system, pY NPs and SH2 NPs assembly was interrupted with addition of 200 μM free pY-peptide or 2 μl of buffer (**Figure 4.1**). While mixing shear stress had no affect on NP assembly, particles with 200 μM free peptide rapidly disassembled, dispersing over time.

The robust association of pY-NPs with SH2-NPs indicated that phospho-dependent NP assembly may provide a rapid mechanism for probing kinase activity. To begin, a kinase substrate (SRVGEEEHVYSFPNKQKSAEC) derived from paxillin was chosen for its Crk SH2 binding and specificity to Abl.(*245, 246*) Three versions of this peptide substrate were synthesized and attached to NPs: a phosphorylated substrate (pY-Abl) (~11 peptides/NP), an unphosphorylated substrate (Y-Abl) (~10 peptides/NP), and a substrate where the receptor tyrosine was replaced with a phenylalanine (F-Abl) (~10 peptides/NP). Abl kinase rapidly directed assembly in solutions containing Y-Abl NPs with SH2 NPs, while an F-Abl peptide control remained dispersed in DLS (**Figure 4.2A**). We next probed the ability of NP self-assembly to transduce kinase activity into NMR T2 relaxation changes using a 4.7T Bruker MRI (Figure 2b,c). Quantifiable T2 relaxation enhancements in solutions containing Y-Abl NPs with SH2 NPs were observed in the presence of as little as 7 femtomoles of added kinase (110 pM kinase concentrations =

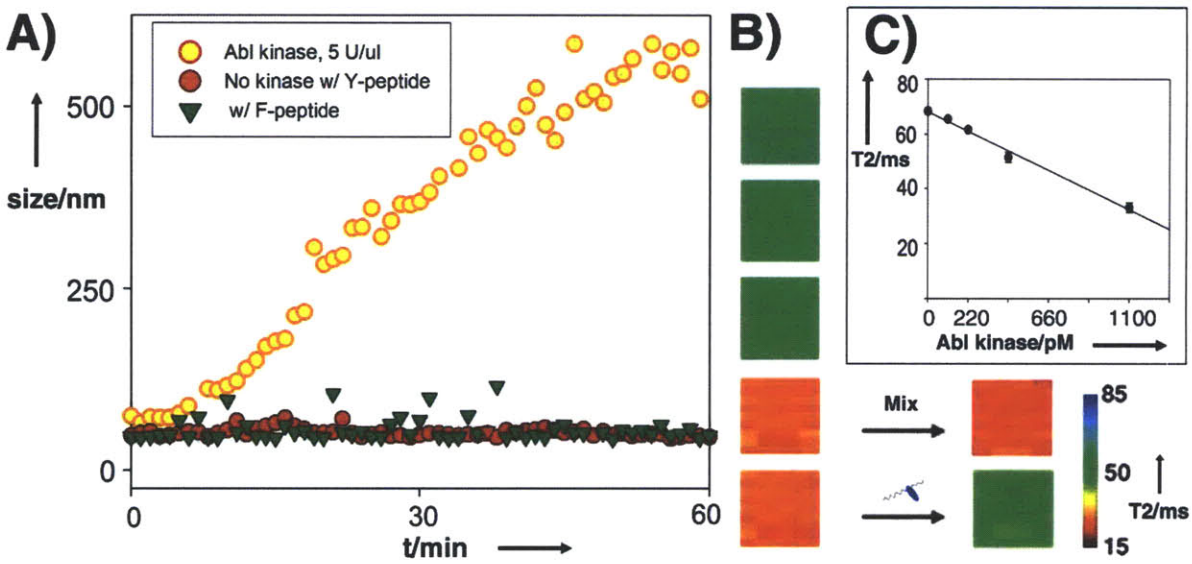

Figure 4.2. *Kinase-directed nanoparticle assembly*. (A). Abl kinase (5 U/µl) (yellow dots) was added to a mixture of SH2 NPs and tyrosine-containing, Abl substrate NPs at 2 min and NP radius was observed over time using dynamic light scattering (DLS). Controls without kinase (red dots) with phenylalanine-Abl substrate NPs (green triangle) did not assemble. (B) In MRI, T2 relaxation was enhanced by Abl kinase-directed assembly (bottom two wells) and was reversed by addition of 200 µM free phosphopeptide, but not by mixing alone. Controls lacking enzyme (top), containing phenylalanine substrate NPs (second from top), or 200 µM free pY substrate (third from top) did not show enhancement. (C) Dose dependent T2 relaxation enhancement of SH2 NPs and Y-peptide NPs 3 hours following Abl kinase addition (12 nM NPs).

0.05 U/µl) (**Figure 4.2C**). Further, T2 enhancement was lost upon addition of free pY-Abl substrate, demonstrating that kinase-directed NP assembly depended on phosphopeptide-SH2 domain interactions that were reversible by competition (**Figure 4.2B**). As NPs coalesce, tyrosine-linked phosphates become sequestered in SH2 domain binding pockets. Having demonstrated that addition of free pY-peptide was able to reverse NP binding, we sought to examine whether phosphatase activity could oppose kinase-directed self-assembly by removing phosphates from tyrosine residues as they

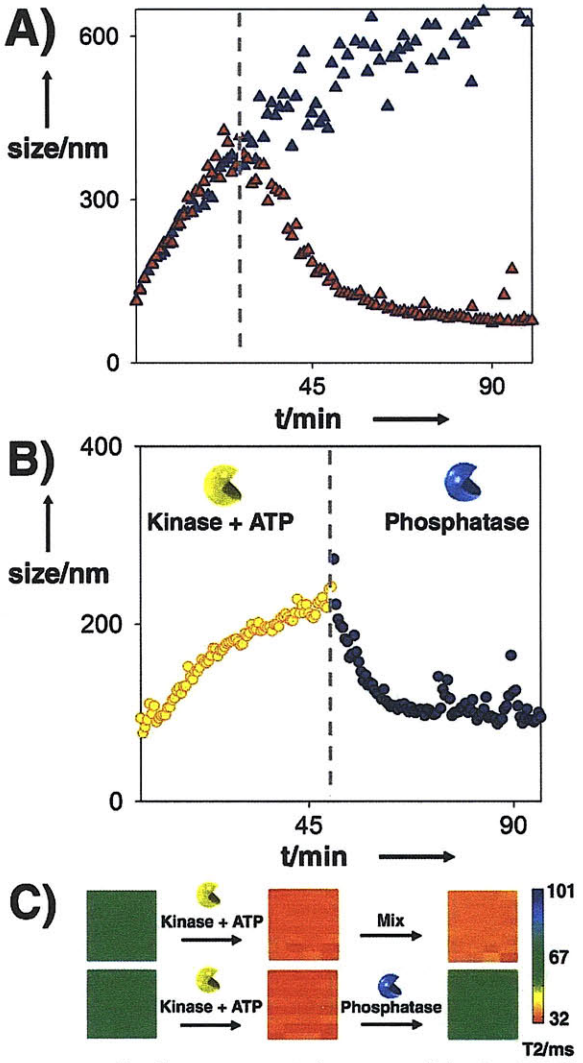

Figure 4.3. *Phosphatase reversal of nanoparticle assembly in DLS and MRI.* (A) SH2 NPs and pY-Abl substrate NPs were allowed to assemble prior to addition of phosphatase (2U/μl) (red) or vehicle control at 25 min (blue). (B) NPs were exposed to Abl kinase (2.5 U/μl), followed by phosphatase (5 U/μl). (C) Kinase-directed assembly (2.5 U/μl) and phosphatase disassembly (5 U/μl) was visualized via T2 relaxation enhancement in MRI.

dynamically disassociate with SH2 domains. To begin, we tested YOP phosphatase's ability to counteract the rapid association of pY-Abl NPs with SH2 NPs. Similar to the

competition test performed previously (**Figure 4.1A**), assembly of pY-Abl NPs with SH2 NPs was interrupted and reversed by addition of phosphatase, but not by buffer alone (Figure 3a). Additionally, when Y-Abl NPs and SH2 NPs were first exposed to Abl kinase and subsequently to an excess of antagonistic phosphatase, kinase-catalyzed NP assembly was efficiently reversed by the excess phosphatase (**Figure 3B,C**).

Together, these results illustrate the ability of this NP system to continuously sense cycling kinase/phophatase activities in MR. Importantly, phosphatase is able to both halt NP assembly (by removing phosphates from free NPs) and to deconstruct phospho-dependent nanoassemblies (by removing phosphates as they dynamically disassociated with SH2 domains). We believe the rapid reversal of NP assembly (either via monomer competition or substrate de-phosphorylation) and the enhancement of NP avidity over anticipated monovalent binding (assembling at NP concentrations 1000-fold below peptide/SH2 affinities) are indications of polyvalent NP binding.(*148*) Unlike monovalent interactions, the disassociation rate of polyvalent species is accelerated by the presence of monomeric competitor.(*247*) Synthetically, polyvalency has been exploited to develop improved biological inhibitors,(*148*) targeting agents,(*248, 249*) and affinity chromatography procedures.(*247*) Here, we exploit polyvalent binding to engineer a reversible NP system that assembles into stable nanostructures, yet may also be rapidly disassembled by competition.

4.3 Conclusions

In summary, we present the design and synthesis of a NP system that processes two antagonistic enzymes inputs (tyrosine kinase/phosphatase) to output enhanced T2 relaxation in the presence of net kinase activity. Phosphopeptide-directed assembly

enables rapid MR visualization of kinase activity at nanomolar NP and picomolar kinase concentrations. To the best of our knowledge, this represents the first demonstration of a NP sensor that reversibly processes two specific, antagonistic enzyme inputs. Looking forward, as MRI field strengths increase and methods for labeling cells with nanomaterials advance,(*212, 250, 251*) optimizations of this design may enable a variety of novel real-time assays to monitor kinase and phosphatase inhibition or to image cytosolic enzyme activities in optically opaque media and *in vivo* using MRI. Further, the modularity of our design should enable key features to be altered without requiring significant re-engineering. For example, this technology may be extended to incorporate new nanoparticle cores (ex. semiconductor, plasmonic) or to sense other antagonistic biological stimuli (other kinase/phosphatase pairs, acetylase/deacetylase pairs, etc).

4.4 Materials and Methods:

All chemicals and reagents were purchased from Sigma-Aldrich unless specified. Plasmid expressing GST-Cys-SH2 was generously supplied by Dr. Barbara Imperiali (Department of Chemistry, MIT). Peptides were synthesized following standard Fmoc solid phase peptide synthesis method using an ABI Model 433A peptide synthesizer in MIT center for cancer research biopolymer laboratory. Nanoparticle size was measured using Zetasizer (Malvern Instruments). MRI images were taken on a Bruker 4.7T magnet. All enzyme reactions were carried out at 30 oC unless specified otherwise. Aminated nanoparticles were synthesized according to published procedures.

Expression and purification of SH2 domain: BL21-Gold(DE3) cells harbouring GST-Cys-Crk SH2 plasmid (pGEX4T-Cys-CrkSH2) were grown to midlog phase in LB media containing carbenicillin (50 μg/ml) at 37 oC, 220 rpm. Protein expression was induced

with addition of 0.1 mM IPTG after cells were cooled to 16 oC and then, cells were incubated at 16 oC for 21 hrs. The cells were centrifuged at 5000 rpm, 4 oC for 30 min, and the cell pellet was resuspended in a lysis buffer (1xPBS, 100 mM EDTA, 1 % Triton X-100, 10 % glycerol, 1 mg/ml lysozyme, 1xprotease inhibitor cocktail set III (CalbioChem)) and incubated for 30 min at 4oC. After sonication, the soluble fraction was isolated from cell debris after centrifugation (14000 rpm, 30 min) and purified using glutathione sepharose 4B affinity column (Amersham Biosciences) following manufacture's protocol. Eluted proteins were dialyzed with 7 kD MW cutoff dialysis cassette (Slide-a-Lyzer, Pierce) against 1xPBS and characterized by SDS-PAGE. To remove GST tag, protein solution (1 mg/ml) was treated with TEV protease (50 units/ml, Invitrogen) in a TEV protease buffer (50 mM Tris-HCl, 0.5 mM EDTA, pH 8.0) in the presence of 1 mM DTT. After 4 hr incubation at 25 oC, the cleavage reaction mixture was subject to glutathione column and then, Ni+2-NTA column to sequentially remove cleaved GST tag and TEV protease, respectively. To ensure that cysteine thiols of cys-SH2 domain were fully reduced, cys-SH2 domain was passed through reducing column (Reduce-Imm Immobilized Reductant Column, Pierce) following manufacture's instruction immediately prior to nanoparticle conjugation.

Preparation of peptide-presenting nanoparticles and SH2-conjugated nanoparticles: First, maleimide-activated NPs were prepared by conjugating NHS-PEO12-maleimide (succinimidyl-[(N- maleimidopropionamido)-dodecaethyleneglycol] ester, Pierce) to aminated NPs. Typically, NPs (0.25 mg Fe) were incubated with 4 mM of NHS-PEO12-maleimide for 30 min at 25 oC and then purified using a magnetic field filtration column (Miltenyi Biotec). SH2 conjugated particles were prepared by

incubating Cys-SH2 (1 mg/ml) with maleimide presented NPs (0.25 mg Fe) for 3 hrs at RT. Unreacted Cys-SH2 domain was removed using a magnetic field filtration column. Peptides were conjugated by activating amine-NPs with NHS-PEO12-maleimide as above, followed by addition of peptide substrate. Particles were filtered 2 hours after peptide addition. The peptides used in this investigation were synthesized as follows:

CRK SH2-binding:

TAMRA-C(Ahx)QpYDHPNI-CONH2

TAMRA-C(Ahx)QYDHPNI-CONH2

Non-Binding Abl substrate:

TAMRA-(Ahx)EAIpYAAPFAKKKC-CONH2

CRK SH2-binding Abl substrates:

TAMRA-(Ahx)SRVGEEEHVpYSFPNKQKSAEC-CONH2

TAMRA-(Ahx)SRVGEEEHVYSFPNKQKSAEC-CONH2

TAMRA-(Ahx)SRVGEEEHVFSFPNKQKSAEC-CONH2

(Ahx:aminohexanoic acid)

Quantification of peptide/SH2 numbers per NP: The yield of the SH2 domain-NP reaction was quantified by performing a bicinchroninic acid protein assay (BCA Protein Assay Kit, Pierce, Rockford, IL, USA) on modified vs unmodified NPs after purification. SH2 NPs were compared with their parent PEO-NPs containing a gradient of albumin. 220ug of SH2 domain (~13kDa) were conjugated per 1mg of Fe in NPs (805,000 mg Fe/mole NPs). Peptide attachment yields were quantified by monitoring the increase in

purified NP absorbance at 555nm following TAMRA-peptide conjugations (TAMRA extinction: 90,000 M-1 cm-1).

SH2-binding peptide-mediated nanoparticle assembly: Nanoparticles presenting CRK SH2-binding peptide (either phosphorylated or unphosphorylated) or non-binding Abl substrate (phosphorylated) were incubated with CRK-SH2 NPs at 10μg Fe/ml (12 nM NP concentration) and monitored with DLS over time.

Kinase-directed nanoparticle assembly: Nanoparticles presenting kinase substrate peptide (10 μg Fe/ml; 12nM) and SH2-presented nanoparticles (10 μg Fe/ml; 12nM) were mixed in a kinase reaction buffer (20 mM Tris-HCl, pH 7.5, 2 mM MgCl2, 20 mM NaCl, 0.2 mM EGTA, 0.4 mM DTT, 0.004 % Brij 35, 0.2 mM ATP) in a total volume of 50 μl. Kinase reaction was initiated by adding indicated amount of Abl kinase (New England Biolabs). NP assemblies were characterized by DLS over time or MRI.

Phosphatase-directed nanoparticle disassembly: First, SH2 nanoparticles (5 μg Fe/ml; 6nM) were added to phosphorylated tyrosine containing peptide nanoparticles (5 μg Fe/ml; 6 nM) in a buffer solution (20 mM Tris-HCl pH 7.5, 20 mM NaCl, 0.4 mM Na2EDTA, 2 mM DTT, 0.004 % Brij 35) to initiate nanoparticle assembly. YOP protein tyrosine phosphatase (New England Biolabs, 2 U/μl) was added when size of assembled nanoparticles reached to about 400 nm in radius.

Reversal of kinase induced nanoparticle assembly by phosphatase: First, nanoparticle assembly was initiated following same protocols described above. Then, YOP phosphatase (5 U/μl in final concentration) was directly added into a kinase reaction mixture. Size measurement was restarted right after thoroughly mixing the reaction mixture.

MRI imaging of nanoparticles: All nanoparticle solutions were prepared in final concentration of 10 μg Fe/ml (12 nM) in 70 μl of kinase reaction buffer. Nanoparticle mixtures were incubated at 30oC for 3 hrs after kinase additions (0, 0.05, 0.1, 0.2, 0.5 U/μl) and then, MRI images were taken using a 4.7T Bruker magnet (7cm bore) using T2-mapping Carr-Purcell-Meiboom-Gill pulse sequence. To reverse the assembly, YOP phosphatase (4 U/μl) or free pY-peptide (0.1 mM) was added to an assembled nanoparticle solution containing 0.2 U/μl Abl kinase. The MRI image was taken after 10 min incubation at room temperature.

Section II: Engineering *Indirect* Nanoparticle Interactions for Cancer Targeting *In Vivo*

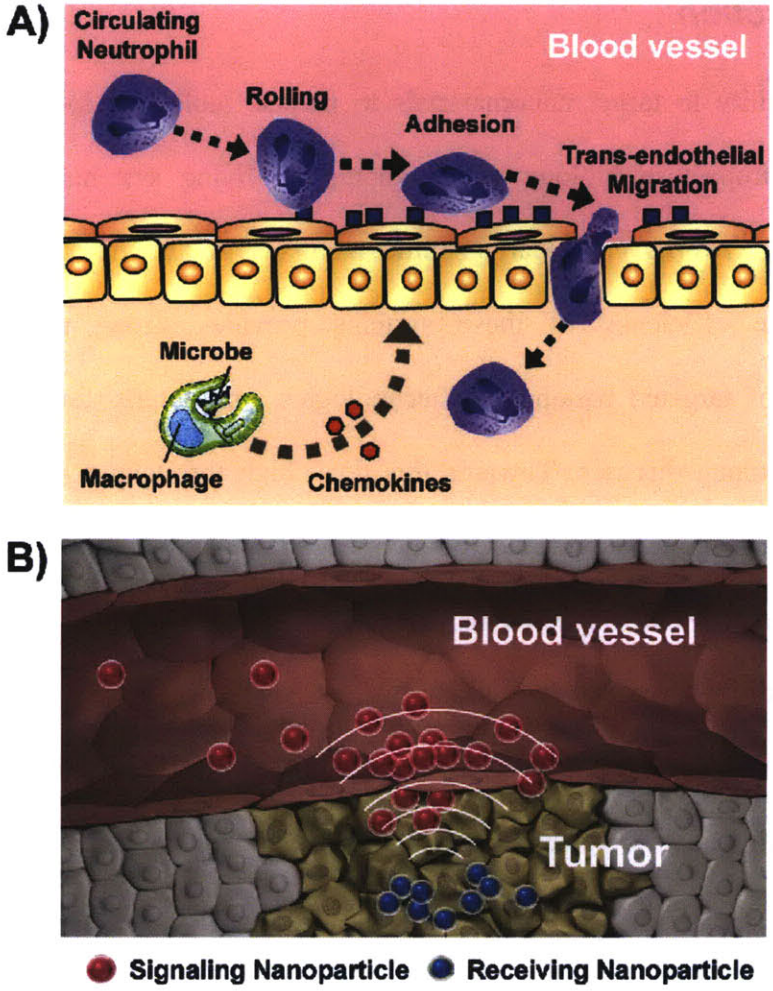

Scheme II. *Inspired by mechanisms of remote communication in biology, the second section of this thesis describes nanoparticles that remotely communicate with one another via biological intermediates to amplify tumor targeting.* A) In areas of infection, tissue resident macrophages engulf microbes and produce cytokines to remotely stimulate the infiltration of circulating leukocytes in the blood stream (where concentrations exceed $>10^6$ cells/ml blood). This process occurs as chemokines diffuse to the local blood vessels and stimulate upregulation of integrins to recruit neutrophil rolling, firm adhesion, and local transmigration into the tissue to amplify cellular assistance. B) Inspired by this process, we set out to engineer mechanisms by which two distinct populations of nanoparticle could communicate to improve tumor imaging and drug delivery. Here, an initial population of 'Signaling' nanoparticles has homed to tumors and, after arrival, remotely signals to 'Receiving' nanoparticles in circulation to extravasate and bind.

Chapter 5: *In Vivo* Nanoparticle Surface Chemistry: 'Clickable' Nanomaterials for Receptor Targeting

5.1 Introduction

The ability to target nanomaterials to precise biological locations would have wide-ranging impact in biology and medicine. In living systems, highly controlled transportation networks continually shuttle payloads to and from specific molecular addresses. The efficiency of these systems provides strong motivation for the advancement of targeted nanoparticle technologies, particularly for the diagnosis and treatment of human diseases. Towards this goal, high throughput strategies for ligand discovery have generated a multitude of chemical and biological motifs with the potential to direct nanomaterials to specific biomolecular targets. However, translation of these ligands towards *in vivo* nanoparticle targeting has been limited by the number of nanoparticle attachment methods that are efficient, generalizable, aqueous-compatible, chemically orthogonal to broad ranges of functional groups, and suitable for *in vivo* applications.

Previous work has demonstrated that *in vivo* bacteriophage display may be used to select for peptide sequences that mimic the ability of endogenous shuttles to target vascular and parenchymal tissue addresses (*252-256*). Already, linear peptide candidates of phage screens, as well as small molecule targeting candidates, have been translated towards nanomaterial targeting (*248, 249, 257, 258*), primarily via use of exogenous or non-essential thiols, carboxylic acids, or amines. Still, some of the most powerful targeting motifs developed to date are those that contain essential thiol, amine, and

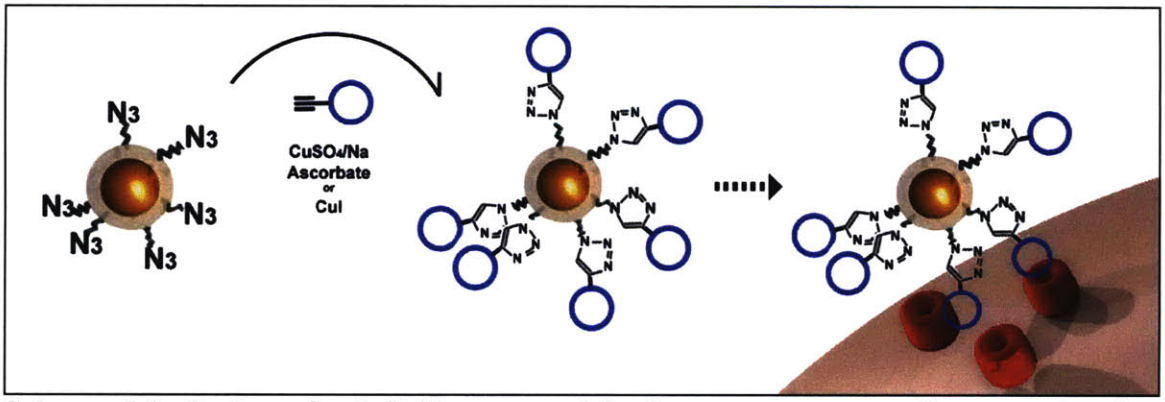

Scheme 5.1. *Design of a "click" nanoparticle that targets tumor cells in vitro and in vivo*. Cross-linked, fluorescent, superparamagnetic iron oxide nanoparticles are modified to display azido-PEG groups. Conjugation of cyclic targeting peptides (purple circles) bearing pendant alkynes to azido-PEG nanoparticles via the copper(I)-catalyzed Huisgen 1,3-dipolar cycloaddition ("click" reaction) allows specific targeting of the nanoparticles to cells expressing the receptor (red).

carboxyl groups, thereby prohibiting their specific attachment via traditional methods. In particular, conformationally-constrained, disulfide-cyclized targeting peptides are desirable for their enhanced affinity to biological receptors (*259, 260*), and resistance to proteolytic degradation *in vivo* relative to their linear counterparts (*261, 262*). However, specific intramolecular cyclization makes it difficult to add exogenous cysteine residues, while essential amines and carboxyl groups prohibit selective conjugation via exogenous lysine, aspartic acid, or glutamic acid residues. Additionally, non-covalent methods of ligand attachment relying on hydrophobic or electrostatic effects, although widely used *in vitro*

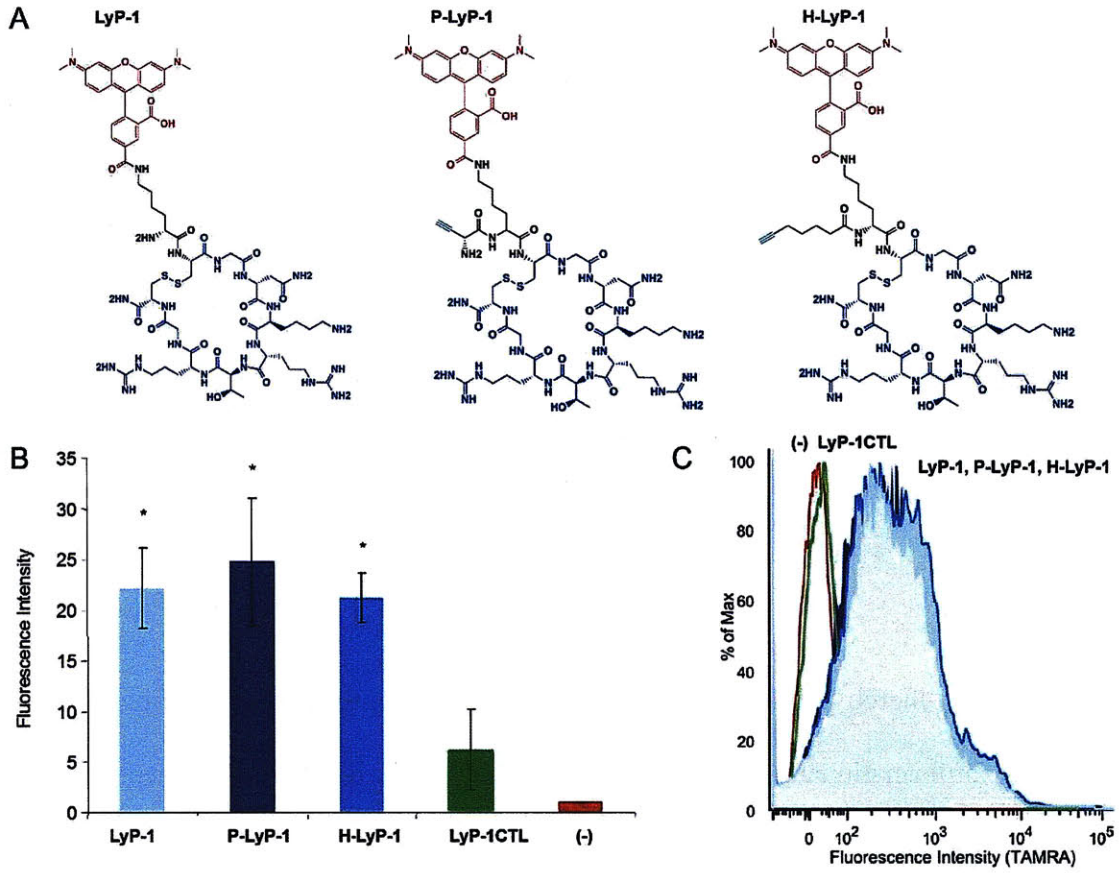

Figure 5.1. *Native and alkyne-bearing LyP-1 peptides target p32-expressing MDA-MB-435 cells in vitro.* (A) Structures of LyP-1, propargylglycine-LyP-1, and Heptynoic acid-LyP-1, all labeled with a TAMRA fluorophore (red). The cyclic nonapeptide is in blue. The pendant alkyne moieties were conjugated to the N-terminus of the peptide during standard FMOC peptide synthesis. (B) Flow cytometry shows that peptides bearing different alkyne groups target MDA-MB-435 cancer cells similarly, while a scrambled control (LyP-1CTL) do not target (P=propargylglycine, H=6-heptynoic acid, $*p<0.01$, unpaired Student's *t*-test). (C) Flow cytometry histogram shows LyP-1, P-LyP-1, and H-LyP-1 peptides (in different shades of blue) target MDA-MB-435 cells *in vitro*, while LyP-1CTL peptide (green) did not show targeting relative to peptide-free control cells (red).

(*44, 263, 264*), are unlikely to remain stable in blood or to resist rapid clearance *in vivo*.

Recently, the copper(I)-catalyzed Huisgen 1,3-dipolar cycloaddition or "click" chemistry has emerged as an extraordinarily selective chemistry and an attractive solution in

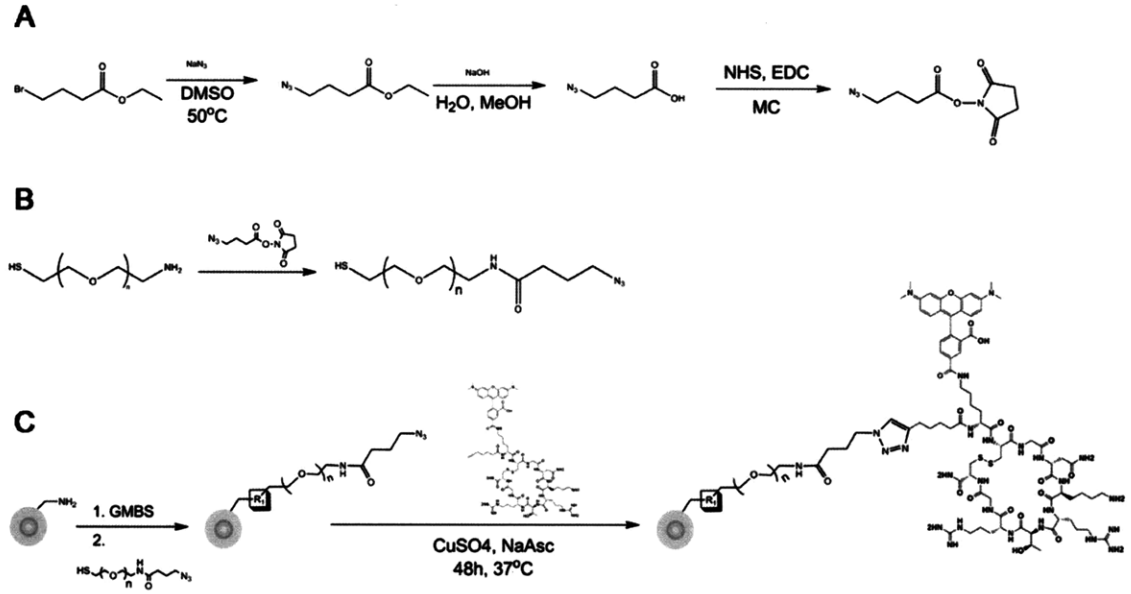

Scheme 5.2. *Synthesis of LyP-1-coated nanoparticles using "click" chemistry.* (A) Synthesis of Succinimidyl 4-azidobutyrate. (B) Synthesis of azide-PEG-thiol by linking Succinimidyl 4-azidobutyrate to a 5kDa thiol-PEG-amine. (C) Aminated, cross-linked, fluorochrome-labeled superparamagnetic iron-oxide nanoparticles are activated with GMBS, filtered, and then reacted with the thiol-PEG-azide from (B) to yield azido-PEG bearing nanoparticles. After purification, the particle solutions were reacted with alkyne-bearing LyP-1 peptides with $CuSO_4$ / Na Ascorbate as catalysts to yield LyP-1-coated nanoparticles for *in vitro* and *in vivo* use.

applications where commonly used thiol-reactive (maleimide, 2-pyridyldithio, iodoacetyl) or amine-reactive (NHS, epoxy, aldehyde, EDC) chemistries are not suitable (*265*). *In vitro*, "click" chemistry has been utilized to generate functionalized polymers (*266-268*), surfaces(*269-271*), and nanoparticles (*272-280*), and meets the criteria for broad utility in nanoparticle functionalization (chemical orthogonality, aqueous efficiency, applicability for diverse substrates). However the use of "click" nanoparticles for *in vivo* applications has not been investigated. Particularly, as opposed to small molecule reagents with circulation times on the order of minutes (*258*), ligand

attachments on long circulating nanomaterials must remain stable against *in vivo* degradation for hours while nanoparticles circulate systemically and identify molecular targets.

Here, we find that alkyne-azide "click" chemistry provides a facile, single-step method for specifically linking the cyclic tumor-targeting peptide LyP-1 (CGNKRTRGC; (*252, 281*)), which contains essential thiol and amine groups, to polymer-coated magneto-fluorescent nanoparticles. LyP-1 binds to p32, a mitochondrial proteins that is both overexpressed and aberrantly localized at the cell surface of tumor cells, macrophages and lymphatic endothelial cells in certain experimental tumors and in human cancers (*282, 283*). We find that "click" LyP-1 nanoparticles are able stably traverse the systemic circulation, extravasate into tumors, and penetrate the tumor interstitium to specifically bind to receptors on p32-expressing cells in the tumors. Together, these results provide strong motivation for future use of "click" functionalization as a strategy for developing nanoparticles for *in vivo* biomedical applications.

5.2 Results and Discussion

In order for "click" chemistry to be applied to the development of peptide-targeted nanomaterials, peptides must be able to harbor pendant alkyne or azide moieties without abating peptide activity. To investigate the efficacy of targeting peptides harboring pendant alkyne moieties, LyP-1 peptide (CGNKRTRGC) and untargeted cyclic control peptide, LyP-1CTL (CRVRTRSGC) in which the essential NKRTR motif is replaced with RVRTR to maintain net charge but abate p32 targeting(*281*), were synthesized to incorporate either of two alkyne moieties (the unnatural amino acid

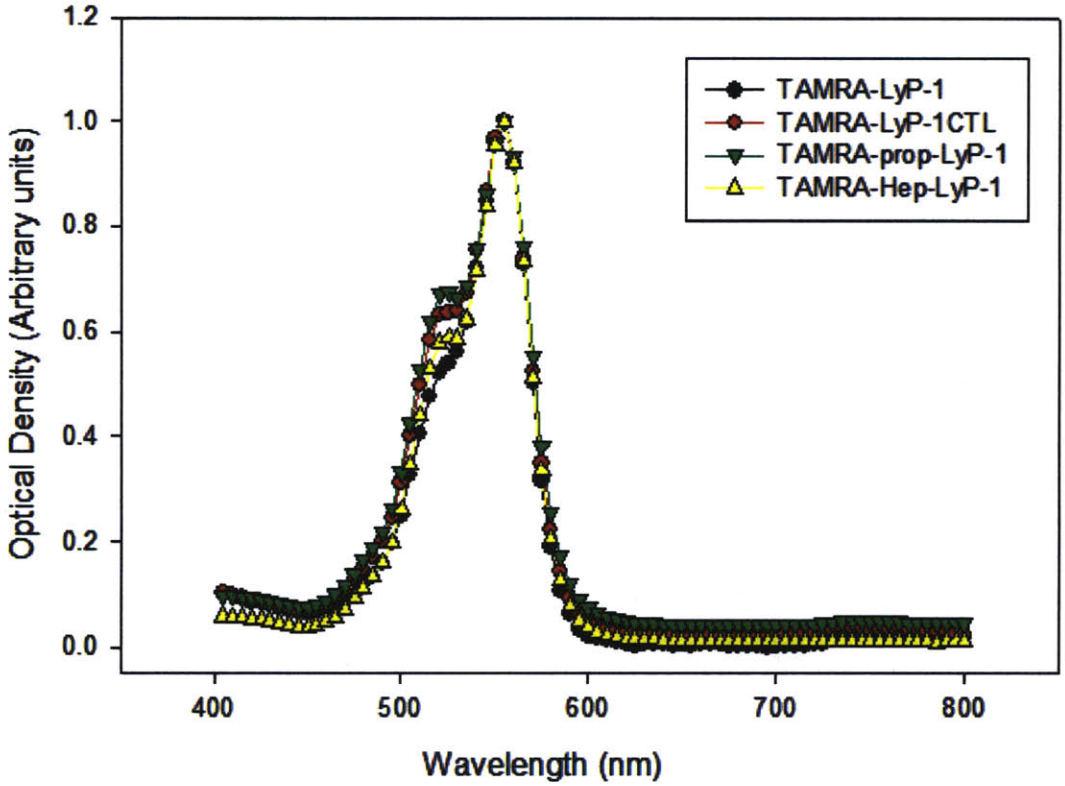

Figure 5.2: *Fluorophore-labeled LyP-1 Peptide Spectra.* UV-Vis spectra for LyP-1 and LyP-1CTL peptides synthesized with varying pendant alkyne groups (prop= propargylglycine; Hep=heptynoic acid)

propargylglycine or 6-heptynoic acid) and a 5,6-carboxytetramethylrhodamine fluorophore (TAMRA) (**Figure 5.1A; Figure 5.2**). Because the alkyne moieties provide molecularly small chemical handles that may be incorporated in FMOC synthesis to either the N- or C-terminal of essential peptide sequences, we hypothesized their presence could be tailored to allow chemical attachment to azido-nanomaterials without interfering with LyP-1 peptide activity. In previous investigations, we found that N-terminal addition of visible and near-infrared fluorophores do not disrupt peptide binding to its receptors (*252, 281*). Accordingly, we reasoned alkyne moieties located near the N-

terminus would be well-tolerated by the peptide (**Figure 5.1A**). To verify the specificity and efficacy of alkyne-LyP-1 targeting, 10 μM of LyP-1, bearing either propargylglycine, heptynoic, or no alkyne group were incubated for 45 minutes on monolayers of MDA-MB-435 human tumor cells, which have been shown to bind and internalize LyP-1 and express p32 at the cell surface (*281, 282*), LyP-1CTL peptides were included as a control sequence to verify targeted enhancement of uptake over non-specific cyclic peptide structures. Cellular uptake of LyP-1 peptide was quantified via flow cytometry (**Figure 5.1B**) and plotted as the populational fluorescent intensity, relative to cells incubated with vehicle alone. *In vitro* targeting of LyP-1 peptides bearing either propargylglycine or 6-heptyoic acid was similar to that of native LyP-1 and control peptides (Figure 1C), indicating that alkyne modifications N-terminal to targeting sequences were innocuously chaperoned by peptides and did not affect cell binding.

We next probed the effect of three variables on "click" reaction conditions between our peptides and an azido-PEG-amine (catalyst, catalyst concentration, and reaction time). Azido-PEG-amine was chosen to emulate the azido-PEG surface of the nanoparticles to be used subsequently and to provide a model reaction amenable to HPLC quantitation of product formation. Copper(I) catalyst was added either directly as an iodinated salt (Cu(I)I), or indirectly as soluble copper sulfate ($Cu(II)SO_4$) and reduced by sodium ascorbate *in situ*. The degree of product formation was measured via HPLC with mass spectrometric verification of product identity. The addition of the azido-PEO-amine rendered peptides more hydrophilic and decreased retention times compared to unconjugated peptides. As shown in **Table 5.1**, product formation proceeded more

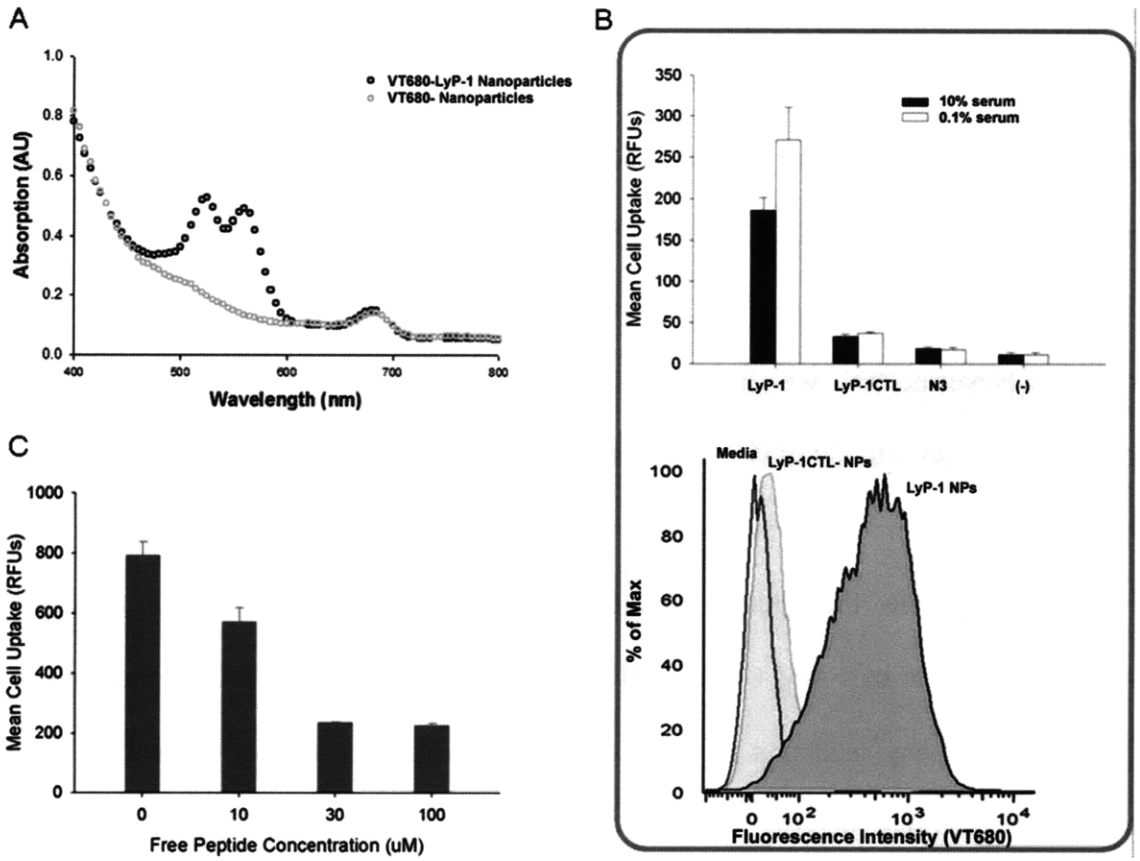

Figure 5.3. *LyP-1-conjugated nanoparticles target p32-expressing MDA-MB-435 cells in vitro, while nanoparticles conjugated to control cyclic peptides (LyP-1CTL) do not target.* (A) The amount of peptide bound per particle was quantified spectrophotometrically by measuring the absorbance of the TAMRA dyes added following the click reaction. With the addition of catalyst $CuSO_4$/Na ascorbate (dark circles), the TAMRA absorbance at 555nm was quantified to equal approximately 30 peptides per particle, whereas no TAMRA signal was observed without catalyst (light circles). (B) LyP-1-nanoparticles or control LyP-1CTL-nanoparticles (both at ~30 peptides per particle), or parent azido-bearing particles (N3), were added to MDA-435-MB cancer cells in normal 10% serum (dark green) and 0.1% serum-starved (light green) conditions. Flow cytometry histogram shows marked increase in uptake of LyP-1-nanoparticles (blue) vs. LyP-1CTL-nanoparticles (green) and particle-free control cells (red). Each error bar represents 6 parallel experiments. (C) Addition of free LyP-1 peptides at concentrations from 10 to 100 uM inhibited cellular uptake of LyP-1-coated nanoparticles, suggesting that the LyP-1 peptide and LyP-1-labeled particles target the same receptor.

completely in the tested reaction conditions for the heptynoic acid-LyP-1, likely due to reduced steric hindrance provided by the extended hydrocarbon chain. Optimal reaction conditions were found to be either: 1 mM $CuSO_4$ / 5 mM Na ascorbate or 1 mM -100 mM CuI for 72 h. Notably, the reaction yields with 10 mM $CuSO_4$ levels were dramatically lower than 1mM, likely due to global precipitation of reduced Cu(I) in solution. Nevertheless, we found 1mM $CuSO_4$ reactions to yield more reliable conjugations than 1 to100 mM CuI reactions, possibly because the insolubility of CuI in aqueous solutions produced variations in the amount of available catalyst delivered to the reactions. Therefore, the optimal conditions for subsequent nanoparticle modification were determined to be 1 mM $CuSO_4$ and 5 mM Na ascorbate. Under these conditions we did not observe any reduction of peptide disulfide bonds due to copper catalyst or Na ascorbate reduction as determined by MALDI mass spectrometry and HPLC analysis.

Having verified that alkyne-bearing LyP-1 peptides could effectively target p32-expressing MDA-MB-435 cancer cells and become linked to azido-bearing PEG polymers, we next developed a protocol for linking these peptides onto azido-PEG bearing, near-infrared fluorochrome-labeled (VivoTag 680) iron oxide nanoparticles. Dextran-caged iron oxide nanoparticles were used as the parent formulation to provide a highly stable, relatively non-cytotoxic, and *in vivo*-tested nanoparticle scaffold. Briefly, a heterobifunctional linker bearing an azide on one end an N-hydroxysuccinimide leaving group on the other was synthesized and attached to an amine-PEG-thiol polymer (MW 50000 Da) via its terminal amine (**Schematic 5.2A, 5.2B**). Azido-PEG-thiol polymers

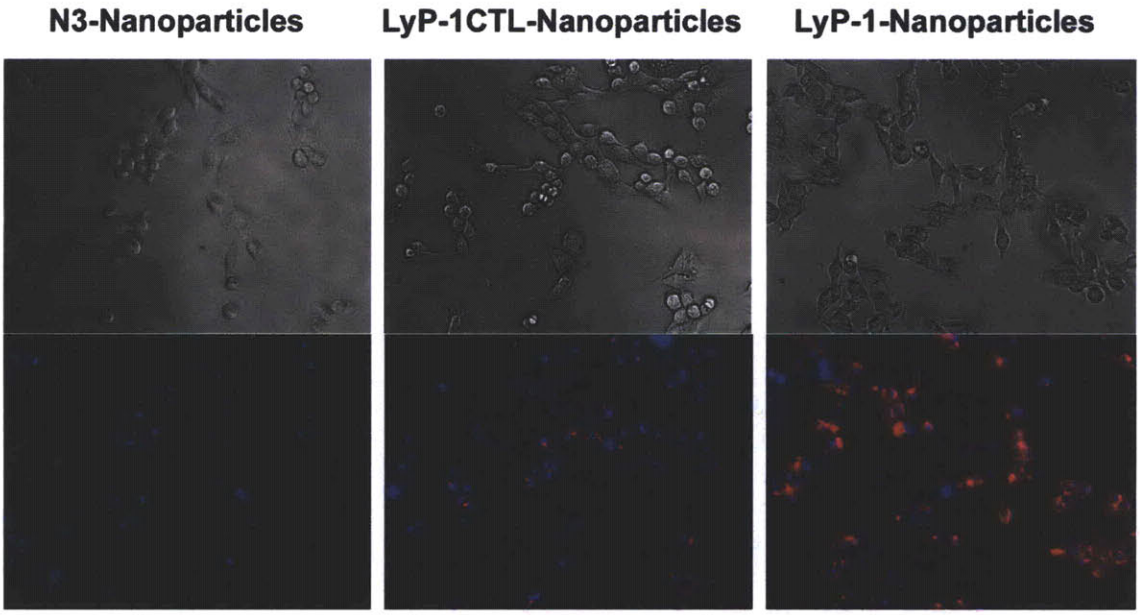

Figure 5.4. *Tumor cell targeting with LyP-1 nanoparticles.* LyP-1-nanoparticles target MDA-MB-435 cancer cells (right). Fluorescence imaging of cells incubated with LyP-1-nanoparticles showed increased near-infrared fluorescence (red). Uptake of azido-bearing or scrambled control peptide (LyP-1CTL)-bearing nanoparticles are not visible or show minor background (left and middle).

were subsequently linked to surface of cross-linked, aminated, and fluorochrome-labeled dextran-coated iron oxide nanoparticles via the linker N-[γ-maleimidobutyryloxy] succinimide ester (GMBS) (**Schematic 5.2C**). Long PEG polymers were utilized to carry pendant azide groups in order to enhance particle circulation time *in vivo* and to provide a generalizable nanoparticle surface, whereby optimized "click" attachment conditions might be applicable to other PEG-coated organic and inorganic nanomaterials in the future. Azido-PEG particles were purified from excess polymer and linked to alkyne-bearing peptides in 1 mM $CuSO_4$, 5 mM Na ascorbate. Finally, the conjugated nanoparticles were purified and sterile filtered for *in vitro* and *in vivo* applications.

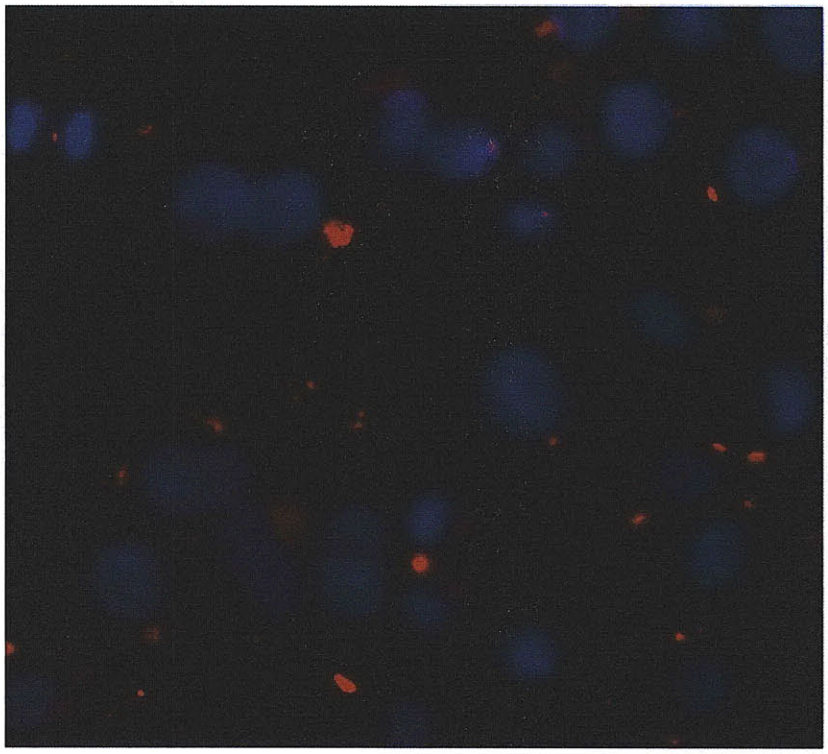

Figure 5.5: *LyP-1-nanoparticles target MDA-MB-435 cancer cells and become localized in endosome-like compartments over 24hrs in vitro*. Cells were incubated with LyP-1-nanoparticles for 30min, washed, and incubated for 24hrs before nuclear staining and imaging. PEG-LyP-1 nanoparticles no longer show diffuse membranous staining, but have become localized into punctuate compartments, implying endosomal sequestration away from cell surface

Peptide valency on nanoparticles was assessed spectrophotometrically by quantifying the number of TAMRA dyes added onto nanoparticles following "click" reaction (**Figure 5.3A**). In the presence of catalyst, approximately 30 peptides were added per nanoparticle for both LyP-1 and LyP-1CTL peptides, whereas no addition was observed in the absence of catalyst (**Figure 5.3A**). LyP-1 nanoparticles, LyP-1CTL nanoparticles, or azide nanoparticles were incubated over MDA-MB-435 tumor cells for 2 hours and

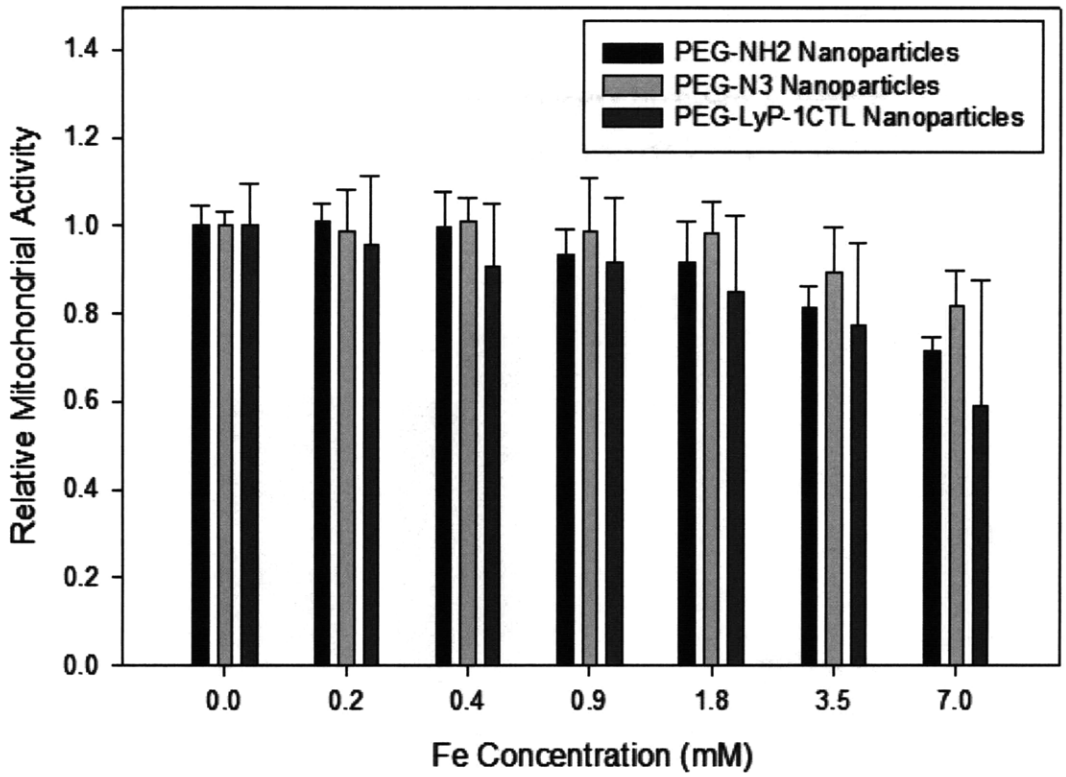

Figure 5.6: *Probing "Click" Nanoparticle Cytotoxicity to Human Cell Cultures.* Human HeLa cervical cancer cells were incubated with parent NH2-PEG-NPs, PEG-N3-NPs, or PEG-LyP-1CTL-NPs at varying concentrations for 24 hrs, rinsed, and incubated with media containing thiazolyl blue tetrazolium bromide (MTT reagent) at 0.5mg/ml. After 3hr, blue precipitates begin to form within cells as a result of mitochondrial activity. Quantitaion of cellular viability via absorbance of DMSO:isopropanol-solubilized MTT reagent showed that all three NP peparations have TC_{50} values of greater than 7mM, which is over 35-times that used *in vitro* here (100nM NPs used in cell culture and FACS expts = 0.2mM Fe) and greater than sixteen times the maximum blood concentrations during *in vivo* experiments (200nM NP concentration in blood immediately after injection = 0.4mM Fe).

nanoparticle accumulation was quantified using flow cytometry (**Figure 5.3B**). LyP-1-nanoparticles showed significant tumor cell accumulation, while LyP-1CTL-nanoparticles or azide-nanoparticles displayed minimal cell uptake (**Figure 5.3B**). The effect of serum on nanoparticle uptake was also studied, as low serum levels enhance the

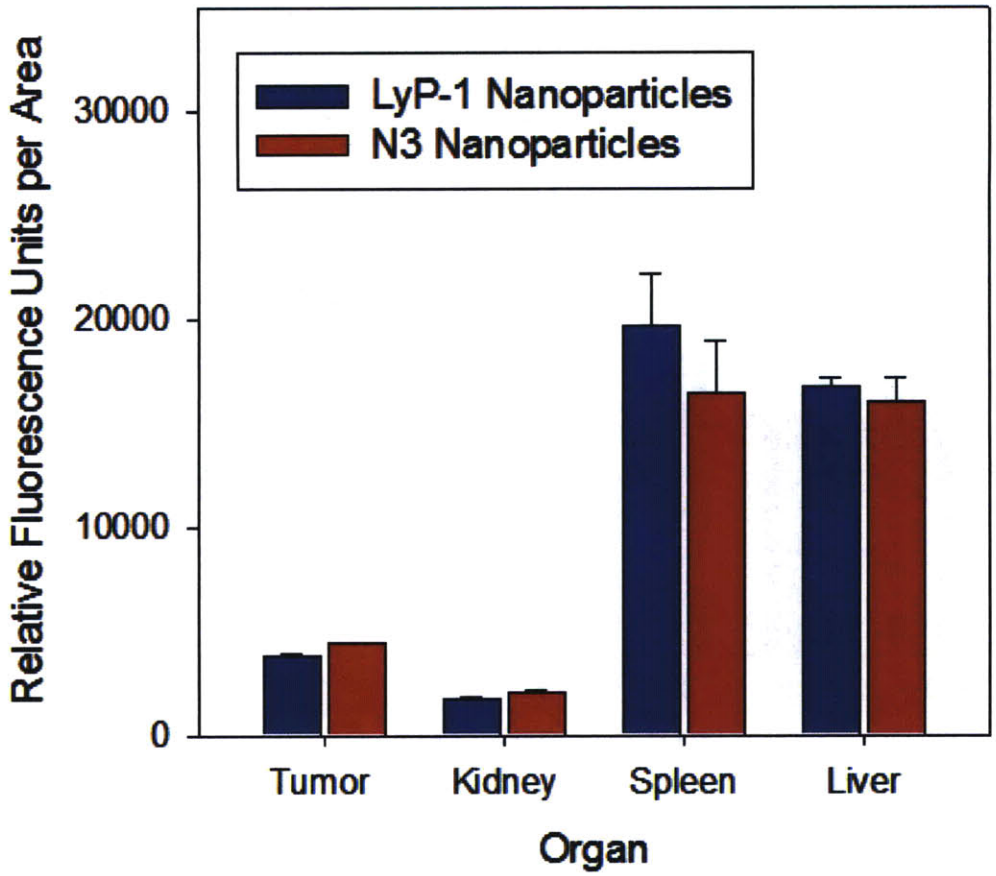

Figure 5.7: *Near-Infrared Fluorescence Analysis of LyP-1- and Azido-Nanoparticle Tumor Accumulation.* Near-infrared fluorochrome-labeled nanoparticles bearing terminal azide groups (red) or LyP-1 peptides (blue) were injected intravenously via the tail vein into mice bearing human MDA-MB-435 cancer xenografts (4 mice). After particles had cleared the systemic circulation (24hrs), mice were sacrificed and tumor, liver, spleen, and kidneys were fluorescently imaged for nanoparticle accumulation (LI-COR Odyssey). As expected for nanoparticles above the renal filtration limit, clearance was predominately via reticuloendothelial system uptake (liver and spleen). Nanoparticle accumulation in tumors was slightly decreased for peptide-modified nanoparticles, likely due to a decrease in the particle circulation time following cationic peptide attachment and concomitant decrease in the passive targeting.

stress-induced expression of the p32 receptor (*281*). The slight increase in LyP-1-nanoparticle targeting in lower serum levels provided further validation of receptor-

specific targeting, as decreased serum protein concentrations lowers the likelihood of non-specific serum protein mediated uptake. To further confirm the uptake specificity of LyP-1-nanoparticles, free LyP-1 peptide was added to cells along with LyP-1-particles (**Figure 5.3C**). Dose-dependent inhibition of uptake was observed with LyP-1 peptide concentrations from 10 to 100 μM, suggesting the free LyP-1 and LyP-1-labeled particles share common cellular receptors. We attribute the large excess of free peptide required for inhibition compared to the concentration of nanoparticles used (100nM) to the presence of multiple copies of the LyP-1 peptide on each nanoparticle, thus improving nanoparticle avidity to receptors through polyvalent binding (*284*). In order to visualize LyP-1 peptide-mediated cell uptake, nanoparticles bearing pendant LyP-1 peptides, control LyP-1CTL peptides, or azides were incubated over MDA-MB-435 cells for 30 minutes, washed, incubated with a nuclear stain, and imaged via epifluorescence microscopy (**Figure 5.4**). LyP-1-nanoparticles were seen associated with cells, while markedly less binding of azide-bearing or control peptide-bearing nanoparticles was not observed. If the same staining procedure was instead performed at 24 hrs post incubation, LyP-1-nanoparticles were seen in punctate locations consistent with sequestration in endosome-like compartments (**Figure 5.5**). To assess the cytotoxicity of "click" nanoparticles, NH2-PEG-, azido-PEG- and peptide-conjugated nanoparticles were incubated for 24hrs of incubation above HeLa cell cultures (**Figure 5.6**). In all three formulations, the TC50 is >7mM Fe, or over 16 times higher than maximal blood concentrations during *in vivo* experiments performed here and 32 times higher than concentrations used *in vitro* here.

Having found that "click" attachment of homing peptides could mediate the targeting nanoparticles *in vitro*, we evaluated the ability of "click" chemistry to direct nanoparticle targeting to specific tumor cells *in vivo*. Again, near-infrared fluorochrome-labeled (VivoTag 680) nanoparticles were "clicked" to LyP-1 peptides, resulting on average of ~30 LyP-1 peptides per particle, while the parent azido-PEG nanoparticles were used as a negative control. Each population of nanoparticles was injected intravenously into mice bearing human MDA-MB-435 cancer xenografts. Nanoparticles were allowed to circulate and distribute in mice for 24hrs, after which the mice were sacrificed and organs collected for immunohistochemical or whole organ fluorescence analysis. Vascular staining with anti-CD31 antibodies showed that azide nanoparticles in tumors remained localized within the immediate periphery of blood vessels (**Figure 5.8B**). This perivascular distribution of untargeted nanomaterials is in agreement with previous histological and intravital observations of passive liposomal accumulation in tumors(*285, 286*). By contrast, LyP-1 "click" nanoparticles appeared to have extravasated from the tumor vasculature, penetrated into the interstitial space of the tumor, and bound to p32-expressing cells (**Figure 5.8B**, **5.8C**). As a result, the fraction of LyP-1 nanoparticles that get sequestered beyond the perivascular space was significantly higher than that of azido-nanoparticles (**Figure 5.8D**) ($P<0.005$). This pattern was observed in all injected mice and is characteristic of LyP-1 peptide and phage homing observed previously(*252*). Interestingly, previous LyP-1 bacteriophage experiments showed that the LyP-1-expressing phage concentrate in non-vascularized sites of tumors within minutes after injection while insertless phage do not reach these regions(*252*). Thus, there

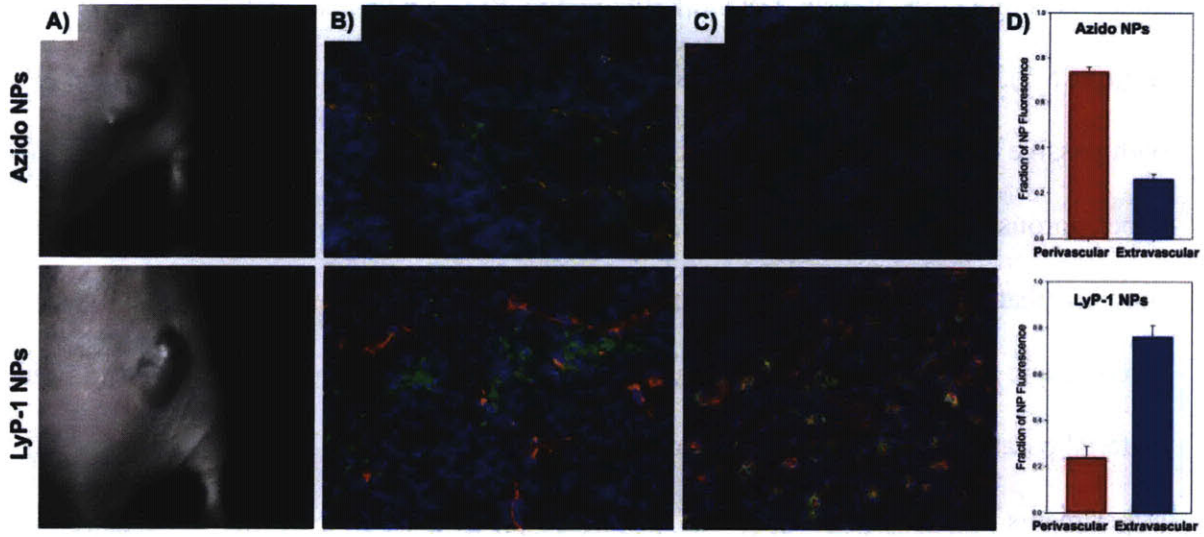

Figure 5.8: *"Click" LyP-1-nanoparticle targeting to tumor cells in vivo.* Nanoparticles bearing only azide groups (top) or labeled with LyP-1 peptides (bottom) that are matched in circulation time were injected intravenously via the tail vein into mice bearing human MDA-MB-435 cancer xenografts. Histological sections were obtained 24 hours post injection. (A) Light reflectance images of mice bearing the tumor xenografts. (B) Fluorescent LyP-1-nanoparticles (VT680 fluorescence pseudocolored as green) did not colocalize with CD31, a blood vessel marker (red) while untargeted azide-PEG nanoparticles remained localized to the blood vessels or their immediate periphery. (C) LyP-1-nanoparticles (green) accumulated in regions of high p32 expression (red), whereas untargeted, azido-bearing nanoparticles did not accumulate in these areas. D) Histological quantitation using CD31 stain to assess nanoparticle localization to immediate periphery of blood vessels. The fraction of LyP-1 nanoparticles outside of the perivascular space of CD31-stained blood vessels is significantly higher than azido-nanoparticles ($P<0.005$) as assessed from 3 randomly chosen views in each set of mice ($n=3$). Together, LyP-1-coated nanoparticles penetrate into the tumor interstitium to target p32-expressing cells.

may be unique transportation pathways within tumors that are exploited by this ligand after extravasation that are not available to untargeted materials. In the future, the localization of LyP-1 nanoparticles in avascular tumor regions may be of use for directing therapeutics into hypoxic regions of tumors, where most nanoparticle therapies do not reach. Whole organ assessment of near-infrared tumor fluorescence demonstrated that, despite the distinct microscopic behavior of LyP-1 nanoparticles, the macroscopic

tumor accumulation of LyP-1 nanoparticles and PEG-azide nanoparticles was similar (**Figure 5.7**), indicating that the targeted accumulation of LyP-1-nanoparticles was on par with passive delivery, whereby long-circulating materials accumulate in tumors via their hyper-porous vasculature over time(*287, 288*). These results are in accordance with data showing that the development of targeted nanoparticle formulations that amplify the macroscopic accumulation in tumors requires systematic *in vivo* optimization of multiple material parameters, including target avidity, circulation time, and particle size(*150, 289*). Experiments of this kind are ongoing in order to probe the power of the LyP-1 targeting ligand for amplifying the accumulation and efficacy of nanoparticle-based imaging and therapeutic agents.

5.3 Conclusions:

In this work, we have demonstrated that "click" chemistry may be used to develop nanoparticles that seek out specific cells *in vivo* based on their surface expression of protein markers. Ultimately, these findings suggest that "click" chemistry meets the criteria of being applicable under aqueous conditions, efficient, orthogonal to thiol- and amine-containing targeting motifs, and stable in the complex *in vivo* environments of the blood and tumor milieu. In the future, this work may empower the development of "click" nanomaterials that seek out specific tumor cell types, including tumor stem cells and angiogenic endothelial cells, or amplify the macroscopic accumulation of imaging agents or therapeutics in tumors. Further, the modularity of this "click" attachment strategy should allow it to be adapted to a diversity of *in vivo* nanoparticle platforms and both biological and synthetic ligands, potentially empowering novel on-nanoparticle screen approaches to targeted nanomaterial development.

5.4 Materials and Methods:

Unless otherwise stated all reagents were purchased from Sigma-Aldrich and all reactions were performed at room temperature.

Iron Oxide Nanoparticle Synthesis. Cross-linked, amininated, fluorescent, superparamagnetic iron oxide nanoparticles were synthesized according to the published protocol (*241, 243*). Briefly, dextran-coated iron oxide nanoparticles were synthesized, purified, and subsequently cross-linked using epichlorohydrin. After exhaustive dialysis, particles were aminated by adding 1:10 v/v ammonium hydroxide (30%) and incubated on a shaker overnight. Aminated-nanoparticles were subsequently purified from excess ammonia using a Sephadex G-50 column and concentrated using a high-gradient magnetic-field filtration column (Miltenyi Biotec). The near infrared-fluorochrome VivoTag 680 was added to remotely detect particle accumulation *in vitro* and *in vivo* by reacting in 0.1M HEPES buffer with 0.15M NaCl at pH 7.2. DMSO-solubilized fluorochromes were added into particle solutions at 4°C under mixing and allowed to warm to room temperature to react for 2 hours. The yield was approximately 10 fluorochromes per nanoparticle for all experiments.

Succinimidyl 4-azidobutyrate synthesis (**Schematic 5.2**). Ethyl 4-azidobutyrate (1). To a solution of ethyl 4-bromobutyrate (5.85 g, 30 mmol) in dimethyl sulfoxide (DMSO, 20 ml), sodium azide (2.925 g, 45 mmol) was added with stirring. The reaction mixture was stirred for 22 hrs at 55 ^{o}C, and cooled to room temperature. Water was added to the reaction mixture and extracted with ethyl ether (3 x 30 ml). Combined organic

layer was washed with water and brine, and reduced *in vacuuo* to afford 3.80 g of the azido compound 1.

4-Azidobutyric acid (2). Ethyl 4-azidobutyrate 1 (3.14 g, 20 mmol) was dissolved in aqueous sodium hydroxide solution (1 N, 24 ml) with minimum amount of methanol to make the solution homogeneous. The reaction mixture was stirred for 3 hrs at room temperature. After removal of methanol *in vacuo*, the aqueous solution was acidified to pH 0 with HCI and extracted with ethyl ether (3 x 50 ml). The ether layer was then dried over sodium sulfate and filtered. Removal of solvent gave the acid 2 (2.25 g).

Succinimidyl 4-azidobutyrate (3). To a solution of N-hydroxyl succinimide (1.65 g, 14.3 mmol) in methylene chloride (100 ml) was added acid 2 (1.68 g, 13 mmol) followed by 1-Ethyl-3-[3-dimethylaminopropyl]carbodiimide hydrochloride (EDAC, 2.74 g, 14.3 mmol). After stirring for 4 hrs at room temperature, the reaction mixture was washed with water and brine, dried over sodium sulfate, and filtered. Solvent was removed under reduced pressure to yield 1.15 g of the succinimidyl 4-azidobutyrate 3.

Peptide Synthesis. Peptides were synthesized in the MIT Biopolymers Lab and their composition was confirmed via HPLC and mass spectrometry. The LyP-1 and LyP-1CTL peptides were synthesized with either heptynoic acid or propargylglycine at the N-terminus for conjugation. Each peptide is also labeled with a TAMRA fluorophore (Anaspec) via a lysine residue separated by an aminohexanoic acid (Ahx) spacer. (final sequence for LyP-1: Heptynoic acid or propargylglycine – K(Tamra)[Ahx] – CGNKRTRGC; for LyP-1CTL: Heptynoic acid or propargylglycine – K(Tamra)[Ahx] –

CRVRTRSGC). Peptides were cyclized by bubbling air into 10 μM aqueous peptide solutions overnight. Finally, peptide solutions were lyophilized for subsequent use.

"Click" attachment of peptides to nanoparticles. Succinimidyl 4-azidobutyrate was linked to 5kDa thiol-PEG-amine polymers in 0.1M HEPES 0.15M NaCl pH 7.2 for 1 hour at a 2:1 molar ratio between linker and polymer. Simultaneously, amino-modified, fluorochrome-labeled nanoparticles were activated with N-[γ-maleimidobutyryloxy] succinimide ester (GMBS) (dissolved in DMSO) cross-linker under similar conditions at a 200:1 molar ratio between cross-linker and nanoparticles. To remove excess GMBS, nanoparticle samples were filtered on a G50 column into 50mM Na Phosphate buffer at pH 7.2 supplemented with 10mM EDTA. Purified nanoparticles were then combined with the polymer reaction mixture and allowed to react at room temperature overnight. Azido-PEG-nanoparticles were then purified from excess polymer and succinimidyl 4-azidobutyrate on a size exclusion column (ACA-44 media: Pall) into 0.1M HEPES pH 7.2 buffer. Finally, the azide-PEG-bearing particles were concentrated using Amicon Ultra-4 (Millipore) filters and stored at 4°C.

To optimize catalyst concentrations for the "click" reaction by HPLC, a 10-fold excess of azido-PEG-NH_2 or O-(2-Aminoethyl)-O′-(2-azidoethyl)pentaethylene glycol (Polypure) was added to a 100 μM peptide solution. $CuSO_4$ and Na ascorbate were dissolved in H_2O and added to the reaction mixture to final concentrations of 1 mM/5 mM and 10 mM/50 mM $CuSO_4$/Na Ascorbate. This mixture was shaken at 37°C for various times (1 day to 3 days), after which it was characterized via HPLC.

Alkyne-bearing peptides (35:1 peptide:nanoparticle molar ratio), $CuSO_4$ (1 mM), and sodium ascorbate (5 mM) in H_2O were added to a solution of particles and the mixture was shaken at 37°C for 48 h. Following the reaction, nanoparticles were purified from copper catalyst and excess peptides by filtration in ACA-44 size exclusion media into 0.1M HEPES 0.15M NaCl pH 7.2 buffer.

Cell Culture. Cell uptake experiments were performed using a human MDA-MB-435 cancer cell line. Grow media was minimum essential medium eagle (Invitrogen) with fetal bovine serum (10%; Invitrogen). Cells were passaged into 96-well plates and used at 60-80% confluency.

For peptide uptake experiments, LyP-1 or LyP-1CTL peptides were added to cell monolayers in serum-containing media at a final concentration of 10 μM. After 45 minutes of incubation at 37 °C, cells were washed with media, PBS, treated with trypsin (0.25%) and EDTA, and resuspended in 1% BSA (in PBS) for flow cytometry (BD LSRII). Fluorescence data on 10,000 cells was collected for each sample.

For nanoparticle uptake experiments, particles bearing an LyP-1, LyP-1CTL, or terminal azides were added to the cells in serum media at a final concentration of 100 nM. After 2 h of incubation, cells were trypsinized and assayed for particle fluorescence by flow cytometry. For peptide inhibition experiments, free LyP-1 peptides (10 μM to 100 μM) were first incubated with the cells for 1 h. The cells were then washed with media and 100 nM of LyP-1-coated nanoparticles were added to the cell culture. For imaging, cells were washed with PBS and observed using a 20x objective. Images were

captured with a CCD camera mounted on a Nikon TE200 inverted epifluorescence microscope.

In vivo Studies of Nanoparticle Targeting. Nude athymic mice were inoculated subcutaneously with human cancer cells (MDA-MB-435). After tumors had reached ~.5 cm^3 in size, LyP-1- and azide-bearing nanoparticles were injected intravenously in the tail vein (1mgFe/kg). Twenty-four hours after the injection, tumor tissues were excised, snap frozen, and cut into 15 μm histological sections. Rat anti-mouse CD-31 (1:50, BD Pharmingen) and polyclonal anti-p32 antibody (1:200; (*282*)) were used for immunohistochemical staining of frozen tissue sections. The corresponding secondary antibodies were added and incubated for 1 hour at room temperature: Alexa Fluor 594 goat anti-rat IgG (1:500, Invitrogen) for CD-31 and Alexa Fluor 594 goat anti-rabbit IgG (1:500, Invitrogen) for p32 antibody. The slides were washed three times with PBS and mounted in Vectashield Mounting Medium with DAPI (Vector Labs). The stained tumor sections were observed with a fluorescence microscope (Nikon, Tokyo, Japan). Histological quantitation of nanoparticles localization was done using ImageJ software. Stacks of CD31-stained sections and nanoparticle fluorescence images were utilized for intra- and extravascular particle distribution quantitation. Regions with CD31-staining were selected to denote intravascular accumulation of nanoparticles and surrounding areas were classified as extravascular. The net nanoparticle fluorescence signal above background was quantified for each of these regions to determine the approximate percent of nanoparticle fluorescence localized to the vasculature vs the extravascular space. Three sections from each set of mice were randomly chosen for analysis.

Chapter 6: Development of a Novel Building Block for *In Vivo* Nanosystem Construction: Gold Nanorod Antennas for Ultra-Sensitive Photothermal Tumor Therapy

6.1 Introduction:

The electromagnetic properties of plasmonic nanomaterials have been harnessed to develop ultra-sensitive diagnostic(*37, 38*), spectroscopic(*39, 40*), and, recently, therapeutic technologies(*41-44*). In particular, tunable plasmonic nanomaterials have attracted attention for their immense optical absorption coefficients and potential as injectable nanoantennas that target tumors and locally convert otherwise benign electromagnetic energy to thermal energy for ablation. Currently, tumor ablation approaches in clinical practice, including radio frequency, laser, and focused ultrasound methods, lack intrinsic tumor specificity to energy absorption. The inability to selectivity heat tumor tissues over surrounding compartments necessitates efforts to externally direct applied energy towards tumor tissues, making effective treatment of tumor margins and complex tumor geometries very challenging. By providing a tumor-specific heat source, nanoantennas could considerably broaden the clinical applicability of thermal therapies by simplifying their integration with current therapeutic practices (including improving margin clearance in surgery and synergizing with regional radiation therapies) and reducing morbidity due to off-target heating. Further, by pulsing the external energy source used, tumor-targeted nanoantennas can theoretically ablate with single-cell precision, thereby providing improved accuracy over standard surgical methods and opening the possibility of precisely treating complex tumor margins in sensitive tissues. To date, preparations of gold nanoshells and nanorods have shown considerable efficacy for tumor ablation using NIR-light(*41, 42, 48, 107*), with the most recent data showing

complete resorption of ~55% and ~25% of irradiated tumors, respectively(*108, 109*). These results highlight the clinical promise of these technologies and also motivate the further development of superior nanomaterials and improved methods for optimizing irradiation regimens, which could synergistically improve photothermal therapies. From a material perspective, the development of nanoantennas with enhanced circulation times *in vivo*, increased absorption coefficients per weight, and narrower absorption spectra would more efficiently permeate into tumors after intravenous administration, amplify the photothermal contrast between antennas and normal tissue, and allow improved tumor treatment at lower laser intensities or at greater depths *in vivo*. From a procedural perspective, despite a rich history of heat transfer modeling in the hyperthermia field, the use of quantitative modeling to predict the *in vivo* function of plasmonic nanomaterials has widely remained absent from their testing(*41, 42, 48, 108, 109*). Because the efficacy of photothermal therapy is driven by both the potency of nanoantenna absorption in tumors and the dose of near-infrared irradiation, translation of plasmonic materials to effective clinical use will benefit from cohesive integration of biodistribution data with photothermal modeling to predict and customize the 4D irradiated temperature profiles in tumors.

Recently, rod-shaped gold nanoparticles have emerged as precisely-tunable plasmonic nanomaterials that may be synthesized in bulk, have narrow size distributions, optical absorption coefficients 10^4-10^6-fold higher than conventional organic fluorochromes, and theoretical per micron absorption coefficients exceeding those of NIR-absorbing gold nanoshells(*6, 46, 290*). The long precedence of gold nanoparticles in clinical rheumatoid arthritis therapies, make gold nanorods (NRs) appealing new

candidates for nano-antenna-based photothermal ablation and a wide array of other biomedical applications. Already, gold NRs have been utilized for a diversity of biological purposes, including multiplexed *in vitro* detection(*291*), two-photon fluorescence imaging(*292*), and photothermal heating of tumor and bacterial cell targets(*43, 44, 109, 293-295*). In addition to their plasmon resonance, the superior atomic number and high material density of gold nanomaterials ($z=79$, $\rho=19.3$ g/cm^3) compared to clinical formulations of iodine-based reagents ($z=53$) have attracted interest for x-ray CT angiography and a few spherical nanoparticle reagents have been developed for *in vivo* use(*29, 65*).

Here, we describe the development of PEG-coated gold NRs as highly-absorbing nanoantennas for photothermal tumor destruction under the guidance of biodistribution-based photothermal modeling. We chose a PEG polymer coating, due to the widespread clinical use of variable length PEG polymers for extending the circulation time of protein therapeutics(*296, 297*) and for nanoparticle formulations, such as the drug-loaded liposomes: Doxil™. We find that PEG-NRs are highly stable, relatively non-cytotoxic *in vitro*, superior photothermal antennas compared to a gold nanoshell preparation *in vitro*, and are improved x-ray absorbing agents compared to a clinical iodine standard. Following intravenous administration, we find PEG-NRs to be among the longest circulating inorganic nanomaterials described to date ($t_{1/2}$~17 hrs) allowing passive accumulation into xenograft tumors. Using 4D biodistribution-based heat-transfer simulations, we designed a therapeutic irradiation regimen that was able to fully destroy all irradiated tumors on mice injected with PEG-NRs, using half the light intensity of previous nanoshell therapies.

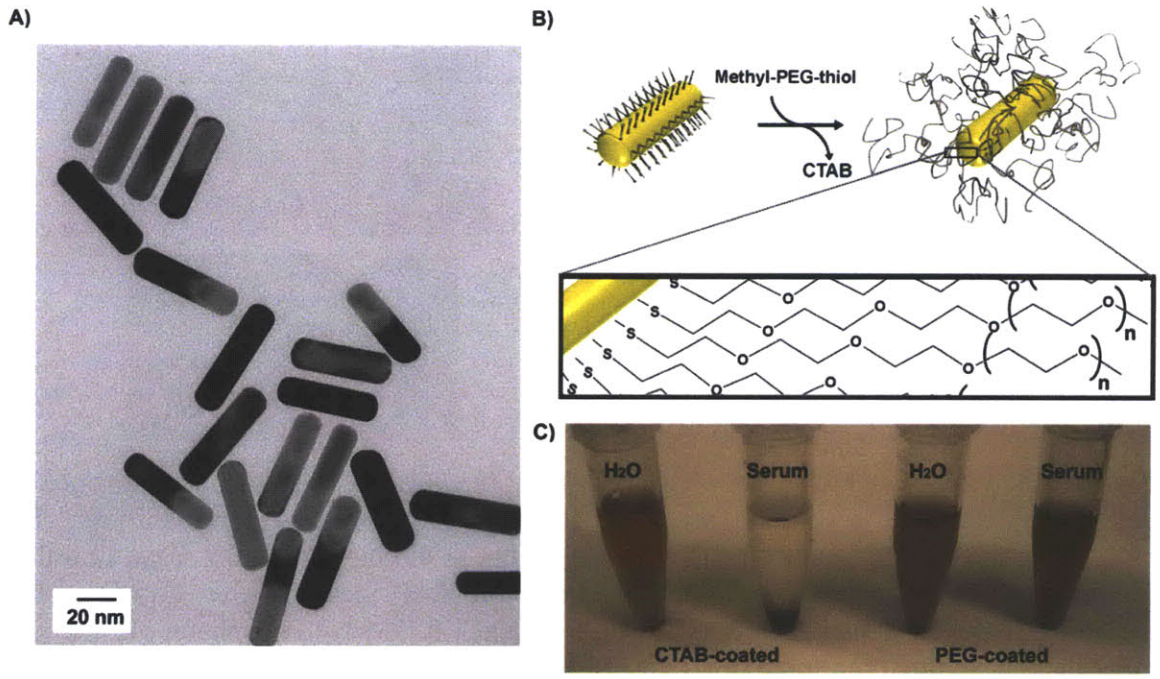

Figure 6.1: *Structure and synthesis of highly absorbing, polyethylene glycol (PEG)-protected gold nanorods.* A) Near-infrared absorbing (810 nm longitudinal plasmon resonance peak) gold nanorods were imaged via transmission electron microscopy (TEM). B) Schematic of process to drive CTAB-nanorod conversion to PEG-nanorods under dialysis with rendering and molecular schematic of PEG coating on nanorod surface C) PEG-nanorods show prolonged stability in biological media (>1000 hrs) while CTAB-coated nanorods precipitated over time.

6.2 Results and Discussion:

In principle, gold nanoparticles are attractive for medical applications because various formulations have been approved by the Food and Drug Administration (FDA) and in clinical use for decades. However, one barrier facing the widespread biological use of gold nanorods has been the need to replace the cationic cetyl trimethylammonium

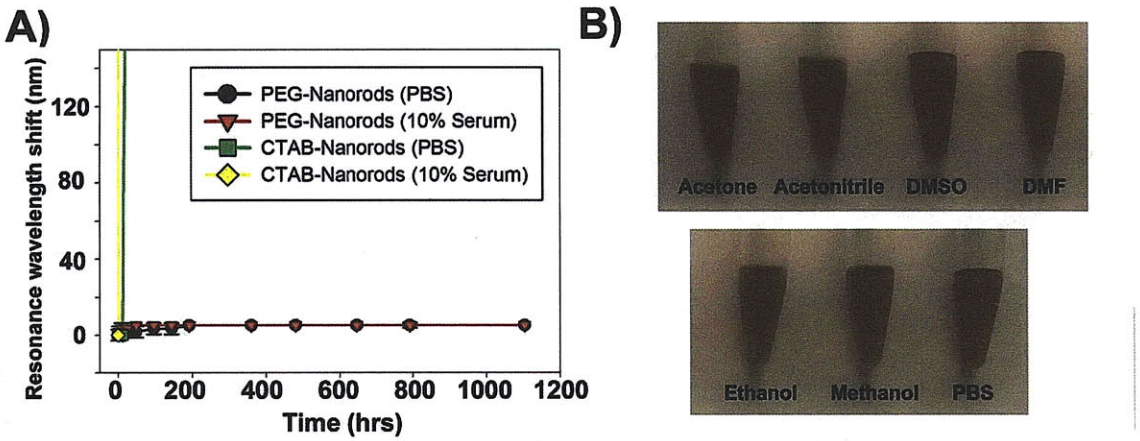

Figure 6.2: *PEG-Nanorod Synthesis and Stability In vitro.* A) The plasmon resonance of gold nanomaterials is highly sensitive to aggregation-mediated red-shifting. By monitoring plasmon resonance peak over >1000 hrs in biological solutions, we find that PEG-nanorods show prolonged stability in biological media while CTAB-coated nanorods aggregated over time in PBS (0.15 M NaCl 0.1 M Na Phosphate, pH 7.2) or 10% human serum monitored for over 1000 hrs *in vitro*. B) PEG-NRs were readily dispersed in a variety of solvents, including acetone, acetonitrile, dimethyl sulfoxide (DMSO), dimethylformamide (DMF), ethanol, methanol, or PBS.

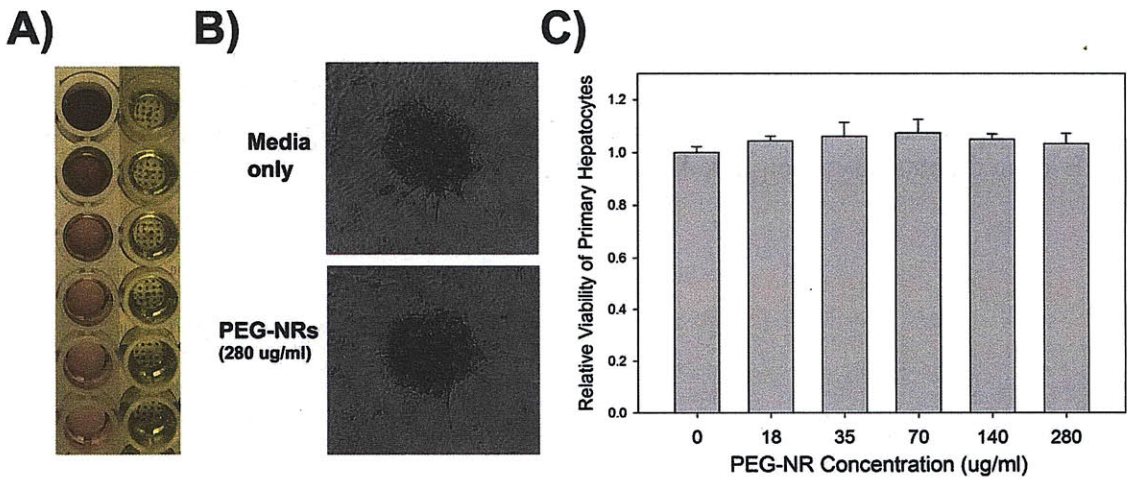

Figure 6.3: *Probing Nanorod Cytotoxicity to Primary Rat Hepatocyte cocultures.* A) Primary rat hepatocyte: 3T3-J2 human fibroblast co-cultures were incubated with PEG-NRs at varying concentrations for 24 hrs (left column), rinsed, and incubated with media containing thiazolyl blue tetrazolium bromide (MTT reagent) at 0.5 mg/ml. After 1hr, blue precipitates begin to form within hepatocytes as a result of mitochondrial activity (right column). B) Microscopy shows cultures incubated with PEG-NRs at maximal concentrations to show similar morphology to controls. C) Quantitaion of cellular viability via absorbance of DMSO:isopropanol-solubilized MTT reagent shows no cytotoxicity of PEG-NRs, even at concentrations of 20-times that used *in vitro* here and approximately equal to maximum blood concentrations during *in vivo* experiments.

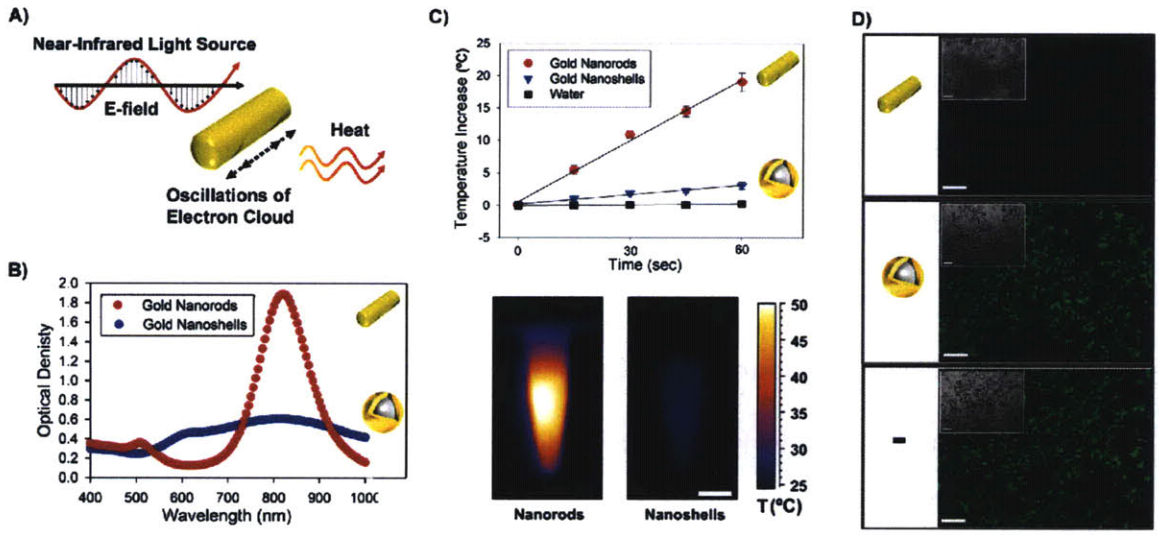

Figure 6.4: *Spectral and photothermal properties of highly-absorbing gold nanorods compared to gold nanoshells.* A) Schematic of photothermal heating of gold nanorods. The dimensions of gold nanorods are tuned to have a near-infrared plasmon resonance, at which point nanoparticle electrons resonantly oscillate and dissipate energy as heat. B) Spectra for PEG-gold nanorods (red) and PEG-gold nanoshells (blue), a benchmark for tunable plasmonic nanomaterials, at equal gold concentrations. C) Rate of temperature increase for triplicate PEG-nanorod and PEG-gold nanoshell solutions (7 μg Au/mL, 810 nm laser, 2 W/cm^2, n=3 each) (top). Infrared thermographic image of PEG-nanorods vs PEG-gold nanoshells following 2 minutes of irradiation (scale bar=5 mm) (bottom). D) *In vitro* photothermal toxicity of PEG-nanorods over human cancer cells in culture (MDA-MB-435). Tumor cells were incubated with PEG-nanorods (14 μg/mL; above), PEG-nanoshells (14 μg/mL; middle), or media alone (below) and treated with laser irradiation (2 W/cm^2, 810 nm, 5 min). Calcein AM staining indicates destruction of cells with PEG-nanorods, while cells irradiated in the presence of nanoshells or media remained viable. Phase region of calcein staining inset (all scale bars=10 μm).

bromide (CTAB) surfactants used to drive their anisotropic growth with hydrophilic, biocompatible coatings. We found that NRs, with axial sizes of 12.7 nm (+/- 3.4) and 47 nm (+/- 9.3) (Figure 6.1A), coated in CTAB are cytotoxic and colloidally unstable in 0.15 M NaCl or 10% human serum (Figure 6.1B, 6.1C). After PEGylation (Figure 1B), gold

NRs contained ~20,000 polymers per particle by the SPDP assay(*298*) and were rendered highly stable *in vitro*, showing minimal spectral shifting, which would indicate particle destabilization and aggregation, even after >1000 hours in 0.15 M NaCl or 10% human serum (**Figure 6.1C, 6.2**). Additionally, PEG-NRs could be dispersed in a variety of solvents, including acetone, acetonitrile, DMSO, DMF, ethanol, and methanol, further highlighting the stability of their coating and their amenability to future chemical processing and functionalization (**Fig. 6.2**). After 24 hrs of incubation above primary rat hepatocyte co-cultures, an *in vitro* liver model that was previously used to elucidate semiconductor quantum dot toxicity(*59*) and has shown utility for rank-ordering pharmacological toxicities(*299*), PEG-NRs displayed no significant alterations in mitochondrial activity compared to saline alone, even at doses 20 times above that used over cells *in vitro* here and equal to maximal blood concentrations during *in vivo* therapy experiments (**Figure 6.3**), highlighting their potential biocompatibility for medical applications.

In light of the prior utility of gold nanoshells for photothermal tumor therapy, they were used as a benchmark here to evaluate the photothermal performance of PEG-NRs (**Figure 6.4A, 6.4B**). PEGylated Nanoshell preparations with similar composition and spectra to those used for photothermal *in vivo* applications (*41, 42, 48*) (~120 nm silica cores and ~15 nm gold shells, 810 nm peak plasmon resonance; **Figure 6.4B**). PEG-NRs exhibited <1/3 the spectral bandwidth and ~3 times higher extinction coefficient per gram gold than PEG-nanoshells (FWHM of PEG-NRs: 130 nm; PEG-nanoshells: 490 nm) (**Figure 6.4B**). Additionally, under identical experimental conditions, irradiated PEG-NR solutions generated heat >6 times more rapidly than PEG-nanoshells per gram gold

(**Figure 6.4C**). These findings are consistent with theoretical calculations indicating that gold nanorods of this size exhibit superior per micron absorption coefficients to gold nanoshells(*290*). Accordingly, incubation of PEG-NRs with MDA-MB-435 human tumor cells *in vitro* enabled their widespread destruction with levels of NIR-light that were insufficient for nanoshell-mediated toxicity (**Figure 6.4D**). Exposure to individual stimuli: NRs, nanoshells, or laser; did not affect cell viability.

In order to translate the photothermal efficacy of PEG-NRs to *in vivo* therapy, we next developed a method through which PEG-NRs could be heated under the guidance of biodistribution-based computational photothermal modeling. To model and customize patient irradiation regimens, we sought to acquire nanoparticle distributions remotely using x-ray CT, a desirable imaging modality due to its high 3D anatomical resolution, rapid imaging speed, quantitative dynamic range of detection, full body penetration, and ubiquitous clinical use. To investigate the ability of PEG-NRs to act as dense x-ray absorbing agents for x-ray CT, solutions of PEG-NRs were serially diluted and imaged using a GE microCT scanner (**Figure 6.5A**). The resulting relationship between PEG-NR concentration and x-ray contrast was highly linear and exhibited ~2-fold amplified x-ray contrast compared to a clinical iodine standard per mole (**Figure 6.5B**, **Figure 6.6A**), analogous to that found previously for spherical gold nanoparticle reagents(*29, 65*). In addition to providing enhanced x-ray absorption, PEG-NRs allow NIR photothermal heating, while iodine reagents show no heating above water alone (**Figure 6.6B,C**).

To assess the utility of the high x-ray absorption of PEG-NRs for remote detection *in vivo*, ~3 pmoles of PEG-NRs (~1 μmole Au) were directly injected into the

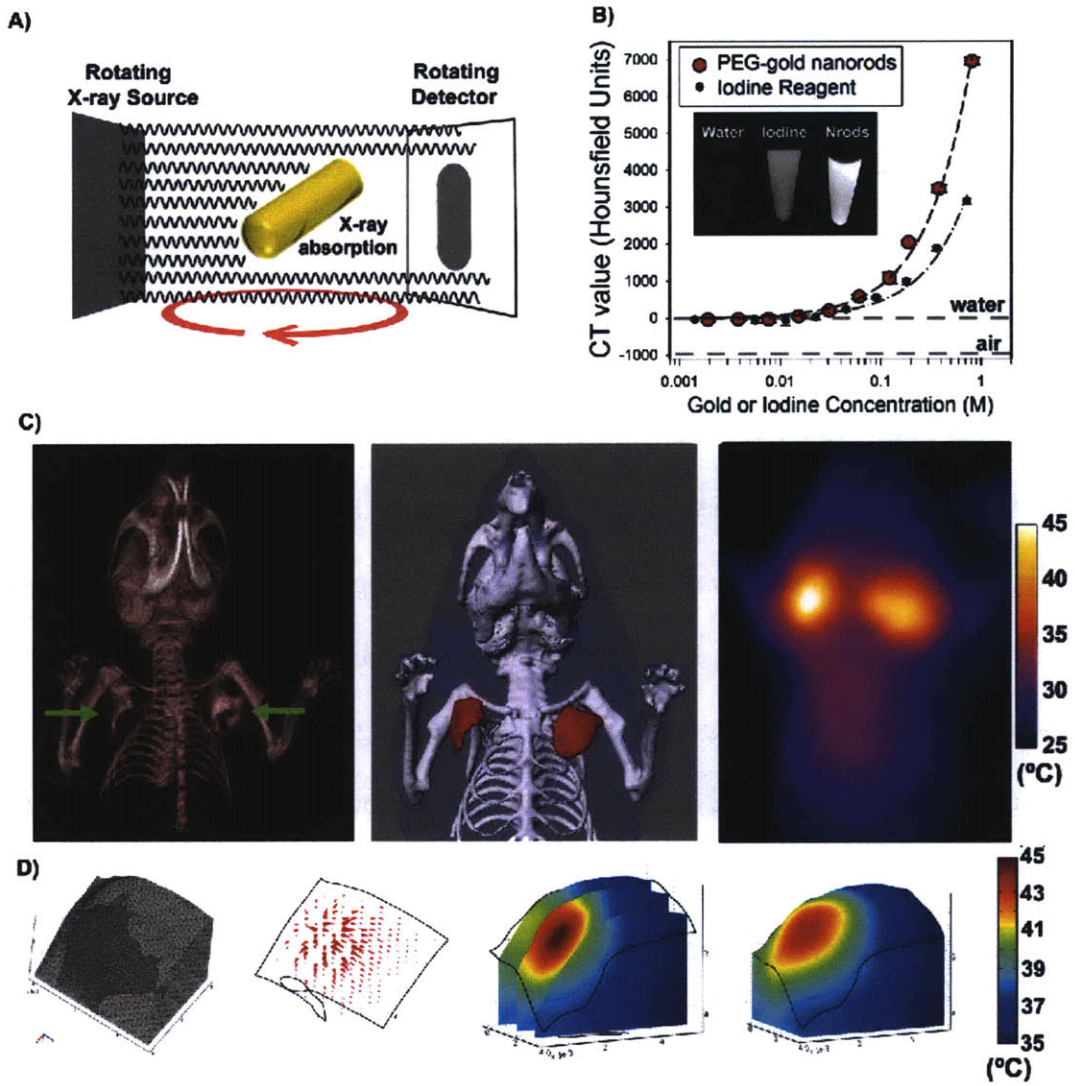

Figure 6.5: *X-ray computed tomography, quantitative photothermal modeling, and near-infrared photothermal heating of gold nanorods in vivo.* A) Schematic of x-ray absorption by gold nanorods in x-ray CT. B) X-ray CT number of PEG-nanorods compared to an iodine standard (Isovue-370) C) PEG-nanorods were intratumorally administered to mice bearing bilateral MDA-MB-435 tumors and imaged using x-ray CT to visualize 3D PEG-nanorod distribution in tumors (left). A 3D solid model of the complete geometry was rapidly reconstructed by image processing for use with computational photothermal modeling (middle, red=PEG-nanorods). Experimental thermographic surveillance of NIR-irradiation after x-ray CT (~.75 W/cm2, 1 min) (right) D) Meshed geometry of the left tumor chosen as the computational domain (left). Plot of theoretical heat flux propagation inside the tumor upon irradiation (middle-left). Predicted internal temperature distribution at 3 different planes inside the tumor (middle-right) along with surface temperature map (right) matching the left tumor in C)

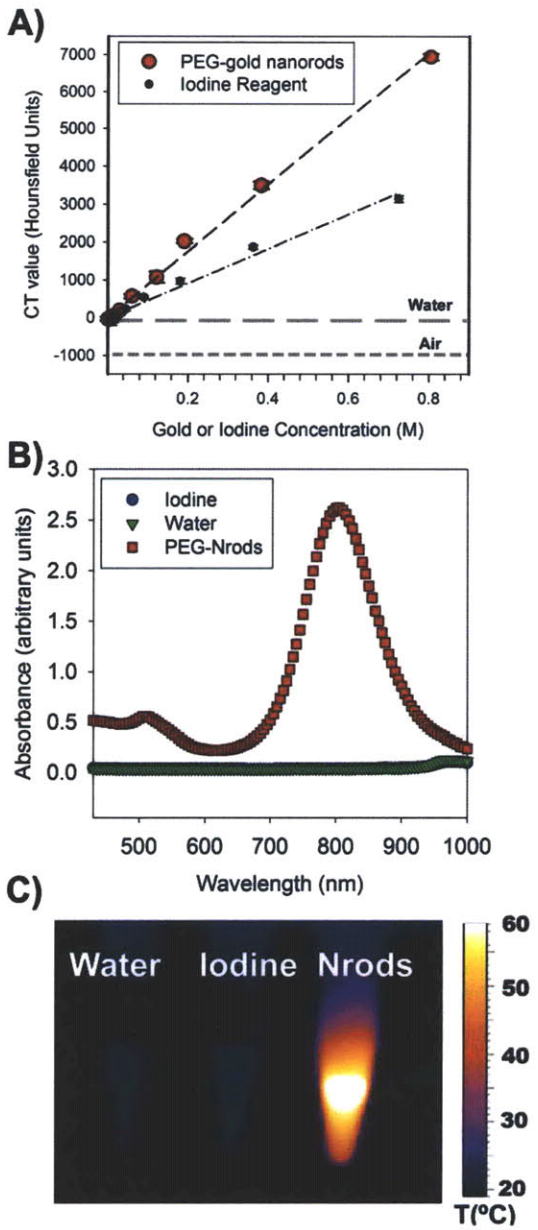

Figure 6.6: *X-ray Absorption, Optical Spectra, and Photothermal Comparison between PEG-Nanorods and Clinical Iodine X-ray Computed Tomography Reagent.* A) X-ray computed tomography number of PEG-nanorods compared to an iodine standard (Isovue-370). Linear x-axis plot of the same data presented in Figure 2B, clarifying linearity of PEG-gold nanorod detection via x-ray CT B) Optical extinction spectra of PEG-Nanorods (0.045 mg/ml Au) vs solution of an iodine-based clinical regent (350 mg/ml iodine) and saline. Notably, iodine reagents lack absorbance in the near-infrared that could allow remote photothermal heating. B) Photothermal heating comparison between PEG-Nanorods, iodine, and saline monitored using infrared thermography (810 nm NIR light, 2 W/cm^2).

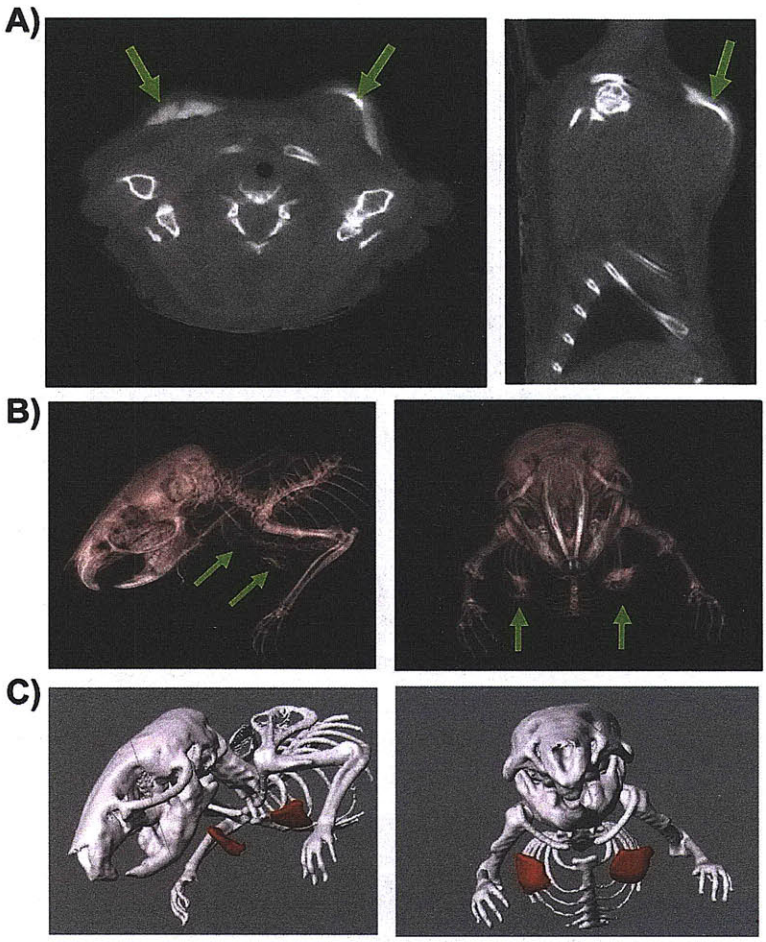

Figure 6.7: *Linking PEG-Nanorod X-ray Tomography with Computational Modeling.* A) Transverse and sagittal slices showing PEG-Nanorod distributions following intratumoral administration into bilateral breast tumors B) 3D reconstructions depicting geometry of PEG-NR injections C) Importation of 3D x-ray CT data into geometries for 4D photothermal modeling (red= PEG-nanorods, white=skeletal structure).

tumors of mice bearing bilateral human MDA-MB-435 tumors, implanted either in the mammary fat pad or the rear flank. We found that x-ray CT rapidly detailed the 3D distribution of PEG-NRs in tumors, showing clear distinction between NRs and soft tissues (**Figure 6.5C**, **6.7, 6.8**). To understand the relationship between the nanoparticle

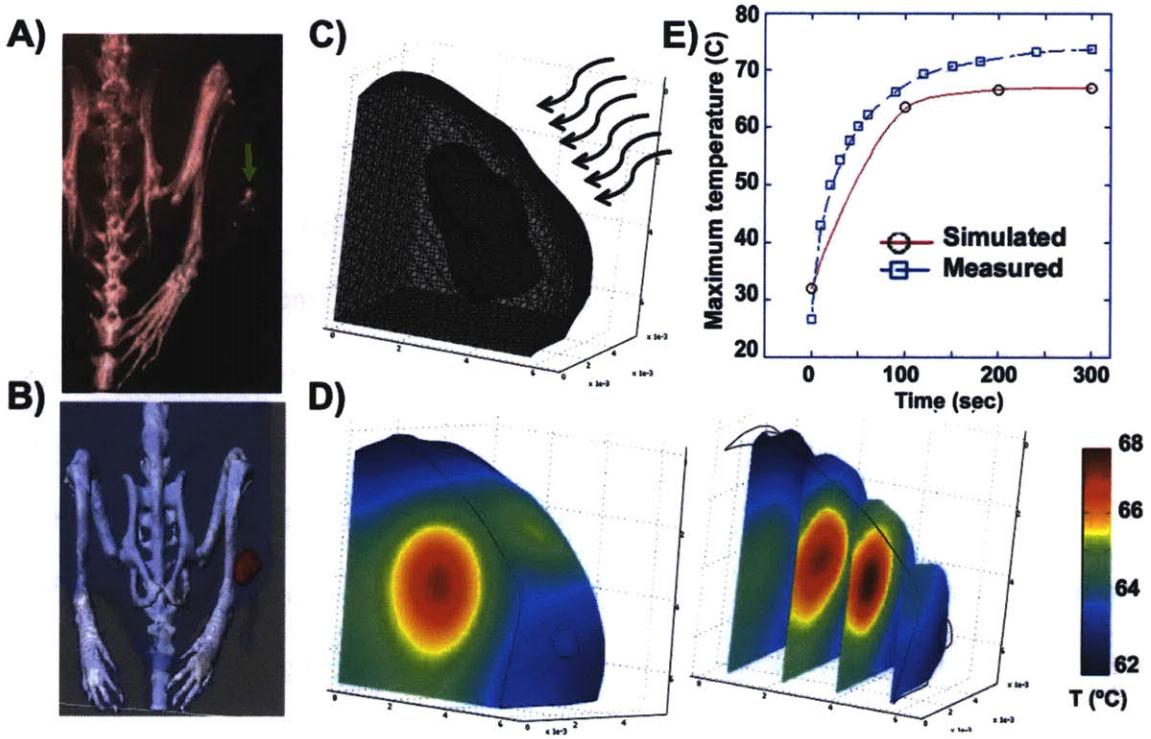

Figure 6.8: *X-ray CT-Fused Computational Modeling of Photothermal Tumor Heating.* A) X-ray CT image of PEG-Nanorod distribution in tumor B) A 3D solid model of the complete geometry was reconstructed by image processing for use with computational photothermal modeling. C) Meshed geometry of the injected tumor chosen as the computational domain with laser orientation and intensity matching that used (1 W/cm^2) (laser direction signified by curved arrows) D) Plot of theoretical surface temperature distribution (left) and the internal predicted temperature profiles inside the computational geometry of the tumor (right) 240 sec following the onset of irradiation. E) Graphical comparison between simulated and thermographically measured maximum surface temperatures over time after the onset of irradiation.

distribution in tumors and the associated processes of thermal deposition and flux during irradiation, a finite element model of PEG-NR heating was developed based on the Pennes bioheat transfer equation, including: 1) 3D skeletal, soft tissue, and PEG-NR geometries transferred from x-ray CT imaging; 2) Temperature-dependent optical

absorption and scattering 3) Heat transfer, including surface thermal flux, internal diffusive flux, and temperature-dependent perfusive thermal flux in tissues; and 4) an extracorporeal NIR-laser of variable intensity, beam diameter, and orientation matching that used (see Materials and Methods). X-ray CT data was exported into ScanIP and ScanFE image processing softwares for skeletal, nanorod, and soft tissue geometry construction and subsequently into COMSOL Multiphysics modeling software for photothermal simulations. Exported geometries enabled rapid delineation PEG-NRs along with skeletal structures and surrounding soft tissues for spatially defining model parameters (**Figure 6.5C**, **6.7, 6.8**). Computational, finite element heat transfer simulations were performed using PEG-NRs and tumor geometries as computational domains to evaluate the feasibility of applying 4D modeling to the process of photothermal heating under irradiation (**Figure 6.5D**, **6.8**). Simulations revealed the intratumoral vectors of thermal flux extending from regions of PEG-NRs as well as the internal and surface temperature history expected for irradiation at varying laser intensities (**Figure 6.5D**, **6.8**). At matched computational and experimental laser intensities, simulated surface heating behavior qualitatively and quantitatively matched the observed surface temperature values and distributions acquired using infrared thermographic observation (**Figure 6.5D**, **6.8**). We believe this establishes the potential of fusing quantitative imaging with computational modeling to provide insight into the unintuitive, highly complex phenomena of *in vivo* photothermal heating. Next, we proceeded to explore the power of this modeling to quantitatively predict *in vivo* heating following intravenous tumor targeting.

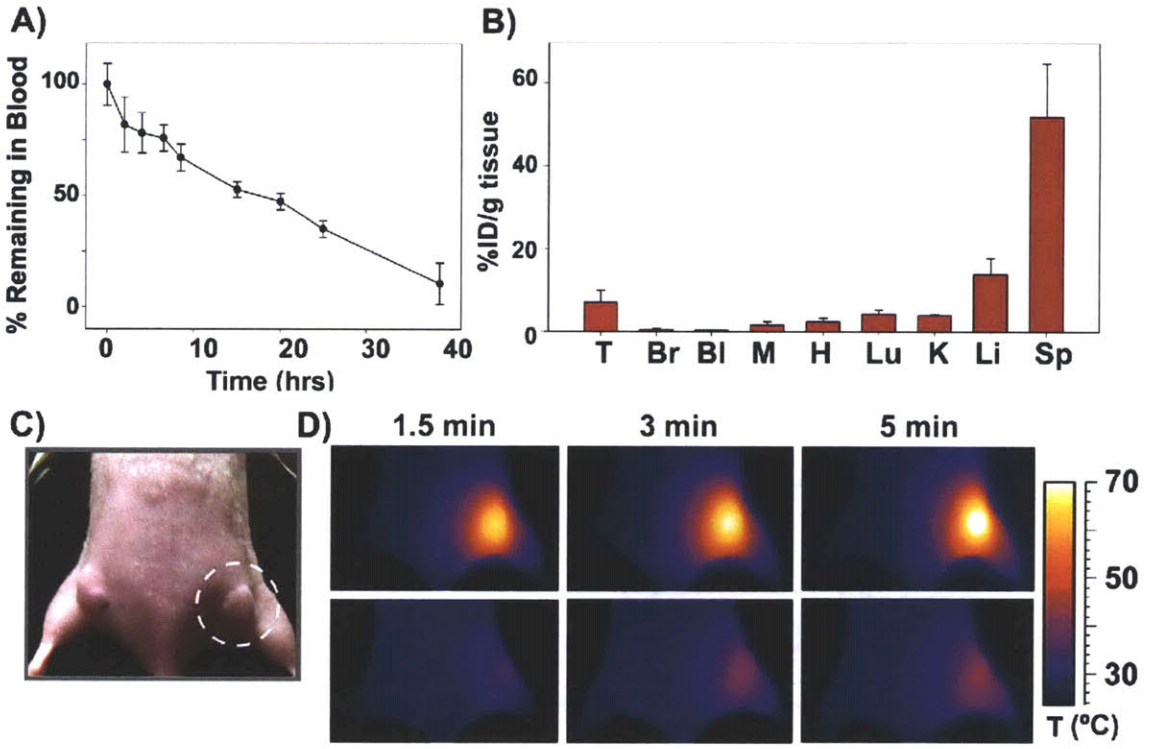

Figure 6.9: *Long circulation time, passive tumor targeting, and photothermal heating of passively-targeted gold nanorod antennas in tumors.* A) PEG-nanorods were intravenously administered (20 mg/kg) to 3 mice bearing MDA-MB-435 tumors and blood was withdrawn over time to monitor clearance from circulation. B) PEG-nanorod biodistribution and targeting to MDA-MB-435 tumors 72hrs following intravenous administration, quantified via ICP-MS (3 mice). (T=tumor, Br=brain, Bl=bladder, M=muscle, H=heart, Lu=lung, K=kidney, Li=liver, Sp=spleen) (Data is tabulated in ST1) C) PEG-nanorods or saline were intravenously administered (20 mg/kg) to mice bearing MDA-MB-435 tumors on opposing flanks. After nanorods had cleared from circulation (72 hrs after injection) the right flank was irradiated using an 810nm diode laser (2 W/cm^2; beam size indicated by dotted circle). D) Thermographic surveillance of photothermal heating in PEG-NR-injected (top) and saline-injected (bottom) mice.

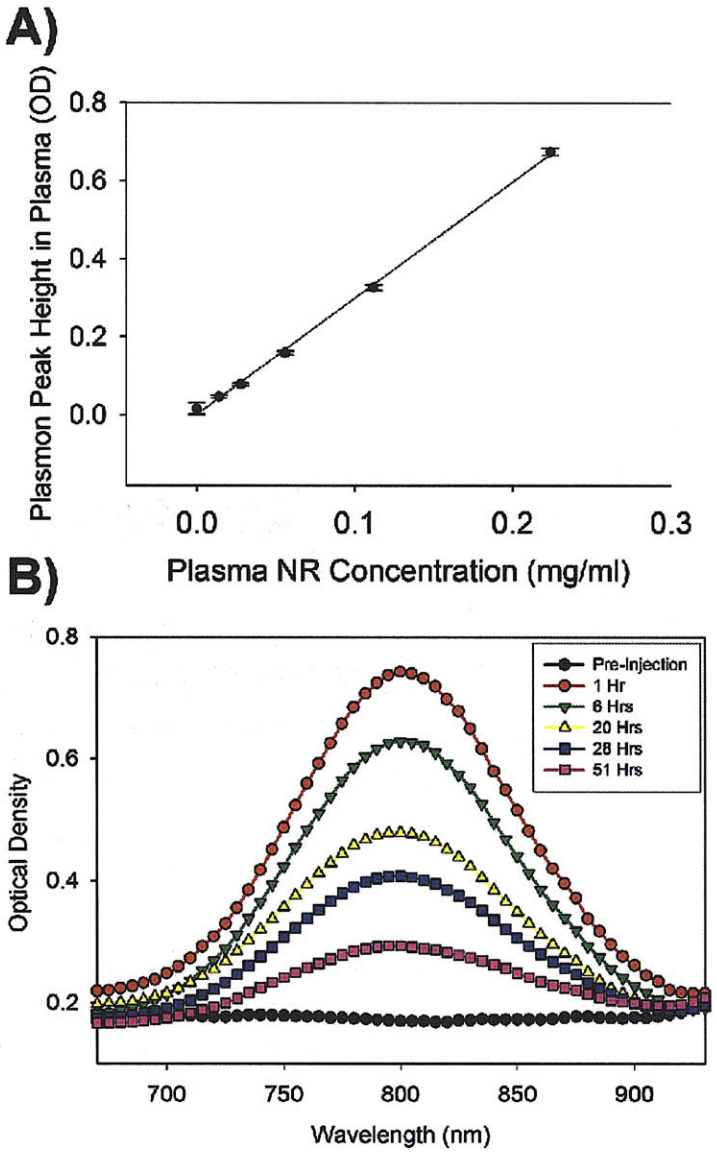

Figure 6.10: *Assessing PEG-NR concentration in plasma via plasmon resonance peak height.* A) PEG-NRs at various concentration were diluted into plasma and spectrophotometrically analyzed to assess NR concentration via the NIR plasmon resonance peak. NRs could be rapidly quantified between ~0.2 mg/ml (the approximate concentration in plasma immediately following injection in mice) and ~0.02 mg/ml. B) Following injection, this method could be applied to rapidly detect PEG-NRs in the plasma of injected mice over time, showing that PEG-NRs maintain their plasmon resonance throughout their blood circulation *in vivo*.

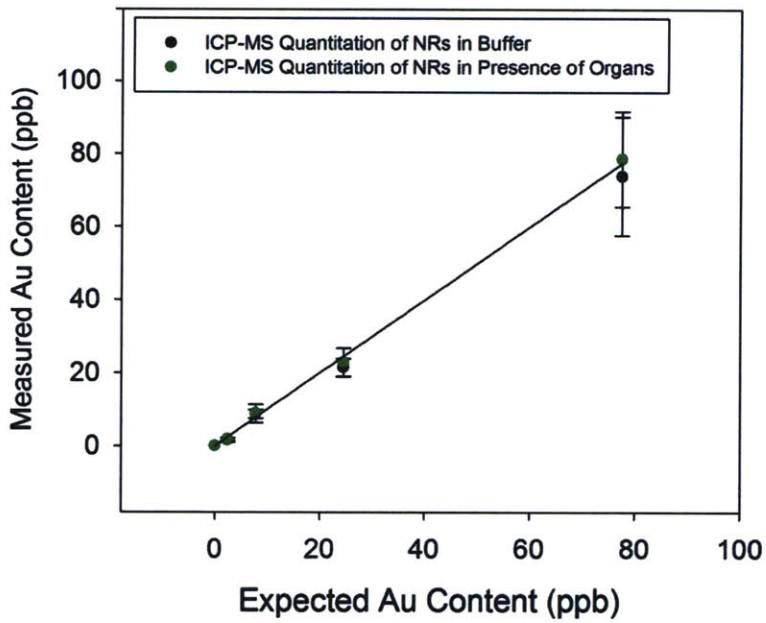

Figure 6.11: *Assessing PEG-NR concentration in organs via ICP-MS Au quantitiation.* PEG-NRs at various concentration were diluted into buffer or into glass vials containing 200 mg sections of liver. Samples were all prepared for ICP-MS quantitation to assess the linearity of Au detection and whether the presence of organs affected quantitation. The samples were made to approximate a range of ~2% to 70% ID/g for 200 mg tissues. Results are plotted for triplicate samples and plotted against the ideal relationship of y=x.

We next investigated the behavior of PEG-NRs following intravenous administration in mice in order to systemically target tumors through the enhanced permeability and retention (EPR) effect(*14*). For PEG-NRs to passively target tumors via the EPR effect and act as nanoantennas for photothermal therapy, they must be able to traverse the systemic circulation, deter protein opsonization and reticuloendothelial system (RES) clearance, permeate through transendothelial pores in tumor blood vessels, and be retained in the tumor interstitium. Following intravenous administration to tumor-bearing mice (20 mg Au/kg), our PEG-NRs were found to exhibit blood half-lives of ~17 hrs (**Figure 6.9A**) and to maintain their 810 nm longitudinal plasmon resonance

throughout this time, allowing spectrophotometric detection in serum over time (**Figure 6.10**).

To quantitatively assess tumor accumulation of PEG-NRs, nude mice bearing MDA-MB-435 human tumors were intravenously administered with PEG-NRs and, once NRs had cleared from circulation (72 hrs), organs were removed for gold quantitation. Here, inductively-coupled plasma mass spectrometry (ICP-MS) was used to quantify the accumulation of exogenously-administered gold in tissues. ICP-MS Au NR detection was found to be highly sensitive and linear across a relevant range for gold NR detection (**Figure 6.11**). As expected for nanomaterials above the renal filtration limit, PEG-NRs were found to clear via RES uptake with splenic clearance dominating hepatic (**Figure 6.9B**), a pattern analogous to that observed previously for PEG-protected 10 nm diameter spherical gold nanoparticles(*65*). Importantly, passive tumor accumulation of PEG-NRs after injection was found to be highly efficient, even at 72 hrs post injection, accumulating at ~7% ID/g (**Figure 6.9B**), allowing PEG-NRs to amplify the tumor absorption coefficient of 810 nm light by ~7 fold. Based on empirical studies of passive tumor targeting, the enhancement of the PEG-NR circulation time over reported PEG-nanoshell formulations should amplify their passive tumor accumulation in tumors, which, in concert with their enhanced photothermal heat generation *in vitro*, would be expected to provide overall enhanced photothermal contrast between tumors and normal tissue. However, as PEG-nanoshells are not commercially available, a side-by-side *in*

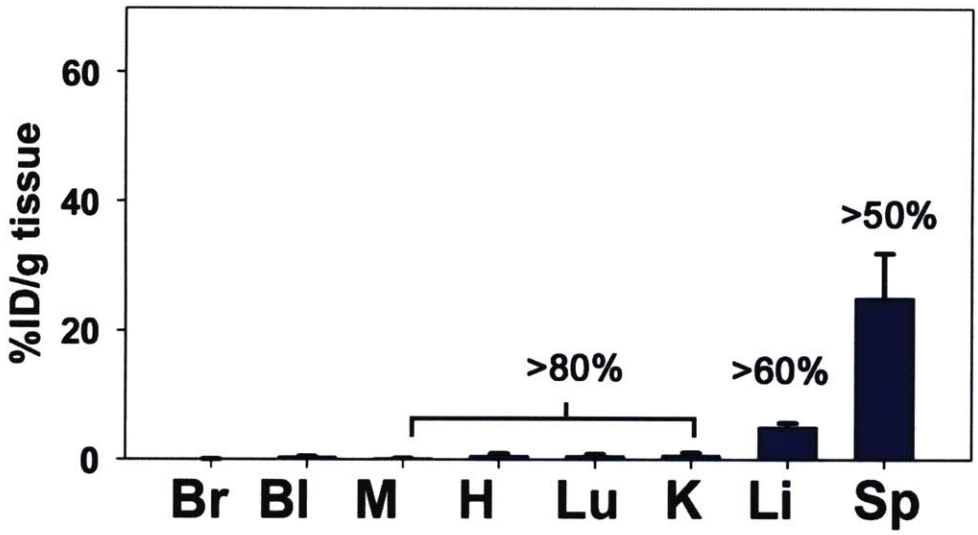

Figure 6.11: *PEG-NR biodistribution in tumor-free mice at 2 months following intravenous injection.* PEG-nanorod biodistribution 2 months following intravenous administration, quantified via ICP-MS (3 mice). Percent values indicate the clearance (or decrease in %ID/g) that occurred during this time period compared to values of organs collected 72 hrs after particle injection (Br=brain, Bl=bladder, M=muscle, H=heart, Lu=lung, K=kidney, Li=liver, Sp=spleen).

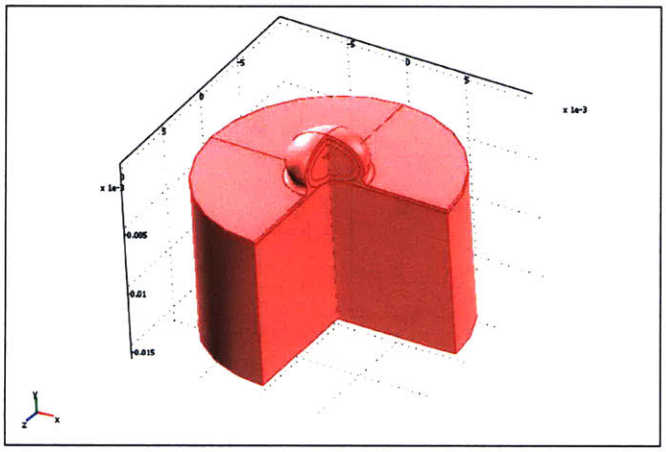

Figure 6.12: *Compuatational domain for modeling photothermal therapy following intravenous administration of PEG-Nanorods*. For intravenous photothermal modeling, a cylindrical domain of 20 mm diameter around the tumor with a depth of 12 mm for the muscle domain was considered for computation. The outer shell of the tumor was considered to be of 0.5 mm thickness.

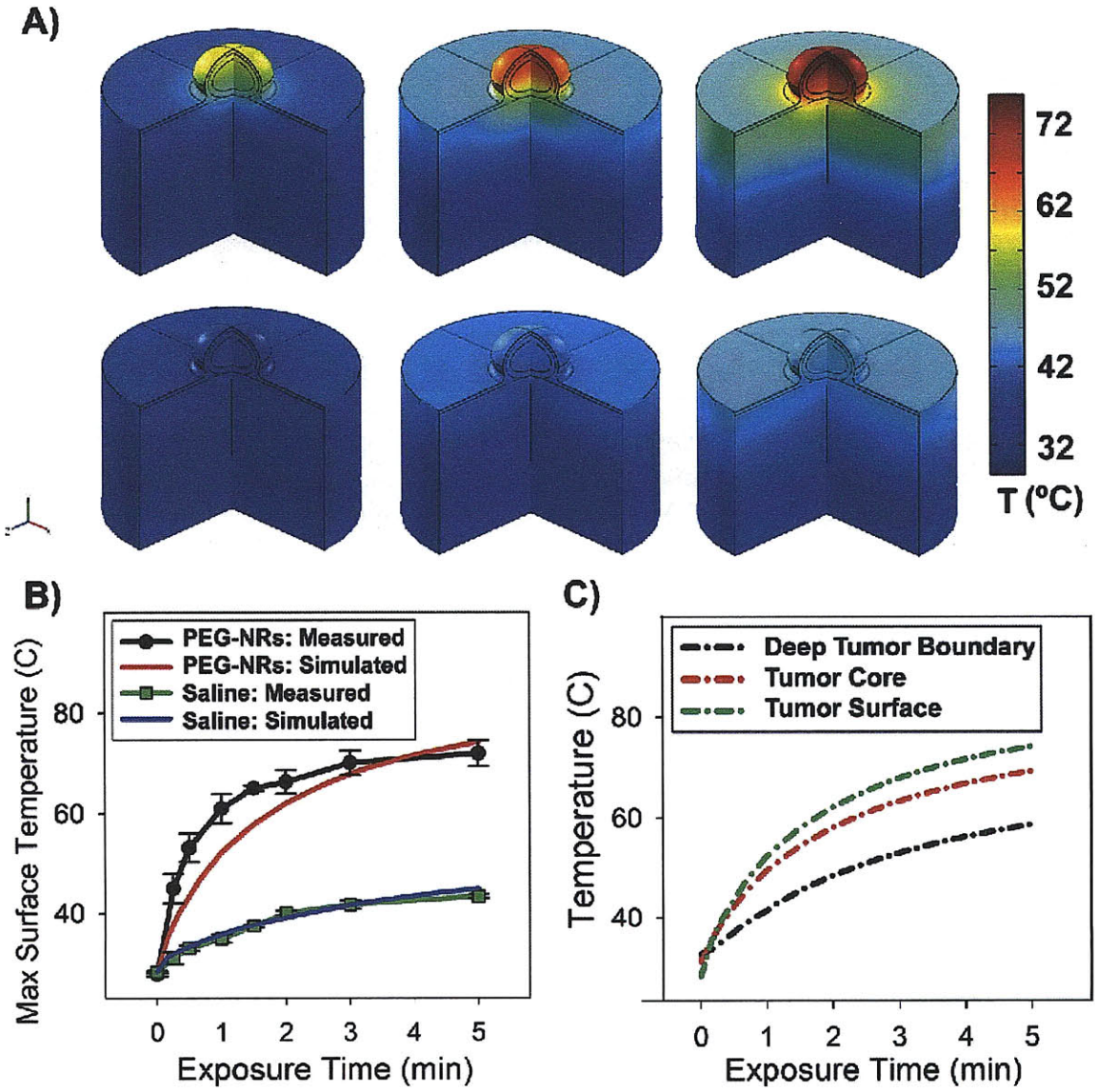

Figure 6.12: *Quantitative photothermal modeling of gold nanorod tumor heating A) 3D finite element modeling of PEG-nanorod heating in vivo.* Simulated 3D temperature distributions matching thermographic time points in 4D) are shown for PEG-nanorod (top) and control tumor irradiation (bottom). B) Thermographically measured and simulated tumor surface temperatures over time for irradiation of PEG-nanorod or saline mice. C) Simulated temperature increases various depths for PEG-nanorod- and saline-injected mice. By 5 minutes following the onset of irradiation, the entire PEG-nanorod tumor is predicted tumor to have reached ablative temperatures of >60°C, motivating the choice of this irradiation regimen for subsequent therapeutic trials.

vivo comparison could not be pursued. Separately, to study the long-term clearance of PEG-NRs from RES organs, tumor-free mice were injected with PEG-NRs and sacrificed two months after injection. During these two months, injected mice showed no signs overt NR toxicity such as weakness, belabored breathing, or failure to thrive. Organ analysis demonstrated that the %ID/g values for tissues decreased by >50% in all organs and by >80% in muscle, heart, lungs, and kidneys (**Figure 6.11**), indicating the existence of routes for gold nanorod clearance after uptake in tissues.

Having observed their efficient passive homing to human tumors via the EPR effect, the ability of PEG-NRs to remain active as optical nanoantennas for photothermal tumor heating after clearance from the systemic circulation (~72 hrs) was subsequently investigated. Either PEG-NRs (20 mg Au/kg) or a saline solution was administered intravenously into mice bearing two MDA-MB-435 tumors on opposite flanks. Once PEG-NRs had cleared from circulation (72 hrs), irradiated tumors on PEG-NR-injected mice rapidly heated to temperatures of over 70°C (**Figure 6.9C, 6.9D**), whereas saline-injected mice displayed less focal temperature increases with maximum surface temperatures of approximately 40°C (**Figure 6.9D**). To inform the development of near-infrared radiation doses that would fully destroy tumors, photothermal heating simulations were again conducted using the intravenous biodistribution data and computational domains containing ellipsoidal tumor geometries matching those used in experiments (**Figure 6.11**). Photothermal heating simulations closely matched experimental surface temperature data (**Figure 6.9D**, **Figure 6.12A, Figure 6.12B**), suggesting that tumor-targeted nanoantennas substantially retained their photothermal efficacy during the 72 hrs after injection *in vivo*. Further, the simulations predicted that

the entire tumor volume, including the deepest tumor:tissue interface, would be heated to ablative temperatures (>60°C) by 5 minutes following the onset of laser irradiation (**Figure 6.12C**). Thus, a 5 minute, 2 W/cm^2 irradiation regimen was utilized for subsequent therapeutic experiments in an effort to provide fully destructive photothermal tumor treatment.

To test the prediction that a single dose of PEG-NRs could destroy tumors under the computationally-designed protocol of NIR irradiation, nude mice bearing bilateral human MDA-MB-435 tumors were injected with either PEG-NRs or saline. Following intravenous clearance of PEG-NRs, the right flank of each mouse was irradiated for 5 min (810 nm, 2 W/cm^2) and all tumors were measured at regular intervals over time. Within 10 days all the irradiated, PEG-NR-targeted tumors completely disappeared by external observation, while all other tumors, including those exposed to laser after saline injection, continued to grow uninhibited (**Figure 6.13A**). To assess the survival benefit of PEG-NR-directed tumor ablation, mice bearing a single MDA-MB-435 tumor were divided between 4 cohorts: PEG-NRs + laser, PEG-NRs – laser, saline + laser, saline – laser; and all tumors were measured over time (**Figure 6.13B**). By twenty days following treatment, all irradiated, PEG-NR-injected mice displayed only a minor scar with no evidence of tumor regrowth, while all other surviving mice harbored thriving tumors (**Figure 6.13B**, **Figure 6.13C**). Over the course of >50 days of observation, no irradiated, PEG-NR-injected mice showed evidence of recurrence, while all mice in controls had to be euthanized by day 33. Body weights of PEG-NR-treated mice were monitored over time and showed no obvious losses due to tumor ablation and resorption (**Figure 6.14**). In

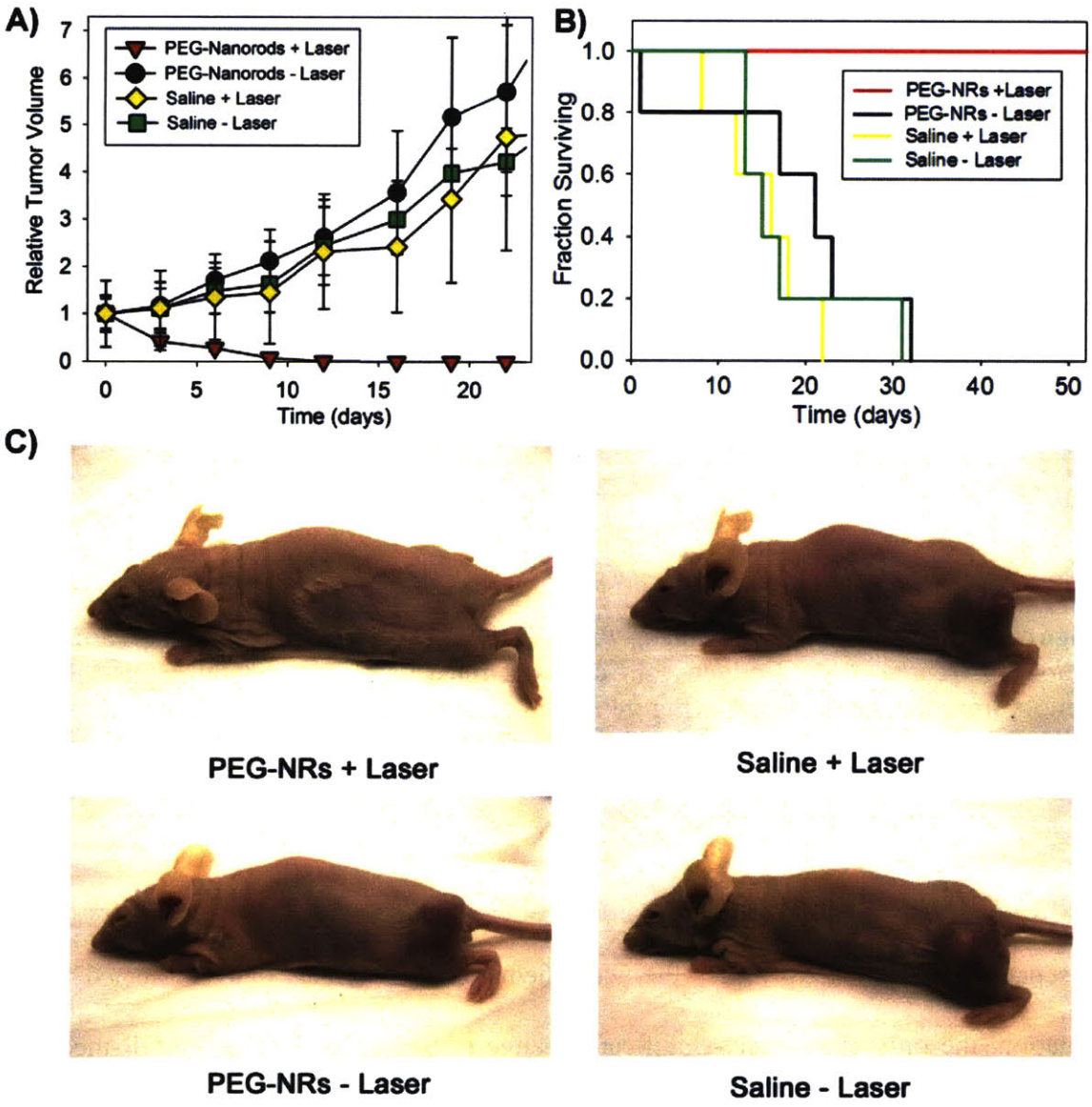

Figure 6.13: *Photothermal destruction of human tumors in mice using long-circulating gold nanorods.* A) Mice harboring two MDA-MB-435 human tumors on opposite flanks were injected with either saline or PEG-nanorods. After PEG-nanorods had cleared from circulation (72 hrs after injection), the right flank of each mouse was exposed to the computationally-designed irradiation regimen (810 nm, 2 W/cm2, 5 min). Volumetric changes in tumor sizes are plotted over time following irradiation. B) Mice harboring one MDA-MB-435 human tumor were injected with either saline or PEG-nanorods and irradiated as in A). Survival of mice following irradiation is plotted versus time after irradiation. C) At 20 days following irradiation, NIR-irradiated, all PEG-nanorod-injected mice showed only a minor scar and no evidence of tumor regrowth, while all other treatment groups harbored thriving tumors.

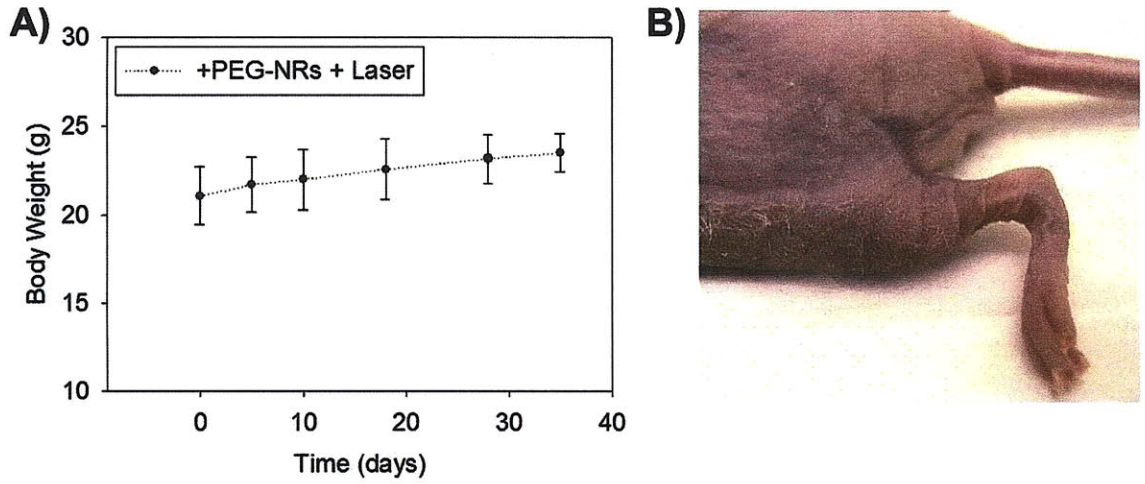

Figure 6.14: *Weight of irradiated, PEG-NR-injected mice during tumor resorption following treatment.* A) Body weight curve of mice bearing unilateral MDA-MB-435 tumors from the survival study (Figure 5C). No obvious body weight loss was observed following PEG-NR-mediated tumor therapy. C) Close view of site of tumor resportion showing only evidence of minor scar.

a separate experiment to assess the acute hematological effects of NR-directed tumor ablation, the only statistically-significant change observed in response to NR-mediated tumor ablation was a slight increase in the percent of band neutrophils in NR + Laser sets ($p<0.05$ for NR+ Laser vs. NR, Saline + Laser, and Saline) (**Figure 6.15)** likely due to an acute inflammatory response to tumor ablation.

Here we present the development of an integrated system for nanoantenna-based photothermal tumor therapy involving: the synthesis of long-circulating gold NRs as efficient NIR-nanoantennas, biodistribution data acquisition via x-ray CT nanomaterial

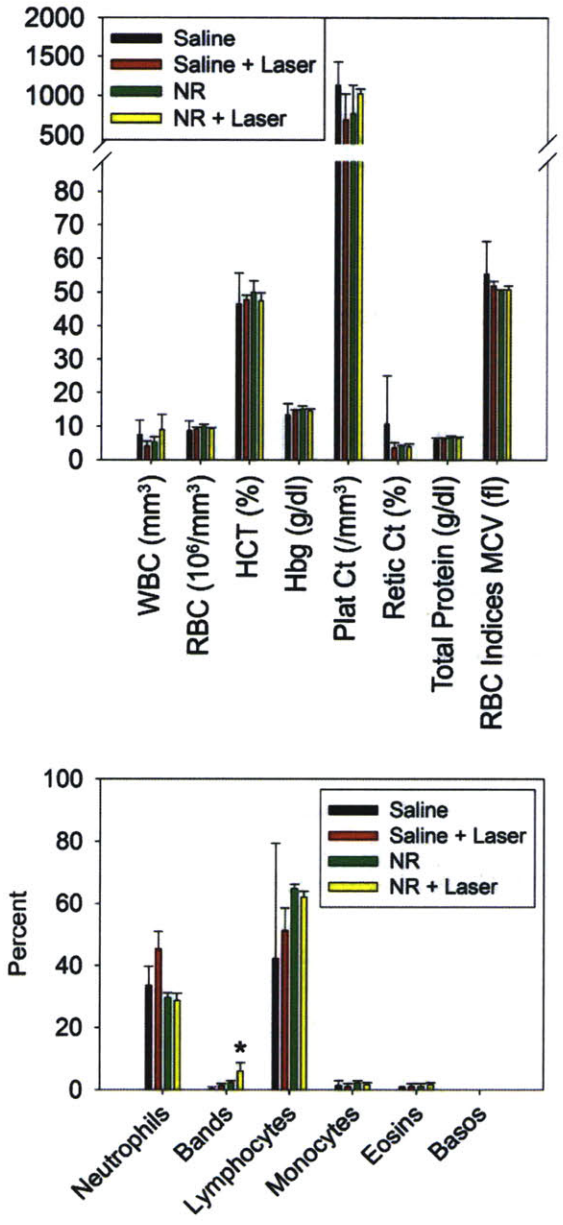

Figure 6.15: *Hematological effects of PEG-NR irradiation in mice.* To explore the effects of NR administration and near-infrared ablation, mice bearing bilateral MDA-MB-435 tumors were injected with either saline or PEG-NRs and, 72 hrs later, either exposed to the therapeutic tumor irradiation protocol under anaesthetic (~2 W/cm^2, 5 min, 810 nm) or anaesthetized without irradiation (n=3 each set). Following irradiation or comparable time under anaesthetic, blood was collected for hematology and mice were sacrificed. The only statistically-significant change observed in response to NR-mediated tumor ablation was a slight increase in the percent of band neutrophils ($p<0.05$ for NR+ Laser vs NR, Saline + Laser, and Saline), likely due to an acute inflammatory response to tumor ablation.

imaging or *ex vivo* spectrometry, and photothermal computational modeling to guide surgical irradiation planning. Broadly, the efficacy of a nanoantenna for photothermal therapy depends both on intrinsic (optical absorption coefficient, material cytotoxicity) and extrinsic (polymer coating, macrophage affinity, and circulation time) material characteristics, as well as external parameters, such as the use of optimized dosing and irradiation protocols for effective treatment.

We show that PEG-nanorods exhibit superior intrinsic absorption and photothermal efficacy compared with gold nanoshells (~6 times greater heat generation per weight gold), as well as substantially improved circulation times *in vivo* (~17 hrs vs ~4 hrs), extrinsically imparted by their polymer coating(*41, 42*). Surveying literature on inorganic nanoparticle circulation times *in vivo*, the circulation half-life of PEG-NRs is among the longest achieved to date. Previously, polymer-stabilized inorganic nanomaterials have been described with circulation half-lives of a few hours *in vivo*(*28, 300*), including a variety of other gold nanoparticle preparations(*29, 301-303*), and on occasion with circulation times of ~10-15 hrs in mice(*14, 65, 116*). Elsewhere, another PEG-nanorod formulation was developed for *in vivo* applications, but showed a 30 min half-life without investigation into their ability to passively target tumors or mediate *in vivo* photothermal heating(*302*). Because nanoparticle circulation time has been shown to determine the efficiency of nanoparticle accumulation in tumors via the EPR effect, in mouse cancer models and in clinical cancer treatment(*14*), the long circulation time reported here has potential to directly translate to improved clinical tumor accumulation over previous nanoantennas.

Beyond the material determinants of nanoantenna efficacy, the irradiation protocol utilized (ie. beam intensity, shape, cross-section, duration, direction, etc.) and nanoantenna dosing regimen directly control the rates of energy capture and dissipation to surrounding tissues *in vivo*. While nanoantennas have the potential to increase the selectivity of tumor ablation, unoptimized irradiation of tissues carries the risks of either unnecessary morbidity due to collateral damage or ineffective therapy due to incomplete treatment of tumor margins. Here, we show that quantitative biodistribution data incorporated into computational modeling can help anticipate the photothermal heating in tumors and surrounding tissues during irradiation. Future developments of the quantitative model presented here could enable rapid quantitative modeling of photothermal temperature gradients in arbitrarily complex 3D tissues and provide a route towards a priori personalization of irradiation regimens. As a proof-of-principle, we establish a means of integrating whole subject x-ray CT data with quantitative heat transfer modeling, offering a new route towards merging the clinical paradigms of imaging and therapy for personalized 4D radiation planning and optimization. Further, using a computationally planned therapeutic method, we show that intravenous administration of PEG-NR nanoantennas enabled complete destruction of all irradiated tumors, under otherwise benign near-infrared light.

6.3 Conclusions:

We believe our findings motivate future investigation into the long-term biodistribution of PEG-NRs, more extensive analysis of their potential toxicity *in vivo*, and the development of methods for detecting low concentrations of PEG-NRs in whole animals to remotely quantify intravenous tumor targeting. Methods for actively targeting

nanorods to tumors, particularly to vascular epitopes, could potentially enhance their specificity for tumors or direct their additional accumulation in premalignant lesions and metastatic lymphatics. Finally, we provide evidence that the application of quantitative biodistribution-based modeling to the *in vivo* testing of nanomaterials can provide insight into their function and direct procedural optimization.

6.4 Materials and Methods:

Preparation of PEG-coated gold nanorods: Highly stable, ~13 nm x 47 nm (Figure 1A) CTAB-coated gold nanorods with longitudinal plasmon resonance at 810 nm (Nanopartz, a division of Concurrent Analytical Inc., Salt Lake City, UT) were centrifuged at 16,000 rcf to concentrate and gently resuspended in 250 μM 5 kDa methyl-PEG-thiol (Laysan Bio, U.S., Arab, AL). Thiol activity of polymers was quantified spectraphotometrically using 5,5′-Dithiobis(2-nitrobenzoic acid) (Sigma, St. Louis, MO) against a dithiothreitol (Sigma) gradient to verify that polymer stocks were fully reduced. The solution of 5 kDa methyl-PEG-thiol and CTAB-coated gold nanorods was gently mixed at room temperature for 1 hr and dialyzed exhaustively against ultrapure water (18 MΩ cm^{-1}) via cellulose ester membrane dialysis to drive PEG addition (Spectrapor, Rancho Dominguez, CA). Dialyzed samples were filtered through 100 kDa filters (Millipore, Billerica, MA) to remove excess polymer and stored at 4°C. To quantify the number of polymers per particle, NRs were coated as described with an amino-PEG-thiol polymer. After dialysis and extensive filtration on 100 kDa centrifugal filters, amino NRs were harvested and an SPDP assay was performed to quantify the number of amines(*298*).

Stability and cytotoxicity: Solutions of PEG-NRs or CTAB-NRs (~60 μg Au/ml) were normalized and incubated in PBS or 10% human serum for extended periods of time. At regular intervals, samples were spectrophotometrically analyzed for plasmon resonance peak shifts, which would indicate particle aggregation. To assess material toxicity, micropatterned primary hepatocyte:human fibroblast co-cultures were prepared as described previously(*59*). 24 hrs following liver co-culture seeding, coculture wells were exposed in triplicate to a gradient of PEG-NRs (from 0 to 280 μg Au/ml) and allowed to incubate for 24 hrs. At this point, PEG-NRs were removed, cells were washed repeatedly, and viability was assessed via an MTT viability assay (Sigma), a colorimetric viability assay for mitochondrial dehydrogenase enzyme activity read using a spectrophotometer (SpectraMax, Molecular Devices, Sunnyvale, CA).

Photothermal comparison between PEG-nanorods and PEG-nanoshells: Gold nanoshells (Nanocomposix, San Deigo, CA) with 120 nm silica core and ~15 nm gold shell were mixed with methyl-PEG-thiol as described(*41, 42, 48*). Both PEG-nanoshells and PEG-NRs were brought to 7 μg Au/mL, as determined by inductively coupled plasma mass spectrometry (ICP-MS). Tubes containing 200 μl of these solutions were broadly irradiated, under identical conditions, by an 810 nm diode laser (RPMC Lasers Inc) at 2 W/cm^2. During irradiation, an infrared thermographic camera (FLIR, Goleta, CA Thermacam S60) was used to measure peak sample surface temperature. To assess photothermal cell toxicity, MDA-MB-435 human cancer cells (ATCC) were cultured in a 96-well microplate and grown to 80% confluency using ATCC-recommended media. Cells were incubated with either PEG-NRs (14 μg/mL), PEG-nanoshells (14 μg/mL), or media alone. For each, triplicate wells were exposed to the diode laser light (5 min, 2

W/cm^2) or no laser. After treatment, cells were incubated with Calcein AM (5 μg/mL in culture medium; 1hr incubation, Invitrogen Carlsbad, CA), a fluorescent indicator of esterase activity in viable cells, and imaged using phase and fluorescence microscopy.

X-ray Computed Tomography of PEG-nanorods. PEG-NRs were suspended in PBS after concentration via membrane centrifugation and serially diluted over a 1000-fold concentration gradient. A clinical iodine standard was similarly diluted for comparison (Isovue-370). X-ray computed tomography was performed in a GE eXplore Locus microCT scanner (80 kV, 450 μA, 45 μm resolution). For *in vivo* imaging, mice were imaged prior to NR injection to reveal the baseline level of soft tissue x-ray contrast. 10 μl of PEG-NRs (~3pmol) were injected with a 30 gauge needle directly into the center of the tumor and the needle was maintained in place for ~10 seconds to allow the tumor to accommodate the additional fluid. Following intratumoral administration, mice were imaged and irradiated (~.75 W/cm^2, 810 nm). X-ray CT images were exported as DICOM files for exportation into modeling software (See supporting methods).

Inductively coupled plasma mass spectrometry (ICP-MS). Samples for ICP-MS (Thermo-Scientific Finnigan ELEMENT2) analysis were frozen, lyophilized, and dissolved in aqua regia, prepared by adding 100 μl of nitric acid + 300 μl of 37% hydrochloric acid for 72 hrs to dissolve gold particles. Then, samples were brought up into 10 mLs of 9.6 mL 2% HNO_3 and analyzed via ICP-MS against standards. Control saline and organ samples with exogenously added PEG-NRs were utilized to calibrate the linearity of this method.

In vivo circulation time and biodistribution of PEG-nanorods. Nude mice were bilaterally injected subcutaneously in the hind flank with ~$2x10^6$ MDA-MB-435 cells. After 2-3 weeks animals were anaesthetized with isoflurane and injected through the tail vein with PEG-NRs in 0.15 M NaCl, 0.1 M Na Phosphate buffer, pH 7.2 (20 mg Au/kg). 10 µl blood samples were withdrawn periodically from the sub-orbital space, diluted with PBS containing 10 mM EDTA, centrifuged to remove RBCs, and read on a spectrophotometer to assess PEG-NR plasmon peak height. For biodistribution experiments, following vascular clearance of PEG-NRs (72 hrs), injected animals were euthanized and organs were collected, weighed, and lyophilized for ICP-MS quantification of PEG-NR biodistribution.

In vivo photothermal heating of gold nanorods and photothermal therapy. For both initial modeling and growth curve assessments following photothermal treatment, nude mice were bilaterally injected in the hind flank with ~$2x10^6$ MDA-MB-435 cells. After 2-3 weeks animals were anaesthetized with isoflurane and injected through the tail vein with PEG-NRs in PBS (20 mg Au/kg) or PBS alone. Following vascular clearance of PEG-NRs (72 hrs), the right flank of mice was irradiated (2 W/cm^2, 810 nm, 1 cm beam diameter). Thermographic imaging of photothermal heating was utilized to facilitate modeling of 3D temperature distributions in tumors (n=3 mice for each set). To explore the hematological effects of NR administration and near-infrared ablation, mice bearing bilateral MDA-MB-435 tumors were injected with saline or PEG-NRs and, 72 hrs later, either exposed to the therapeutic tumor irradiation protocol under anesthesia (~2 W/cm^2, 5 min, 810 nm) or anesthesia without irradiation (n=3 each set). Following exposure, blood was collected for hematology and mice were sacrificed. Therapeutic assessment

of the affect of PEG-NR heating on tumor growth was conducted similarly (n=4 mice in each treatment set). Both irradiated and unirradiated tumors of each mouse in the therapeutic assessment trial were measured at regular intervals using digital calipers. Survival studies were conducted using mice that were unilaterally injected in the hind flank with ~$2x10^6$ MDA-MB-435 cells (n= 5 mice in each treatment set). Tumor sizes were measured over time and mice were considered dead once tumors exceeded 500 mm^3.

Finite Element Modeling of Photothermal Tumor Heating

To reveal the magnitude and kinetics of *in vivo* photothermal heat generation by the nanorods and native tissue, the temporal and spatial propagation of thermal gradients, and to assess the timescale within which the entire tumor volume would reach ablative temperatures, a finite element computer simulation of the photothermal ablation process was developed and carried out. The tumor was approximated as a paraboloid, resting above the muscle and covered by skin of 300 μm thickness. The bio-heat transfer equation of Pennes (1948) was applied to the computational domain in the form(*304*):

$$\rho c\,(\partial T/\partial t) + \nabla . (-k \nabla T) = \rho_b c_b w_b (T_b - T) + Q_{met} + Q_{laser}$$

Where, ρc is the heat capacity of the muscle, tumor periphery, tumor core or skin as appropriate in the respective regions. The heat capacity of blood is $\rho_b c_b$ and its perfusion rate in the respective domain is w_b. Q_{met} and Q_{laser} are the metabolic and laser heat generation in the tissues respectively. For intravenous photothermal modeling, a cylindrical domain of 20 mm diameter around the tumor with a depth of 12 mm for the muscle domain was considered for computation. The shell of the tumor was considered to

be of 0.5 mm thickness having higher rate of blood perfusion than the tumor core. A cut view of the computational domain is shown in Fig S10.

The blood perfusion rate is known to be different in tumor periphery, tumor core, healthy tissues and skin. Hence, they have been taken accordingly from literature (Fujita et al., 1998) as follows

$w_b = F[1]$ for $T < 39^0C$

$= F[1+ (p-1) (T-39)/(45-39)]$ for $39^0C < T < 45^0C$

$= F[p- (p-1) (T-45)/(51-45)]$ for $45^0C < T < 51^0C$

$= F[1]$ for $T > 51^0C$

The maximum perfusion rate and the parameter p for different region are given as

Tissue	F (m^3/kg/s)	p
Tumor core	5×10^{-7}	1
Tumor periphery	1.67×10^{-6}	2
Muscle	8.3×10^{-6}	9
Skin	8.3×10^{-6}	9

The thermophysical properties of various regions were taken from accepted values as

Tissue	Density	Specific heat	Thermal conductivity
	m^3/kg	J/(kgK)	W/(mK)
Tumor core	1050	3700	0.5
Tumor periphery	1050	3700	0.5
Muscle	1050	3700	0.5
Skin	1200	3700	0.2
Blood	1000	4200	-

The metabolic heat generation rate is taken to be 400 W/m^3.

Laser heat generation in tissues is a widely studied area. Welch (1984) gave a good overview of the various models available in this area(*305*). Seeing various possibilities, the following equation for heat generation, which is a modification of his equation (12) for the present geometry, was chosen:

$$Q_{laser} = \alpha I_0 \exp[-r^2/[2\sigma(0) \exp(\beta z_c)]]\exp[-(\alpha+\beta)z_c]$$

Where I_0 is the laser irradiation intensity in W/m^2, r is the radial distance from the center, and z_c is the depth of the location from the skin. The parameters α and β are the absorption and scattering coefficient (in m^{-1}) of the tissues respectively. To incorporate the curvature of the tumor's surface and the internal multi-layer tissue structure (skin, tumor), the following modification was made:

$$Q_{laser} = \alpha I_0 \exp[-r^2/[2\sigma(0) \exp(\beta z_c)]]\exp[-(\alpha+\beta)(z_c-c-d)] \exp[-(\alpha_s+\beta_s)(z_s)] \exp[-(\alpha_t+\beta_t)z_t]$$

Here, c is the depth of the skin surface from the tumor vertex at a given radial position, d is the depth of the normal tissue above a location, z_s is the depth of the skin above a location and z_t is the depth of the tumor tissue above a location. The suffixes: s and t indicate skin and tumor absorption and scattering coefficients, respectively; the values of which were taken to be 0.4 and 5.3 cm^{-1} in absence of nanorods(*306*). For the experiments with nanorods, the absorption coefficient of the tumor was predicted to be 3.07 cm^{-1} based on the Nrod biodistribution data (~7% ID/g; 20 mg/kg injected dose; 0.1 cm^3 tumor volume) and *in vitro* absorption measurements. Jain et al (2006) showed that the extinction coefficient of ~13 nm x 47 nm nanorods is dominated by absorption and hence we assumed that nanorods only enhance the tumor absorption coefficient, with insignificant alteration of large endogenous scattering coefficients(*307*). The surface heat loss coefficient to the environment was taken as 15 W/m^2K, which is a typical value for natural convection on planar surfaces.

Finite element method (FEM) using the multiphysics enabled software COMSOL was used for modeling. After careful grid variation, a total of 4436 triangular elements per half symmetry plane was chosen to represent tumor heating. The temperature tolerance was at the default value of 0.0001 and a direct matrix inversion technique was used.

Simulation of localized injected nanorod geometry using X-Ray tomography data

For the purpose of simulating the 3D geometry of injected nanorods and the resulting thermal flux upon irradiation, a multi-step procedure was performed to translate 3D X-ray CT images into a form amenable to computational modeling of photothermal heating. For the present cases, 406 DICOM slices were exported, including the tumor, muscle, and the internal skeletal details, as well as the distribution of injected nanorod solutions as shown in Fig. 3 and supplementary Figs. 5 and 6. Subsequently these data were imported in the image processing software Scan IP and reconstructed based on the grey scale values of the scan to form volumetric geometries for nanorods, skeletal structures, and soft tissues as shown in Fig. 3D supplementary Figs.5C and 6B. Next, the solid model was imported to the meshing software Scan FE and proper surface meshing was carried out. Finally, the 3D meshed geometries were imported to COMSOL Multiplysiscs and the thermal analysis was carried in an identical fashion to the previous description in the ellipsoidal geometry.

Chapter 7: Nanoparticles that Communicate to Amplify Tumor Targeting *In Vivo*

7.1 Introduction:

Advances in nanotechnology have produced an expansive toolkit of nanodevices with unique electromagnetic properties(*4, 32, 54*) and the capacity to encapsulate and programmably release a diversity of therapeutics, ranging from small molecules(*17, 93, 308, 309*) to oligonucleotides(*310, 311*). Over the past three decades, approaches to targeting these materials *in vivo* have predominantly focused on tuning the properties of individual particles including geometry, surface chemistry, ligand type and ligand density (*14, 16, 90, 141, 142, 145, 169-172*). These materials are typically administered as populations of >1 trillion nanoparticles *in vivo* to carry out identical, often competitive functions. While these approaches have resulted in some improvements in targeted nanoparticle delivery, the overall tissue accumulation remains low, typically due to inter-nanoparticle competition and microenvironmental challenges such as restricted transvascular transport and receptor availability.

In contrast to such systems composed of near-identical constituents, natural systems frequently generate complex behaviors through collective interactions between multiple system components—enabling emergent processes such as computation, amplification, and dynamic communication. For example, the recruitment of inflammatory cells to regions of infection is coordinated by resident tissue macrophages that emit chemokines which diffuse through the interstitium to enhance endothelial adhesion molecule expression and enable the recruitment of circulating neutrophils. This

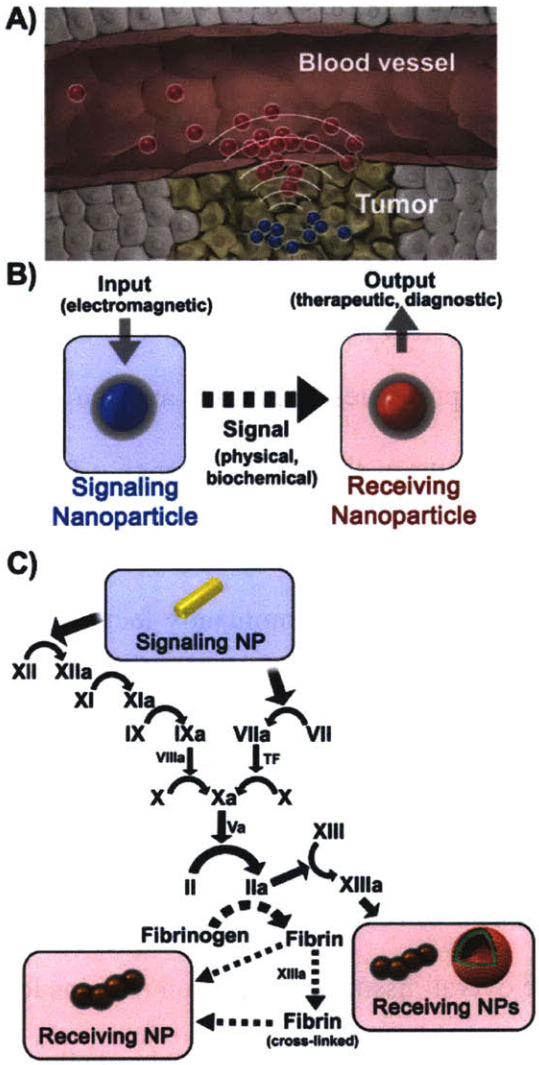

Schematic 7.0. *Architecture and information flow in nanoparticle signaling networks.* A) Generic architecture for nanoparticle signaling networks. Extravascular nanoparticles that have targeted tumors signal remotely to recruit intravascular nanoparticles. B) Information flow in nanoparticle signaling networks. Extravascular Signaling nanoparticles convert an electromagnetic signal into a local physical signal that is biologically-transduced into a local biochemical signal for circulating therapeutic or diagnostic Receiving nanoparticles. C) Signaling pathway between Signaling and Receiving nanoparticles. Tumor-targeted, extravascular plasmonic gold nanorods (Signaling nanoparticle (NP)) initiate coagulation cascade activation by photothermally disrupting tumor vessels and activating the extrinsic and intrinsic coagulation pathways, respectively. The resulting biomolecular amplification of the coagulation cascade is channeled to recruit organic (drug-loaded liposomes) or inorganic (iron oxide nanoworms) via activity of the coagulation transglutaminase FXIII (solid path on right) or via targeting of polymerized fibrin (dotted path on left).

signaling pathway transmits spatial information to circulating immune cells and ultimately results in an amplified local response. Inspired by this process, we considered the design of nanoparticle systems that interact to produce emergent behaviours with the capacity to enhance *in vivo* diagnostics, regenerative medicines, and other therapeutics (**Scheme 7.1A**).

We devised a two-component nanoparticle signaling network to amplify tumor targeting *in vivo*. In this system, interstitial Signaling nanoparticles provide a physical stimulus that is biologically transduced into an abundant biochemical signal for Receiving nanoparticles in circulation (**Scheme 7.1B**). Specifically, the Signaling nanoparticles consist of intravenously-injected, polymer-protected gold nanorods (NRs) that passively-target xenograft tumors in mice. Remote, photothermal heating of tumor-targeted NRs locally increases vascular permeability, exposing circulating plasma to the tumor interstitium and activating the coagulation cascade to generate an abundant biochemical signal for coagulation-targeted Receiving nanoparticles (**Scheme 7.1C**). To explore the modularity of this technique, two types of nanoparticles were explored: a model imaging agent (magnetofluorescent iron oxide nanoworms) and a model therapeutic agent (doxorubicin-loaded liposomes). Furthermore, to investigate whether information could be channeled to Receiving nanoparticles through multiple molecular pathways in coagulation, two types of targeting strategies were explored: peptide coatings that recognize fibrin directly and peptides that target coagulation enzyme activity by acting as a substrate for the coagulation transglutaminase Factor XIII (FXIII) (**Scheme 7.1C**).

7.2 Results and Discussion:

We first set out to examine the transduction of tumor heating into localized coagulation by evaluating fibrin deposition in tumors as a function of temperature (**Figure 7.1A**). Purified fibrinogen (the precursor to fibrin) and albumin (an abundant blood protein unrelated to coagulation) were labelled with unique near-infrared fluorochromes to allow simultaneous assessment of coagulation-dependent and independent protein tropism to heated tumors. Mixtures of fibrinogen and albumin were intravenously injected into athymic (*nu/nu*) mice bearing bilateral human MDA-MB-435 tumors, after which one tumor was heated using a temperature-controlled water bath. At 24 hours, mice were sacrificed and the relative levels of tumor fibrin(ogen) and albumin were assessed fluorescently. We observed a marked induction of fibrin(ogen) accumulation in tumors between 45°C and 53°C, with little accompanying increase in albumin accumulation, indicating that heat specifically directed coagulation cascade activation in tumors(**Figure 7.1C, 7.2**). Immunohistochemical staining for fibrin(ogen) in tumors from uninjected mice corroborated these findings, demonstrating that exogenous fibrinogen administration did not artificially drive accumulation in heated tumors (**Figure 7.3**).

Having probed the thermal sensitivity of coagulation in tumors, we next investigated whether tumor-targeted gold NRs could localize coagulation to. Rod-shaped gold nanoparticles are precisely-tunable plasmonic nanomaterials that may be synthesized in bulk, have narrow size distributions, optical absorption coefficients 10^4-10^6-fold higher than conventional organic fluorochromes (*6, 46, 290*). Previously, we demonstrated that polyethyleneglycol-coated gold NRs (PEG-NRs) have >17 hr circulation half-lives in mice, enabling passive targeting to tumors via their fenestrated, angiogenic blood vessels(*312, 313*) and precise tumor heating using otherwise benign

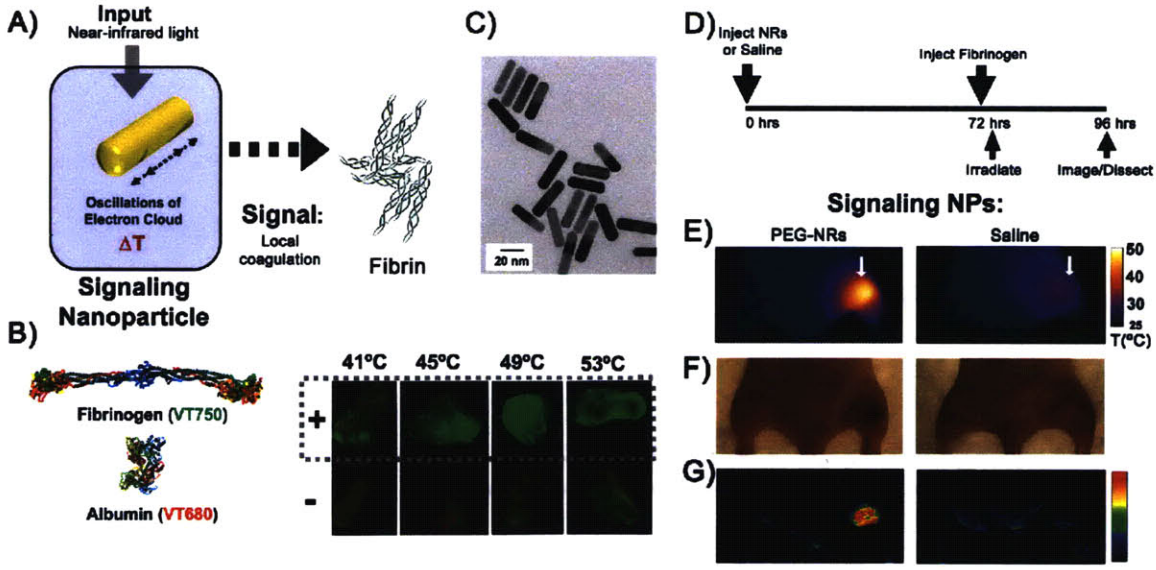

Figure 7.1. *'Signaling nanoparticle' characterization.* A) Schematic of nanorod-directed stimulation of the coagulation cascade. Gold nanorods (NRs) are passively targeted to tumors to photothermally specify coagulation cascade activation in tumors. B) Transmission electron microscopy of near-infrared absorbing NRs. C) Probing the coagulation-dependent and –independent protein tropism to heated tumors. Fibrinogen and albumin were labelled with unique near-infrared fluorochromes and injected into mice bearing bi-lateral MDA-MB-435 tumors. Immediately following injection, one tumor on each mouse was heated using a temperature-controlled water bath. At 24 hrs post-injection, mice were dissected and both tumors imaged for the relative abundance of fibrinogen (green) and albumin (red). Both heated (+ row) and unheated (- row) tumors are displayed across the temperatures tested. D) Experimental timeline for exploring fibrinogen deposition in PEG-NR heated tumors. E) Thermographic imaging of PEG-NR- and saline-injected mice under broad NIR irradiation of the right flank. F) Visible light image of mice 24 hrs after NIR-irradiation. G) Fluorescence reflectance imaging of mice to visualize fibrinogen tropism to PEG-NR-heated tumors.

near-infrared (NIR) energy. Here, PEG-NRs (10 mg Au/kg) or saline were intravenously administered to mice bearing bilateral MDA-MB-435 tumors (**Figure 7.1D**). After PEG-NR clearance from circulation (72 hrs post-injection), fluorescent fibrinogen was intravenously injected and the right flanks of mice were irradiated with near-infrared light (~1 W/cm^2), generating focal tumor surface temperatures of ~49°C in PEG-NR-injected mice, while saline-injected tumor surface temperatures remained below ~37°C (**Figure**

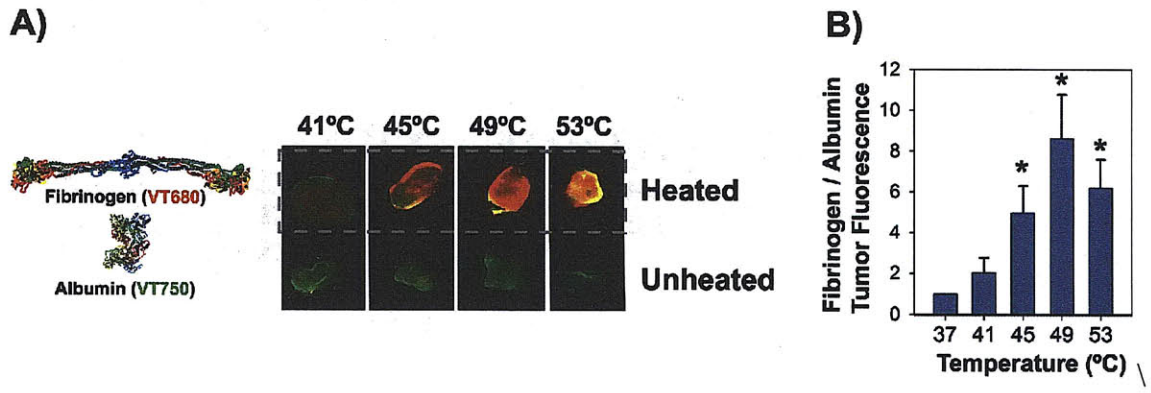

Figure 7.2. *Specific fibrinogen tropism to heated tumors.* A) Probing the coagulation-dependent and –independent protein tropism to heated tumors. Fibrinogen and albumin were labelled with unique near-infrared fluorochromes in the opposite channels as in Figure 1A (VT680 and VT750, respectively) and injected in mice under identical conditions. Reversing the fluorophore labelling on fibrinogen and albumin enables quantitation of protein tropism to heated tumors independent of any potential optical or molecular fluorophore bias. At 24 hrs post-injection, mice were dissected and both tumors imaged for the relative abundance of fibrinogen (red) and albumin (green). Both heated (+ row) and unheated (- row) tumors are displayed across the temperatures tested. B) Quantitation of fibrinogen:albumin fluorescence ratio across tested tumor temperatures. Data taken under conditions of 1A and S1A were utilized to quantify the relative abundance of fibrinogen and albumin in heated tumors vs unheated. At 45-53˚C, fibrinogen abundance in tumors was significantly enhanced over albumin ($P<0.05$; 1-sided t-test; 4-mice per temperature).

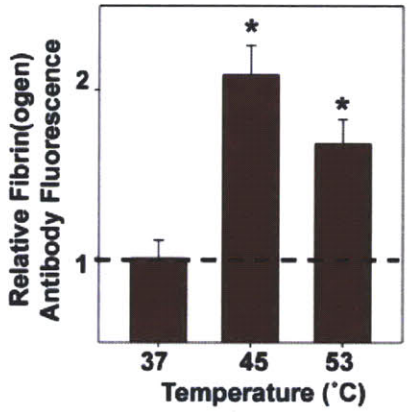

Figure 7.3. *Histopathological analysis of anti-fibrin(ogen) binding to unheated and heated tumors*. Quantitation of anti-fibrin(ogen) binding to sections from unheated and externally-heated tumors. As an independent measure of fibrin(ogen) deposition in heated tumors, uninjected mice bearing bilateral MDA-MB-435 tumors had one tumor immersed in a temperature-controlled water bath for 20 minutes and were sacrificed 24 hrs later for histological sectioning. Fluorescent quantification showed significantly enhanced abundance of antibody binding at both 45 and 53˚C ($P<0.0001$, 1-sided t-test, 6 separate regions analyzed in each condition).

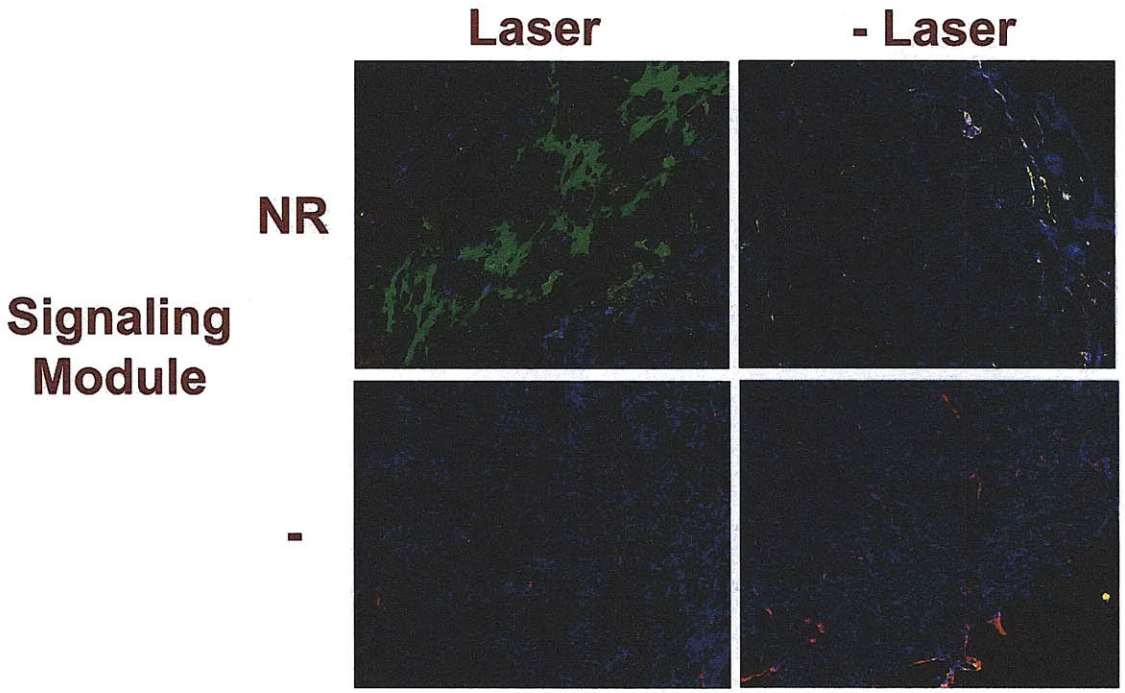

Figure 7.4. *Histopathological analysis of NR-directed fibrinogen deposition in tumors.* Mice bearing bilateral MDA-MB-435 tumors were injected with PEG-NRs (10 mg Au/kg) or saline and, 72 hrs later, injected with fluorescently-labeled fibrinogen (VT750) and broadly irradiated on their right side (~1 W/cm^2, 810 nm, 20 min). At 24 hrs post-injection, mice were sacrificed and tumors isolated for histological analysis of fibrinogen distribution (Red=CD31 antibody stain, Blue= DAPI nuclear stain, Green=fibrinogen distribution).

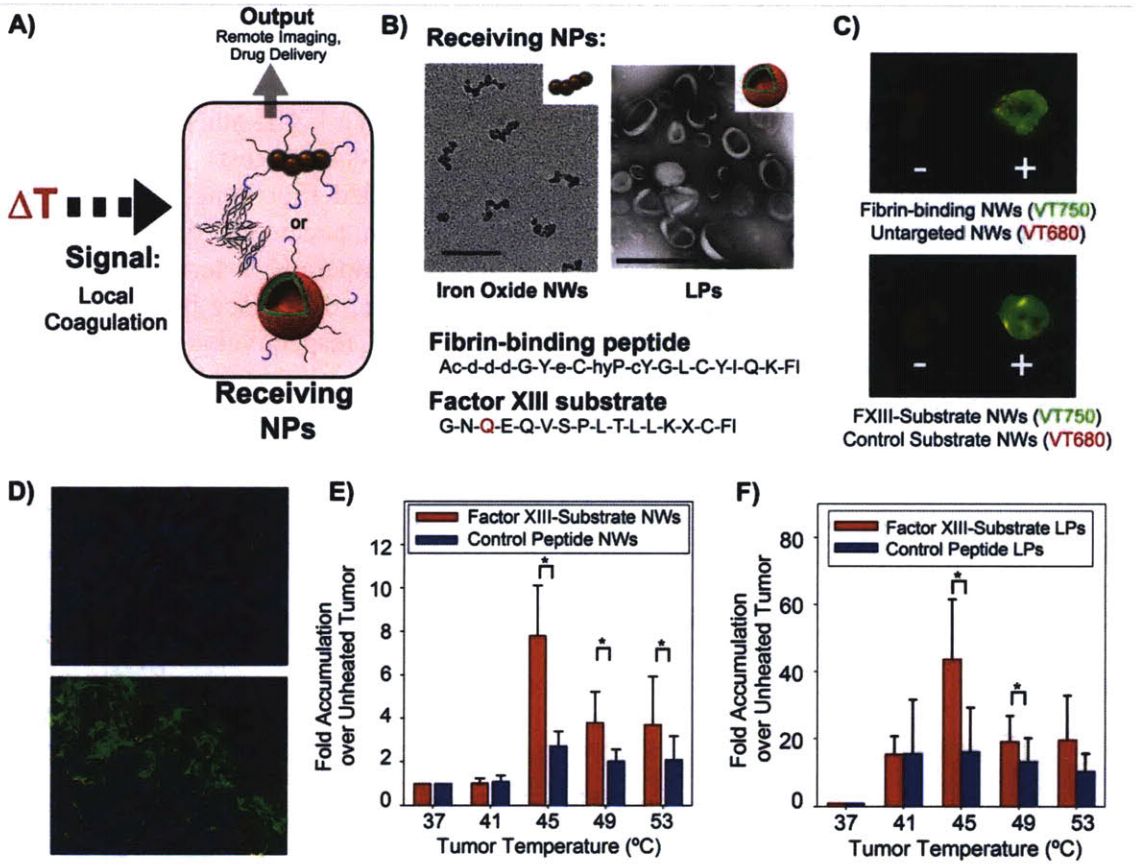

Figure 7.5. *'Receiving nanoparticle' synthesis and testing.* A) Schematic of Receiving NP homing to regions of coagulation cascade activity. Multimodal nanoworm (NW) imaging agents and drug-loaded liposomes (Lps) (top and bottom, respetively) were derivatized with coagulation-targeting peptides to form Receiving NPs that accumulate in regions of fibrin deposition (fibrin in grey). Receiving NP characterization utilized temperature-controlled water baths to initially probe the thermal sensitivity of Receiving NP homing to tumors. B) Nanostructure and biological activity of Receiving NPs. Transmission electron microscopy images of the two classes of nanomaterials utilized in Receiving NP synthesis: iron oxide nanoworms (NWs; scale bar=50 nm) and doxorubicin-loaded liposomes (Lps; scale bar=400 nm). Two peptides were utilized to direct Receiving NPs with targeting specificity for coagulation: a fibrin-binding peptide and a glutamine-containing substrate for the coagulation transglutaminase FXIII to respectively direct particle binding and covalent attachment in regions of coagulation. C) Fluoresence reflectance imaging of Receiving NP homing to externally-heated tumors. Mixtures of targeted (green) and untargeted (red) NWs, labelled with the unique NIR-fluorochromes VT750 and VT680, respectively, were intravenously injected into mice bearing bilateral MDA-MB-435 tumors. Immediately following injection, one tumor was submerged in a temperature-controlled water bath for 20 min and mice were dissected at 24 hrs for fluorescent organ imaging. Overlaid fluorescence images are shown for targeted (green) and untargeted (red) Receiving NP accumulation in both heated (+, 45°C heating) and naïve (-) tumors from the same mouse. D) Histopathological analysis of Receiving NP homing to heated tumors. Histological sections from naïve (top) and heated (bottom, 45°C) tumors in FXIII-NW-injected mice were stained for CD31 (red)

and nuclei (blue) and imaged to reveal Receiving NP distribution (green). E) Quantifying the amplification of FXIII-Substrate and Control NW Receiving NP homing to heated over unheated tumors. The fold enhancement of NW targeting is plotted across the range of temperatures tested (n=4, $p<0.05$ for the difference between FXIII-substrate-NWs and Control substrate NWs at 45°C, 49°C, and 53°C; paired, one-sided t-test). F) Quantifying the amplification of FXIII-Substrate and Control Drug-loaded Liposome Receiving NP homing to heated over unheated tumors. The fold enhancement of doxorubicin accumulation in tumors is plotted across the range of temperatures tested for FXIII-substrate Lps and Control-substrate Lps (n=3, $p<0.05$ for the difference between FXIII-substrate-NWs and Control substrate NWs at 45°C and 49°C, respectively; unpaired, one-sided t-test).

7.1E). At 24 hrs post-injection, irradiated tumors on NR-injected mice displayed macroscopic evidence of injury (**Figure 7.1F)** and localized accumulation of fibrinogen (**Figure 7.1G)**; while tumors with PEG-NRs or near-infrared energy alone lacked these features. Histopathological analysis revealed that fibrin(ogen) deposition formed a broad interstitial mesh in heated tumors, indicating that NR heating could compromise tumor blood vessels to initiate extravascular coagulation (**Figure 7.4)**.

We next set out to develop Receiving nanoparticles that could efficiently target regions of heat-induced coagulation to deliver therapeutics or act as imaging agents (**Figure 7.5A)**. Initially, magnetofluorescent iron oxide nanoworm imaging agents (NWs) (**Figure 7.5B top**) were derivatized with a peptide substrate for the coagulation transglutaminase Factor XIII (G-N-***Q***-E-Q-V-S-P-L-T-L-L-K-X-C-Fluorescein)(*314-316*) to enable incorporation into regions of active coagulation (**Figure 7.5B bottom, 7.6)**. To test the ability of Receiving NWs to home to heated tumors, mixtures of targeted and untargeted NWs, labelled with unique near-infrared fluorochromes, were intravenously injected into mice bearing two MDA-MB-435 tumors. Immediately following injection, one tumor was submerged in a temperature-controlled water bath for 20 min and mice were dissected at 24 hrs for fluorescent organ imaging. We found that the accumulation of FXIII-substrate Receiving NWs was sharply amplified at 45°C

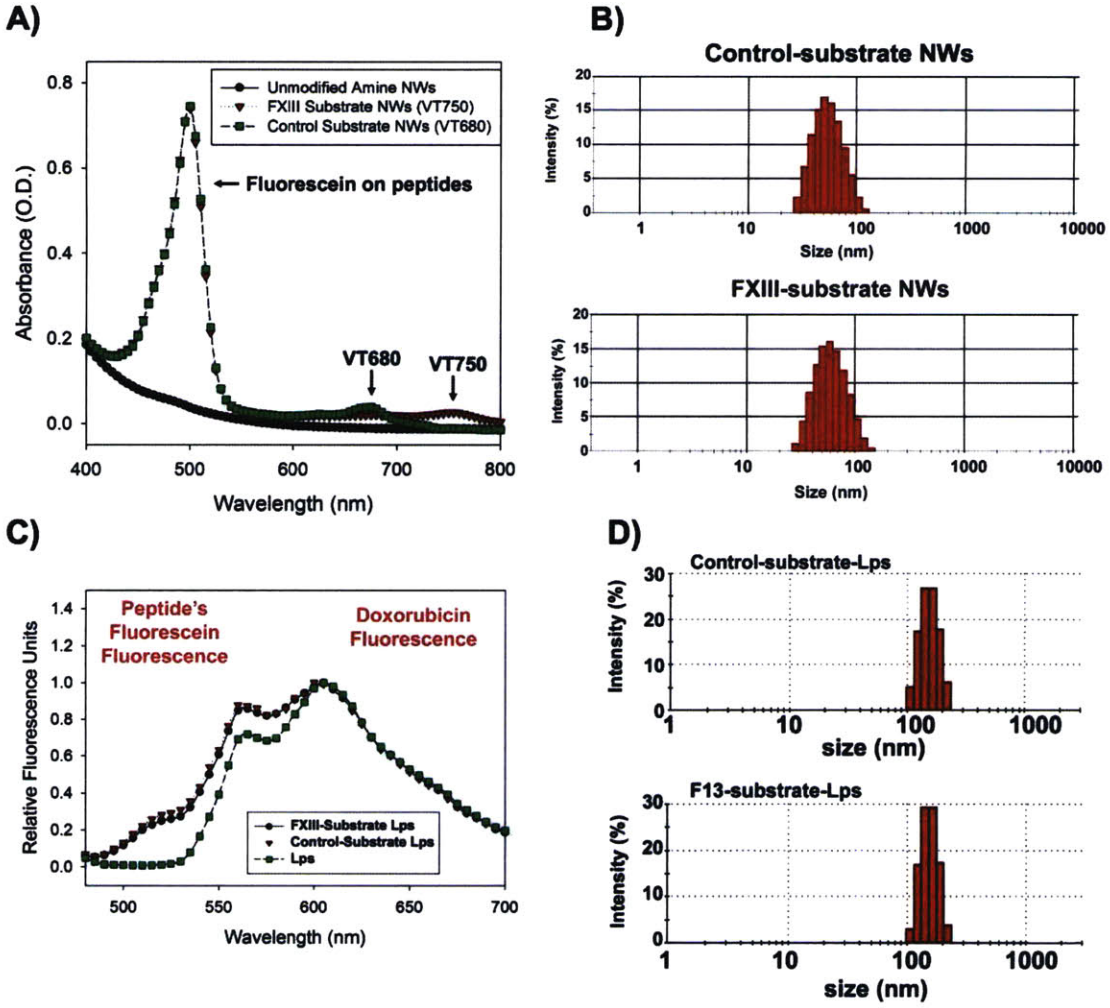

Figure 7.6. *Spectrophotometric, fluorescent, and size characterization of Receiving modules.* A) Spectrophotometric characterization of NW Receiving module functionalization. Aminated NWs were conjugated with NHS-activated NIR fluorochromes (VT680 or VT750) to allow fluorescent imaging and subsequently linked to thiol-containing FXIII-substrate peptides or control-peptides. The spectra NWs were utilized to quantify the number of peptides and NIR-fluorochromes per particle (~600 FXIII- or control-peptides/NW and ~12-15 fluorochromes/NW, respectively). Conjugation conditions were optimized to produce populations with approximately equal numbers of peptides in the FXIII-NWs and control-NWs. B) Dynamic light scattering characterization of FXIII-NW and control-NW Receiving modules. After peptide functionalization with NIR-fluorochromes and peptides, samples were analyzed via DLS to probe the hydrodynamic size of each conjugate. C) Fluorescent characterization of FXIII-Lps and control-Lps. The fluorescence emission spectra of Fluorescein-conataining FXIII- and control- peptides was utilized to ensure similar surface density on Lp conjugates (excitation: 444 nm; cutoff: 455 nm; emission 480 nm-700 nm). D) Dynamic light scattering characterization of FXIII-Lp and control-Lp Receiving modules. After peptide functionalization, Lp Receiving modules were analyzed via DLS to probe the hydrodynamic size of each conjugate.

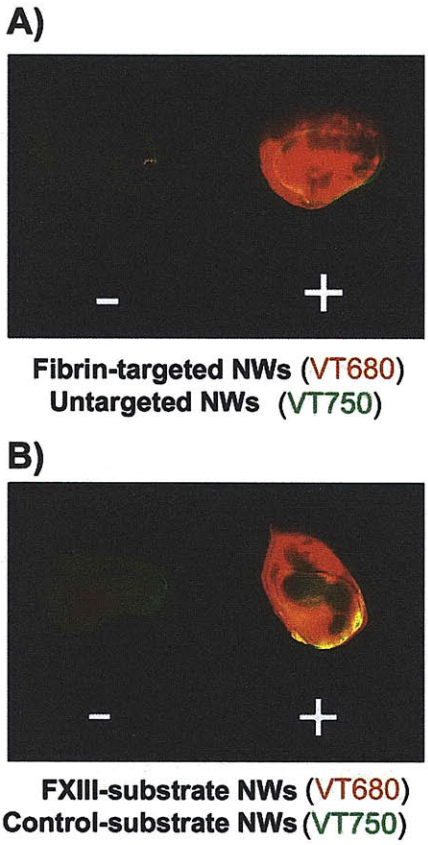

Figure 7.7. *Fluoresence reflectance imaging of Receiving module homing to externally-heated tumors.* Mixtures of targeted (red) and untargeted (green) NWs (labelled with the opposite orientation of NIR-fluorochromes used in Figure 2C to control against potential optical or molecular fluorochrome bias to Receiving module detection in heated vs unheated tumors) VT680 and VT750, respectively, were intravenously injected into mice bearing bilateral MDA-MB-435 tumors. Immediately following injection, one tumor was submerged in a temperature-controlled water bath for 20 min and mice were dissected at 24 hrs for fluorescent organ imaging. Overlaid fluorescence images are shown for targeted (green) and untargeted (red) Receiving module accumulation in both heated ("+", 45°C heating) and naïve ("-") tumors are shown from the same mouse.

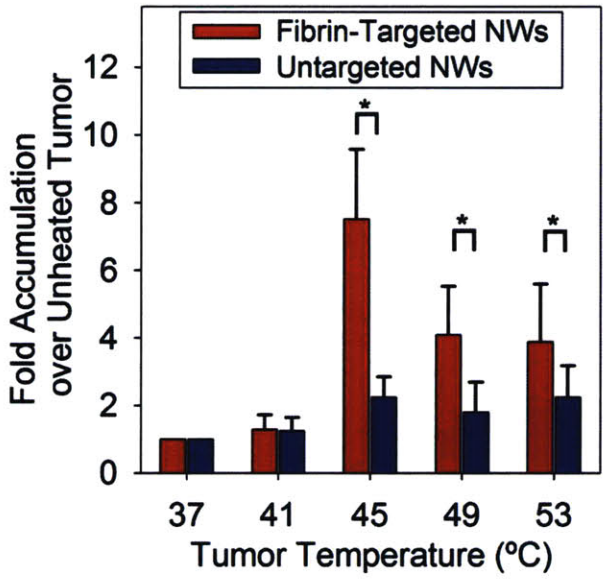

Figure 7.8. *Fluorescent quantification of fibrin-binding and untargeted-NW Receiving module homing to heated over unheated tumors.* The fold enhancement of NW targeting is plotted across the range of temperatures tested (n=4 mice in each set, $p<0.05$ for the difference between fibrin-binding-NWs and untargeted-NWs at 45°C, 49°C, and 53°C, respectively).

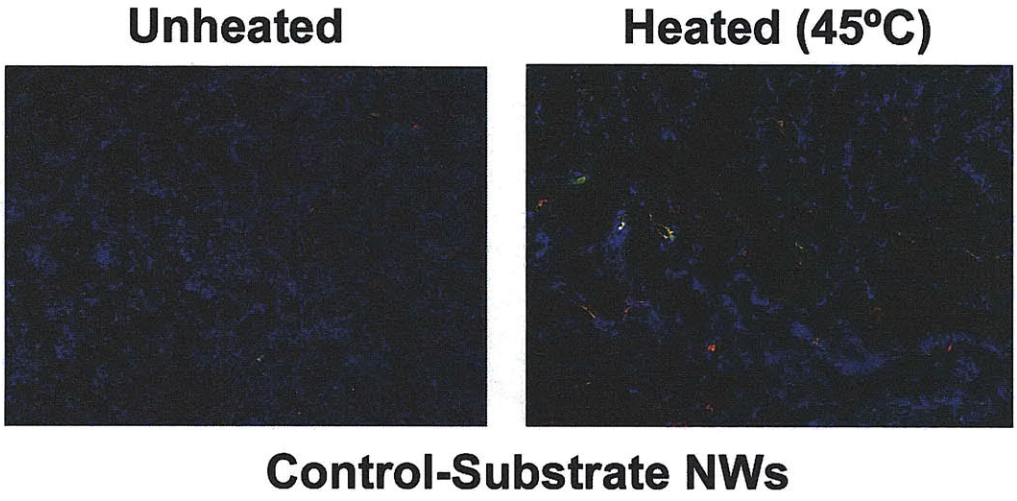

Figure 7.9. *Histopathological analysis of control-substrate NWs.* Mice bearing bilateral MDA-MB-435 tumors were injected with control-substrate NWs and one tumor was heated to 45°C for 20 min. At 24 hrs post-injection, mice were sacrificed and tumors were analyzed for NW distribution in histology using the same exposure conditions for NW imaging as Figure S8, S10, and Figure 2D. (Red=CD31 antibody stain, Blue= DAPI nuclear stain, Green=control-substrate NW distribution)

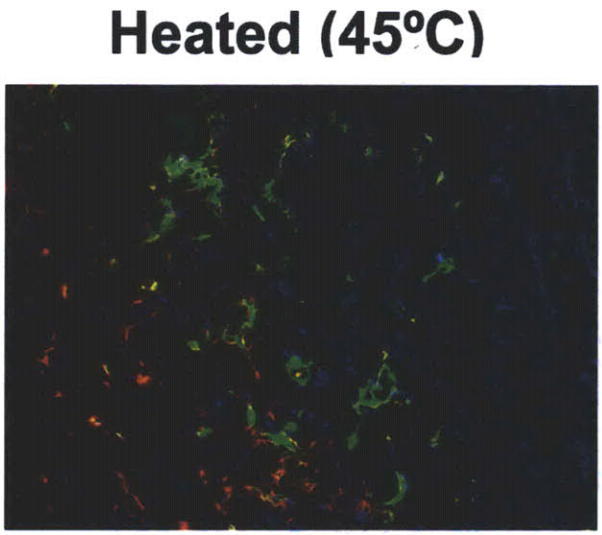

Figure 7.10. *Histopathological analysis of FXIII-substrate localization to areas of anti-fibrin(ogen) staining.* Mice bearing bilateral MDA-MB-435 tumors were injected with FXIII-substrate NWs and one tumor was heated to 45°C for 20 min. At 24 hrs post-injection, mice were sacrificed and tumors were analyzed for NW distribution in histology using the same exposure conditions for NW imaging as Figure S8, S9, and Figure 2D. (Red=anti-fibrin(ogen) antibody stain, Blue= DAPI nuclear stain, Green=FXIII-substrate NW distribution)

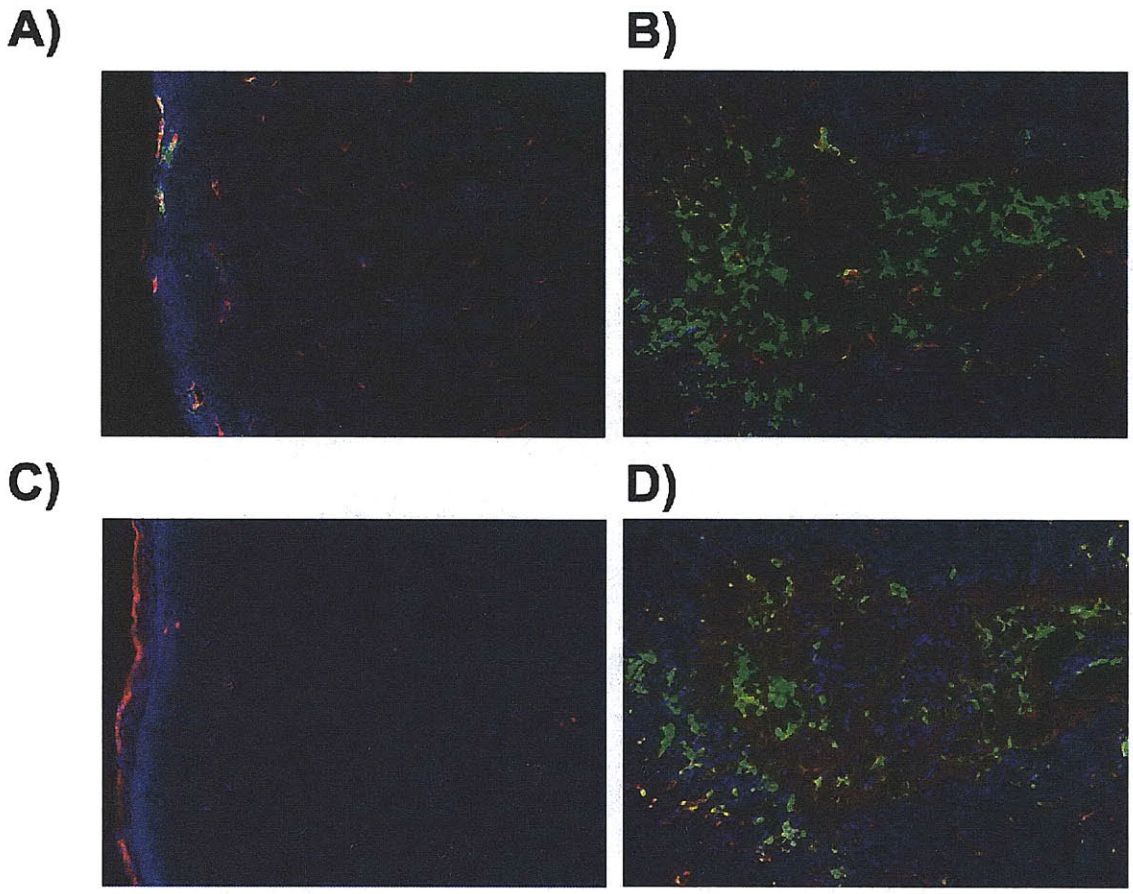

Figure 7.11. *Histopathological analysis of fibrin-targeted NWs in heated and unheated tumors.* Mice bearing bilateral MDA-MB-435 tumors were injected with fibrin-binding NWs and one tumor was heated to 45°C for 20 min. At 24 hrs post-injection, mice were sacrificed and tumors were analyzed for fibrin-NW distribution in histology. A) Distribution of fibrin-targeted NWs in unheated tumors. (Red=CD31 antibody stain, Blue= DAPI nuclear stain, Green=fibrin-targeted NW distribution) B) Co-localization of fibrin-targeted NWs with anti-fibrin(ogen) antibody staining in heated tumors. (Red=CD31 antibody stain, Blue= DAPI nuclear stain, Green=fibrin-targeted NW distribution)

compared to Control-NWs bearing peptides without the essential glutamine for FXIII cross-linking (**Figure 7.5C, 7.5D, 7.6**), enabling nearly an order of magnitude increase in tumor targeting compared to unheated tumors. The specificity of heat-induced targeting to coagulation persisted up to 53°C, although the magnitude of accumulation decreased (**Figure 7.5E**), likely indicating that higher temperatures accelerated intravascular coagulation and occlusion, diminishing the perfusion required for delivery of Receiving NWs into tumors. Histopathologically, FXIII-substrate NWs showed marked extravasation and interstitial spreading in heated tumors compared with controls (**Figure 7.5D, 7.9, 7.10**), illustrating the capacity of thermal energy to dismantle tumor vascular barriers and enable abundant interstitial penetration.

To explore a separate mechanism for targeting coagulation, NWs were separately derivatized with a fibrin-binding peptide (Ac-d-d-d-***G-Y-e-C-hyP-cY-G-L-C-Y-I-Q***-K-Fluorescein) (**Figure 2B**) and tested in a similar assay. Fibrin-binding Receiving NWs also exhibited nearly a 10-fold amplification of targeting to water-bath heated tumors (**Figure 2C, 7.7, 7.8**), with prominent extravascular accumulation histopathologically (**Figure 7.11**).

Therapeutic Receiving nanoparticles were constructed by modifying doxorubicin-loaded liposomes (Lps) with FXIII substrates(**Figure 7.6, 7.12**). Here, tumor heating to 45°C directed the accumulation of over 40-times higher doses of doxorubicin in tumors compared with unheated controls and significantly enhanced targeting over control substrate-modified Lps (**Figure 7.5F**).

After probing each component of the system independently, we studied the ability of the fully integrated signaling network to amplify tumor targeting *in vivo* (**Figure**

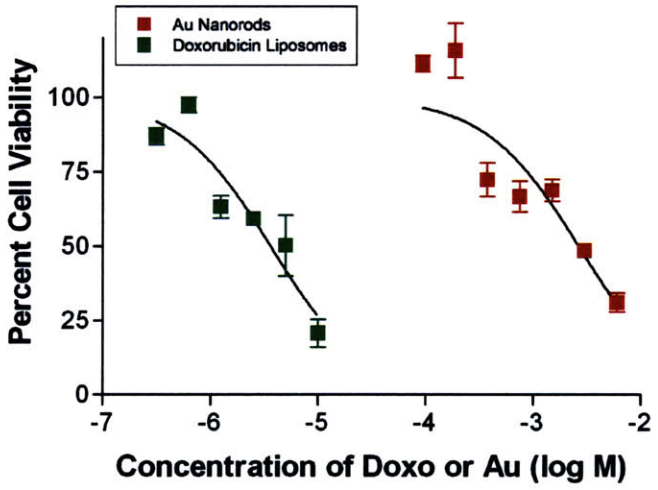

Figure 7.12. *Cytotoxicity experiments to assess intrinsic toxicity of Au nanorods and doxorobicin-loaded liposomes.* Cytotoxicity assessments were conducted using Human HeLa cervical cancer cultures (ATTC) in 96well plates grown to ~70% confluency. Cells were incubated with various dilutions of either PEG-NR or Lp formulations assessed for viability after 24hrs of incubation using the fluorogenic intracellular esterase sensor Calcein acetoxymethylester (each point represents the average of 4 wells in a 96-well plate).

7.13A). Signaling NRs (or saline) were intravenously-injected into mice bearing bilateral MDA-MB-435 tumors. After NR clearance from circulation (72 hrs), mixtures of active and inactive Receiving nanoparticles (FXIII-NWs and Control-NWs) labelled with distinct near-infrared fluorochromes were co-injected intravenously, followed by laser irradiation of the entire right flank of the mouse (~0.75 W/cm^2, 810 nm, 20 min) under infrared thermographic observation. At 96 hrs, the entire mouse and then the individual

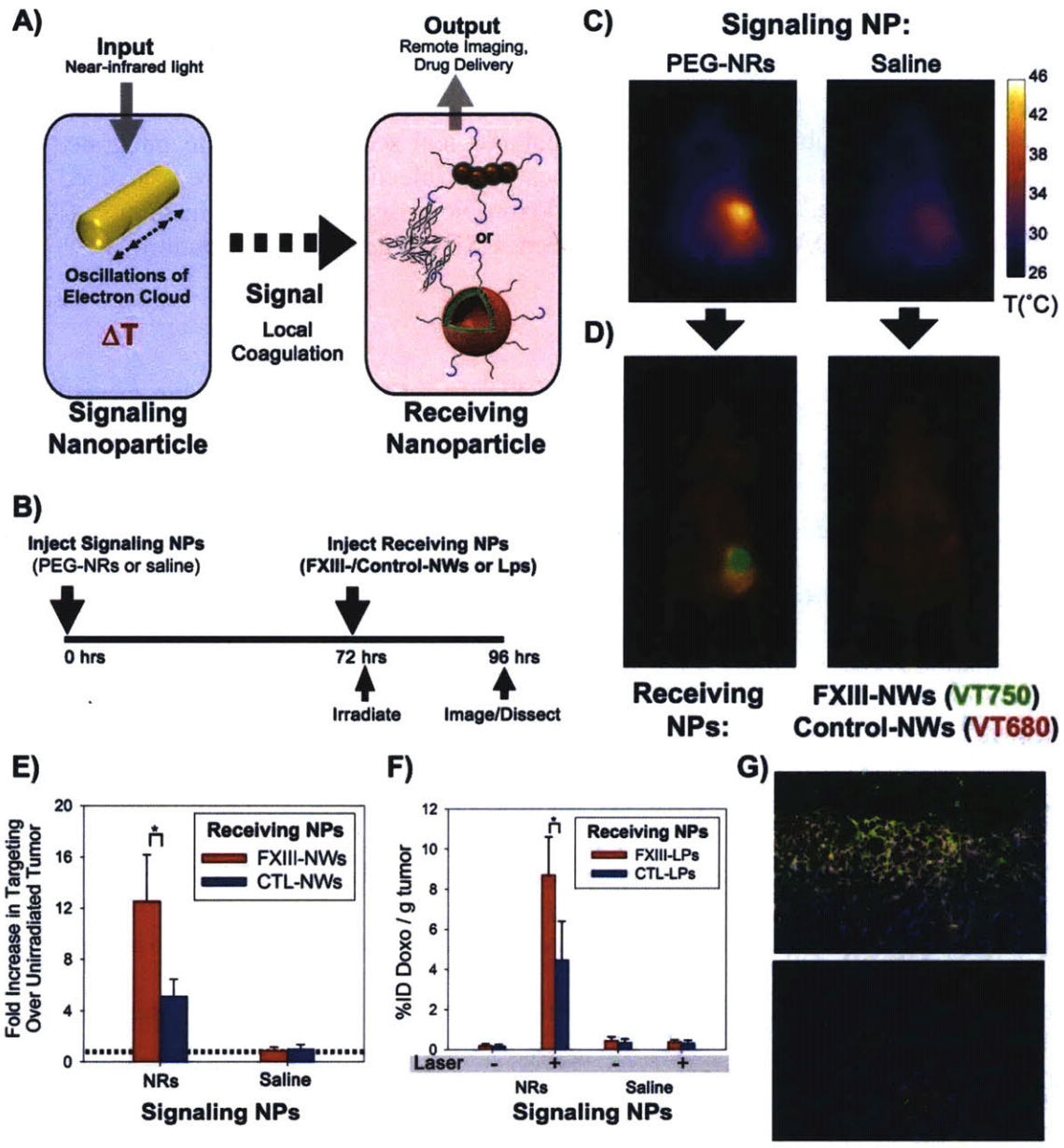

Figure 7.13. *Integrated function of nanoparticle signaling networks.* A) Schematic of integrated nanoparticle signaling networks. B) Experimental timeline for testing nanoparticle signaling networks. C) Thermographic imaging of photothermal PEG-nanorod heating. At 72 hrs post NR- or saline-injection (10 mg Au/kg), mice were co-injected with targeted (FXIII-NWs) and untargeted (Control-NWs) and their right flanks were broadly irradiated (810 nm, ~0.75 W/cm^2, 20 min) while under infrared thermographic surveillance. D) Overlaid fluorescence reflectance image of targeted and untargeted Receiving NP homing. At 24 hrs post-irradiation, whole-animal fluorescence imaging revealed the distributions of targeted (FXIII-NWs, green) and untargeted (Control-NWs, red) Receiving NPs. E) Quantification of NW Receiving NP homing in irradiated vs contralateral unirradiated tumors. After whole-animal imaging, mice were dissected and the fluorescence of each tumor was measured to quantify the homing of

Receiving NPs. F) Quantification of doxorubicin-loaded Lp Receiving NP homing in irradiated vs contralateral unirradiated tumors. After whole-animal imaging, mice were dissected and the fluorescence of each tumor was measured to quantify the homing of Receiving NPs. G) Histopathological analysis of NR-directed FXIII-Substrate Lp targeting and doxorubicin delivery. Histopathological sections from the integrated NP signaling experiments in F). At 24 hrs post-NW injection, mice were sacrificed and tumors were analyzed for FXIII-Lp and doxorubicin distributions in histology. (Red= doxorubicin, Blue= DAPI nuclear stain, Green=FXIII-targeted Lp distribution).

explanted organs were fluorescently imaged (**Figure 7.13B**). Thermographic surveillance of photothermal heating showed focal tumor heating only in NR-injected mice (**Figure 7.13C**) and whole-animal imaging at 96 hrs revealed pronounced homing of FXIII-targeted NWs to NR-heated tumors, with over an order of magnitude increase in accumulation above both unirradiated contralateral tumors and tumors on saline-injected mice (**Figure 7.13D, 7.13E, 7.14**). Histologically, integrated signaling networks produced intense regions of FXIII-NW fluorescence relative to controls, particularly in tumor boundaries where blood vessels were well perfused (**Figure 7.15**). Nanoparticle signaling networks were found to be effective in xenograft cervical tumor models as well, directing several fold amplification in homing of targeted Receiving nanoparticles over untargeted controls (**Figure 7.16**).

When therapeutic FXIII-targeted Receiving liposomes (Lps) were incorporated into the integrated system, the accumulation of doxorubicin in tumors was amplified by over 40-fold (~8% ID/g) as compared to the Lps alone (**Figure 7.13E**). This amplification of drug delivery likely has at least two components: heat-dependent increases in passive accumulation due to improved tumor transport (as indicated by control-Lps and

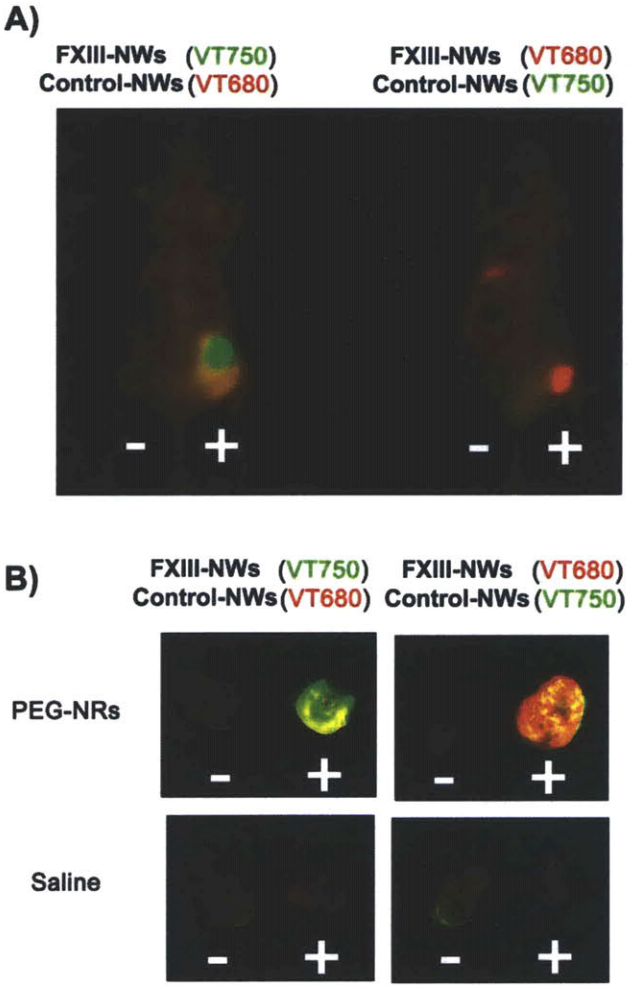

Figure 7.14. *Active NP signaling network experiments from Figure 3D, but with inverted fluorophore-targeting ligand relationships to control against bias and ex-vivo imaging of excised tumors.* A) Simultaneous near-infrared imaging of co-injected: VT750-labeled, FXIII-substrate-NWs (green, left mouse) and VT680-labeled, control-substrate NWs (red, left mouse); or VT680-labeled, FXIII-NW (red, right mouse) and VT750-labeled, control-substrate NWs (green, right mouse). Inversion of fluorochrome-NW relationships prevents optical or molecular bias from fluorophores in homing visualization. + indicates broad laser irradiation (810 nm, 0.75 W/cm^2, 20 min). B) Imaging of NW homing in excised tumors from experiments in Figures 3D and S12A. Each box was imaged using the same acquisition parameters for both VT750 (green) and VT680 (red) and contains the left and right tumors from MDA-MB-435-bearing mice.

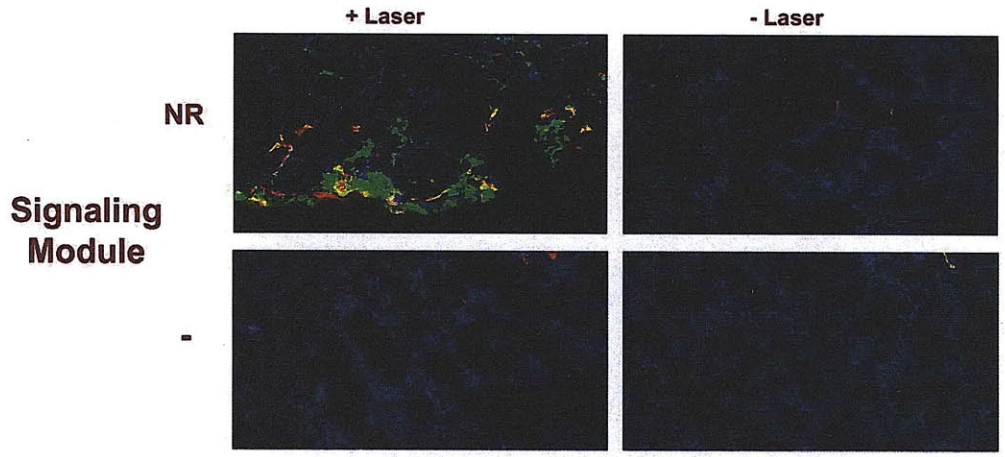

Figure 7.15. *Histopathological analysis of FXIII-targeted NWs with integrated and disconnected NP signaling networks.* Histopathological sections from the integrated NP signaling experiments in Figures 3C, 3D, 3E and S12. At 24 hrs post-NW injection, mice were sacrificed and tumors were analyzed for FXIII-NW distribution in histology. (Red=CD31 antibody stain, Blue= DAPI nuclear stain, Green=FXIII-targeted NW distribution).

consistent with previous observations (*105*) and specific biochemical recognition of the coagulation process by the peptide coating. (**Figure 7.13F**) Histologically, FXIII-Lps formed a broad interstitial mesh in NR-heated tumors, with released doxorubicin fluorescence emanating from the nuclei of surrounded tumor cells (**Figure 7.13G**).

The efficacy of therapeutic nanoparticle signaling networks was evaluated in mice bearing single MDA-MB-435 human carcinoma tumors. PEG-NRs (10 mg/kg) or saline were injected into mice and, once NRs had cleared from circulation (72 hrs), we administered a single intravenous dose of FXIII-substrate-Lps, Control-substrate-Lps, or saline (2 mg/kg doxorubicin), followed immediately by irradiation with near-infrared light (~0.75 W/cm^2, 810 nm, 20 min). We found that the integrated system significantly-

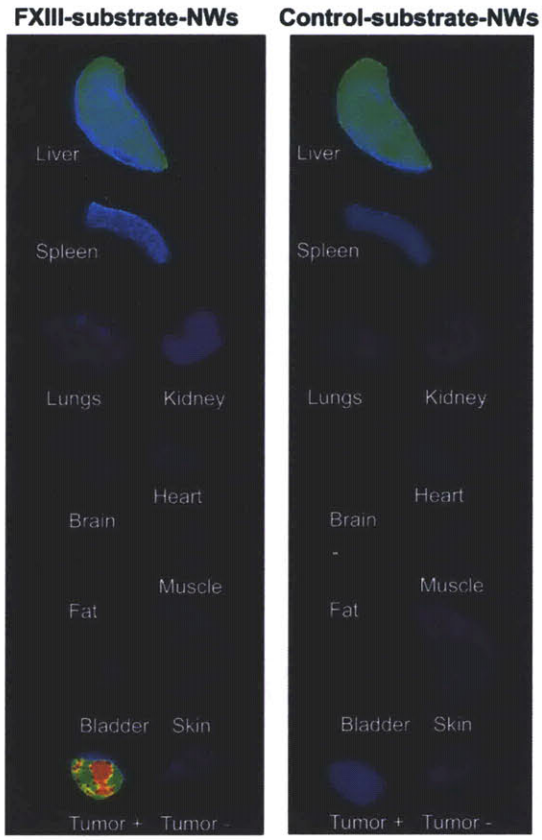

Figure 7.16. *Portability of NP signaling networks across xenograft tumor types.* Athymic (*nu/nu*) mice bearing bilateral Hela human cervical cancer tumors were injected with PEG-NRs and, 72 hrs later, a mixture of FXIII-substrate-NWs and control-substrate-NWs, labelled with unique NIR-fluorophores, as described for MDA-MB-435 tumor-bearing mice in Figure 3. Immediately following injection of NW mixtures, the right flanks of mice were broadly irradiated with a diode laser source. At 24 hrs post-injection, the homing of FXIII-NWs and control-NWs was visualized using NIR fluorescent organ imaging. ("Tumor +" indicates the irradiated tumor; "Tumor –" was not exposed to diode irradiation)

enhanced tumor therapy, directing a prolonged inhibition in tumor growth compared with its isolated components (FXIII-Lps, Control-Lps, NRs) and control systems (NRs +Control-Lps) (**Figure 7.17A, 7.17B)** ($P<0.02$ for NR + FXIII-Lps compared to all other treatment groups at each day from 5-24 after treatment; one-sided t-test) without detectable weight loss due to systemic toxicity (**Figure 7.18)**.

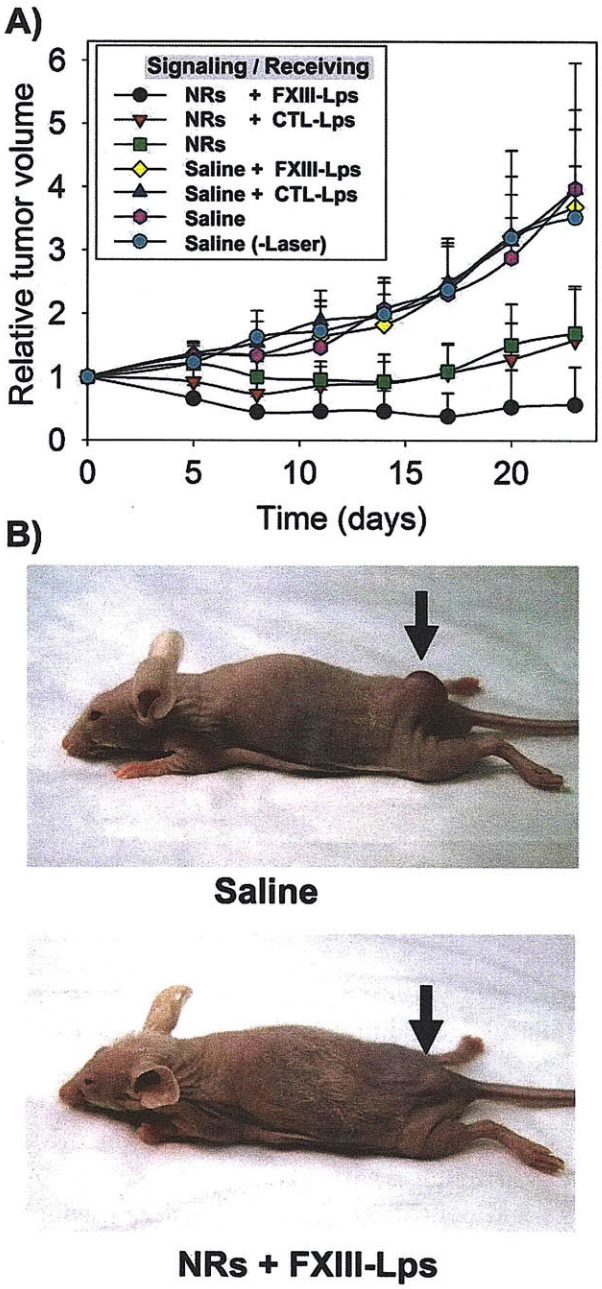

Figure 7.17. *Tumor therapy using nanoparticle signaling networks.* A) Tumor volumes for active NP signaling networks and controls. Tumors in all treatment groups except Saline (-laser) were exposed to near-infrared irradiation for 20 min (~0.75 W/cm^2, ~810 nm) ($P<0.02$ for NR + FXIII-Lps and all other treatment sets between days 5 and 24; one-sided t-test, n=6 or 7 mice in each set). B) Representative images of active signaling network treatment results (NRs + FXIII-Lps, below) compared with untreated controls (Saline, above) (20 days post-treatment).

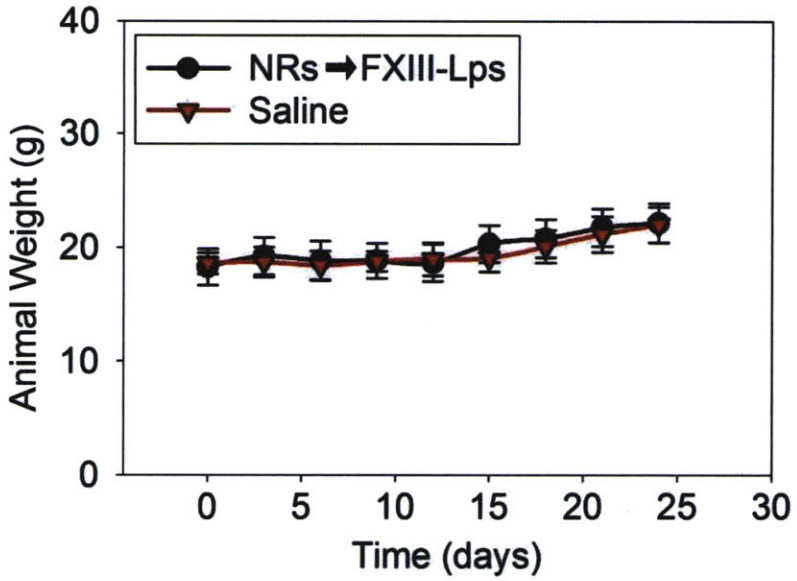

Figure 7.18. *Animal weights for mice treated with therapeutic signaling networks compared with those administered saline only.*

7.3 Conclusions:

This chapter describes the design, construction, and testing of a nanoparticle signaling network that amplifies the delivery of imaging or therapeutic agents to tumors. The network architecture incorporates two synthetic components that co-opt a biological cascade to transduce a physical signal (local heating) into a spatially-localized, amplified biochemical signal (fibrin/FXIII activity). Given the generality of vessel damage-induced coagulation across tumor types and organisms, this framework provides a robust platform on which to further customize the signal generation by molecular targeting of the Signaling nanoparticles to other tissue or disease types. In addition, strategies to locally activate the clotting cascade without an external trigger have the potential to produce a fully autonomous system (*317*). In contrast to the current paradigm of engineering complex nanoparticle functions into a population of near-identical components, we

believe the strategy of building interactive, higher-order nanosystems with emergent, system-scale properties provides new avenues for developing next-generation diagnostics and therapeutics.

7.4 Materials and Methods:

PEG-NR Signaling Module Synthesis. PEG-NRs were synthesized as described previously (von Maltzahn et al., Cancer Research (In Review)). Briefly, highly stable, ~13 nm x 47 nm (Figure 1A) CTAB-coated gold nanorods with longitudinal plasmon resonance at 810 nm (Nanopartz, a division of Concurrent Analytical Inc., Salt Lake City, UT) coated in 250 μM 5 kDa methyl-PEG-thiol (Laysan Bio, U.S., Arab, AL). The solution of 5 kDa methyl-PEG-thiol and CTAB-coated gold nanorods was gently mixed at room temperature for 1 hr and dialyzed exhaustively against ultrapure water (18 MΩ cm^{-1}) via cellulose ester membrane dialysis (Spectrapor, Rancho Dominguez, CA) to drive PEG addition. Dialyzed samples were filtered through 100 kDa filters (Millipore, Billerica, MA) to remove excess polymer and stored at 4˚C.

Fibrinogen deposition in heated tumors. Bovine fibrinogen (Sigma) and albumin (Sigma) were reacted with near-infrared fluorochromes (VT750-NHS or VT680-NHS) at a 2:1 fluorophore: protein molar ratio in PBS for ~2 hrs and dialyzed extensively at 4˚C against PBS to remove unreacted fluorophores. The product of the dialysis was passed through a 0.1μm filter, quantified using a BCA protein assay (Pierce), and assessed for fluorophore labelling via the absorption at the peak fluorphore absorbance (λ_{max}=750 and 680 nm, respectively, for VT750 and VT680). This reaction generated fibrinogen and albumin protein stocks carrying ~1 fluorophore/protein. To assess whether fibrinogen and albumin

home to heated tumors, ~1 nanomole of both proteins (bearing distinct NIR-fluorophores) was injected intravenously into mice bearing bi-lateral MDA-MB-435 carcinoma tumors. Immediately following injection, one tumor on each mouse was externally heated using a temperature-controlled water bath set to between 41-53˚C for 20 min. At 24 hrs post-injection, mice were dissected and both tumors fluorescently imaged for the relative abundance of fibrinogen and albumin (LI-COR Odyssey Infrared Imaging System). To ensure that fluorophores did not optically or molecularly skew homing results, all fluorescent experiments were performed with equal numbers of mice allocated to VT750-fibrinogen/VT680-ablumin and VT680-fibrinogen/VT750-albumin administration at each temperature tested. Increases in protein tropism to heated tumors were analyzed by combining the fold increase in targeting observed for both fluorophore orientations (n=4 mice at each temperature tested).

Photothermal heating of passively-targeted nanorod Signaling modules in vivo. Nude mice were injected subcutaneously in the hind flank with ~$2x10^6$ MDA-MB-435 cells. After 2-3 weeks animals were anaesthetized with isoflurane and injected through the tail vein with PEG-NRs in 0.15 M NaCl, 0.1 M Na Phosphate buffer, pH 7.2 (10 mg Au/kg, ~150ul bolus). All photothermal heating of NRs was conducted at 72 hrs post administration (a time point after which they had completely cleared circulation) under the guidance of infrared thermography to continually illuminate the surface temperature of irradiated regions (FLIR Thermacam S60). A custom diode laser (RPMC Lasers Inc, 810nm, 30 W) was utilized to broadly irradiate the right flank of tumor-bearing mice at ~0.75 W/cm^2 and ~1 W/cm^2 to maintain desired peak tumor temperatures in NR-injected

mice (~46°C for initial fibrinogen-homing experiments and integrated signaling network implementation; 20 min exposure).

Immunohistochemical analysis in tumors. For histologic analysis, frozen sections of tumors were prepared. The sections were first fixed with acetone. Rat anti-mouse CD-31 (1:50, BD PharMingen) and biotinylated mouse fibrin(ogen) antiserum (1:50, Nordic) were used for immunochemical staining of tumor tissue sections. The corresponding secondary antibodies were added and incubated for 1 hour at room temperature: AlexaFluor-594 goat anti-rat or rabbit IgG (1:1,000; Molecular Probes), streptavidin Alexa Fluor 594 (1:1000; Molecular Probes). The slides were washed three times with PBS and mounted in Vectashield Mounting Medium with DAPI. At least three images from representative microscopic fields were analyzed for each tumor sample.

Peptide Synthesis. The three peptides used in this work: a fibrin-binding peptide (Ac-d-d-d-***G-Y-e-C-hyP-cY-G-L-C-Y-I-Q***-K-(K-Fluorescein)) (binding sequence in bold), a peptide substrate for the transglutaminase Factor XIII (G-N-***Q***-E-Q-V-S-P-L-T-L-L-K-X-C-(K-Fluorescein)) (active glutamine in bold; X=6-aminohexanoic acid linker), and a control substrate for FXIII (G-N-***A***-E-Q-V-S-P-L-T-L-L-K-X-C-(K-Fluorescein)) (single amino acid substitution in bold) were synthesized via standard FMOC solid-phase peptide synthesis (MIT Biopolymers Core or Tufts University Core Facility). Products were HPLC-purified to >90% purity and characterized via mass spectrometry. Fibrin-binding peptides were cyclized by bubbling air into 10 μM aqueous peptide solutions overnight, followed by lyophilization for subsequent use.

Receiving Module NP Syntheses. Superparamagnetic, dextran-caged iron oxide nanoworms (NWs) with a longitudinal size of ~55 nm were synthesized, aminated using 20% v/v ammonium hydroxide, and derivatized with near-infrared fluorophores as described previously[27]. Fibrin-binding peptides were attached to NWs via their exogenous lysine by first reacting fluorophore-labelled NWs with the bifunctional linker NHS-PEO_5-NHS (Pierce) in phosphate buffered saline pH 7.2 (PBS) at a 5000:1 linker:NW molar ratio to prevent cross-linking. Following activation with linker, NWs were filtered using a gel filtration column (G50 media) and incubated overnight with cyclized fibrin-binding peptides at ~1000:1 peptide:NW ratio with shaking. After ~12 hrs, NWs were purified from extra peptides by repeated filtration on centrifugal membrane filters (100 kDa size cutoff, Centricon, Millipore) and finally dispersed in PBS for spectrophotometric analysis of peptide labelling. Factor XIII-substrates were attached to NWs via their exogenous cysteine similarly, but with the linker NHS-PEO_{12}-Maleimide (Pierce) in place of the bifunctional NHS-PEO_5-NHS linker. All peptide-functionalized NWs were characterized via dynamic light scattering (DLS) and intravenously injected *in vivo* to ensure targeted NWs and control NWs exhibited similar circulation times.

Doxorubicin-loaded liposome synthesis. Hydrogenated soy sn-glycero-3-phosphocholine (HSPC), cholesterol, and 1,2-distearoyl-snglycero-3-phosphoethanolamine-N-polyethylene glycol 2000 [DSPE-PEG(2k)], 1,2-Distearoyl-sn-Glycero-3-Phosphoethanolamine-N-[Maleimide(Polyethylene Glycol 2000)] [DSPE-PEG(2k)-MAL] were purchased from Avanti Polar Lipids (Alabaster, AL). Doxorubicin was purchased from Sigma Chemical Co. (St.Louis, MO). For peptide conjugation, liposomes

with maleimide groups were prepared from HSPC, cholesterol, DSPE-PEG(2k), and DSPE-PEG(2k)-MAL in the molar ratio of 75:50:3:3 by lipid film hydration and membrane (100 nm) extrusion method(*318*). Encapsulation of doxorubicin (DOX) into the liposomes was then carried out using the pH gradient-driven loading protocol(*319*). Free doxorubicin was removed by gel filtration on Sephadex G-50. After doxorubicin loading, the maleimide-terminated liposomes were reacted with thiols on peptides (FXIII and control) for 2 hrs and then purified by by gel filtration on Sephadex G-50. The peptide-conjugated doxorubicin liposomes were stored in PBS at 4 °C before use.

In vitro cytotoxicity: Cytotoxicity assessments were conducted by the MIT Nanomaterials Toxicity Core using Human HeLa cervical cancer cultures (ATTC) in 96-well plates grown to ~70% confluency. Cells were incubated in quadruplicate with various dilutions of either PEG-NR or Lp formulations assessed for viability after 24hrs of incubation using the fluorogenic intracellular esterase sensor Calcein acetoxymethylester (Invitrogen).

Quantifying NW homing to tumors. Mixtures of NIR-fluorophore-labelled, targeted and control NWs (bearing VT750 and VT680 or VT680 and VT750, respectively) were co-adminstered intravenously in PBS (2 mg Fe/kg) to tumor-bearing nu/nu mice as described in the Results and Discussion to provide an internal control reference for coagulation-specific NW homing. At 24 hrs post-NW injection, mice were sacrificed and organs were analyzed for both NIR-fluorophores (LI-COR Odyssey Infrared Imaging System). For integrated signaling network characterization, mice were additionally imaged under isofluorane anaesthetic before euthanization using a whole animal fluorescence

reflectance imaging system (Xenogen, IVIS Imaging System) to visualize the specificity of NW homing to tumors. Images from both organ scanning and whole animal imaging are displayed as overlaid fluorescent images from both channels (VT750=green and VT680=red). As with fibrinogen/albumin characterization earlier, all experiments were conducted with VT750-labeled targeted particles alongside VT680-labeled control particles and with VT680-labelled targeted particles alongside VT750-labeled control particles to ensure that fluorophore bias did not perturb results. For initial Receiving module characterization, levels of targeted and control NW homing were plotted by comparing the average NW fluorescence in heated tumors versus unheated tumors (n=4 mice at each temperature). For integrated network evaluation, levels were plotted by comparing the average targeted and untargeted NW fluorescence in irradiated tumors versus un-irradiated tumors (n=4 mice for all conditions).

Quantification of doxorubicin in tissues. MDA-MB-435 xenografts were established in nu/nu mice and administered with FXIII-substrate or control-substrate Lps as described in the Results and Discussion. At 24 hrs post-irradiation or external heating, doxorubicin in tissues was fluorescently quantified in organ homogenates. Briefly, organs were removed, weighed, incubated with 500 μl of 70% EtOH, 0.3 N HCl, and homogenized (Tissue Tearor, Biospec Products) to release doxorubicin from tissues. Following homogenization, another 1 ml of 70% EtOH, 0.3 N HCl, was added to samples and they were centrifuged. Supernatants of samples were analyzed for doxorubicin fluorescence using a fluorescence microplate reader (Molecular Devices, SpectraMax GeminiEM) and compared to standard curves.

Therapeutic assessment of nanoparticle signaling networks. Therapeutic studies were conducted by first intravenously administering PEG-NRs or saline into nu/nu mice bearing a single MDA-MB-435 tumor. At 72 hrs post-injection, mice were intravenously administered FXIII-substrate Lps, control-substrate Lps, or saline (in ~150 μl bolus) and broadly irradiated in the vicinity of the tumor with NIR light to supply the input to the inter-nanoparticle signaling network (810 nm, ~1 W/cm^2, 20 min). An additional cohort of mice was administered saline at 0 and 72 hrs and not exposed to NIR light in order to isolate any therapeutic efficacy of this input in isolation. Each therapeutic cohort included 7 mice, except for the unirradiated saline-only control, which had 6 mice. At regular intervals after treatment, tumors were measured and mice were weighed. Mice were sacrificed when tumors exceeded 500 mm^3.

Chapter 8: Autonomous Signaling Networks for Amplified Nanoparticle Tumor Targeting *In Vivo*

8.1 Introduction:

Technologies with the ability to precisely and abundantly target imaging agents and therapeutics to regions of neoplastic disease could have a dramatic impact on cancer therapy(*22*). Rapid progress in cancer nanotechnology has generated a diverse ensemble of nanomaterials with unique electromagnetic and therapeutic properties(*17, 22, 32, 308*). However, our capacity to home these devices to tumors remains very limited. Over the past three decades, targeted nanomaterials have been predominantly been developed as single-component formulations, wherein specificity to regions of disease is conferred via carrier size and shape or via surface display of various ligand types, including antibodies, peptides, aptamers, and small molecules(*142, 145, 169, 172*).

Evolution has produced more complex targeting strategies that couple the specificity of molecular interactions with potent signaling and amplification mechanisms to enable precise *and* abundant targeting to regions of nascent injury or infection. Blood coagulation, for example, utilizes parallel inter-component communication to sense injuries, amplify initial signals, and orchestrate the deposition of a new tissue. Synthetic biology aims to capture such higher-order biological behaviours and has already produced artificial biosensors, metabolic processes, molecular automata, and genetic circuits(*320, 321*). At the confluence of nanotechnology and synthetic biology lies the potential to build hybrid systems that leverage the strengths of each field (eg. unique

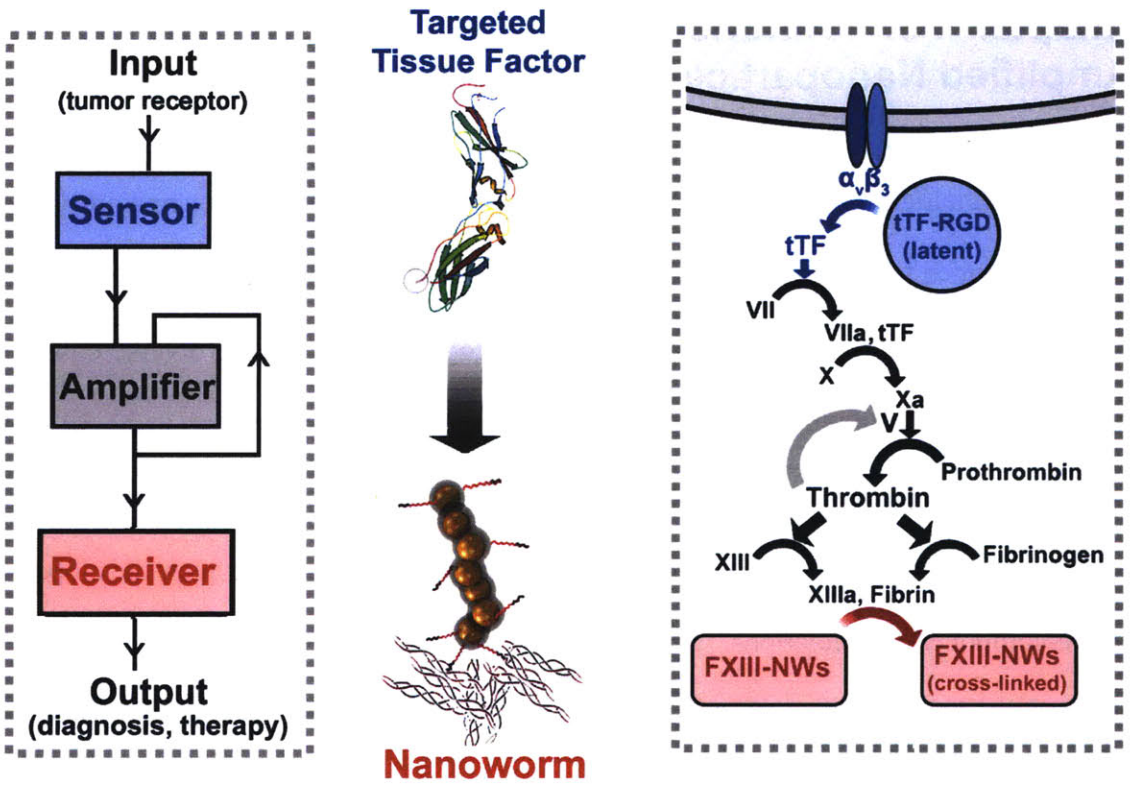

Schematic 8.1. *Signaling network architecture and information flow*. Structure and information flow in signaling networks. Sensors are ligand-targeted, truncated human tissue factor proteins (tTF) proteins that are latent in circulation, but gain coagulation-inducing activity upon binding to target receptors in tumor blood vessels (αvβ3 and CD13/aminopeptidase N for tTF-RGD and tTF-NGR Sensors, respectively). Signaling networks exploit the hardware of the extrinsic coagulation pathway to locally amplify and transmit Sensor output to FXIII-sensing Receiver nanoparticles.

electromagnetic/therapeutic properties vs signal processing/self-replication) to more effectively solve biomedical problems.

Here, inspired by natural signaling mechanisms, we construct autonomous, hybrid biological/nanotechnological signaling networks for amplifying nanoparticle tumor targeting. We sought to build upon the nanoparticle signaling networks in Chapter 7 by constructing a system that functions independently of any exogenous electromagnetic inputs and, therefore, would have the potential to systemically survey host vessels for

tumor processes. Our hybrid network is comprised of two synthetic components that harness the extrinsic coagulation cascade to communicate: tumor-homing truncated human tissue factor (TF) 'Sensors' and coagulation-targeted, magneto-fluorescent 'Receiver' nanoworms (NW) (**Schematic 1**).

To engineer an autonomous signaling network, we utilized a synthetic biological Sensor module that could function as a switch by initiating coagulation signaling in response to molecular interactions in tumor blood vessels. Tissue factor is expressed ubiquitously outside of the vasculature and is the dominant initiating factor for the coagulation cascade. When the extracellular domain of TF is truncated (tTF) and expressed as a soluble protein, its activity towards factor X activation diminishes by 5 orders of magnitude due to separation from cell surface phosphatidylserine co-factors(*322*). This cell surface requirement for TF activity allows synthetic ligand-targeted tTF constructs to specify TF activity to receptors in tumor vessels, where endothelial cell surfaces display increased phosphatidylserine(*323, 324*). Previously Mesters, Berdel and coworkers demonstrated that synthetic tTF proteins expressing the ligands RGD- and NGR- (which target $\alpha_v\beta_3$ and CD13/aminopeptidase N, respectively) provide receptor-specific tumor coagulation in mouse models and, very recently, that synthetic tTF-NGR constructs were well tolerated and diminished tumor perfusion in terminal cancer patients(*323, 324*) (*Blood*, in press). Here, we utilize ligand-targeted synthetic tTF constructs as Sensors to survey host vasculature for receptors associated with angiogenesis and, upon binding, engage the extrinsic coagulation cascade as a signal amplifier to recruit coagulation-targeted Receiver nanoparticles (**Schematic 1**).

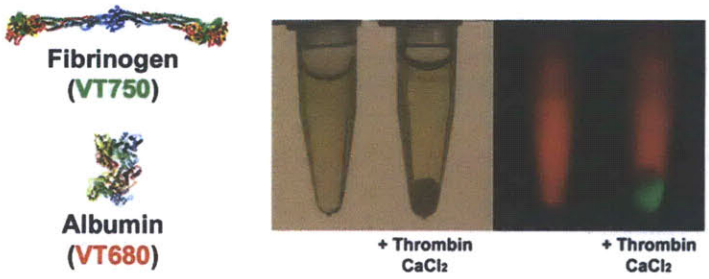

Figure 8.1. *Characterizing fluorophore-labeled fibrinogen and albumin as coagulation-specific and non-specific probes*. Fibrinogen and albumin proteins were labeled with unique near-infrared fluorochromes (VT750 and VT680, respectively) and mixed together into vials of human plasma. Upon addition of thrombin and $CaCl_2$, fibrinogen (green) was rapidly sequestered into the fibrin plug, while albumin fluorescence (red) remained dispersed.

8.2 Results and Discussion:

We initially characterized the function of Sensor and Receiver modules independently. To remotely visualize coagulation-specific and non-specific protein tropism to tumors in response to Sensor administration, we labeled fibrinogen (the precursor for fibrin polymers in coagulation) and albumin (a common serum protein unrelated to coagulation) with unique near-infrared (NIR) fluorophores (VT750 and VT680) (**Figure 8.1**). Purified fluorescent conjugates were co-injected (~1 nanomole each, ~1 fluorophore/protein) alongside varying amounts of targeted (tTF-RGD or tTF-NGR) Sensors into *nu/nu* mice bearing single MDA-MB-435 breast xenograft tumors. At 24 hrs post-injection, Sensor-injected mice harboured tumors with a distinct hemmorhagic appearance (**Figure 8.2**). Fluorescent fibrinogen was found to accumulate within vessel-like tumor structures in Sensor-injected mice, without accompanying albumin accumulation. Such fibrinogen accumulation was not observed in control organs

of Sensor-injected mice and was not significantly evoked by untargeted tTF constructs, even at high doses (**Figure 8.3A, 8.4A**). Histopathologically, fibrinogen deposition in tumors of Sensor-injected mice formed broad intravascular networks (**Figure 8.3B, 8.4B**), illustrating the potential for targeted tTF Sensors to orchestrate intravascular recruitment of circulating agents to tumor vessels.

Receiver nanoworms were synthesized as described previously(*32*) and derivatized with near-infrared (NIR) fluorophores for optical imaging (**Figure 8.3C**). Receivers were designed to attach to regions of coagulation by harnessing the activity of the coagulation transglutaminase Factor XIII. Factor XIII-specific (G-N-***Q***-E-Q-V-S-P-L-T-L-L-K-X-C-Fluorescein) or control (Control) (G-N-***A***-E-Q-V-S-P-L-T-L-L-K-X-C-Fluorescein) peptides, where the single substitution of an alanine for the integrated glutamine nearly abolishes FXIII activity for the Control peptide, were linked to NWs to create FXIII- and Control- Receivers (**Figure 8.5**)(*315*). To probe for coagulation targeting, human plasma clots were formed in the presence of FXIII- or Control-NWs. We found that FXIII-substrate NWs strongly concentrated in human plasma clots *in vitro,* while Control-substrate NWs did not (**Figure 8.3D**).

We next explored the ability of tTF-RGD Sensors to amplify FXIII-NW homing following their simultaneous intravenous injection into *nu/nu* mice bearing MDA-MB-435 tumor xenografts. Integrated signaling networks (tTF-RGD + FXIII-NWs) were compared to control networks (tTF-RGD + Control-NWs), FXIII-NWs in isolation, and to the homing capacity of NW populations bearing RGD targeting ligands. At 24 hrs

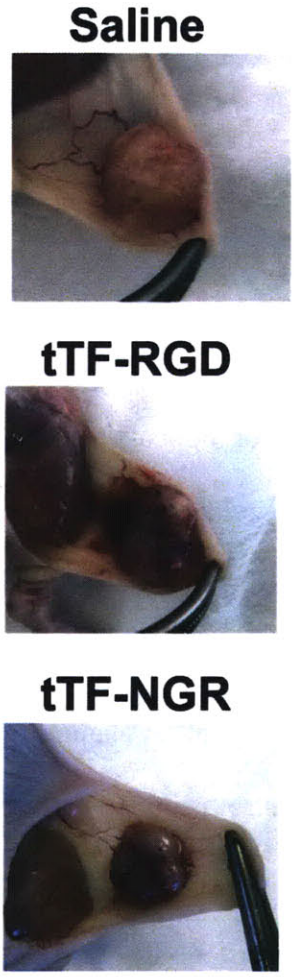

Figure 8.2. *Intraoperative images at 24-hrs post-Sensor injection. Nu/nu* mice bearing a single MDA-MB-435 tumor were intravenously injected with saline, tTF-RGD, or tTF-NGR (1 mg of tTF-RGD or tTF-NGR/kg) and dissected 24 hrs later. Administration of both Sensors led to the macroscopic appearance of tumoral hemorrhage and RBC stasis, while saline-injected mice harbored ivory-hued tumors.

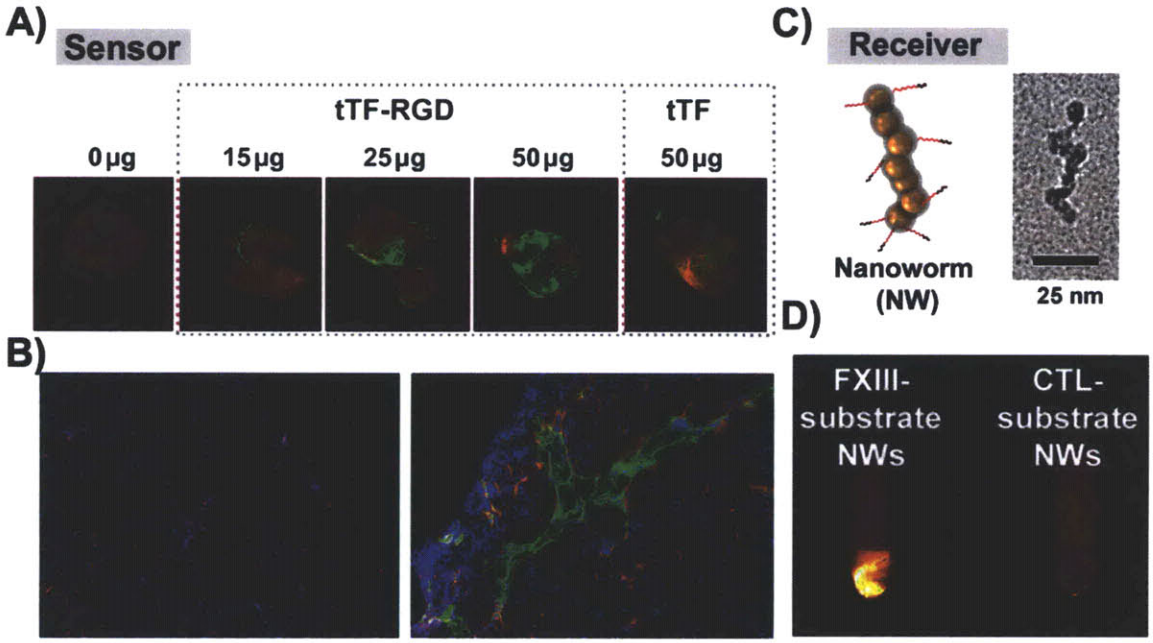

Figure 8.3 *Signaling network component characterization* A) Sensor characterization. tTF-RGD Sensors were injected intravenously at varying doses alongside mixtures of fluorescent fibrinogen (green, VT750) and albumin (red, VT680) (~1 nmole of each protein) to monitor for Sensor-mediated fibrinogen deposition in tumors. Untargeted tTF proteins were similarly injected at the highest dose used with targeted Sensors. B) Histopathologic analysis of tumor fibrinogen distribution without (left panel) and with Sensor co-injection (right panel) (Red = CD31 blood vessel stain; Green = injected fibrinogen fluorescence; Blue = nuclear stain) C) Model Receiver nanoparticles were synthesized by tethering FXIII peptide substrates to fluorescent, polymer-caged iron oxide nanoworms (NWs). D) Fluorescent FXIII- (GN*Q*EQVSPLTLLK) and Control-substrate (GN*A*EQVSPLTLLK) NWs were tested for coagulation targeting *in vitro* by adding thrombin/$CaCl_2$ to solutions of NWs in citrate-stabilized human plasma (3 µg Fe/ml; 25 nM NW).

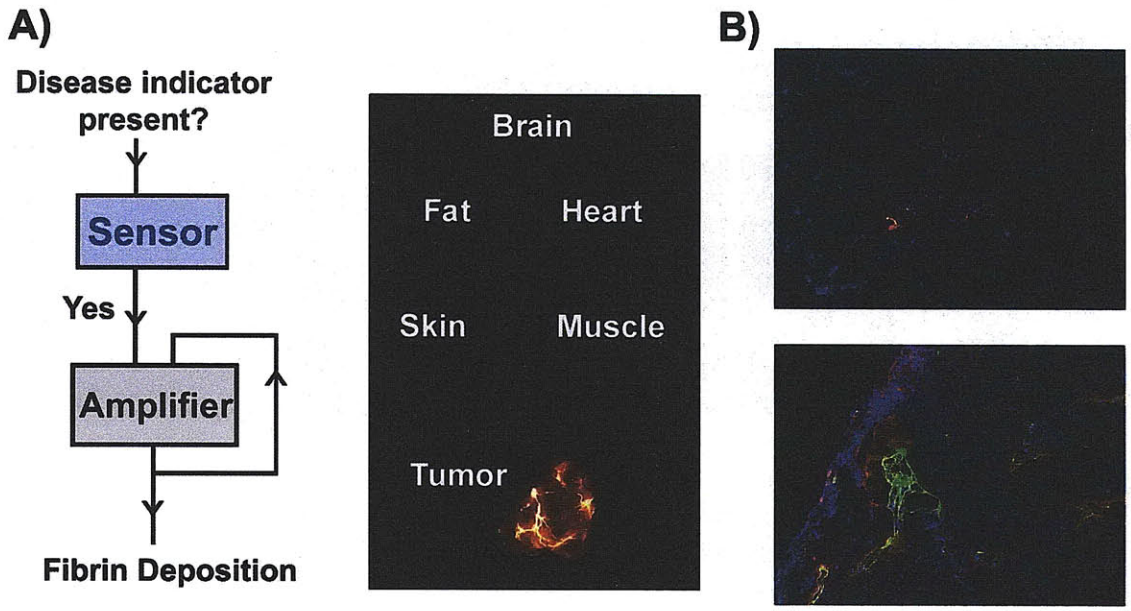

Figure 8.4. *Macroscopic and histopathological distribution of fluorescent fibrinogen in tTF-RGD Sensor-injected mice.* A) Information flow between Sensor and coagulation cascade and macroscopic distribution of fluorophore-labeled fibrinogen at 24 hrs following co-injection with tTF-RGD Sensor (1 mg tTF-RGD/kg) (~1 nmole fibrinogen; VT750 fluorophore). B) Anti-fibrinogen antibody stain co-localizes with injected fibrinogen fluorescence (Red = Anti-fibrinogen; Green = injected fibrinogen fluorescence; Blue = nuclear stain), top = VT750-labeled fibrinogen without tTF-RGD Sensor injection; bottom = VT750-labeled fibrinogen with tTF-RGD Sensor injection (1 mg tTF-RGD/kg);

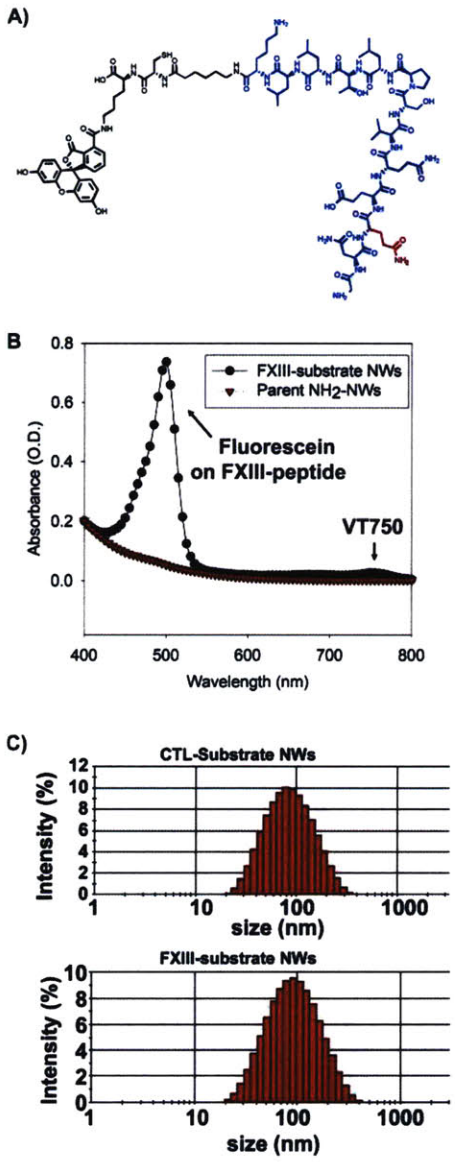

Figure 8.5. *Characterization of superparamagnetic iron oxide nanoworm Receiver nanoparticles*. A) Structure of the Factor XIII substrate peptide used to confer coagulation specificity to NWs (substrate sequence in blue, exogenous cysteine in red and fluoroscein in black). For Control-NW synthesis, an identical peptide was used with the essential glutamine replaced by an alanine residue. This enabled development of two NW Receiver populations with high and low specificity for coagulation via a single amino acid difference in their surface properties. B) UV-visible spectra of FXIII-NWs before and after NIR-fluorophore and peptide conjugation. Changes in the visible spectra of NW conjugates facilitates the quantitative characterization of the number of peptides and fluorophores chaperoned on each particle scaffold (~600 FXIII-substrates/NW and ~25 VT750 fluorophores/NW). C) Dynamic light scattering characterization of FXIII-substrate and Control-substrate NWs. Following modification with FXIII and Control peptide substrates (both at ~600 peptides/NW), NWs retain similar size by light scattering.

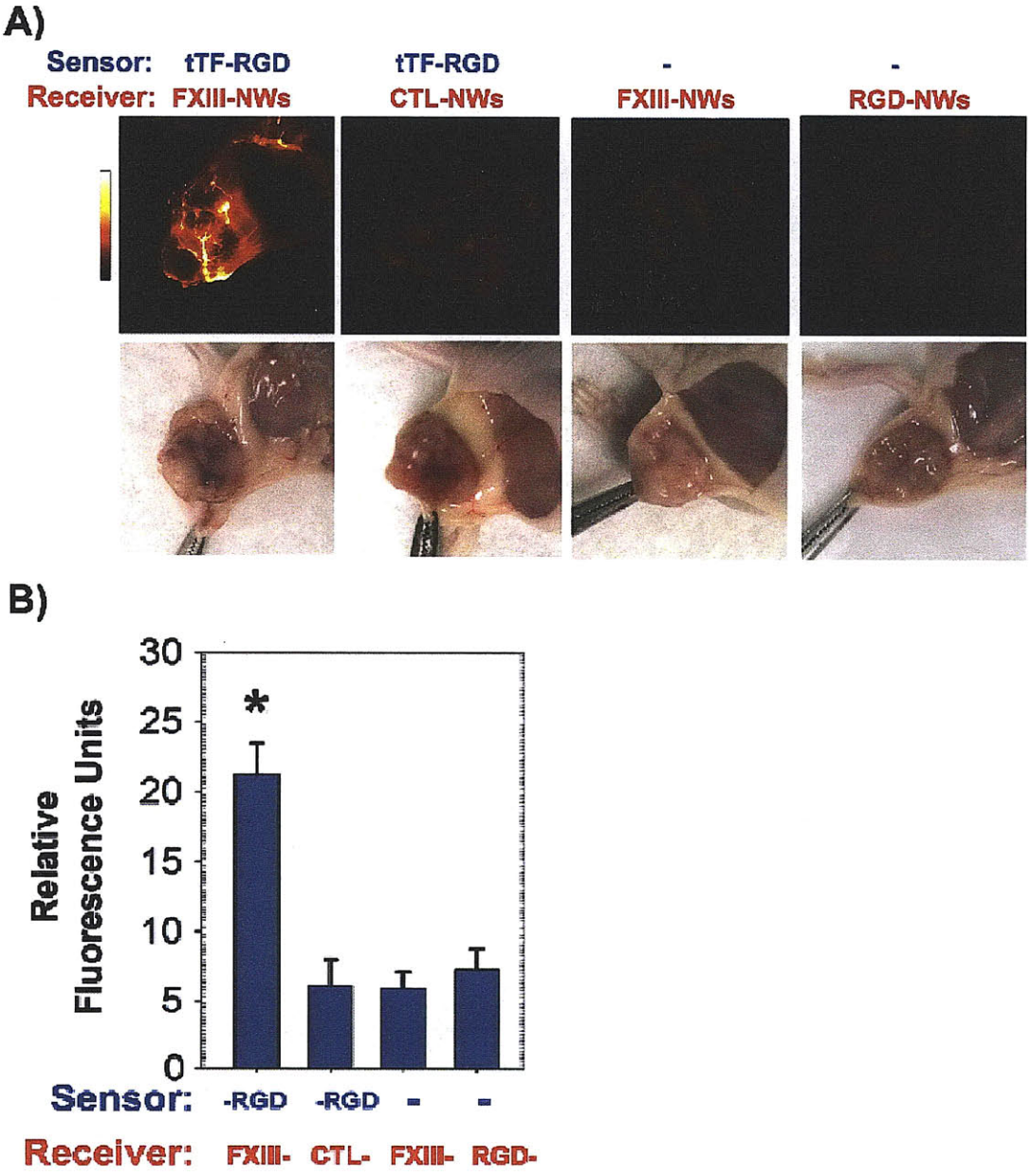

Figure 8.6. *Amplification of nanoparticle targeting in vivo using hybrid signaling network.* A) Intraoperative imaging of NW targeting in hybrid signaling networks. *Nu/nu* mice bearing a single MDA-MB-435 tumor were intravenously injected with integrated (tTF-RGD + FXIII-NWs) or control (tTF-RGD + Control-NWs) signaling networks, FXIII-NWs alone, or NWs targeted by the peptide used to direct Sensor tumor homing (1 mg/kg tTF-RGD; 1.5 mg Fe/kg). At 24 hrs post-injection, tumors were surgically exposed under anaesthetic for fluorescent intraoperative imaging of NW homing to tumors. B) Fluorescent quantitation of NW homing in integrated signaling networks and controls (*$p<0.05$ versus all other sets, n=3 or 4 mice for each set)

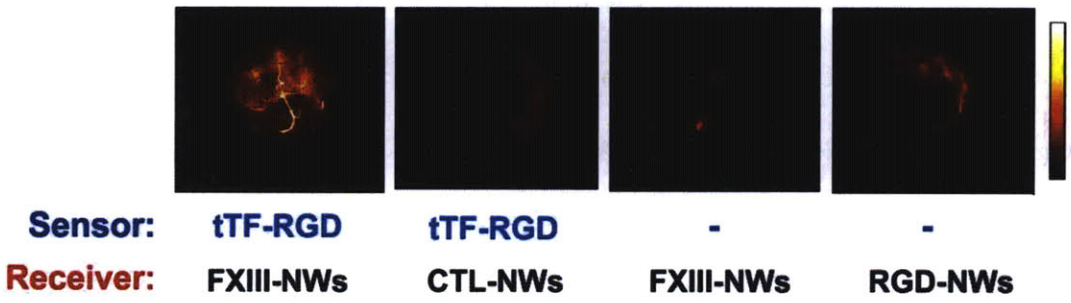

Figure 8.7. *NIR-imaging of NWs from excised tumors in integrated and control signaling networks. Nu/nu* mice bearing a single MDA-MB-435 tumor were intravenously injected with integrated (tTF-RGD + FXIII-NWs) or control (tTF-RGD + Control-NWs) signaling networks, FXIII-NWs alone, or NWs targeted by the peptide used to direct Sensor tumor homing (1 mg/kg tTF-RGD; 1.5 mg Fe/kg). At 24 hrs post-injection, mice were sacrificed and tumors were surgically removed for fluorescent imaging of NW localization to tumors. Integrated networks show dramatic accumulation in characteristically branching vascular pattern, while this effect is absent in all controls.

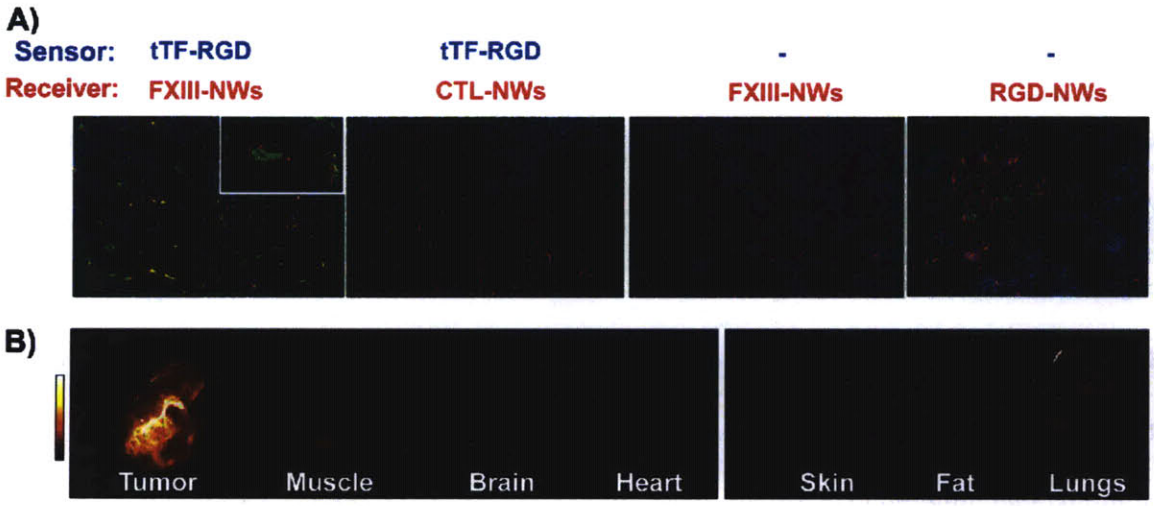

Figure 8.8. *Microscopic and macroscopic characterization of nanoparticle targeting in vivo using hybrid signaling network* C) Histopathologic analysis of NW homing in integrated signaling networks and controls. Green = NW fluorescence; Red = CD31 blood vessel stain; Blue = nuclear stain. D) Tumor specificity of hybrid signaling networks. Excised organs from mice injected with integrated signaling networks (tTF-RGD + FXIII-NWs) were imaged for NW fluorescence at 24 hrs post-injection (1 mg/kg tTF-RGD; 1.5 mg Fe/kg).

post-injection, mice were anaesthetized and tumors were surgically revealed for intra-surgical NIR fluorescent imaging of NW homing (**Figure 8.6A**). Intra-operative imaging revealed marked enhancement of vascular homing of FXIII-NWs in the integrated network (tTF-RGD + FXIII-NWs), with substantially diminished NW accumulation for a control network (tTF-RGD + Control-NWs) and FXIII-NWs in isolation (**Figure 8.6A, 8.6B**). Importantly, integrated networks also generated superior tumor homing compared to the traditional strategy for directly targeting nanoparticles to receptors: RGD-NWs (**Figure 8.6A, 8.6B, 8.7**), demonstrating the central role of signal amplification in communicating the presence of $\alpha_v\beta_3$ integrins to NWs. Histopathological analysis of tumors demonstrated abundant intravascular Receiver homing that filled the lumen of tumor vessels in the case of integrated networks, an effect that was absent in all controls (**Figure 8.8A**). RGD-NWs could be observed in endothelial cells lining some tumor vessels, but at considerably lower concentrations and without the amplified luminal accumulation of FXIII-NWs in integrated networks. As was observed during isolated characterization of Sensors, we found the vascular targeting of FXIII-NWs in integrated signaling networks to be highly specific to tumors, with negligible homing to control tissues, including lungs, heart, fat, brain, skin, muscle (**Figure 8.8B**). To further verify that our signaling networks channel information via the coagulation cascade, we administered integrated networks alongside a strong coagulation inhibitor, heparin, to disrupt thrombin-mediated FXIII activation. Indeed, heparin administration eliminated characteristic vascular homing pattern of FXIII-NWs in integrated networks (**Figure 8.9**).

In order to assess the modularity of receptor-targeted Sensor components, we finally tested tTF-NGR Sensors, which seek out CD13/aminopeptidase N receptors in

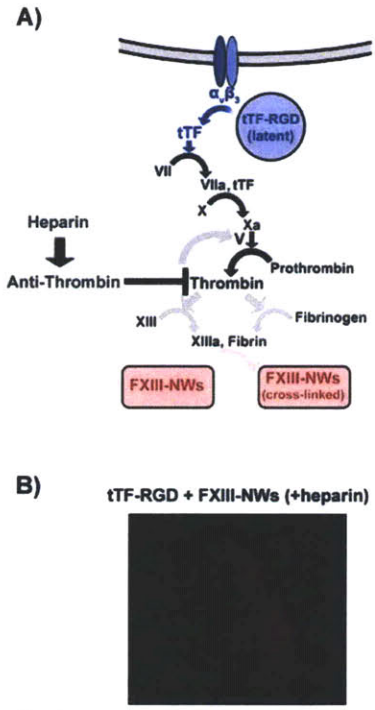

Figure 8.9. *Heparin-mediated disruption of signaling network communication.* A) Schematic of heparin's disruption of communication in hybrid signaling networks. B) *Nu/nu* mice bearing a single MDA-MB-435 tumor were intravenously injected with integrated signaling networks (tTF-RGD + FXIII-NWs; 1 mg/kg tTF-RGD; 1.5 mg Fe/kg) alongside heparin to prohibit thrombin activation (intravenous bolus of 800 units/kg + intraperitoneal bolus of 500 units/kg 30 minutes later). At 24 hrs post-injection, mice were sacrificed and tumors were surgically removed for fluorescent imaging of NW localization to tumors. Tumors on heparin-injected mice lack characteristic vascular pattern of integrated signaling between Sensors and Receivers.

tumor vessels, alongside FXIII-targeted NWs. We found that tTF-NGR Sensors were similarly able to amplify NW targeting to tumors (**Figure 8.10A, 8.10B**), highlighting the capacity for our signaling network architecture to be customized for specific cancer types and stages.

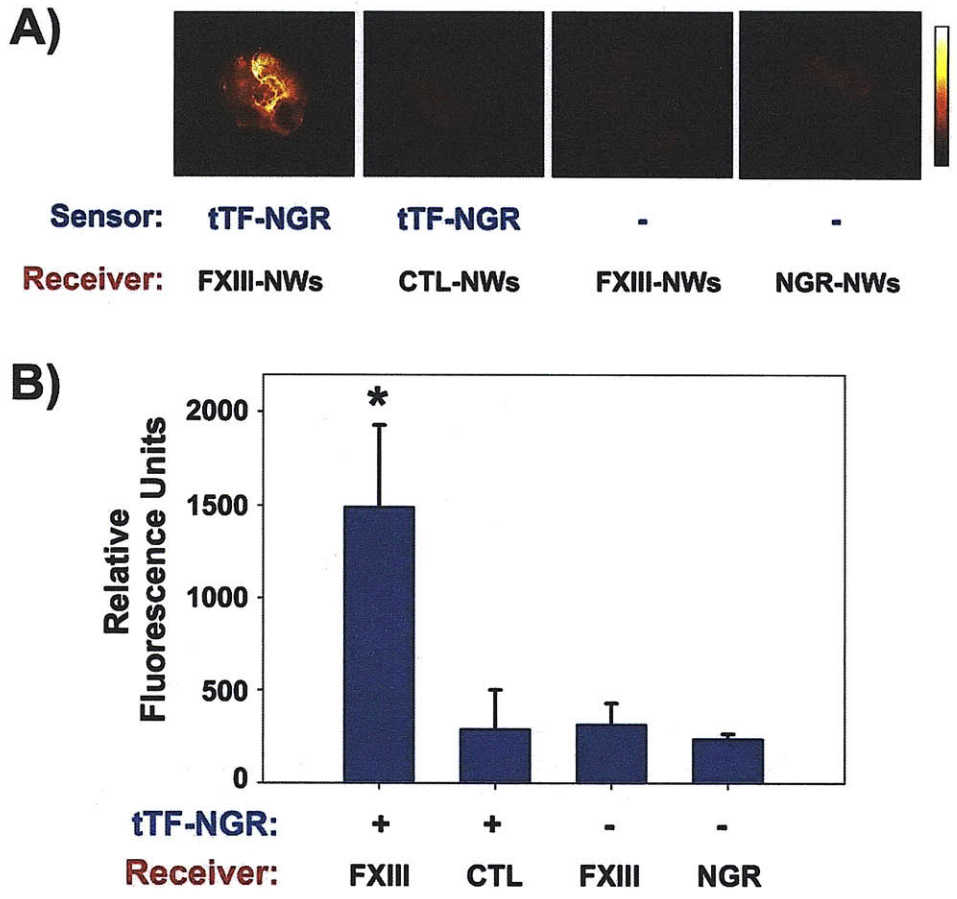

Figure 8.10. *Modularity of hybrid signaling networks: Signaling networks composed using a distinct ligand-targeted tTF enzyme Sensor.* tTF-NGR Sensors survey host vasculature for CD13/aminopeptidase N receptors associated with tumor angiogenesis. Upon binding, tTF-NGR sensors gain activity and transmit their signal to Receiver nanoparticles through the extrinsic coagulation cascade. *Nu/nu* mice bearing a single MDA-MB-435 tumor were intravenously injected with integrated (tTF-NGR + FXIII-NWs) or control (tTF-RGD + Control-NWs) signaling networks, FXIII-NWs alone, or NWs targeted by the peptide used to direct Sensor tumor homing (1 mg/kg tTF-NGR; 1.5 mg Fe/kg). At 24 hrs post-injection, mice were sacrificed and tumors were surgically removed for fluorescent imaging of NW localization to tumors. B) Quantification of average fluorescence from tumor cohorts above (n = 4 mice in each set; * denotes $P<0.05$ between tTF-NGR → FXIII-NWs and all other tumor sets).

8.3 Conclusions:

The hybrid signaling networks developed here demonstrate the potential for ensembles of biological (engineered proteins, viruses, phage) and nanotechnological components (nanoparticles, nanowires, etc) to cooperate to perform complex operations *in vivo*. A fundamental advantage of the strategy presented here over traditional NP targeting approaches is the amplification produced coupling molecular interactions with a biological cascade amplification system. In contradistinction to pre-targeting approaches that require sequential administration of system constituents(*325*), our signaling network components are simultaneously administered and autonomously perform their functions. Finally, because we utilize a human tissue factor Sensor that has been tested in patients, this network architecture may translate to improved clinical cancer imaging and therapeutic systems.

8.4 Materials and Methods:

tTF, tTF-RGD, tTF-NGR Sensor expression and purification

The cDNAs coding for the tTF-containing amino acids 1 - 218 and the respective C - terminal peptide extension were amplified by polymerase chain reaction (PCR) using the primers:

5‘-CATGCCATGGGATCAGGCACTACAAATACTGTGGCAGCATATAAT-3‘(5‘-Primer), 5‘-CGGGATCCTATTATCTGAATTCCCCTTTCTCCTGGCCCAT-3‘ (3’-Primer) for tTF,

5’-CGGGATCCTATTATGGAGAATCACCTCTTCCTCTGAATTCCCC-3’ (3‘-Primer) for tTF-RGD and

5'-CGGGATCCTATTATGCATGTGCTCTTCCGTTACCTCTGAATTCCCC-3' (3'-Primer) for tTF-NGR. With the DNA-Ligation Kit (Novagen, Schwalbach am Taunus, Germany) the cDNA was cloned into the expression vector pET-30(+)a (Novagen) using the BamHI and NcoI sites of the vector. The vectors were introduced in competent *Escherichia coli* cells (BL21 DE3) according to the manufacturer's protocol (Novagen). The bacteria were cultivated in Luria broth medium supplemented with kanamycin (30 µg/ml) at 37°C. When the bacteria cell suspensions reached an OD of ~ 0.6, over-expression of the fusion proteins was initiated by adding 1 mM IPTG (Novagen). After ~16 h, the cells were harvested and 5-7 ml lysis buffer (10 mM Tris-HCl, pH 7.5; 150 mM NaCl; 1 mM $MgCl_2$; 10 µg/ml aprotinin; 20 µl benzonase; 2 mg/ml lysozyme) per gram wet weight were added. The lysed cells were incubated for 90 minutes at room temperature (RT) and centrifuged at 12,000 g for 20 min at 4°C. The pellet was resuspended and homogenized by sonicating in washing buffer (10 mM Tris/HCl, pH 7.5; 1 mM EDTA, 3% Triton X-100). To solubilize the inclusion bodies, 2-4 ml guanidinium buffer (6 M GuCl, 0.5 M NaCl, 20 mM Tris/HCl, pH 7.5; 1 mM DTT) per gram wet weight was added. After incubation overnight at RT, the suspension was centrifuged at 10,000 g for 20 min at 4°C and the supernatant was filtered through a 0.22 µm filter.

The solubilized tTF fusion proteins were refolded and purified by using a multi-step HPLC-based purification process (HPLC unit: ÄKTA purifier 100 System, GE healthcare, Uppsala, Sweden). It consists of an immobilized metal-(copper-)affinity chromatography (IMAC; IMAC Sepharose 6 FF, GE healthcare). The histidine-tagged tTF fusion proteins bind to the immobilized copper ions so that the complete refolding (gradient from 6 M to 0 M urea buffer within 60 min) and washing processes are

performed on the column, from which the tTF Sensor proteins are eluted by applying 300 mM imidazole. During the subsequent gel filtration the IMAC eluate is conditioned by a buffer exchanging step (20 mM Tris/HCl, pH 8; 20 % glycerol) using Sephadex G-25 (GE healthcare) in order to prepare for the following intermediate anion-exchange chromatography step (AIEX; Q Sepharose HP, GE healthcare; used buffers: 20 mM Tris/HCl, pH 8; 20 % glycerol +/- 300 mM NaCl). The concluding polishing step again comprises a gel filtration using Sephadex G25 in order to remove any remaining trace impurities and to exchange the puffer to PBS. The final protein solutions (> 95% purity) are stored at -80°C. Each sample produced was tested for purity (SDS-PAGE, Western Blot, endotoxins, HPLC) and activity (Factor-X coagulation test).

Factor-X activation by tTF Sensor proteins

The ability of the tTF Sensor proteins to enhance the specific proteolytic activation of Factor (F) X by FVIIa was assessed as described by Ruf et al.[1]. Briefly, to each well in a microtiter plate was added 20 µl of: (a) 50 nM recombinant FVIIa (Novo-Nordisc, Bagsværd, Denmark) in TBS-BSA; (b) 0.16 nM - 1.6 µM tTF/tTF-NGR in TBS containing 0.1 % bovine serum albumine (BSA); (c) 25 nM $CaCl_2$ and 500 µM phospholipids (phosphatidylcholine/phosphatidylserine, 70/30, MM; Sigma, München, Germany). After 10 min at RT, 20 µl of the substrate FX (Enzyme Research Laboratories, Swansea, UK) was added in a concentration of 5 µM. Aliquots were removed from the reaction mixture every minute and stopped in 100 nM EDTA. Spectrozyme FXa (American Diagnostica, Greenwich, CT, USA) was added and rates of FXa generation were monitored by the development of color at 405 nm with a microplate reader (Bio-Rad, Hercules, California, USA).

Probing Sensor-mediated tumor coagulation via fibrin(ogen) deposition in tumors. Bovine fibrinogen (Sigma) and albumin (Sigma) were reacted with near-infrared fluorophores (VT750-NHS and VT680-NHS, respectively; Visen Medical) at a 2:1 fluorophore: protein molar ratio in PBS for ~2 hrs and dialyzed exhaustively at 4°C against PBS to remove unreacted fluorophore. The product of the dialysis was passed through a 0.1μm filter, quantified using a BCA protein assay (Pierce), and assessed for fluorophore labeling via the peak fluorophore absorption (λ_{max}=750 and 680 nm, respectively, for VT750 and VT680). After labeling/purification fibrinogen and albumin protein stocks harbored ~1 fluorophore/protein. To assess Sensor-mediated coagulation in mice, ~1 nanomole of both proteins (bearing distinct NIR-fluorophores) were injected intravenously alongside varying amounts of tTF, tTF-RGD, or tTF-NGR into mice bearing a flank MDA-MB-435 carcinoma tumor. At 24 hrs post-injection, mice were dissected and tumors were fluorescently imaged for the relative abundance of fibrinogen and albumin (LI-COR Odyssey Infrared Imaging System). Increases in protein tropism to tumors were analyzed by assessing mean tumor fluorescence (n=4 mice with each type of tTF tested).

Peptide Synthesis. The four peptides used in this work: a peptide substrate for the transglutaminase Factor XIII (G-N-***Q***-E-Q-V-S-P-L-T-L-L-K-X-C-(K-Fluorescein)) (active glutamine in bold), a control substrate for FXIII (G-N-***A***-E-Q-V-S-P-L-T-L-L-K-X-C-(K-Fluorescein)) (single amino acid substitution in bold), the $\alpha_v\beta_3$ targeting ligand (Fluorescein-X-C-G-R-G-D-S-P-COO-), and the CD13/aminopeptidase N targeting ligand (Fluorescein-X-C-G-N-G-R-A-H-A-COO-) were synthesized via standard FMOC

solid-phase peptide synthesis (X=6-aminohexanoic acid linker) (Tufts University Core Facility). Products were HPLC-purified to >90% purity and characterized via mass spectrometry.

Receiver Synthesis. Superparamagnetic, dextran-caged iron oxide nanoworms (NWs) with a longitudinal size of ~60 nm were synthesized, aminated using 20% v/v ammonium hydroxide, and derivatized with near-infrared fluorophores as described previously[1]. FXIII-substrate and Control peptides were attached to NWs via their exogenous cysteine by first reacting fluorophore-labelled NWs with the hetero bifunctional linker NHS-PEO_{12}-Maleimide (Pierce) in phosphate buffered saline pH 7.2 (PBS) at a 5000:1 linker:NW molar ratio. Following activation with linker, NWs were filtered using a gel filtration column (G50 media) and incubated overnight with peptides at ~1000:1 peptide:NW ratio with shaking. After ~12 hrs, NWs were purified from extra peptides by repeated filtration on centrifugal membrane filters (100 kDa size cutoff, Centricon, Millipore) and finally dispersed in PBS for spectrophotometric analysis of peptide labelling. All peptide-functionalized NWs were characterized via dynamic light scattering (DLS) and intravenously injected *in vivo* to ensure targeted NWs and control NWs exhibited similar circulation times.

Quantifying NW homing to tumors in vivo. NIR-fluorophore-labeled peptide-bearing NWs (bearing VT750 fluorophores) were intravenously (2 mg Fe/kg) in PBS to MDA-MB-435 tumor-bearing nu/nu mice alone or alongside tTF Sensors (25 μg). At 24 hrs post-NW injection, mice were sacrificed and organs were analyzed for NIR Receiver fluorescence (LI-COR Odyssey Infrared Imaging System). For intraoperative fluorescent

tumor imaging, mice were anaesthesized and tumors were surgically exposed to reveal detailed tumor fluorescence (LI-COR). Levels of NW homing to tumors were plotted by comparing the average NW fluorescence in fully-excised tumors (n=4 mice at each condition).

Immunohistochemical analysis of tumors. For all histologic analysis, tumors were frozen in Optimal Cutting Temperature embedding media and sections of tumors were prepared in the MIT Koch Institute Histology Core. The sections were first fixed with acetone. Rat anti-mouse CD-31 (1:50, BD PharMingen) and biotinylated mouse fibrin(ogen) antiserum (1:50, Nordic) were used for immunochemical staining of tumor tissue sections. The corresponding secondary antibodies were added and incubated for 1 hour at room temperature, namely AlexaFluor-594 goat anti-rat or rabbit IgG (1:1000 dilution; Molecular Probes), streptavidin Alexa Fluor 594 (1:1000 dilution; Molecular Probes). The slides were washed three times with PBS and mounted in Vectashield Mounting Medium with DAPI. At least three images from representative microscopic fields were analyzed for each tumor sample.

9.0 Perspective and Future Directions

In the past, engineering disciplines have emerged after a significant foundation of quantitative, experimental, and experiential knowledge had been established in a field—e.g. mechanical and civil engineering leveraged thousands of years of experience with construction materials and tools; electrical engineering required the foundational discoveries of Ohm, Faraday, and Maxwell; chemical engineering was built upon the 19th century's developments in the field of chemistry; and biological engineering leveraged the rapid advances in molecular biology during the 20th century. Building upon the immense progress in nanoparticle synthesis over the past twenty years, the field of bionanotechnology is now ripe to begin its own engineering discipline, focused, in part, on incorporating multiple individual nanodevices into cohesive systems that exhibit novel and predictable functions. The primary goal of this thesis was engineer reliable, higher-order nanoparticle systems where mechanisms of inter-nanoparticle interaction and communication produce emergent system behaviors for biomedicine.

In contrast to systems in electrical engineering, biological systems store information via chemical identity and complementarity and process it through largely amorphous molecular pathways that rely on biochemical specificity, local concentration gradients, and dynamic regulation of component activity to propagate and process information. The nanoparticle systems presented here operate in this wet and wireless arena of biology and their function takes inspiration from information processing in both electrical circuits and biological processes.

The first section of this thesis describes mechanisms of nanoparticle interaction and communication that exploit biological recognition elements to promote nanoparticle interactions. Specifically, nanoparticles are modified to harness the high-affinity binding interaction of streptavidin and biotin or to polyvalently utilize the phospho-specific interactions between phospho-tyrosine peptides and SH2 domains. These biological domains provide nanoparticles the opportunity to precisely interact with one another even within complex biological environments, due to the borrowed specificity of these biochemical 'addresses.' Looking forward, because such recognition elements underlie the specificity of virtually all biological information processing, they provide an immense landscape of other addresses through which future populations of nanoparticles could interact with single or multiple partners in a programmatic fashion. Beyond the sensing applications developed herein, these strategies could be used in combination with disease targeting ligands to enable receptor binding to be followed by an elongation phase where nanomaterials locally polymerize upon receptor-bound 'initiators.' Such a process could harness either disease-specific or ubiquitous enzymatic machinery as 'nanoparticle polymerases' to catalyze elongation. For example, tumor proteases could perform this function by removing inhibitory domains on latent nanoparticles in circulation similar to those developed in Chapters 2-3, enabling tumor-programmed nanoparticle assembly onto receptors. Alternatively, soluble factors in the vicinity of diseases could be sequestered by nanoparticles as bridging moieties to link otherwise dispersed nanoparticles into elongated assemblies. Further, nanoparticle systems could be engineered to exploit disease markers as kinetic triggers to initiate otherwise very slow inter-nanoparticle binding events.

Generally, these systems were designed such that biology inputs (enzymes) would direct inter-nanoparticle interactions by revealing or modifying surface moieties that are distinct from inputs themselves. The rate of these processes is driven by Michaelis-Menten kinetics and particle activation proceeds in a linear fashion. In more advanced embodiments, biological inputs could stimulate the release or activation of additional input from particles to produce autocatalytic, exponential behaviours. This could provide initial events to initiate chain-reactions analogous to the amplification networks present in the coagulation cascade and those used in polymerase chain reactions (PCR) that could facilitate enhanced sensing and targeting of disease processes. Further, negative feedback processes could also be engineered into such networks through production of inactivating stimuli in response to peripheral, non-disease related inputs.

In the second section of this thesis, nanoparticles remotely communicate through endogenous biological information pathways in plasma (blood coagulation). Specifically, we describe a system wherein Signaling nanoparticles specifically engage the coagulation cascade in tumors and Receiving nanoparticles sense the abundant downstream products of this process. The information flow in this system is complex: external near infrared energy is locally transduced to heat by tumor-targeted gold nanorods (Signaling nanoparticles), which locally increases microvascular permeability in tumors, which exposes plasma to the tumor parenchyma, which activates the intrinsic and extrinsic coagulation pathways, which generate abundant activity of the protease thrombin, which produces an abundant fibrin network and activates the transglutaminase Factor XIII, which together recruit the amplified accumulation of circulating diagnostic or therapeutic Receiving nanoparticles. Despite its apparent complexity, this network is founded upon

the robust evolutionary processes of injury repair to propagate a message of tumor's location between two nanoparticles with high fidelity. Stated another way, in this process, the biological system is simply performing the function it was evolutionarily selected to (i.e. If (injury) Then (repair)), without the 'knowledge' that it is delivering a message between two populations of synthetic devices. A second system comprised of a nanotechnological and a synthetic biological component was also engineered to hijack the coagulation cascade to transmit and amplify communication between synthetic devices. However, as opposed to the first system that utilizes a class of Signaling nanoparticles capable of generating local vascular injuries in tumors, this second system utilizes a synthetic biological Sensor that provides a new program for the coagulation cascade, causing it to respond to endothelial receptors associated with tumor formation. In the former system, the coagulation cascade was simply performing its intrinsic function of sensing and repairing vascular injuries. In the latter, as long as the synthetic biological Sensor is in circulation (~ minutes after i.v. injection), the cascade is programmed to perform a new function: engage in receptor-expression tumor vessels (in the absence of any injury) through the phosphatidylserine-dependent activity of a re-engineered human tissue factor protein.

Together these systems demonstrate not only that nanoparticles can be engineered to communicate with one another *in vivo,* but that synthetic bio/nanotechnological devices can be utilized to provide unnatural inputs and outputs to endogenous biological information networks and program them to perform tasks they had not explicitly evolved to. This provides a new perspective on the information processing underlying both normal and pathologic biological processes and opens new opportunities for hijacking

molecular and cellular trafficking mechanisms to direct nanoparticle targeting. In its simplest embodiment, this could resemble approaches to insect extermination where foraging drones are tricked into carrying poisons back to the colony. More advanced strategies could actively orchestrate these networks to amplify, redirect, focus, and otherwise control the propagation of information through these networks to enhance disease sensing, targeting, and therapy. For example, while we demonstrated that information could be efficiently transmitted between two synthetic devices *in vivo*, this process could certainly be improved through exogenous manipulation of this network (i.e. unnecessary pathway inhibition, desired pathway supplementation) in an analogous manner to metabolic engineering approaches(*326, 327*). An additional benefit of engineering nanosystems to leverage biological signaling pathways for the bulk of signal processing and transmission is that the complexity of nanoparticles can be minimized, while generating sophisticated network behaviors.

Direct and *indirect* mechanisms of nanoparticle interaction were separately explored in this thesis. This work is meant to provide a starting point for the future engineering of higher-order nanosystems, comprised of numerous nanoparticle populations and incorporating a spectrum of interaction mechanisms. Towards this goal, just as biological systems rely on the robust synthesis of their components (DNA, RNA, protein, glycans, etc.), the development of complex multi-component nanosystems that themselves resemble processes like blood coagulation instead of merely activating them, will require nano-parts of superior fidelity, reliability, and reproducibility. Further, the intended and unintended interactions and communications between nanoparticles and living systems will need to be much more thoroughly understood. As such, tools for

deciphering these in a highly parallel fashion will be needed. Particularly, for *in vivo* applications, methods for rapidly and simultaneously revealing the macroscopic and microscopic biodistribution of multiple nanoparticles, characterizing their 'state' (e.g. integrity of nanoparticle surface chemistries, understanding what proteins have bound to the surface, % payload released, whether the nanoparticle is receptor bound or free, etc.), and understanding the tissue's state (e.g. naïve?, manipulated?, what information pathways are activated?, etc.) will be necessary tools for understanding and accurately predicting nanosystem functions. While the goal of developing bio-synthetic analogues of complex biological systems such as blood coagulation remains far away on the long horizon, we now have the tools to sincerely begin engineering higher-order systems of interactive nanoparticles that can operate at biology's length scale and begin to emulate its complexity. A simple look at the natural world around us should reveal that this is a pretty exciting place to be.

References

1. Y. X. J. Wang, S. M. Hussain, G. P. Krestin, *Eur Radiol* **11**, 2319 (2001).
2. D. D. Stark *et al.*, *Radiology* **168**, 297 (Aug, 1988).
3. R. Weissleder *et al.*, *American Journal of Roentgenology* **152**, 167 (Jan, 1989).
4. Y. N. Xia, N. J. Halas, *Mrs Bulletin* **30**, 338 (May, 2005).
5. K. L. Kelly, E. Coronado, L. L. Zhao, G. C. Schatz, *J Phys Chem B* **107**, 668 (Jan 23, 2003).
6. M. Hu *et al.*, *Chemical Society Reviews* **35**, 1084 (2006).
7. A. R. Tao, S. Habas, P. D. Yang, *Small* **4**, 310 (Mar, 2008).
8. W. C. W. Chan, S. M. Nie, *Science* **281**, 2016 (Sep 25, 1998).
9. A. P. Alivisatos, *Science* **271**, 933 (Feb 16, 1996).
10. D. Astruc, F. Lu, J. R. Aranzaes, *Angew Chem Int Edit* **44**, 7852 (2005).
11. Y. Y. Li *et al.*, *Science* **299**, 2045 (Mar 28, 2003).
12. L. Y. Cheng *et al.*, *Investigative Ophthalmology & Visual Science* **46**, (2005).
13. E. J. Anglin, L. Y. Cheng, W. R. Freeman, M. J. Sailor, *Advanced Drug Delivery Reviews* **60**, 1266 (Aug 17, 2008).
14. S. M. Moghimi, A. C. Hunter, J. C. Murray, *Pharmacol Rev* **53**, 283 (JUN, 2001).
15. G. Storm, S. O. Belliot, T. Daemen, D. D. Lasic, *Adv Drug Deliver Rev* **17**, 31 (Oct, 1995).
16. S. M. Moghimi, J. Szebeni, *Progress in Lipid Research* **42**, 463 (Nov, 2003).
17. R. Gref *et al.*, *Science* **263**, 1600 (Mar 18, 1994).
18. B. W. Stewart, P. Kleihues, (2003).
19. Y. A. Hannun, *Blood* **89**, 1845 (Mar 15, 1997).
20. H. Kantarjian *et al.*, *New England Journal of Medicine* **346**, 645 (Feb 28, 2002).
21. S. G. O'Brien *et al.*, *New England Journal of Medicine* **348**, 994 (Mar 13, 2003).
22. M. Ferrari, *Nat Rev Cancer* **5**, 161 (Mar, 2005).
23. D. Peer *et al.*, *Nature Nanotechnology* **2**, 751 (Dec, 2007).
24. M. E. Davis, Z. Chen, D. M. Shin, *Nature Reviews Drug Discovery* **7**, 771 (Sep, 2008).
25. X. H. Gao, Y. Y. Cui, R. M. Levenson, L. W. K. Chung, S. M. Nie, *Nat Biotechnol* **22**, 969 (AUG, 2004).
26. S. A. Wickline, G. M. Lanza, *Circulation* **107**, 1092 (MAR 4, 2003).
27. S. A. Wickline, G. M. Lanza, *J Cell Biochem*, 90 (2002).
28. O. Rabin, J. M. Perez, J. Grimm, G. Wojtkiewicz, R. Weissleder, *Nature Materials* **5**, 118 (Feb, 2006).
29. D. Kim, S. Park, J. H. Lee, Y. Y. Jeong, S. Jon, *J Am Chem Soc* **129**, 7661 (Jun 20, 2007).
30. L. Josephson, J. Lewis, P. Jacobs, P. F. Hahn, D. D. Stark, *Magnetic Resonance Imaging* **6**, 647 (Nov-Dec, 1988).
31. J. H. Lee *et al.*, *Nature Medicine* **13**, 95 (Jan, 2007).
32. J. H. Park *et al.*, *Advanced Materials* **20**, 1630 (May 5, 2008).
33. Y. W. Jun, J. H. Lee, J. Cheon, *Angewandte Chemie-International Edition* **47**, 5122 (2008).
34. C. L. Nehl, H. W. Liao, J. H. Hafner, *Nano Letters* **6**, 683 (Apr, 2006).
35. Y. G. Sun, B. T. Mayers, Y. N. Xia, *Nano Letters* **2**, 481 (May, 2002).

36. S. J. Oldenburg, R. D. Averitt, S. L. Westcott, N. J. Halas, *Chemical Physics Letters* **288**, 243 (May 22, 1998).
37. R. Elghanian, J. J. Storhoff, R. C. Mucic, R. L. Letsinger, C. A. Mirkin, *Science* **277**, 1078 (AUG 22, 1997).
38. D. S. Grubisha, R. J. Lipert, H. Y. Park, J. Driskell, M. D. Porter, *Anal Chem* **75**, 5936 (Nov 1, 2003).
39. J. B. Jackson, S. L. Westcott, L. R. Hirsch, J. L. West, N. J. Halas, *Appl Phys Lett* **82**, 257 (Jan 13, 2003).
40. X. M. Qian *et al.*, *Nat Biotechnol* **26**, 83 (Jan, 2008).
41. L. R. Hirsch *et al.*, *P Natl Acad Sci USA* **100**, 13549 (NOV 11, 2003).
42. D. P. O'Neal, L. R. Hirsch, N. J. Halas, J. D. Payne, J. L. West, *Cancer Lett* **209**, 171 (JUN 25, 2004).
43. R. S. Norman, J. W. Stone, A. Gole, C. J. Murphy, T. L. Sabo-Attwood, *Nano Lett* **8**, 302 (Jan, 2008).
44. X. Huang, I. H. El-Sayed, W. Qian, M. A. El-Sayed, *J Am Chem Soc* **128**, 2115 (Feb 15, 2006).
45. N. R. Jana, L. Gearheart, C. J. Murphy, *Journal of Physical Chemistry B* **105**, 4065 (May 17, 2001).
46. C. J. Murphy *et al.*, *J Phys Chem B* **109**, 13857 (Jul 28, 2005).
47. A. Agrawal *et al.*, *Journal of Biomedical Optics* **11**, (Jul-Aug, 2006).
48. A. M. Gobin *et al.*, *Nano Letters* **7**, 1929 (Jul, 2007).
49. T. S. Troutman, J. K. Barton, M. Romanowski, *Optics Letters* **32**, 1438 (Jun 1, 2007).
50. P. C. Li *et al.*, *Optics Express* **16**, 18605 (Nov 10, 2008).
51. A. De La Zerda *et al.*, *Nature Nanotechnology* **3**, 557 (Sep, 2008).
52. G. Jia *et al.*, *Environmental Science & Technology* **39**, 1378 (Mar 1, 2005).
53. J. W. Sigler *et al.*, *Annals of Internal Medicine* **80**, 21 (1974).
54. W. C. Chan, S. Nie, *Science* **281**, 2016 (Sep 25, 1998).
55. X. Michalet *et al.*, *Science* **307**, 538 (Jan 28, 2005).
56. M. Bruchez, M. Moronne, P. Gin, S. Weiss, A. P. Alivisatos, *Science* **281**, 2013 (Sep 25, 1998).
57. X. G. Peng *et al.*, *Nature* **404**, 59 (Mar 2, 2000).
58. X. Michalet *et al.*, *Science* **307**, 538 (Jan 28, 2005).
59. A. M. Derfus, W. C. W. Chan, S. N. Bhatia, *Nano Letters* **4**, 11 (Jan, 2004).
60. R. Weissleder, *Nature Biotechnology* **19**, 316 (Apr, 2001).
61. B. B. Goldberg, J. B. Liu, F. Forsberg, *Ultrasound in Medicine and Biology* **20**, 319 (1994).
62. E. C. Unger *et al.*, *Advanced Drug Delivery Reviews* **56**, 1291 (May 7, 2004).
63. G. M. Lanza *et al.*, *Circulation* **94**, 3334 (Dec 15, 1996).
64. K. C. Crowder *et al.*, *Ultrasound in Medicine and Biology* **31**, 1693 (Dec, 2005).
65. Q. Y. Cai *et al.*, *Invest Radiol* **42**, 797 (Dec, 2007).
66. E. T. Kisak, B. Coldren, C. A. Evans, C. Boyer, J. A. Zasadzinski, *Current Medicinal Chemistry* **11**, 199 (Jan, 2004).
67. J. N. Weinstein, L. D. Leserman, *Pharmacology & Therapeutics* **24**, 207 (1984).
68. V. P. Torchilin, *Nature Reviews Drug Discovery* **4**, 145 (Feb, 2005).

69. D. C. Drummond, O. Meyer, K. L. Hong, D. B. Kirpotin, D. Papahadjopoulos, *Pharmacological Reviews* **51**, 691 (Dec, 1999).
70. A. Gabizon, H. Shmeeda, Y. Barenholz, *Clinical Pharmacokinetics* **42**, 419 (2003).
71. A. A. Gabizon, *Clinical Cancer Research* **7**, 223 (Feb, 2001).
72. V. P. Torchilin, *Advanced Drug Delivery Reviews* **58**, 1532 (Dec 1, 2006).
73. X. Guo, F. C. Szoka, *Accounts of Chemical Research* **36**, 335 (May, 2003).
74. V. A. Slepushkin *et al.*, *Journal of Biological Chemistry* **272**, 2382 (Jan 24, 1997).
75. I. Cheong *et al.*, *Science* **314**, 1308 (Nov 24, 2006).
76. D. Needham, G. Anyarambhatla, G. Kong, M. W. Dewhirst, *Cancer Research* **60**, 1197 (Mar 1, 2000).
77. B. M. Discher *et al.*, *Science* **284**, 1143 (May 14, 1999).
78. J. C. M. Lee *et al.*, *Biotechnology and Bioengineering* **73**, 135 (Apr 20, 2001).
79. P. J. Photos, L. Bacakova, B. Discher, F. S. Bates, D. E. Discher, *Journal of Controlled Release* **90**, 323 (Jul 31, 2003).
80. D. R. Arifin, A. F. Palmer, *Biomacromolecules* **6**, 2172 (Jul-Aug, 2005).
81. F. Ahmed *et al.*, *Molecular Pharmaceutics* **3**, 340 (May-Jun, 2006).
82. S. Dhar, F. X. Gu, R. Langer, O. C. Farokhzad, S. J. Lippard, *Proceedings of the National Academy of Sciences of the United States of America* **105**, 17356 (Nov 11, 2008).
83. J. M. Chan *et al.*, *Biomaterials* **30**, 1627 (Mar, 2009).
84. J. Cheng *et al.*, *Biomaterials* **28**, 869 (Feb, 2007).
85. E. Bilensoy, *Febs Journal* **273**, 35 (Jun, 2006).
86. R. Karnik *et al.*, *Nano Letters* **8**, 2906 (Sep, 2008).
87. V. P. Torchilin, *Journal of Controlled Release* **73**, 137 (Jun 15, 2001).
88. V. P. Torchilin, *Pharmaceutical Research* **24**, 1 (Jan, 2007).
89. K. Kato *et al.*, *Journal of Clinical Oncology* **24**, 83s (Jun 20, 2006).
90. Y. Geng *et al.*, *Nature Nanotechnology* **2**, 249 (Apr, 2007).
91. G. von Maltzahn, S. Vauthey, S. Santoso, S. U. Zhang, *Langmuir* **19**, 4332 (May 13, 2003).
92. N. Tang *et al.*, *Journal of the National Cancer Institute* **99**, 1004 (Jul 4, 2007).
93. J. H. Park, G. von Maltzahn, E. Ruoslahti, S. N. Bhatia, M. J. Sailor, *Angewandte Chemie-International Edition* **47**, 7284 (2008).
94. S. Cammas *et al.*, *Journal of Controlled Release* **48**, 157 (Oct 13, 1997).
95. M. C. Jones, M. Ranger, J. C. Leroux, *Bioconjugate Chemistry* **14**, 774 (Jul-Aug, 2003).
96. C. Giacomelli *et al.*, *Biomacromolecules* **7**, 817 (Mar, 2006).
97. S. Sengupta *et al.*, *Nature* **436**, 568 (Jul 28, 2005).
98. L. F. Zhang *et al.*, *Acs Nano* **2**, 1696 (Aug, 2008).
99. J. L. Meyer, *Cancer Research* **44**, 4745 (1984).
100. E. J. Hall, L. Roizintowle, *Cancer Research* **44**, 4708 (1984).
101. M. Ahmed, S. N. Goldberg, *International Journal of Hyperthermia* **20**, 781 (Nov, 2004).
102. E. L. Jones *et al.*, *Journal of Clinical Oncology* **23**, 3079 (May 1, 2005).

103. H. R. Moyer, K. A. Delman, *International Journal of Hyperthermia* **24**, 251 (May, 2008).
104. P. Wust *et al.*, *Lancet Oncology* **3**, 487 (Aug, 2002).
105. G. Kong, R. D. Braun, M. W. Dewhirst, *Cancer Research* **60**, 4440 (Aug 15, 2000).
106. G. Kong, R. D. Braun, M. W. Dewhirst, *Cancer Research* **61**, 3027 (Apr 1, 2001).
107. H. Xie, K. L. Gill-Sharp, P. O'Neal, *Nanomed-Nanotechnol* **3**, 89 (Mar, 2007).
108. W. D. James, L. R. Hirsch, J. L. West, P. D. O'Neal, J. D. Payne, *J Radioanal Nucl Ch* **271**, 455 (Feb, 2007).
109. E. B. Dickerson *et al.*, *Cancer Lett* **269**, 57 (Sep 28, 2008).
110. G. H. Wu *et al.*, *Journal of the American Chemical Society* **130**, 8175 (Jul 2, 2008).
111. A. Perro, S. Reculusa, S. Ravaine, E. B. Bourgeat-Lami, E. Duguet, *Journal of Materials Chemistry* **15**, 3745 (2005).
112. A. Perro, S. Reculusa, E. Bourgeat-Lami, E. Duguet, S. Ravaine, *Colloids and Surfaces a-Physicochemical and Engineering Aspects* **284**, 78 (Aug 15, 2006).
113. K. H. Roh, D. C. Martin, J. Lahann, *Nature Materials* **4**, 759 (Oct, 2005).
114. L. Hong, S. Jiang, S. Granick, *Langmuir* **22**, 9495 (Nov 7, 2006).
115. L. Nie, S. Y. Liu, W. M. Shen, D. Y. Chen, M. Jiang, *Angewandte Chemie-International Edition* **46**, 6321 (2007).
116. R. Weissleder, A. Bogdanov, E. A. Neuwelt, M. Papisov, *Adv Drug Deliver Rev* **16**, 321 (SEP, 1995).
117. M. G. Harisinghani, R. Weissleder, *Plos Med* **1**, 202 (DEC, 2004).
118. Y. Matsumura, H. Maeda, *Cancer Research* **46**, 6387 (Dec, 1986).
119. A. Pluen *et al.*, *Proceedings of the National Academy of Sciences of the United States of America* **98**, 4628 (Apr 10, 2001).
120. F. Yuan *et al.*, *Cancer Research* **54**, 3352 (Jul 1, 1994).
121. F. Yuan *et al.*, *Cancer Research* **55**, 3752 (Sep 1, 1995).
122. H. Hashizume *et al.*, *Am J Pathol* **156**, 1363 (APR, 2000).
123. S. K. Hobbs *et al.*, *P Natl Acad Sci USA* **95**, 4607 (APR 14, 1998).
124. R. K. Jain, *Cancer Metast Rev* **9**, 253 (NOV, 1990).
125. R. K. Jain, *Adv Drug Deliver Rev* **46**, 149 (MAR 1, 2001).
126. R. Duncan, *Nat Rev Drug Discov* **2**, 347 (MAY, 2003).
127. P. M. Winter *et al.*, *Circulation* **108**, 2270 (Nov 4, 2003).
128. S. A. Wickline, A. M. Neubauer, P. Winter, S. Caruthers, G. Lanza, *Arterioscl Throm Vas* **26**, 435 (Mar, 2006).
129. E. Ruoslahti, D. Rajotte, *Annu Rev Immunol* **18**, 813 (2000).
130. E. Ruoslahti, *Nature Reviews Cancer* **2**, 83 (Feb, 2002).
131. E. Ruoslahti, *Annu Rev Cell Dev Biol* **12**, 697 (1996).
132. D. Putnam, J. Kopecek, *Adv Polym Sci* **122**, 55 (1995).
133. A. K. Patri *et al.*, *Bioconjugate Chem* **15**, 1174 (NOV-DEC, 2004).
134. T. M. Allen, G. J. R. Charrois, P. Sapra, *Abstr Pap Am Chem S* **226**, U458 (SEP, 2003).
135. R. Pasqualini, E. Ruoslahti, *Nature* **380**, 364 (Mar 28, 1996).
136. J. W. Smith, E. Ruoslahti, *Biotechnology & Genetic Engineering Reviews, Vol 14* **14**, 51 (1997).

137. D. S. Wilson, J. W. Szostak, *Annual Review of Biochemistry* **68**, 611 (1999).
138. G. P. Smith, V. A. Petrenko, *Chemical Reviews* **97**, 391 (Mar-Apr, 1997).
139. L. Cerchia, J. Hamm, D. Libri, B. Tavitian, V. de Franciscis, *Febs Lett* **528**, 12 (SEP 25, 2002).
140. V. Bagalkot, O. C. Farokhzad, R. Langer, S. Jon, *Angew Chem Int Edit* **45**, 8149 (2006).
141. O. C. Farokhzad *et al.*, *Proceedings of the National Academy of Sciences of the United States of America* **103**, 6315 (Apr 18, 2006).
142. R. Weissleder, K. Kelly, E. Y. Sun, T. Shtatland, L. Josephson, *Nature Biotechnology* **23**, 1418 (Nov, 2005).
143. X. Montet, M. Funovics, K. Montet-Abou, R. Weissleder, L. Josephson, *J Med Chem* **49**, 6087 (Oct 5, 2006).
144. D. Simberg *et al.*, *P Natl Acad Sci USA* **104**, 932 (Jan 16, 2007).
145. M. E. Akerman, W. C. W. Chan, P. Laakkonen, S. N. Bhatia, E. Ruoslahti, *P Natl Acad Sci USA* **99**, 12617 (OCT 1, 2002).
146. R. M. Schiffelers *et al.*, *Nucleic Acids Research* **32**, (2004).
147. J. H. Rao, J. Lahiri, L. Isaacs, R. M. Weis, G. M. Whitesides, *Science* **280**, 708 (May 1, 1998).
148. M. Mammen, S. K. Choi, G. M. Whitesides, *Angew Chem Int Edit* **37**, 2755 (1998).
149. S. Hong *et al.*, *Chemistry & Biology* **14**, 107 (Jan, 2007).
150. D. W. Bartlett, H. Su, I. J. Hildebrandt, W. A. Weber, M. E. Davis, *Proc Natl Acad Sci U S A* **104**, 15549 (Sep 25, 2007).
151. D. B. Kirpotin *et al.*, *Cancer Res* **66**, 6732 (Jul 1, 2006).
152. G. M. Thurber, S. C. Zajic, K. D. Wittrup, *J Nucl Med* **48**, 995 (Jun, 2007).
153. S. Christian *et al.*, *J Cell Biol* **163**, 871 (NOV 24, 2003).
154. E. Ruoslahti, *Cancer Cell* **2**, 97 (AUG, 2002).
155. E. Ruoslahti, D. Rajotte, *Annu Rev Immunol* **18**, 813 (2000).
156. D. W. Bartlett, H. Su, I. J. Hildebrandt, W. A. Weber, M. E. Davis, *Proceedings of the National Academy of Sciences of the United States of America* **104**, 15549 (Sep 25, 2007).
157. M. K. Khan *et al.*, *Technology in Cancer Research & Treatment* **4**, 603 (Dec, 2005).
158. Y. W. Cho *et al.*, *Biomaterials* **28**, 1236 (Feb, 2007).
159. J. F. Hainfeld, D. N. Slatkin, T. M. Focella, H. M. Smilowitz, *British Journal of Radiology* **79**, 248 (Mar, 2006).
160. K. J. Harrington *et al.*, *British Journal of Cancer* **83**, 232 (Jul, 2000).
161. S. Kommareddy, M. Amiji, *Journal of Pharmaceutical Sciences* **96**, 397 (Feb, 2007).
162. J. F. Kukowska-Latallo *et al.*, *Cancer Research* **65**, 5317 (Jun 15, 2005).
163. E. Kajiwara *et al.*, *Journal of Controlled Release* **120**, 104 (Jul 13, 2007).
164. G. Hu *et al.*, *International Journal of Cancer* **120**, 1951 (May 1, 2007).
165. D. C. Bibby *et al.*, *International Journal of Pharmaceutics* **293**, 281 (Apr 11, 2005).
166. S. S. Nigavekar *et al.*, *Pharmaceutical Research* **21**, 476 (Mar, 2004).

167. D. W. Bartlett, M. E. Davis, *Biotechnology and Bioengineering* **99**, 975 (Mar 1, 2008).
168. S. Hussain, A. Pluckthun, T. M. Allen, U. Zangemeister-Wittke, *Molecular Cancer Therapeutics* **6**, 3019 (Nov, 2007).
169. L. D. Leserman, J. Barbet, F. Kourilsky, J. N. Weinstein, *Nature* **288**, 602 (Dec 11, 1980).
170. T. D. Heath, R. T. Fraley, D. Papahdjopoulos, *Science* **210**, 539 (Oct 31, 1980).
171. J. D. Hood *et al.*, *Science* **296**, 2404 (Jun 28, 2002).
172. O. C. Farokhzad *et al.*, *Cancer Research* **64**, 7668 (Nov 1, 2004).
173. R. Schwaab *et al.*, *Thrombosis and Haemostasis* **74**, 1402 (Dec, 1995).
174. P. M. Green, D. R. Bentley, R. S. Mibashan, I. M. Nilsson, F. Giannelli, *Embo Journal* **8**, 1067 (Apr, 1989).
175. C. M. Niemeyer, *Angew Chem Int Edit* **40**, 4128 (2001).
176. N. L. Rosi, C. A. Mirkin, *Chem Rev* **105**, 1547 (Apr, 2005).
177. C. A. Mirkin, R. L. Letsinger, R. C. Mucic, J. J. Storhoff, *Nature* **382**, 607 (AUG 15, 1996).
178. A. Tsourkas, O. Hofstetter, H. Hofstetter, R. Weissleder, L. Josephson, *Angew Chem Int Edit* **43**, 2395 (2004).
179. J. M. Perez, L. Josephson, T. O'Loughlin, D. Hogemann, R. Weissleder, *Nature Biotechnology* **20**, 816 (AUG, 2002).
180. J. M. Perez, F. J. Simeone, Y. Saeki, L. Josephson, R. Weissleder, *Journal of the American Chemical Society* **125**, 10192 (AUG 27, 2003).
181. M. Zhao, L. Josephson, Y. Tang, R. Weissleder, *Angew Chem Int Edit* **42**, 1375 (2003).
182. J. M. Perez, L. Josephson, R. Weissleder, *Chembiochem* **5**, 261 (Mar 5, 2004).
183. J. M. Perez, T. O'Loughin, F. J. Simeone, R. Weissleder, L. Josephson, *J Am Chem Soc* **124**, 2856 (Mar 27, 2002).
184. T. J. Harris, G. von Maltzahn, A. M. Derfus, E. Ruoslahti, S. N. Bhatia, *Angew Chem Int Ed Engl* **45**, 3161 (May 5, 2006).
185. J. J. Storhoff, A. D. Lucas, V. Garimella, Y. P. Bao, U. R. Muller, *Nat Biotechnol* **22**, 883 (Jul, 2004).
186. D. G. Georganopoulou *et al.*, *Proceedings of the National Academy of Sciences of the United States of America* **102**, 2273 (FEB 15, 2005).
187. C. J. Loweth, W. B. Caldwell, X. G. Peng, A. P. Alivisatos, P. G. Schultz, *Angewandte Chemie-International Edition* **38**, 1808 (1999).
188. Y. Choi, N. H. Ho, C. H. Tung, *Angewandte Chemie-International Edition* **46**, 707 (2007).
189. J. Grimm, J. M. Perez, L. Josephson, R. Weissleder, *Cancer Res* **64**, 639 (Jan 15, 2004).
190. P. Gillis, F. Moiny, R. A. Brooks, *Magnetic Resonance in Medicine* **47**, 257 (FEB, 2002).
191. R. A. Brooks, F. Moiny, P. Gillis, *Magnetic Resonance in Medicine* **45**, 1014 (JUN, 2001).
192. J. M. Perez, F. J. Simeone, A. Tsourkas, L. Josephson, R. Weissleder, *Nano Letters* **4**, 119 (JAN, 2004).

193. M. M. Stevens, N. T. Flynn, C. Wang, D. A. Tirrell, R. Langer, *Advanced Materials* **16**, 915 (JUN 4, 2004).
194. G. M. Whitesides, B. Grzybowski, *Science* **295**, 2418 (MAR 29, 2002).
195. P. Alivisatos, *Nature Biotechnology* **22**, 47 (JAN, 2004).
196. G. Giannelli, J. FalkMarzillier, O. Schiraldi, W. G. StetlerStevenson, V. Quaranta, *Science* **277**, 225 (JUL 11, 1997).
197. D. R. Edwards, G. Murphy, *Nature* **394**, 527 (AUG 6, 1998).
198. J. M. Fang *et al.*, *Proceedings of the National Academy of Sciences of the United States of America* **97**, 3884 (APR 11, 2000).
199. J. L. Seltzer *et al.*, *Journal of Biological Chemistry* **265**, 20409 (NOV 25, 1990).
200. J. M. Harris, R. B. Chess, *Nature Reviews Drug Discovery* **2**, 214 (MAR, 2003).
201. R. Gref *et al.*, *Science* **263**, 1600 (MAR 18, 1994).
202. E. Morgunova *et al.*, *Science* **284**, 1667 (JUN 4, 1999).
203. C. Bremer, C. H. Tung, R. Weissleder, *Nature Medicine* **7**, 743 (JUN, 2001).
204. M. G. Harisinghani *et al.*, *New England Journal of Medicine* **348**, 2491 (JUN 19, 2003).
205. C. Bremer, S. Bredow, U. Mahmood, R. Weissleder, C. H. Tung, *Radiology* **221**, 523 (NOV, 2001).
206. T. Jiang *et al.*, *Proceedings of the National Academy of Sciences of the United States of America* **101**, 17867 (DEC 21, 2004).
207. M. D. Sternlicht, Z. Werb, *Annual Review of Cell and Developmental Biology* **17**, 463 (2001).
208. M. E. Stearns, M. Wang, *Cancer Research* **53**, 878 (FEB 15, 1993).
209. A. Talvensaari-Mattila, P. Paakko, T. Turpeenniemi-Hujanen, *British Journal of Cancer* **89**, 1270 (OCT 6, 2003).
210. B. Davidson *et al.*, *Gynecologic Oncology* **73**, 372 (JUN, 1999).
211. Y. Lalatonne, J. Richardi, M. P. Pileni, *Nature Materials* **3**, 121 (FEB, 2004).
212. A. M. Derfus, W. C. W. Chan, S. N. Bhatia, *Adv Mater* **16**, 961 (Jun 17, 2004).
213. Z. Wang, R. Levy, D. G. Fernig, M. Brust, *J Am Chem Soc* **128**, 2214 (Feb 22, 2006).
214. C. Chang, Z. Werb, *Trends in Cell Biology* **11**, S37 (NOV, 2001).
215. H. Kanayama *et al.*, *Cancer* **82**, 1359 (APR 1, 1998).
216. B. I. Ratnikov, E. I. Deryugina, A. Y. Strongin, *Laboratory Investigation* **82**, 1583 (NOV, 2002).
217. L. A. Rudolph-Owen, R. Chan, W. J. Muller, L. M. Matrisian, *Cancer Res* **58**, 5500 (Dec 1, 1998).
218. D. L. Hulboy, S. Gautam, B. Fingleton, L. M. Matrisian, *Oncol Rep* **12**, 13 (Jul, 2004).
219. M. M. Pacheco, M. Mourao, E. B. Mantovani, I. N. Nishimoto, M. M. Brentani, *Clin Exp Metastasis* **16**, 577 (Oct, 1998).
220. J. L. Seltzer *et al.*, *J Biol Chem* **265**, 20409 (Nov 25, 1990).
221. B. E. Turk, L. L. Huang, E. T. Piro, L. C. Cantley, *Nat Biotechnol* **19**, 661 (Jul, 2001).
222. L. M. Luttrell, Y. Daaka, R. J. Lefkowitz, *Curr Opin Cell Biol* **11**, 177 (Apr, 1999).
223. T. Boulikas, *Crit Rev Eukaryot Gene Expr* **5**, 1 (1995).

224. A. P. Wolffe, J. J. Hayes, *Nucleic Acids Res* **27**, 711 (Feb 1, 1999).
225. M. A. Schwartz, M. D. Schaller, M. H. Ginsberg, *Annu Rev Cell Dev Biol* **11**, 549 (1995).
226. G. Manning, D. B. Whyte, R. Martinez, T. Hunter, S. Sudarsanam, *Science* **298**, 1912 (DEC 6, 2002).
227. A. Ullrich, J. Schlessinger, *Cell* **61**, 203 (APR 20, 1990).
228. B. J. Druker *et al.*, *New Engl J Med* **344**, 1031 (APR 5, 2001).
229. T. G. Lugo, A. M. Pendergast, A. J. Muller, O. N. Witte, *Science* **247**, 1079 (MAR 2, 1990).
230. Z. Songyang *et al.*, *Cell* **72**, 767 (Mar 12, 1993).
231. J. M. Perez, L. Josephson, T. O'Loughlin, D. Hogemann, R. Weissleder, *Nat Biotechnol* **20**, 816 (Aug, 2002).
232. A. Y. Ting, K. H. Kain, R. L. Klemke, R. Y. Tsien, *Proc Natl Acad Sci U S A* **98**, 15003 (Dec 18, 2001).
233. J. D. Violin, J. Zhang, R. Y. Tsien, A. C. Newton, *J Cell Biol* **161**, 899 (JUN 9, 2003).
234. Y. Wang *et al.*, *Nature* **434**, 1040 (Apr 21, 2005).
235. A. Prinz, M. Diskar, A. Erlbruch, F. W. Herberg, *Cell Signal* **18**, 1616 (Oct, 2006).
236. F. Rininsland *et al.*, *P Natl Acad Sci USA* **101**, 15295 (Oct 26, 2004).
237. M. D. Shults, B. Imperiali, *J Am Chem Soc* **125**, 14248 (Nov 26, 2003).
238. M. D. Shults, K. A. Janes, D. A. Lauffenburger, B. Imperiali, *Nat Methods* **2**, 277 (Apr, 2005).
239. T. Atanasijevic, M. Shusteff, P. Fam, A. Jasanoff, *Proc Natl Acad Sci U S A* **103**, 14707 (Oct 3, 2006).
240. Y. Choi, N. H. Ho, C. H. Tung, *Angew Chem Int Ed Engl* **46**, 707 (Dec 4, 2006).
241. L. Josephson, C. H. Tung, A. Moore, R. Weissleder, *Bioconjug Chem* **10**, 186 (Mar-Apr, 1999).
242. S. Palmacci, and Josephson, L, in *U.S. Patent* (1993), vol. 5, pp. 176
243. T. Shen, R. Weissleder, M. Papisov, A. Bogdanov, Jr., T. J. Brady, *Magn Reson Med* **29**, 599 (May, 1993).
244. M. E. Vazquez, J. B. Blanco, B. Imperiali, *J Am Chem Soc* **127**, 1300 (Feb 2, 2005).
245. S. L. Bellis, J. T. Miller, C. E. Turner, *J Biol Chem* **270**, 17437 (Jul 21, 1995).
246. M. D. Schaller, J. T. Parsons, *Mol Cell Biol* **15**, 2635 (May, 1995).
247. J. Rao, J. Lahiri, L. Isaacs, R. M. Weis, G. M. Whitesides, *Science* **280**, 708 (May 1, 1998).
248. D. Simberg *et al.*, *Proc Natl Acad Sci U S A* **104**, 932 (Jan 16, 2007).
249. R. Weissleder, K. Kelly, E. Y. Sun, T. Shtatland, L. Josephson, *Nat Biotechnol* **23**, 1418 (Nov, 2005).
250. H. Duan, S. Nie, *J Am Chem Soc*, (Feb 24, 2007).
251. Z. Medarova, W. Pham, C. Farrar, V. Petkova, A. Moore, *Nat Med*, (Feb 25, 2007).
252. P. Laakkonen, K. Porkka, J. A. Hoffman, E. Ruoslahti, *Nat Med* **8**, 751 (Jul, 2002).

253. S. M. Lee *et al.*, *Mol Cancer Res* **5**, 11 (Jan, 2007).
254. D. Rajotte, E. Ruoslahti, *J Biol Chem* **274**, 11593 (Apr 23, 1999).
255. K. Porkka, P. Laakkonen, J. A. Hoffman, M. Bernasconi, E. Ruoslahti, *Proc Natl Acad Sci U S A* **99**, 7444 (May 28, 2002).
256. E. Ruoslahti, *Biochem Soc Trans* **32**, 397 (Jun, 2004).
257. G. R. Reddy *et al.*, *Clin Cancer Res* **12**, 6677 (Nov 15, 2006).
258. C. Zhang *et al.*, *Cancer Res* **67**, 1555 (Feb 15, 2007).
259. R. J. Giordano *et al.*, *Chem Biol* **12**, 1075 (Oct, 2005).
260. G. Colombo *et al.*, *J Biol Chem* **277**, 47891 (Dec 6, 2002).
261. A. Rozek, J. P. Powers, C. L. Friedrich, R. E. Hancock, *Biochemistry* **42**, 14130 (Dec 9, 2003).
262. E. Ruoslahti, M. D. Pierschbacher, *Science* **238**, 491 (Oct 23, 1987).
263. J. J. Green *et al.*, *Nano Lett* **7**, 874 (Apr, 2007).
264. K. Sokolov *et al.*, *Cancer Res* **63**, 1999 (May 1, 2003).
265. H. C. Kolb, M. G. Finn, K. B. Sharpless, *Angew Chem Int Ed Engl* **40**, 2004 (Jun 1, 2001).
266. J. W. Lee *et al.*, *Bioconjug Chem* **18**, 579 (Mar-Apr, 2007).
267. P. Wu *et al.*, *Chem Commun (Camb)*, 5775 (Dec 14, 2005).
268. Q. Shi, X. Chen, T. Lu, X. Jing, *Biomaterials* **29**, 1118 (Mar, 2008).
269. D. I. Rozkiewicz *et al.*, *Chembiochem* **8**, 1997 (Nov 5, 2007).
270. S. Ciampi *et al.*, *Langmuir* **23**, 9320 (Aug 28, 2007).
271. G. K. Such, E. Tjipto, A. Postma, A. P. Johnston, F. Caruso, *Nano Lett* **7**, 1706 (Jun, 2007).
272. H. Li, F. Cheng, A. M. Duft, A. Adronov, *J Am Chem Soc* **127**, 14518 (Oct 19, 2005).
273. S. Cavalli, A. R. Tipton, M. Overhand, A. Kros, *Chem Commun (Camb)*, 3193 (Aug 14, 2006).
274. M. Fischler *et al.*, *Chem Commun (Camb)*, 169 (Jan 14, 2008).
275. J. A. Opsteen, R. P. Brinkhuis, R. L. Teeuwen, D. W. Lowik, J. C. van Hest, *Chem Commun (Camb)*, 3136 (Aug 14, 2007).
276. P. Antoni, D. Nystrom, C. J. Hawker, A. Hult, M. Malkoch, *Chem Commun (Camb)*, 2249 (Jun 14, 2007).
277. Q. Zeng *et al.*, *Chem Commun (Camb)*, 1453 (Apr 14, 2007).
278. J. L. Brennan *et al.*, *Bioconjug Chem* **17**, 1373 (Nov-Dec, 2006).
279. E. Y. Sun, L. Josephson, R. Weissleder, *Mol Imaging* **5**, 122 (Apr-Jun, 2006).
280. F. Said Hassane, B. Frisch, F. Schuber, *Bioconjug Chem* **17**, 849 (May-Jun, 2006).
281. P. Laakkonen *et al.*, *Proc Natl Acad Sci U S A* **101**, 9381 (Jun 22, 2004).
282. V. Fogal, Zhang, L., and Ruoslahti, E., *Cancer Research* **(Submitted)**.
283. D. B. Rubinstein *et al.*, *Int J Cancer* **110**, 741 (Jul 10, 2004).
284. X. Montet, M. Funovics, K. Montet-Abou, R. Weissleder, L. Josephson, *J Med Chem* **49**, 6087 (Oct 5, 2006).
285. S. Unezaki *et al.*, *Int J Pharm* **144**, 11 (Nov 22, 1996).
286. D. H. Son *et al.*, *Ejc Suppl* **4**, 47 (Nov, 2006).
287. S. M. Moghimi, J. Szebeni, *Prog Lipid Res* **42**, 463 (Nov, 2003).
288. S. M. Moghimi, A. C. Hunter, J. C. Murray, *Pharmacol Rev* **53**, 283 (Jun, 2001).

289. F. Gu *et al.*, *P Natl Acad Sci USA* **105**, 2586 (Feb 19, 2008).
290. P. K. Jain, K. S. Lee, I. H. El-Sayed, M. A. El-Sayed, *J Phys Chem B* **110**, 7238 (Apr 13, 2006).
291. C. Yu, H. Nakshatri, J. Irudayaraj, *Nano Lett* **7**, 2300 (Aug, 2007).
292. H. Wang *et al.*, *Proc Natl Acad Sci U S A* **102**, 15752 (Nov 1, 2005).
293. A. G. Skirtach *et al.*, *Adv Mater* **20**, 506 (Feb 4, 2008).
294. L. Tong *et al.*, *Adv Mater* **19**, 3136 (Oct 19, 2007).
295. T. B. Huff *et al.*, *Nanomedicine-Uk* **2**, 125 (Feb, 2007).
296. J. M. Harris, R. B. Chess, *Nat Rev Drug Discov* **2**, 214 (Mar, 2003).
297. R. Duncan, *Nat Rev Drug Discov* **2**, 347 (May, 2003).
298. L. Josephson, C. H. Tung, A. Moore, R. Weissleder, *Bioconjugate Chemistry* **10**, 186 (Mar-Apr, 1999).
299. S. R. Khetani, S. N. Bhatia, *Nat Biotechnol* **26**, 120 (Jan, 2008).
300. B. Ballou, B. C. Lagerholm, L. A. Ernst, M. P. Bruchez, A. S. Waggoner, *Bioconjug Chem* **15**, 79 (Jan-Feb, 2004).
301. G. F. Paciotti *et al.*, *Drug Deliv* **11**, 169 (May-Jun, 2004).
302. T. Niidome *et al.*, *J Control Release* **114**, 343 (Sep 12, 2006).
303. X. Qian *et al.*, *Nat Biotechnol* **26**, 83 (Jan, 2008).
304. H. H. Pennes, *J. Appl. Physiology* **1**, 93 (1948).
305. A. J. Welch, *IEEE J. Quantum Electronics* **20**, 1471 (1984).
306. T. J. W. M. Motamedi , A.J. Welch, *Laser Inst. Amer. Los Angeles, CA,.* (1983).
307. P. K. Jain, S. Eustis, M. A. El-Sayed, *Journal of Physical Chemistry B* **110**, 18243 (Sep 21, 2006).
308. S. Sengupta *et al.*, *Nature* **436**, 568 (Jul 28, 2005).
309. D. C. Litzinger, L. Huang, *Biochimica Et Biophysica Acta* **1113**, 201 (Aug 14, 1992).
310. A. Akinc *et al.*, *Nature Biotechnology* **26**, 561 (May, 2008).
311. D. G. Anderson, D. M. Lynn, R. Langer, *Angewandte Chemie-International Edition* **42**, 3153 (2003).
312. H. Hashizume *et al.*, *Am J Pathol* **156**, 1363 (Apr, 2000).
313. H. Maeda, *Adv Enzyme Regul* **41**, 189 (2001).
314. F. A. Jaffer *et al.*, *Circulation* **110**, 170 (Jul 13, 2004).
315. C. H. Tung *et al.*, *Chembiochem* **4**, 897 (Sep 5, 2003).
316. K. Overoye-Chan *et al.*, *Journal of the American Chemical Society* **130**, 6025 (May 7, 2008).
317. P. E. Thorpe, *Clin Cancer Res* **10**, 415 (Jan 15, 2004).
318. M. J. Hope, M. B. Bally, G. Webb, P. R. Cullis, *Biochimica Et Biophysica Acta* **812**, 55 (1985).
319. L. D. Mayer, M. B. Bally, M. J. Hope, P. R. Cullis, *Biochimica Et Biophysica Acta* **816**, 294 (1985).
320. F. J. Isaacs, D. J. Dwyer, J. J. Collins, *Nature Biotechnology* **24**, 545 (May, 2006).
321. J. Hasty, D. McMillen, J. J. Collins, *Nature* **420**, 224 (Nov 14, 2002).
322. L. R. Paborsky, I. W. Caras, K. L. Fisher, C. M. Gorman, *J Biol Chem* **266**, 21911 (Nov 15, 1991).
323. T. Kessler *et al.*, *Clinical Cancer Research* **11**, 6317 (Sep 1, 2005).
324. X. M. Huang *et al.*, *Science* **275**, 547 (Jan 24, 1997).

325. R. M. Sharkey, D. M. Goldenberg, *Cancer Investigation* **24**, 82 (2006).
326. J. E. Bailey, *Science* **252**, 1668 (Jun 21, 1991).
327. H. Kitano, *Nature* **420**, 206 (Nov 14, 2002).